

Aerosol typing over Europe and its benefits for the CALIPSO and EarthCARE missions

**Statistical analysis based on multiwavelength aerosol
lidar measurements from ground-based EARLINET
stations and comparison to spaceborne CALIPSO data**

Der Fakultät für Physik und Geowissenschaften
der Universität Leipzig
eingereichte

DISSERTATION

zur Erlangung des akademischen Grades

DOCTOR RERUM NATURALIUM
(DR. RER. NAT.)

vorgelegt

von Diplom-Meteorologin Anja Schwarz, geb. Hiebsch
geboren am 10. Juli 1982 in Magdeburg

Leipzig, den 6. August 2015

Table of Contents

| | | |
|----------|---|-----------|
| 1 | Introduction | 1 |
| 2 | Aerosol typing – Current state of research | 5 |
| 2.1 | Methods of aerosol classification | 5 |
| 2.1.1 | Optical Properties of Aerosols and Clouds (OPAC) | 7 |
| 2.1.2 | Aerosol typing with lidar | 7 |
| 2.1.3 | CALIPSO aerosol typing scheme | 9 |
| 2.1.4 | Aerosol typing by using the Mahalanobis distance | 10 |
| 2.1.5 | Lidar algorithms to retrieve information on aerosol components | 11 |
| 2.2 | Major aerosol types and their source regions | 12 |
| 2.2.1 | Marine aerosol | 12 |
| 2.2.2 | Desert dust | 13 |
| 2.2.3 | Biomass-burning (smoke) aerosol | 16 |
| 2.2.4 | Polluted continental aerosol | 18 |
| 2.2.5 | Clean continental aerosol | 20 |
| 2.2.6 | Tropospheric volcanic aerosol | 21 |
| 2.2.7 | Stratospheric aerosol | 22 |
| 2.2.8 | Aerosol mixtures | 22 |
| 2.2.9 | Aerosols over Europe | 23 |
| 2.3 | Results of aerosol typing studies | 24 |
| 2.4 | Verification of CALIPSO observations | 36 |
| 2.4.1 | Representativeness of CALIPSO measurements | 36 |
| 2.4.2 | Validation of CALIPSO aerosol products | 37 |
| 2.5 | Approaches of the aerosol typing and verification of the CALIPSO classification scheme presented in this thesis | 40 |
| 3 | EARLINET and CALIPSO | 41 |
| 3.1 | EARLINET – European Aerosol Research Lidar Network | 41 |
| 3.1.1 | Setup of the network | 41 |
| 3.1.2 | Measurement principle and available products | 42 |

| | | |
|----------|--|-----------|
| 3.1.3 | Data set | 49 |
| 3.2 | CALIPSO – Cloud–Aerosol Lidar and Infrared Pathfinder Satellite Observations | 52 |
| 3.2.1 | CALIOP instrument | 52 |
| 3.2.2 | Data evaluation | 53 |
| 3.2.3 | CALIPSO Lidar products | 56 |
| 4 | Auxiliary data and tools for stand-alone aerosol typing | 61 |
| 4.1 | Meteorological parameters | 61 |
| 4.2 | Modeling tools for aerosol source identification | 62 |
| 4.2.1 | FLEXPART | 62 |
| 4.2.2 | HYSPLIT | 63 |
| 4.3 | Aerosol source information | 63 |
| 4.3.1 | NAAPS Global Aerosol Model | 63 |
| 4.3.2 | DREAM dust forecast | 64 |
| 4.3.3 | AERONET Sun photometer data | 64 |
| 4.3.4 | MODIS fire maps | 65 |
| 5 | Vertically resolved aerosol characterization over Europe | 67 |
| 5.1 | Data evaluation concept | 67 |
| 5.1.1 | Feature finding | 68 |
| 5.1.2 | Feature classification | 69 |
| 5.1.3 | Feature comparison | 71 |
| 5.2 | Case studies | 74 |
| 5.2.1 | Saharan dust: Potenza, 16–17 April 2009 | 74 |
| 5.2.2 | Biomass-burning aerosol: Thessaloniki, 14–15 August 2008 | 76 |
| 5.2.3 | Mixture of dust and marine aerosol: Potenza, 8 July 2008 | 79 |
| 5.2.4 | Mixture of smoke and pollution aerosol: Athens, 29–30 July 2008 | 80 |
| 6 | Statistical analysis | 83 |
| 6.1 | Aerosol optical parameters from EARLINET measurements | 84 |
| 6.1.1 | Occurrence of major aerosol types | 86 |
| 6.1.2 | Optical properties of pure aerosol types | 90 |
| 6.1.3 | Optical properties of aerosol mixtures | 92 |
| 6.1.4 | Conversion factors for the harmonization of space missions | 100 |
| 6.2 | Aerosol layers in correlative EARLINET and CALIOP data – A comparison study | 107 |
| 6.2.1 | EARLINET aerosol layers detected by CALIPSO | 109 |
| 6.2.2 | Validation of the CALIPSO aerosol typing scheme | 115 |

| | |
|------------------------------|------------|
| 7 Summary and Outlook | 121 |
| Bibliography | 127 |
| List of Figures | 161 |
| List of Tables | 165 |
| List of Abbreviations | 167 |
| List of Symbols | 171 |

Chapter 1

Introduction

Aerosols – solid or liquid airborne particles – affect local radiation fluxes, the radiation budget of the atmosphere, and thus climate, because of their scattering and absorption characteristics. This influence on the incoming solar and outgoing terrestrial radiation is called direct radiative effect of aerosols. Various global aerosol models were used to estimate the aerosol direct radiative effect (aerosol-laden vs. clear-sky atmosphere) and also values of the aerosol direct radiative forcing, which is the change in aerosol direct radiative effect from pre-industrial to present-day conditions (not including climate feedbacks) [Heald *et al.*, 2014]. Results are summarized in the reports of the Intergovernmental Panel on Climate Change (IPCC) [Houghton *et al.*, 2001; Forster *et al.*, 2007; Stocker *et al.*, 2014]. There are still large uncertainties in the calculation of the aerosol direct radiative effect and the forcing values. Since aerosols show type-dependent optical characteristics, which have different effects on the aerosol direct radiative forcing in total, main aerosol components such as sulfate, black carbon, sea salt, and dust as well as their contributions have to be identified in order to provide more accurate information for aerosol transport models and radiative-transfer simulations [e.g., Nishizawa *et al.*, 2008a; Biniotoglou *et al.*, 2015; Pitari *et al.*, 2015].

Parameters needed for radiative-transfer modeling cannot be directly measured, but must be derived from scattering and extinction (= scattering and absorption) measurements [e.g., Shin *et al.*, 2014]. Detailed information on optical properties of different aerosol species can be determined from, e.g., in-situ as well as active and passive remote-sensing observations. In-situ measurements are only selective in space and time and not representative for the whole atmosphere, but additionally provide information on the chemical composition of the aerosol. The characterization of the observed aerosols from optical footprints without dealing with chemical components is called *aerosol typing* [Müller *et al.*, 2007a]. Within the last years, ground-based remote sensing has become a powerful method for the typing of aerosols. Measurements with passive sensors, e.g., sun photometers, are performed to gain detailed information on

the aerosol concentration and geographical as well as temporal variability [Kaufman *et al.*, 1997]. Sun photometer measurements only provide information about the whole atmospheric column. Since aerosol lifetime and climate response depend on altitude [Hansen *et al.*, 1997; Huang *et al.*, 2015], the vertical aerosol distribution and, hence, the profiling of aerosols is important for the accurate evaluation of the aerosol direct radiative effect [Oikawa *et al.*, 2013; Vuolo *et al.*, 2014]. For that purpose, the active **light detection and ranging** (lidar) technique, which allows for vertically resolved measurements, is used. A lidar maps the temporal and spatial evolution of the atmosphere. Vertical profiles of backscatter (180° scattering) and extinction coefficients can be derived at different wavelengths from the intensity of that part of the (pulsed) laser light that is scattered back to the lidar receiver.

Measured aerosol type-dependent properties are summarized in so-called aerosol classification models to account for specific scattering and absorption characteristics of different aerosol species [Dubovik *et al.*, 2002; Cattrall *et al.*, 2005]. The aerosol typing presented within this thesis is based on advanced multiwavelength lidar measurements of the ground-based **European Aerosol Research Lidar Network** (EARLINET) [Bösenberg *et al.*, 2001; Pappalardo *et al.*, 2014]. EARLINET stations perform regular measurements for specific locations and aerosol situations. In the present study, aerosol layers of selected EARLINET observations were investigated with respect to the aerosol source region. The aerosol type was discriminated manually by using a set of different tools (transport and trajectory models, as well as other observational data). Thus, optical properties for different aerosol types observable over Europe were derived. Values of other systematic studies on aerosol typing based on different lidar parameters presented by, e.g., Müller *et al.* [2007a], Burton *et al.* [2012, 2013, 2014], and Groß *et al.* [2013, 2015], which mainly rely on investigations of short-term data gained from several measurement campaigns, were verified and specified based on representative regular climatological EARLINET measurements.

The aerosol-type-dependent properties that were determined within this thesis can be used for the development of algorithms. These algorithms are strongly needed for the exploitation of the ever-expanding amount of observational data from ground, air and space-based applications, which is additionally increased by the ability of instruments to measure autonomously and continuously. A target categorization, i.e., the determination of different aerosol types, has to be applied to observational data whenever possible and ideally in an automated way. There is a clear trend of algorithm development that allows aerosol typing directly within the data analysis procedure and, thus, enables target classification that can be provided on-line or at least in near-real time. A very promising example was recently presented by Baars *et al.* [2015].

Furthermore, aerosol classification models are used in processing schemes of passive measurements [cf., e.g., Tanré *et al.*, 1997; Russell *et al.*, 2014] and in retrievals of

Table 1.1: Active and planned long-term spaceborne lidar observations.

| | | | |
|----------------|---------------------------------------|---------------------------------|--------------------------------|
| Mission | CALIPSO ¹ | ADM-Aeolus ² | EarthCARE ³ |
| Period | 2006–ongoing | launch expected 2016 | launch expected 2018 |
| Lidar | CALIOP ⁴ (532, 1064 nm) | ALADIN ⁵ (355 nm) | ATLID ⁶ (355 nm) |

spaceborne lidars. An example is given by *Illingworth et al.* [2014] for the Earth Clouds, Aerosols and Radiation Explorer (EarthCARE). A further study was recently presented by *Amiridis et al.* [2015]. The authors report on a three-dimensional multi-wavelength global aerosol and cloud optical climatology (Lidar climatology of Vertical Aerosol Structure for space-based lidar simulation studies – LIVAS), which is optimized to be used for future space-based lidar end-to-end simulations with realistic atmospheric scenarios as well as retrieval algorithm testing activities.

An overview of the ongoing and planned missions with space lidars is presented in Table 1.1 [*Stoffelen et al.*, 2005; *Ansmann et al.*, 2006; *Reitebuch et al.*, 2009; *Winker et al.*, 2009; *Illingworth et al.*, 2014]. The timetable of the missions shows that there will be more than 12 years of vertically resolved lidar measurements from space. These measurements have to be harmonized with respect to each other in order to establish an unique long-term global data set that is needed for the synergistic approach of satellite and ground-based observations together with model calculations. That approach is of high interest to the scientific community in order to achieve an accurate quantification of aerosol radiative forcing [e.g., *Diner et al.*, 2004]. The harmonization of the spaceborne lidar measurements poses a challenge due to the use of different lidar instrument types, observations at different wavelengths, and different measured parameters. Within the framework of this thesis, so-called wavelength conversion factors were determined, which can be used to relate results from the different space missions to each other. Calculations are based on ground-based EARLINET measurements. Since ground-based measurements cannot provide information about the vertical aerosol distribution on a global scale, especially over the oceans, there is a strong need for additional spaceborne observations. However, one shortcoming of the Cloud–Aerosol Lidar Infrared Pathfinder Satellite Observation (CALIPSO) satellite is that

¹ Cloud–Aerosol Lidar and Infrared Pathfinder Satellite Observations of the National Aeronautics and Space Administration (NASA) and the French government space agency CNES

² Atmospheric Dynamics Mission-Aeolus of the European Space Agency (ESA)

³ Earth Clouds, Aerosols and Radiation Explorer of ESA and the Japan Aerospace Exploration Agency (JAXA)

⁴ Cloud–Aerosol Lidar with Orthogonal Polarization

⁵ Atmospheric Laser Doppler Lidar Instrument

⁶ Atmospheric Lidar

the aerosol classification scheme is applied in the beginning of the satellite lidar data retrieval and, thus, contains a number of assumptions that influence the subsequent data processing [Omar *et al.*, 2009]. In contrast, type and constitution of atmospheric aerosols can be characterized from EARLINET measurements without the need of *a priori* assumptions. For this reason, EARLINET data were also used within this study to validate the spaceborne aerosol typing included in the CALIPSO classification scheme.

This thesis is structured as follows: In Chapter 2 possibilities for an aerosol classification or so-called aerosol typing are introduced and major aerosol types are explained in more detail. Furthermore, a summary of former studies about the classification of aerosols and representative values for aerosol-type-dependent parameters are given. An overview of EARLINET and CALIPSO including the measurement principle of the applied lidar techniques and available data products is presented in Chapter 3. In Chapter 4 auxiliary data and tools that were used for the stand-alone aerosol typing including the assessment of meteorological conditions are summarized. The description of the procedure to identify and classify aerosol layers in the EARLINET data can be found in the beginning of Chapter 5. This chapter also contains exemplary case studies of specific aerosol situations. Results of the statistical evaluation of EARLINET measurements including the mentioned conversion factors are presented in the first part of Chapter 6. In the second part of this chapter findings of the comparison of the aerosol typing based on data of selected EARLINET lidars against results of the CALIPSO aerosol classification scheme are shown. Finally, Chapter 7 contains results and conclusions and closes with an outlook.

Chapter 2

Aerosol typing – Current state of research

This chapter overviews the current state of research in terms of aerosol classification based on optical properties, the so-called aerosol typing. In Section 2.1 methods of aerosol classification are presented. Aerosol types, which can be observed over Europe, are introduced in Section 2.2. Results of the aerosol typing derived so far mainly based on lidar observations are summarized in Section 2.3, followed by most important findings of studies regarding the applicability of CALIPSO observations for aerosol typing purposes (cf. Section 2.4). Finally, the approaches of the aerosol typing based on EARLINET data and the validation of the CALIPSO classification scheme presented in this thesis are introduced in Section 2.5.

2.1 Methods of aerosol classification

The typing of aerosols implies the adequate characterization of aerosols in the climate system without describing their physical and chemical properties in detail. This approach neglects explicit information on size distributions, composition, phase, shape, and the internal and external mixing state of particles. Instead, macroscopic parameters such as mean optical properties of the ensemble of particles are used for the description. Depending on the application, a number of 5–10 aerosol types appears to be sufficient to cover the major global aerosol components. However, a general and unique aerosol classification scheme is not available so far. There are different approaches how an aerosol typing can be done depending on the instruments available and on the scientific issue behind.

Since years the question concerning the estimation of the anthropogenic aerosol radiative forcing has been posed. Aerosols were broadly classified being of anthropogenic

or natural origin to separate man-made from natural aerosol effects. The most important aerosol types from natural sources are sea salt and mineral dust. Smoke from biomass burning can be of natural origin as well, but is often related to anthropogenic activities. Periodically, when a major volcanic eruption injects large amounts of sulfuric gases into the stratosphere where they condense to sulfuric acid droplets, volcanic aerosols influence the global radiation budget significantly. Ash and gases emitted from volcanic sources into the troposphere may contribute to the regional aerosol load in certain areas. Furthermore, soil particles, pollen, and other biogenic material contribute to the aerosol at continental sites. Anthropogenic activities modify the natural aerosol load of the Earth's atmosphere drastically. Particles and precursor gases are emitted through industrial combustion processes, car, train, air and ship traffic, as well as agricultural and individual human activities. Sulfates, soot, nitrates, ammonium and organic carbon are typical constituents of anthropogenic aerosol. These chemical predominant species (e.g., sulfates, black carbon, organic carbon, etc.) can be used to classify aerosols in case of direct measurements of the speciation of particle samples. Further classification of aerosols can be done by their hygroscopicity as being water-soluble or water-insoluble, which is especially useful for studies concerning aerosol-cloud interactions.

The increased application of active and passive instruments for spaceborne observations has afforded global daily measurements of aerosol optical properties that are useful for type-dependent classification [Omar *et al.*, 2009]. The collaboration between different research groups around the world working on satellite aerosol retrievals shall be strengthened by the International Satellite Aerosol Science Network (AERO-SAT), which was constituted in September 2013 during the AeroCom (Aerosol Comparisons between Observations and Models) meeting. AERO-SAT is an unfunded activity. Its tasks are to advance the satellite aerosol retrieval research and product development and to coordinate scientific activities of mutual benefit (e.g., intercomparisons, common definitions, common tools, common formats, etc.). Moreover, the communication and coordination between producers of satellite information on aerosol properties and the global user community shall be stimulated. Within AERO-SAT there is a Working Group on Aerosol Typing. One of its objectives is to review methods for the retrieval of information on aerosol type from satellite and ground-based remote sensing. Information can be found at <http://www.aero-sat.org/wg-aerosol-typing.html>. Further efforts regarding the harmonization of satellite products were made, e.g., within the Climate Change Initiative (CCI) project Aerosol_cci (2010–2013) of the European Space Agency (ESA) [Holzer-Popp *et al.*, 2013]. The objective of this study was the development of algorithms for the production of long-term total column aerosol optical depth (AOD) data sets from European Earth Observation sensors.

In the following, the current most common approaches used for aerosol typing ac-

ording to optical properties are introduced in more detail. Explanations on optical properties and the theoretical background of the lidar technique are given in Section 3.1.2 in the next chapter.

2.1.1 Optical Properties of Aerosols and Clouds (OPAC)

The software package OPAC [Hess *et al.*, 1998] consists of data sets of optical properties (extinction, scattering, and absorption coefficients, single-scattering albedo, asymmetry factor, and the phase function) of cloud and aerosol components in the solar and terrestrial spectral range for different humidity conditions. Moreover, derived optical parameters like mass extinction coefficients and Ångström exponents can be determined. In case of aerosols calculations are based on microphysical data (particle size distribution and spectral refractive index) under the assumption of spherical particles. Aerosols originate from different sources and processes and, thus, often a mixture of particles is present in the atmosphere. “To describe the wide range of possible compositions, the aerosol particles are modeled as components [Deepak and Gerber, 1983], each of them meant to be representative for a certain origin. The defined aerosol components [insoluble, water-soluble, soot, sea salt (accumulation and coarse mode), mineral (nucleation, accumulation, and coarse mode, and transported), sulfate droplets] are described by individual microphysical properties resulting from the internal mixture of all chemical substances that have a similar origin. The aerosol components may then be externally mixed to form aerosol types [continental (clean, average, polluted), urban, desert, maritime (clean, polluted, tropical), Arctic, Antarctic, mineral transported, free troposphere, stratosphere]. External mixture means that there is no physical or chemical interaction between particles of different components” (cf. Hess *et al.* [1998]). OPAC is intended to serve as a tool for scientists who need to describe the optical properties of the atmosphere for climate-modeling purposes. Recently, an improved version of OPAC was made freely available at www.rascin.net [Koepke *et al.*, 2015]. For the new version OPAC 4.0, optical properties of mineral particles are modeled with respect to their non-sphericity. The application of more realistic shapes for mineral particles improves modeling of optical properties and, therefore, remote-sensing procedures for desert aerosol and the derived radiative forcing.

2.1.2 Aerosol typing with lidar

A further approach is the aerosol typing from optical data derived from lidar observations. Lidar is an effective tool for aerosol characterization and aerosol type determination, because the size of aerosol particles is of the order of the optical wavelengths. Thus, aerosol parameters measured with lidar sensitively depend on the actual parti-

cle properties. Particles from different sources, which show different sizes, absorption properties, and shapes, can be distinguished with lidar by their spectral scattering characteristics and their light-depolarizing behavior.

In general, information on the particle type can be retrieved from lidar observations when independent information on extinction and backscattering and, thus, on the extinction-to-backscatter ratio, which is referred to as the lidar ratio, is available, when extinction and backscattering are measured at several wavelengths, and/or when the depolarization of the backscattered light is determined. In numerous studies it was demonstrated that, e.g., the lidar ratio is a quantity valuable for aerosol characterization [Ansmann *et al.*, 2002; Müller *et al.*, 2002, 2003a, 2005; Mattis *et al.*, 2004; Groß *et al.*, 2013]. The lidar ratio depends on the microphysical and chemical properties of the scattering particles and, therefore, varies significantly for different aerosol types. It contains, e.g., information on the absorption and the size of the aerosol particles. In further studies the particle linear depolarization ratio was used for an aerosol-type separation [Sugimoto and Lee, 2006; Nishizawa *et al.*, 2007; Tesche *et al.*, 2009a; Ansmann *et al.*, 2011b, 2012; Groß *et al.*, 2011b; Tesche, 2011; Mamouri and Ansmann, 2014].

Multiwavelength Raman lidars as operated in EARLINET typically measure the extinction coefficient at 355 and 532 nm and the backscatter coefficient at 355, 532, and 1064 nm. From these measurements lidar ratios in the ultraviolet and visible wavelength regions as well as spectral extinction and backscatter properties in terms of Ångström exponents and color ratios can be derived. Past analyses of these quantities reveal that characteristic values can be attributed to different aerosol types and, therefore, are perfect parameters for aerosol typing [Sasano and Browell, 1989; Ansmann and Müller, 2005; Müller *et al.*, 2007a; Tesche *et al.*, 2009a, 2011a; Groß *et al.*, 2011b, 2012, 2013; Weinzierl *et al.*, 2011; Burton *et al.*, 2012, 2013, 2014]. For instance, results of the aerosol typing based on lidar observations reported by Müller *et al.* [2007a] are shown in Figure 2.1. The study distinguishes marine aerosol, desert dust, urban haze, arctic haze, forest-fire smoke, and Southeast Asian aerosol. It also shows that significant differences are found when the same type of aerosol is investigated in different regions of the globe or after different transport times.

Also synergistic approaches of lidar and sun-photometer coincident observations were applied to enhance aerosol characterization. For instance, the Lidar/Radiometer Inversion Code (LIRIC) [Chaikovskiy *et al.*, 2008, 2012] combines the multiwavelength lidar technique with sun/sky photometry and enables the retrieval of vertical profiles of optical and microphysical properties separately for fine- and coarse-mode particles. Wagner *et al.* [2013] evaluated LIRIC to determine microphysical properties of volcanic and desert dust. Lopatin *et al.* [2013] developed the Generalized Aerosol Retrieval from Radiometer and Lidar Combined Data (GARRLiC) algorithm, which

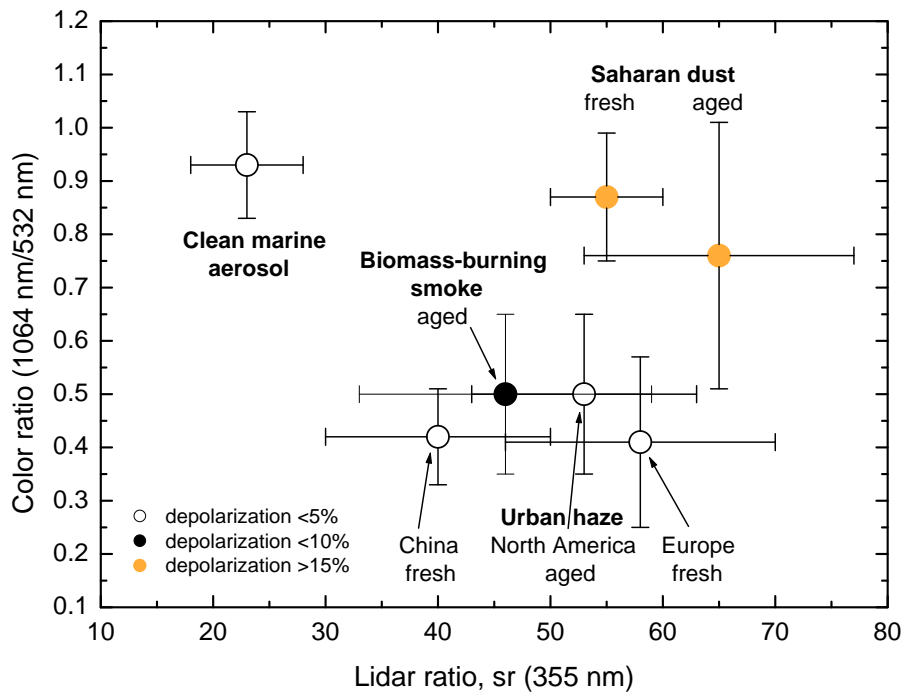


Figure 2.1: Color ratio (ratio of the backscatter coefficients at 1064 and 532 nm) versus lidar ratio at 355 nm for different aerosol types observed with multiwavelength Raman lidars from 1996–2007. Data are derived from Table 1 of Müller *et al.* [2007a]. Error bars indicate one standard deviation of each quantity from the mean of all observations.

can be regarded as an extended version of LIRIC. The GARRLiC concept pursues an even deeper synergy of lidar and radiometer data in the retrievals, e.g., by using the lidar profile information to improve the retrievals of Sun photometers of the Aerosol RObotic NETwork (AERONET; cf. Section 4.3.3).

2.1.3 CALIPSO aerosol typing scheme

Another method for aerosol typing is realized in the CALIPSO aerosol typing scheme. This scheme was developed to select a specific lidar ratio that is needed for the data processing, since CALIOP is a simple backscatter lidar [Omar *et al.*, 2005, 2009; Young and Vaughan, 2009; Young *et al.*, 2013]. Thus, in case of CALIPSO a preliminary typing must be performed without having all inferable optical parameters available. The CALIPSO algorithm is based on aerosol models with type-dependent size distributions and refractive indices and can classify/select six different aerosol types: desert dust, biomass burning, background (clean continental), polluted continental, polluted dust, and marine. The selection of the aerosol types is performed based on the type of the underlying surface (snow/ice or tundra, and land or water), the height of the identified

aerosol layer (elevated layer yes or no), and measured values of the linear volume depolarization ratio as well as of the integrated attenuated backscatter coefficient. After the selection of an aerosol type the respective pre-defined lidar ratio is used for the data evaluation. An illustration of the CALIPSO aerosol typing scheme and a detailed explanation can be found in Section 3.2.2 (cf. Figure 3.4).

2.1.4 Aerosol typing by using the Mahalanobis distance

For the classification of aerosols more and more information become available, e.g., aerosol optical depth, complex refractive index, single-scattering albedo, and depolarization of backscatter, each at several wavelengths, plus several particle size and shape parameters. Objective, multi-dimensional analysis methods are required for an optimal use of these various data products. The Mahalanobis distance [*Mahalanobis*, 1936] can be used to sort points, each representing an observation, into classes or clusters that have pre-defined special characteristics, e.g., certain aerosol optical properties. The Mahalanobis distance from each point to each prespecified class is calculated to classify a point (i.e., a measurement) regarding its smallest distance to a certain class. *Burton et al.* [2012] made use of the Mahalanobis distance to classify observed aerosols into types (e.g., pollution, biomass burning, dust, marine) by using a set of four different parameters including the particle linear depolarization ratio at 532 nm, the extinction-to-backscatter ratio at 532 nm, the backscatter-related 532-to-1064-nm color ratio, and the ratio of aerosol depolarization ratios at 1064 nm and 532 nm.

A similar method, which makes explicit use of uncertainties in input parameters, is described by *Russell et al.* [2014]. The authors developed and applied the method for classifying aerosols observed from space by using only the optical and physical information retrieved from a single pixel or neighboring group of pixels (i.e., without using location, trajectory analysis or other auxiliary information). The algorithm uses Mahalanobis classification with prespecified clusters (classes). The prespecified clusters needed for the determination of the Mahalanobis distance were defined using parameters retrieved from AERONET stations where a single aerosol type tends to dominate in certain months. In this study of *Russell et al.* [2014] seven clusters were defined: pure dust, polluted dust, urban-industrial/developed economy, urban-industrial/developing economy, dark biomass smoke, light biomass smoke, and pure marine. The prespecified clusters were then applied to a five-year record of retrievals from the spaceborne Polarization and Directionality of the Earth's Reflectances 3 (POLDER 3) polarimeter on the Polarization and Anisotropy of Reflectances for Atmospheric Sciences coupled with Observations from a Lidar (PARASOL) spacecraft [e.g., *Hasekamp et al.*, 2011; *Tanré et al.*, 2011]. Details can be found in *Russell et al.* [2014].

2.1.5 Lidar algorithms to retrieve information on aerosol components

Nishizawa et al. [2010] and *Nishizawa et al.* [2011] developed forward and backward types of algorithms to analyze lidar data to understand the spatial and temporal distribution of aerosols. The authors focussed on the classification of several main aerosol components in the atmosphere and estimated the concentration of each component by retrieving vertical profiles of extinction coefficients, and further the extinction-to-backscatter (lidar) ratio, under clear-sky as well as under cloudy conditions. The algorithms make use of aerosol models, which consider three different aerosol components: water-soluble aerosols with mode radius in the fine-mode region and sea salt as well as dust with mode radius in the coarse-mode region. Water-soluble particles are defined as small particles with weak light absorption, consisting of a mixture of sulfate, nitrate, and organic carbon particles (= organic water-soluble substances) and, hence, most of them are anthropogenic aerosols. The size distribution for each aerosol component is supposed to be log-normal. While the water-soluble and sea-salt particles are reasonably assumed to be spherical, the dust particles are treated as randomly oriented spheroids to account for their non-sphericity [*Mishchenko et al.*, 1997, 2004; *Dubovik et al.*, 2006]. An external mixture of each aerosol component is assumed.

The algorithms were developed based on methods of *Sugimoto et al.* [2003] and *Nishizawa et al.* [2007, 2008a] and are similar to the Fernald method [*Fernald*, 1984] apart from the use of information from three measurement channels of the lidar: the perpendicular and parallel components returned from linearly polarized laser pulses at 532 nm, and the total component (i.e., perpendicular plus parallel) at 1064 nm.

The algorithms classify fine-mode particles (water-soluble particles) and coarse-mode particles (sea salt or dust) by using the spectral relationship of the scattering coefficients, which depends on the size of the particles. The depolarization data is used in addition to determine, if an aerosol layer contains dust particles or sea salt. A detailed description of the algorithms and work flows can be found in *Nishizawa et al.* [2007] and *Nishizawa et al.* [2011].

A further algorithm developed by *Nishizawa et al.* [2008b] retrieves the extinction coefficients of water-soluble particles, dust, and soot by using three-channel data of the extinction coefficient (α) at 532 nm and backscatter coefficient (β) at 532 and 1064 nm. Since this algorithm ($1\alpha + 2\beta$) does not use the depolarization data effectively and assumes that the dust particles are spherical, *Nishizawa et al.* [2011] plan to improve this algorithm by introducing spheroid models that will lead to effective use of depolarization data (δ) as well as $1\alpha + 2\beta$ data. With these adjustments ($1\alpha + 2\beta + 1\delta$ algorithm) the retrieval of the extinction coefficients of four aerosol components shall be realized. Furthermore, the authors want to develop an $1\alpha + 1\beta + 1\delta$ algorithm based

on their knowledge of the techniques applied so far to retrieve extinction coefficients for three aerosol components using three-channel data of α , β and δ at 355 nm derived from the high-spectral-resolution lidar (HSRL) [Shiple *et al.*, 1983; Shimizu *et al.*, 1983; Grund and Eloranta, 1991; She *et al.*, 1992; Piironen and Eloranta, 1994; Liu *et al.*, 1999; Eloranta, 2005; Esselborn *et al.*, 2008; Hair *et al.*, 2008] installed on the EarthCARE satellite.

2.2 Major aerosol types and their source regions

Within this thesis a validation of the spaceborne aerosol typing provided by CALIPSO is performed based on results of the aerosol typing from ground-based EARLINET data. Therefore, the aerosol types that are applied for the classification mainly rely on the types used in the CALIPSO classification scheme [Omar *et al.*, 2009] and updates given in the Data Quality Summary (http://www-calipso.larc.nasa.gov/resources/calipso_users_guide/data_summaries/layer/). In the following, characteristic optical properties, extracted from former studies, are presented for major aerosol types. Findings about the distribution of aerosol types that can be observed over the northern hemisphere are shown in Figure 2.2. Numbers given in the following provide an overview how an aerosol typing can be done by using parameters like the lidar ratio or Ångström exponents. The exact definition of the parameters and the theory behind is explained in Chapter 3.

2.2.1 Marine aerosol

Marine aerosol consists of sea-salt-containing water droplets produced by wind stress on the ocean surface or by the release of dimethyl sulfide (DMS) from phytoplankton [Hoppel *et al.*, 1990; Fitzgerald, 1991; Heintzenberg *et al.*, 2000; Smirnov *et al.*, 2002]. As the microphysical and optical properties of marine aerosol are relatively well understood, this aerosol can be well distinguished from other aerosol types in terms of optical properties. Marine aerosol particles are liquid, comparably large (significant component of supermicrometer-sized particles), and non-absorbing. Consequently, optical parameters, e.g., Ångström exponents are low, lidar ratios are of the order of 20–30 sr, and depolarization ratios are lower than 10% [Franke *et al.*, 2001, 2003; Cattrall *et al.*, 2005; Müller *et al.*, 2007a; Burton *et al.*, 2012; Dawson *et al.*, 2015]. The similar light-scattering behavior of water clouds may lead to ambiguities when using optical parameters in cloud–aerosol discrimination schemes in the marine boundary layer, which is typically of 500–1000 m height over the oceans.

At continental sites clean marine aerosols are hard to observe. Possible source regions

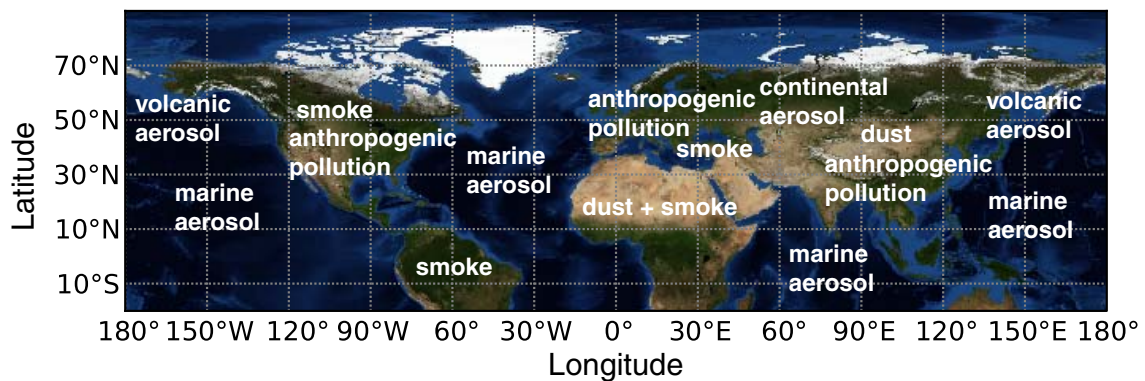


Figure 2.2: Generalized overview of characteristic aerosol types observable over the northern hemisphere.

of marine aerosol that might be detected at EARLINET stations are the North Atlantic/North Sea region, the Baltic Sea, the Mediterranean Sea, and the Black Sea. Most of the EARLINET stations of marine influence whose data were used for investigations presented in this thesis also represent densely populated areas, so that undisturbed measurements of clean oceanic aerosols are quite unlikely. The dense population of Europe's shorelines as well as the intense ship traffic cause a mixture of marine aerosols with anthropogenic pollution what has to be taken into consideration when exploiting data from stations close to the North Sea or the Mediterranean Sea [Wandinger *et al.*, 2004]. In addition, the orographic situation with very specific coastal circulation pattern complicates the observational conditions. Only under certain meteorological conditions EARLINET stations close to the coast may detect pure marine aerosol [De Tomasi *et al.*, 2006]. Within this study only a few cases with clean marine air were identified. In most circumstances, marine air was mixed with other aerosols such as pollution or dust.

2.2.2 Desert dust

Mineral dust particles originate from the erosion of sediments of fine soil in arid regions, especially in geographical lows and foothills where dry (paleo) lakes and rivers (wadis) exist [Prospero *et al.*, 2002; Schepanski *et al.*, 2007; Liu *et al.*, 2008; Allen *et al.*, 2013]. Dust particles are mobilized and a large amount is lofted by dynamical processes and often transported over distances of several thousand kilometers [Hamonou *et al.*, 1999; Ansmann *et al.*, 2003; Mahowald *et al.*, 2014]. The largest aerosol source of the globe is the Saharan desert [Dubovik *et al.*, 2008; Heintzenberg, 2009] whose emissions influence not only Europe quite frequently [Mattis *et al.*, 2002; Ansmann *et al.*, 2003; Müller *et al.*, 2003b; Papayannis *et al.*, 2008], but also other regions on the globe like, e.g., the Amazonian rain forest [Koren *et al.*, 2006; Ansmann *et al.*, 2009; Baars *et al.*,

2011; Yu *et al.*, 2015], Barbados [Weinzierl *et al.*, 2014], and the Gulf of Mexico [Liu *et al.*, 2008].

Within the framework of the SAharian Mineral dUst experiMent (SAMUM) project [Ansmann *et al.*, 2011a] the relationship between chemical composition, shape morphology, size distribution, and optical effects of mineral dust aerosol together with its temporal and spatial distribution were investigated during two comprehensive field campaigns in the summer of 2006 and in the winter of 2008. The two campaigns were designed with identical layout and with a strong focus on vertical profiling to enable column closure experiments. Optical, microphysical, radiative, chemical, and morphological properties of mineral dust particles were determined from field observations (ground-based, airborne, and remote sensing). Modeling studies were performed to investigate the dust transport and radiative effects. The first experiment (SAMUM–1, [Heintzenberg, 2009]) took place in southern Morocco near the Saharan desert close to major source regions of mineral dust in central Algeria and western Tunisia [Knippertz *et al.*, 2009]. The second experiment (SAMUM–2, [Ansmann *et al.*, 2011a]) was conducted at Cape Verde, which is located in the regime of intercontinental long-range transport of mineral dust and biomass-burning smoke from Africa over the Atlantic ocean towards North and South America. The major campaign of SAMUM–2 took place during the winter of 2008 (15 January to 14 February) and, hence, it is (in several publications) referred to as SAMUM–2a or SAMUM–2 winter to separate it from an additional measurement campaign that was conducted from 24 May to 17 June 2008, and which is, therefore, referred to as SAMUM–2b or SAMUM–2 summer. Results of the SAMUM campaigns can be found in two special issues in *Tellus, Series B* (61, 2009 and 63, 2011). A summary, also including results of other studies on optical properties of desert dust aerosol, is given below.

Properties of dust particles are very different compared to those of other aerosol types and, hence, their discrimination is usually easy. Most important for particular optical properties of dust particles is their non-spherical shape and their large size. The former leads to comparably high lidar ratios [Mattis *et al.*, 2002; Esselborn *et al.*, 2009] and causes a significant depolarization of the backscattered light [Freudenthaler *et al.*, 2009]. Their large size results in an almost neutral spectral extinction and backscattering behavior, i.e., the Ångström exponent is 0.0–0.4, the color ratios are of the order of one. A statistical analysis of coordinated EARLINET observations of dust plumes over Europe done for the period 2000–2002, presented by Papayannis *et al.* [2008], indicates a high variability of the lidar ratio and the backscatter-related Ångström exponent, especially at Southern European stations. Esselborn *et al.* [2009] also reported on varying dust lidar ratios (38–50 sr) and could attribute their observations to differences in dust source regions by applying backtrajectory analysis. Tesche *et al.* [2009b] showed very stable values of the order of 55 ± 10 sr at 355, 532, and 1064 nm for

lidar ratios measured in the source region in Morocco during the same measurement campaign, SAMUM-1. These values are clearly larger than the values reported by *Cattrall et al.* [2005] and the ones used in the CALIPSO retrieval (cf. Section 3.2.2). CALIPSO observations in the Saharan dust plume show similar values for 1064 nm [*Liu et al.*, 2008], whereas discrepancies occur at 532 nm. Furthermore, *Schuster et al.* [2012] computed an AERONET-based lidar ratio climatology for sites located in the dust belt. The authors found regionally varying lidar ratios with highest values of 55.4 sr at 532 nm in the non-Sahel regions of Northern Africa and lower lidar ratios in the African Sahel (49.7 sr) and the Middle East (42.6 sr). Results of *Mamouri et al.* [2013] support these findings. *Schuster et al.* [2012] explained this regional variability in the lidar ratio by the regional variability of the real refractive index of dust, which in turn is caused by the variability of the relative proportion of the mineral illite. The results of *Schuster et al.* [2012] support findings from other comparisons, e.g., *Pappalardo et al.* [2010], *Wandinger et al.* [2010], which led to the conclusion, that the assumed lidar ratio of 40 sr for the CALIPSO dust retrievals is too low.

The actual source region and transport pattern determine the dust optical properties observable over Europe. Due to the area of origin (white, yellow, red sand) dust contains different mineral constituents, which add up in corresponding absorption properties of the respective dust particles. For instance, an increase in the iron content affect the absorption properties leading to an increased lidar ratio like it was found during SAMUM-2 at the Cape Verde Islands [*Groß et al.*, 2013]. The transport at low levels over oceans like the Mediterranean Sea leads to a mixing with marine aerosols. Additionally, the mixing with polluted continental aerosol or smoke has to be taken into account during investigations of transported dust layers. Furthermore, the coating of dust particles with sulfuric components, which occurs likely during long-range transports and cloud processing of particles, plays a role and was investigated, e.g., during SAMUM-2 and recently during the Saharan Aerosol Long-range Transport and Aerosol-Cloud-Interaction Experiment (SALTRACE) (cf., e.g., *Weinzierl et al.* [2011]; *Ansmann et al.* [2014]). In case of complex aerosol layering the dust profiling methodology – polarization-lidar photometer networking (POLIPHON) method – can be used for a height-resolved separation of fine-mode and coarse-mode dust properties (dust and non-dust aerosol backscatter and extinction, volume, and mass concentration) as it is shown by *Mamouri and Ansmann* [2014].

It is noteworthy, that dust observations from space have to be corrected for the influence of multiple scattering. *Wandinger et al.* [2010] found that the atmospheric attenuation obtained from space is reduced by 10%–40% in optically dense dust plumes (with particles of effective radii between 1.2 and 6.8 μm [*Weinzierl et al.*, 2009]) due to considerable multiple-scattering effects. Results are based on frequently monitored differences between extinction coefficients for Saharan dust derived from CALIPSO

observations and measured by EARLINET and during SAMUM. In the CALIPSO retrieval of backscatter coefficients, the atmospheric attenuation is corrected with the help of *a priori* lidar ratios from the look-up table. It was found that the value of 40 sr used for dust represents an effective value that accounts well for the reduced attenuation caused by multiple scattering. Therefore, CALIPSO backscatter retrievals work well and comparisons with ground-based observations show good agreement. In contrast, if extinction values are calculated by multiplying the backscatter values with the effective lidar ratio, a systematic underestimation of extinction and, thus, aerosol optical depth is caused. *Wandinger et al.* [2010] asserted that this could be avoided, if a true mean lidar ratio of 55 sr would be used for the extinction calculation.

2.2.3 Biomass-burning (smoke) aerosol

Biomass-burning aerosol or smoke can be of anthropogenic or natural origin. It is produced by, e.g., anthropogenic wood and crop burning or natural forest fires strongly depending on land use, vegetation cycle, seasonal weather conditions, and human behavior. The kind of burning influences the size of the smoke particles and the released amount of soot and, thus, the optical properties of biomass-burning aerosol. Flaming fires emit smaller and highly absorbing particles, whereas larger and less-absorbing particles are produced in smoldering fires. Furthermore, during the transport of smoke processes such as hygroscopic growth, condensation of inorganic and organic vapors, coagulation, and photochemical as well as cloud-processing mechanisms lead to particle growth and changes in optical properties [*Müller et al.*, 2005; *Amiridis et al.*, 2009; *Alados-Arboledas et al.*, 2011; *Nicolae et al.*, 2013; *Vakkari et al.*, 2014].

There are different sources for biomass-burning (smoke) aerosol observable over Europe. A selection of 10-day Moderate Resolution Imaging Spectroradiometer (MODIS, cf. Section 4.3.4) maps of active fires for the northern hemisphere in the period July 2008 to June 2009 presented in Figure 2.3 shows that the fire season in northern mid-latitudes usually lasts from March to October. During the major fire activity from July until September smoke from local crop-burning fires, especially in the croplands of the Ukraine (north of the Black Sea) and around the Mediterranean, can be observed. In addition, in springtime a fire belt stretches from the Ukraine along Southern Siberia toward the Pacific Ocean. Predominantly westerly winds cause a transport via the Pacific, North America, and the Atlantic to Europe where aerosol can be obtained in most cases only after one or two weeks of transport. Between May and October also long-range-transported biomass-burning aerosol from boreal forest fires in North America and Canada to European stations can frequently be observed [*Wandinger et al.*, 2002; *Mattis et al.*, 2003; *Müller et al.*, 2005]. Investigation of optical data of long-range-transported biomass-burning aerosol show a decrease of the Ångström ex-

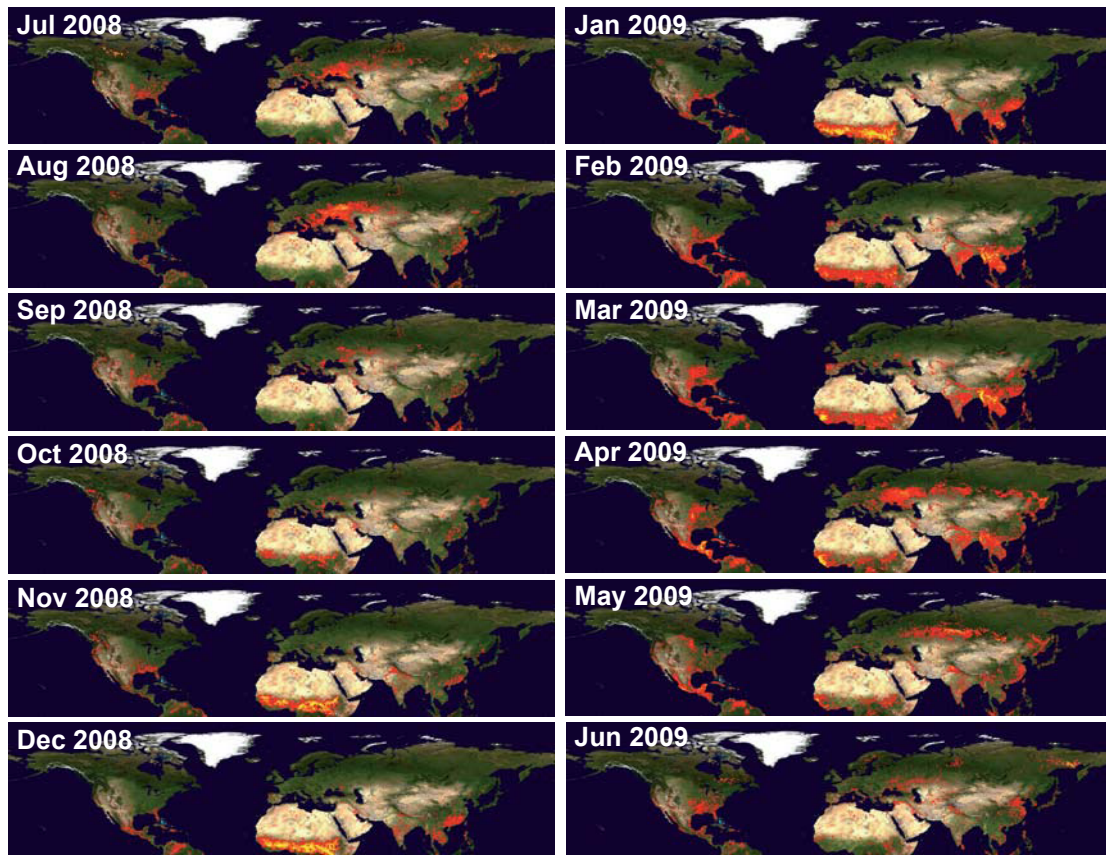


Figure 2.3: Selection of 10-day MODIS maps of active fires (red and yellow dots) for the northern hemisphere in the period July 2008 to June 2009.

ponent from 1.8 to 0.4 due to an increase in the effective particle radius from 0.12 to 0.4 μm during a travel time of 25 days or a travel distance of 25 000 km [Müller *et al.*, 2007b]. In addition, Wandinger *et al.* [2002] and Müller *et al.* [2005] already found extinction-related Ångström exponents close to 0 and backscatter-related Ångström exponents of ≈ 1 for aged smoke particles (after long-range transport of several days). Fresh smoke emitted by wild fires can be observed in Southern Europe during summer time. Analysis of lidar and Sun photometer data from 2001 until 2005 performed by Amiridis *et al.* [2009] over Greece indicated a decrease in the backscatter-related Ångström exponent from 2.5 to 1.0 and an increase in the lidar ratio from values around 45 to values of 80–100 sr when the age of the smoke increases from 5 to 17 days. Alados-Arboledas *et al.* [2011] observed fresh smoke particles over Granada (37.16 N, 3.6 W), Spain and found a rather pronounced accumulation mode and features markedly different from those reported for aged smoke particles. Lidar ratios

were around 60–65 sr at 355 and 532 nm and Ångström exponents about 1.0–1.5. The single-scattering albedo was low with 0.76–0.90, depending on the measurement wavelength. Airborne HSRL measurements evaluated by *Burton et al.* [2012] support these findings of differences in the lidar ratio between fresh and aged smoke. Significantly smaller lidar ratios of 30–60 sr at 532 nm were found for fresh smoke than for advected smoke from Siberian forest fires with values of 60–80 sr. The determined backscatter-related color ratio indicates larger values (smaller particles) for fresh smoke than for aged smoke on average. The particle linear depolarization ratio at 532 nm for fresh smoke was typically low (<2–5%) and also typically lower than for aged smoke (3–8%).

2.2.4 Polluted continental aerosol

Polluted continental aerosol is the major aerosol type obtained in the planetary boundary layer of highly industrialized regions of the globe and, thus, determines the observations in the lower troposphere in Europe. It contains aerosol from anthropogenic pollution and can also be called urban aerosol. As major aerosol sources are fossil fuel combustion and traffic, sulfate particles dominate this aerosol type. Soot, nitrates, ammonium, and organic carbon are present as well. The particles are directly emitted into the atmosphere or produced in the atmosphere by gas-to-particle conversion of emitted precursor gases. Due to that production process polluted continental aerosol mainly consists of small particles with a modal diameter well below 100 nm (Aitken mode). The particles of the accumulation mode are significantly smaller than those of the accumulation mode of aged biomass-burning aerosols of various origins [*Petzold et al.*, 2002; *Hamburger et al.*, 2012]. Polluted continental aerosol particles do not significantly depolarize the backscattered light but cause a strong wavelength dependence of the optical properties, i.e., Ångström exponents >1 and color ratios <0.5. Typical lidar ratios are 50–70 sr depending on the absorption properties determined by the carbon content of the aerosols [*Mattis et al.*, 2004; *Catrrall et al.*, 2005; *Müller et al.*, 2007a]. *Bösenberg et al.* [2003] reported an average lidar ratio of 55 sr at 351 nm for the lowermost 2–3 km over Hamburg, Germany. The transport over long distances, e.g., from North America to Europe, leads to a smaller lidar ratio [*Müller et al.*, 2007a]. Also hygroscopic growth has an influence on polluted continental aerosol [*Granados-Muñoz et al.*, 2015], since pollution consists mainly of water-soluble substances like sulfate and nitrate.

It should be noted that different stages of industrial development and environmental regulations obviously lead to significant differences in the properties of polluted continental aerosol. Small particles dominate the polluted continental aerosol in Europe and the United States of America (U.S.A.), but not in Southeast Asia where an increased amount of large particles is found relative to the fine particle mode. In Southeast Asia

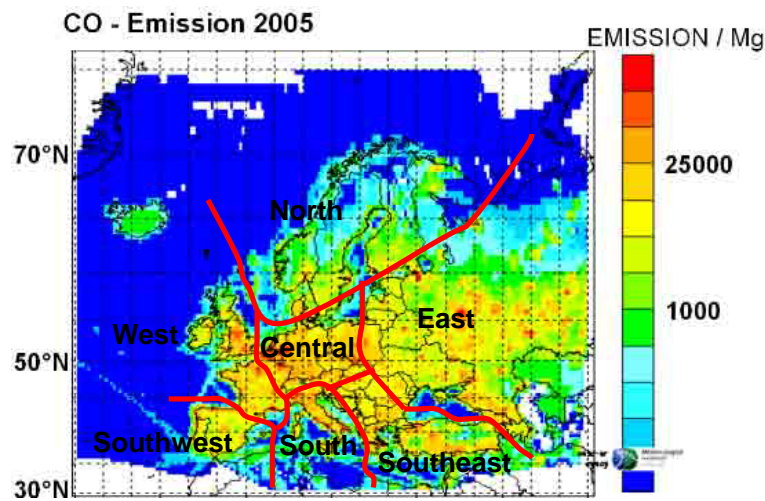


Figure 2.4: Definition of European source regions for polluted continental aerosol defined for the analysis presented in this thesis. The boundaries are overlaid on the EMEP emission map of CO in 2005.

these particles are produced by low-temperature combustion processes in domestic heating, wood and crop burning, but are also due to relaxed environmental regulations. Accordingly, lower Ångström exponents and lidar ratios are observed compared to European or North American aerosols [Ansmann *et al.*, 2005; Catrall *et al.*, 2005; Müller *et al.*, 2006, 2007a; Tesche *et al.*, 2007]. Therefore, a further aerosol type named Southeast Asian aerosol [Catrall *et al.*, 2005] was introduced. Since this aerosol type is not present over the considered European continent, it will not be applied in this thesis.

Source regions for polluted continental aerosol observable over Europe are related to regions where the emission of particulate matter and aerosol precursor gases takes place. Maps showing, e.g., the emission of CO, SO_x, PM_{2.5} (particle mass for particle diameter <2.5 μm), and PM_{coarse} (coarse particle mass) are provided by EMEP (Co-operative Programme for Monitoring and Evaluation of the Long-range Transmission of Air Pollutants in Europe, cf. <http://www.ceip.at>). Based on the EMEP emission inventory and on the distribution of the EARLINET stations, the European anthropogenic source regions could be distinguished according to Figure 2.4. In this way, local pollution in Central (mainly including Germany, Western Poland, Czech Republic, Slovakia, Hungary, Austria, northern parts of Switzerland, Eastern France, and BeNeLux), Western (mainly including Ireland, the United Kingdom, and France), Northern (mainly including Scandinavia), Eastern (mainly including Russia, Ukraine, Belarus, the Baltic States, and Eastern Poland), Southeastern (mainly including the Balkans, Greece, and Turkey), Southern (mainly including Italy and the

surrounding islands, southern parts of Switzerland), and Southwestern (mainly including Spain and Portugal) Europe can be directly related to the respective EARLINET measurement stations (cf. Section 3.1). In addition to the areas defined in Figure 2.4, extra-European source regions are considered, because polluted continental aerosols can also be transported in lofted layers from outside toward Europe. In particular, EARLINET has observed anthropogenic pollution from North America [Müller *et al.*, 2004] for which similar values for lidar ratios of 50–60 sr at 355 nm and 60–70 sr at 532 nm and extinction-related Ångström exponents of about 1.2–1.7, indicating comparably small particles, were observed [Müller *et al.*, 2014].

Further observations in Northern and Central Europe show particles in the free troposphere from time to time in spring [Heintzenberg *et al.*, 2003; Müller *et al.*, 2004], referred to as Arctic haze [Shaw, 1984, 1995]. This pollution is an extremely aged anthropogenic pollution aerosol originating from precursor material advected from industrialized areas of the Northern Hemisphere to the polar regions where it is captured by the polar front in winter [Rahn and Heidam, 1981; Barrie and Hoff, 1985; Marelle *et al.*, 2015]. Solar-induced conversion processes lead to a maximum of Arctic haze in springtime. Müller *et al.* [2007a] report on lidar ratios being around 60 sr at 355 and 532 nm and, thus, well within the variability found for European anthropogenic pollution. However, Ångström exponents are comparably large. Long-lasting sedimentation and coagulation processes lead to a very narrow size distribution with mean particle sizes smaller than what is usually found for free-tropospheric anthropogenic pollution [Müller *et al.*, 2002, 2004, 2005].

In addition, photochemical smog, a further specific type of anthropogenic pollution, can mainly be observed in highly polluted European areas under certain circumstances in summer. Episodes with photochemical smog are often observed in Southeastern Europe during the summer months when particles are formed due to so-called photochemical conversion of precursor gases and an enhanced ozone production leads to hazardous atmospheric pollution levels.

2.2.5 Clean continental aerosol

Clean continental aerosol can also be called continental background or rural aerosol. It represents a mixture of (aged) urban components with particles from agricultural activity and natural sources. Therefore, it may consist of a variety of substances such as sulfates, nitrates, ammonium, soot, organic carbon, mineral soil particles, pollen, and other biogenic material. Depending on the relative contributions of these constituents it may show optical properties reaching from those of urban pollution to those of mineral dust. For this analysis an aerosol layer is defined as clean continental aerosol when the aerosol load (optical depth, mean backscatter coefficient) was low

compared to the average aerosol load at the measurement site. Clean continental aerosols can normally be observed after precipitation events when particulate pollution has been removed from the atmosphere or when clean air masses arrive from remote, less-polluted areas, e.g., from Northern or Northeastern Europe. Typically, no specific sources can be related to such aerosol layers. Anyway, the advection scheme indicated by transport simulations with the FLEXible PARTicle dispersion model (FLEXPART) (cf. Section 4.2.1) was taken following the aerosol source regions defined for polluted continental aerosol. For the lidar-ratio estimate required in the CALIPSO retrieval it is assumed that large particles dominate this aerosol distribution resulting in small lidar ratios of the order of 30–35 sr. These assumptions are consistent with observations under background conditions in Portugal [*Ansmann et al.*, 2001].

2.2.6 Tropospheric volcanic aerosol

Only a few observations of volcanic ash contribute to the data set used for this thesis and so far no further investigations were made. For completeness, some characteristic properties shall be mentioned in the following. *Ansmann et al.* [2010] reported on measurements of a young ash plume about 1.5–2 days after the eruption of the Icelandic volcano Eyjafjallajökull in April 2010. The authors presented that fresh ash consists of large, non-spherical mineral particles with particle linear depolarization ratios of about 35% and lidar ratios of 50–65 sr, optical properties nearly identical to those of desert dust. In addition to ash particles, volcanic eruptions inject large amounts of sulfur dioxide into the atmosphere. Within several days sulfate particles develop, which consist of small droplets and, therefore, do not show a depolarization effect. *Ansmann et al.* [2011b] showed that both components, a fine mode consisting of sulfate particles and a coarse mode consisting of ash, can be observed in the aged volcanic plume and might be separated via depolarization-ratio measurements [*Tesche et al.*, 2009a].

Former studies [e.g., *Pappalardo et al.*, 2004a; *Zerefos et al.*, 2006; *Wang et al.*, 2008] reported on lidar ratios of 50–60 sr and backscatter-related Ångström exponents of 2.7 characteristic for small sulfate particles originating from eruption plumes of Mount Etna, which have been detected occasionally by Southern European EARLINET stations in the past. *Mattis et al.* [2010] evaluated volcanic aerosol layers that were monitored in the upper troposphere and lower stratosphere over Leipzig in 2008 and 2009. These layers were traced back to eruptions of different volcanoes on the Aleutian Islands, Kamchatka, Alaska, and on the Kuril Islands. The authors found a wavelength dependence of the backscatter and extinction coefficients that results in Ångström exponents of 1.0–2.0.

2.2.7 Stratospheric aerosol

Stratospheric aerosol mainly originates from volcanic eruptions, which inject large amounts of sulfur dioxide and in case of very strong eruptions also ash particles directly into the stratosphere. Whereas large particles are usually removed within a few weeks, the precursor gases are converted to well-defined sulfuric-acid droplets through photochemical gas-to-particle conversion. These small particles can only be removed via sedimentation and tropopause foldings. The removal processes take several years. The optical properties of stratospheric aerosols are relatively well understood [e.g., *Wandinger et al.*, 1995; *Jäger and Deshler*, 2002]. The acidity determines the refractive index and can be calculated in dependence on atmospheric temperature and water-vapor mixing ratio. Lidar ratios and Ångström exponents depend on the actual size distribution of the droplets. *Wandinger et al.* [1995] and *Ansmann et al.* [1997] report on values of the lidar ratio reaching from 20 sr for large mean droplet diameters to 70 sr for small mean droplet diameters. Stratospheric volcanic aerosol layers investigated by *Mattis et al.* [2010] featured lidar ratios of 30–60 sr and 30–45 sr at 355 nm and 532 nm, respectively.

2.2.8 Aerosol mixtures

During the development of an aerosol classification scheme for the present study, it turned out that a broad variety of aerosol mixtures were observed over the European continent. Different types of aerosols are mixed during the relatively long pathways of air masses that travel across different aerosol source regions before they are detected over the European continent. For instance, when dust is transported at low altitudes from the Sahara toward Europe, it is mixed with other aerosols from local or regional sources. This situation is often observed at EARLINET stations in the Mediterranean region. Here, dust can be mixed with marine aerosol over the sea, but also with anthropogenic pollution and smoke in the densely populated coastal areas. On the other hand, when aerosol sources are very close to each other a mixing occurs often directly after emission. This is the case when, e.g., smoke or marine aerosol is emitted near densely populated regions characterized by a high amount of polluted continental aerosol. Always a mixture will be observed.

This mixing of aerosols with different optical properties leads to modified characteristic optical properties and requires specific care [e.g., *Lesins et al.*, 2002; *Petzold et al.*, 2011; *David et al.*, 2013]. Sea-salt particles are large and non-absorbing, whereas smoke and pollution aerosol show a considerable absorption and consist of relatively small particles. Thus, mixing of either marine aerosol or absorbing aerosol or both with dust may result in quite different optical properties. Observations of mixtures containing

smoke or pollution aerosol show a decrease in the particle size and increasing Ångström exponents, whereas especially marine particles can lower the lidar ratio significantly [Müller *et al.*, 2007a; Burton *et al.*, 2012, 2013; Groß *et al.*, 2013].

Most of the southern European EARLINET stations are located very close to the Mediterranean Sea, which means that marine particles always have a strong influence on the aerosol optical properties. Müller *et al.* [2007a] reported on mean lidar ratios for polluted marine aerosol that were typically below 50 sr (varying between approximately 30 sr and 40 sr at 532 nm) within the planetary boundary layer (PBL) at the Italian and Greek stations. Furthermore, Burton *et al.* [2012] reported on reduced, compared to pure dust, values for the particle linear depolarization at 532 nm of about 20% to 35% for measurements containing a dusty mix and stated that these values of depolarization are consistent with results from various studies of dust mixed with other species [Léon *et al.*, 2003; Sugimoto and Lee, 2006; Heese and Wiegner, 2008; Groß *et al.*, 2011b; Tesche *et al.*, 2011b; Weinzierl *et al.*, 2011]. Recently, attempts have been made to split mixtures of different aerosol types into pure types [Tesche *et al.*, 2009a; Burton *et al.*, 2014; Müller *et al.*, 2014; Noh, 2014], which can then be processed individually by inversion algorithms to derive microphysical properties [Müller *et al.*, 1999; Böckmann, 2001; Veselovskii *et al.*, 2002, 2013; Kolgotin and Müller, 2008; Müller *et al.*, 2011], but this is beyond the scope of this study.

Polluted dust is the only explicit mixture of different aerosol types considered in the CALIPSO aerosol typing scheme (cf. Section 3.2.2). “This aerosol model is designed to account for episodes of dust mixed with biomass-burning smoke, which are frequent in regions close to strong sources of both [e.g., in West Africa and Asia]. It also accounts for instances of dust mixed with urban pollution as is frequently encountered in parts of Asia and Europe” [Omar *et al.*, 2009]. This mixture was included in the aerosol typing used here. The CALIPSO polluted dust model does not consider mixtures of dust with marine aerosol. The mixing of marine aerosol with continental pollution or smoke plumes is also not taken into account. As already mentioned, the aerosol typing for the EARLINET data was done by using the same aerosol types as included in the CALIPSO classification scheme. In addition, aerosol mixtures were defined by combining the introduced pure aerosol types.

2.2.9 Aerosols over Europe

Within this work the aerosol distribution over Europe is investigated. Former studies showed the presence of various kinds of aerosols over Europe [Ansmann *et al.*, 2002, 2003; Wandinger *et al.*, 2002, 2004; Heintzenberg *et al.*, 2003; Mattis *et al.*, 2003, 2010; Müller *et al.*, 2003b, 2005; Matthias *et al.*, 2004; Pappalardo *et al.*, 2004a; Amiridis *et al.*, 2009; Guerrero-Rascado *et al.*, 2009; Mamouri *et al.*, 2009; Giannakaki *et al.*,

2010; *Alados-Arboledas et al.*, 2011; *Dahlkötter et al.*, 2014]. On the one hand, the aerosol distribution over Europe is caused by the presence of aerosol sources of different aerosol types. There are the surrounding seas like the Mediterranean for marine aerosols. Fires in Southern and South Eastern Europe serve as origin for frequently observed biomass-burning (smoke) aerosols. Highly populated and industrialized regions all over Europe, but mostly in Western and Central Europe, are large sources for polluted continental aerosol, which mainly dominates the aerosol load in the boundary layer. On the other hand, aerosols are lifted into the free troposphere or even into the stratosphere and are transported from their source regions, e.g., the Sahara or North America, over long distances to Europe and around the globe. Observations of long-range transport over Europe provide information on the variability that can be particularly high in such cases both in terms of geometrical and optical properties as demonstrated also by previous EARLINET studies [e.g., *Mona et al.*, 2006; *Villani et al.*, 2006; *Papayannis et al.*, 2008; *Wang et al.*, 2008].

2.3 Results of aerosol typing studies

So far, only few efforts have been made to derive aerosol-type-dependent lidar parameters in a systematic way. First attempts for the characterization of different aerosol types using a three-wavelength elastic-backscatter lidar were made by *Sasano and Browell* [1989]. The authors identified and classified five types of aerosols: continental, maritime, Saharan dust, stratospheric aerosols, and aerosols of the tropical forest. In 1994 the Lidar In-space Technology Experiment (LITE) [*McCormick et al.*, 1993; *Winker et al.*, 1996] provided the first opportunities to observe vertical aerosol distributions globally. *Kent et al.* [1998] described the long-range transport of biomass-burning aerosols and the characterization of the optical properties using LITE observations. However, information gained so far were from elastic-backscatter lidars, for which it is not possible to independently measure the aerosol extinction and backscatter coefficients. Instead, assumptions on the lidar ratio are required within the retrieval, and the need for more accurate lidar ratios to constrain this type of retrieval further motivates aerosol classification and characterization studies.

Dubovik et al. [2002] used AERONET Sun photometer measurements (cf. Section 4.3.3) and identified urban-industrial aerosol from fossil-fuel burning, biomass-burning aerosol from forest and grassland fires, wind-blown desert dust, and marine aerosol. Later, *Cattrall et al.* [2005] expanded this set of aerosol types by adding a Southeast Asian type, counting for a greater number of large particles relative to fine particles compared to urban-industrial pollution aerosol. *Cattrall et al.* [2005] published lidar parameters of five key aerosol types (marine, urban, biomass-burning, dust,

Table 2.1: Lidar parameters (lidar ratio S_λ , backscatter coefficient β_λ , extinction coefficient α_λ , Ångström exponent \hat{a}_λ) retrieved from selected AERONET sites, after *Cattrall et al.* [2005]; indices indicate the wavelength in nm.

| Aerosol type | S_{550} , sr | S_{550}/S_{1020} | β_{550}/β_{1020} | $\alpha_{550}/\alpha_{1020}$ | $\hat{a}_{\alpha,1020-550}$ |
|------------------|----------------|--------------------|----------------------------|------------------------------|-----------------------------|
| Marine | 28±5 | 1.0±0.2 | 1.4±0.1 | 1.5±0.4 | 0.7±0.4 |
| Urban/industrial | 71±10 | 1.9±0.3 | 1.6±0.2 | 3.3±0.5 | 1.7±0.2 |
| Biomass burning | 60±8 | 2.1±0.3 | 1.8±0.3 | 3.8±0.4 | 1.8±0.2 |
| Dust (spheroids) | 42±4 | 1.2±0.1 | 0.9±0.1 | 1.2±0.1 | 0.1±0.1 |
| Southeast Asian | 58±10 | 1.5±0.3 | 1.6±0.2 | 2.4±0.3 | 1.3±0.2 |

and Southeast Asian aerosol). These values are indirectly obtained from sky-radiance and solar-transmittance measurements and the application of scattering models for spherical or spheroidal particles. The findings are summarized in Table 2.1. A deficiency of this study is that it is not based on a distinct case-by-case aerosol typing. Instead, mean values are derived for specific geographic locations and times of the year, for which it is assumed that a certain aerosol type dominates the atmospheric column.

A first automatic classification of aerosol types is reported by *Shimizu et al.* [2004], who used lidar depolarization-ratio measurements to differentiate spherical from non-spherical particles. Furthermore, *Omar et al.* [2005] presented a cluster analysis on 26 aerosol intensive variables derived from a comprehensive AERONET data set to produce and characterize a set of six aerosol types (desert dust, biomass burning, urban-industrial pollution, rural background, polluted marine, and dirty pollution). In Chapter 1 as well as in the previous section it was emphasized that for the CALIPSO aerosol typing *a priori* aerosol-type-dependent lidar ratios are needed. The applied lidar-ratio estimates are partly based on these AERONET Sun photometer observations.

The sun-photometer measurements used in many of the studies described above include information on the entire integrated vertical column and, therefore, could be biased in presence of inhomogeneous aerosol layering. In contrast, from ground-based and airborne lidar observations profiles of the aerosol extinction and backscatter coefficients could be derived independently to characterize vertically resolved aerosol optical properties without using models or assumptions about aerosol type. For instance, high-quality case studies from ground-based Raman lidars [*Ansmann et al.*, 1990] were described by, e.g., *Müller et al.* [2007a, and references therein], *Amiridis et al.* [2009], *Noh et al.* [2009], *Tesche et al.* [2009a,b], and *Alados-Arboledas et al.* [2011]. *Müller et al.* [2007a] presented aerosol-type-dependent optical parameters solely based on

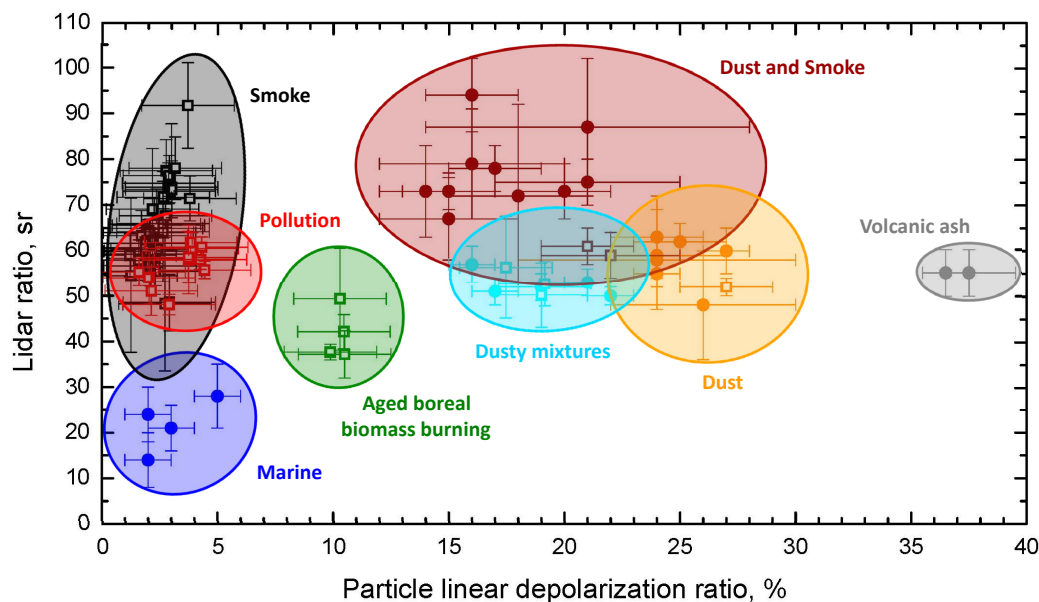


Figure 2.5: Aerosol classification from measurements of lidar ratio and particle linear depolarization ratio at 355 nm. Ground-based observations were performed with the Raman polarization lidars POLIS (University of Munich, dots) and Polly^{XT} (Leibniz Institute for Tropospheric Research, open squares) at Cape Verde (dust, marine, dust and smoke, dusty mixtures; [Groß *et al.*, 2011b]), Leipzig, Germany (pollution, aged boreal biomass-burning aerosol, dusty mixtures), Munich, Germany (volcanic ash; [Groß *et al.*, 2012]), in the Amazon Basin (smoke; [Baars *et al.*, 2012]), and over the North Atlantic (dust, dust and smoke; [Kanitz *et al.*, 2013]). Figure taken from Illingworth *et al.* [2014].

multiwavelength lidar measurements and case-by-case aerosol typing. The data were determined from long-term aerosol and cloud observations in the frame of the German Aerosol Lidar Network (1996–1999) and EARLINET (since 2000) with a stationary multiwavelength Raman lidar at Leipzig over more than a decade. Furthermore, data with transportable Raman lidars were taken in several field campaigns in Europe, Africa, and Asia. Results are illustrated in Figure 2.1 in Section 2.1.2 and are included in Tables 2.2–2.6.

Results of other studies on the aerosol classification from measurements of lidar ratio and particle linear depolarization ratio at 355 nm are summarized in Figure 2.5 [Illingworth *et al.*, 2014]. Ground-based observations were performed with the Raman polarization lidars POLIS (University of Munich, dots) and Polly^{XT} (Leibniz Institute for Tropospheric Research, open squares) at Cape Verde (dust, marine, dust and

smoke, dusty mixtures; [Groß *et al.*, 2011b]), Leipzig, Germany (pollution, aged boreal biomass-burning aerosol, dusty mixtures), Munich, Germany (volcanic ash; [Groß *et al.*, 2012]), in the Amazon Basin (smoke; [Baars *et al.*, 2012]), and over the North Atlantic (dust, dust and smoke; [Kanitz *et al.*, 2013]). These measurements are used for the aerosol classification within EarthCARE [Illingworth *et al.*, 2014].

Baars *et al.* [2015] showed that the attenuated backscatter coefficient at three wavelengths as well as the calibrated volume depolarization ratio can be used to identify aerosol types. The authors referred on a classification in terms of particle size and shape regarding, e.g., small spherical particles and large non-spherical particles as well as mixtures. For future applications it is planned to implement this approach in the CLOUDNET [Illingworth *et al.*, 2007] retrieval at sites for which an appropriate lidar is available to make use of the full instrument synergy, which is required for advanced aerosol-cloud-interaction studies.

In addition to measurements of ground-based lidars, information was gained from airborne HSRL data [Esselborn *et al.*, 2009; Burton *et al.*, 2012, 2013; Groß *et al.*, 2013]. For instance, the findings of Groß *et al.* [2013] and their summary of recent studies showed typical 532-nm lidar ratios of 18 ± 5 sr for marine aerosol [Groß *et al.*, 2011b], 56 ± 5 sr for desert dust [Tesché *et al.*, 2009b], and 60 ± 12 sr for arctic haze [Müller *et al.*, 2007a], which are different from those of Cattrall *et al.* [2005] (cf. Table 2.1). Groß *et al.* [2013] remarked that lidar-ratio assumptions for a specific measurement scene should be supported by additional information. Especially, within sophisticated aerosol classification algorithms and lidar ratio selection schemes (e.g., CALIPSO aerosol typing scheme [Omar *et al.*, 2009]) the lidar ratio has to be chosen with care because questionable extinction data could be generated otherwise and, hence, the retrieval of the climate-relevant aerosol optical depth would be erroneous [Schuster *et al.*, 2012]. Groß *et al.* [2013] used polarization-sensitive HSRL measurements to derive two aerosol-specific properties independent from aerosol load, but dependent of the shape, size, and complex refractive index of the present aerosol particles, the particle lidar ratio and the particle linear depolarization ratio. The authors noted that measurements of these two intensive properties are not sufficient for a classification of aerosol types like, e.g., biomass-burning smoke and anthropogenic pollution, which are obviously harder to separate than others. Therefore, Groß *et al.* [2013] determined the color ratio (ratio of aerosol backscatter coefficient at 532 and 1064 nm) in addition, which is (as the Ångström exponent) also only dependent on the particle type and not on concentration. The authors used algorithms for which a set of aerosol-type-dependent thresholds were defined for each measurement dimension analog to a former study of Weinzierl *et al.* [2011]. Groß *et al.* [2013] also pointed out that high-quality measurements are mandatory as large measurement uncertainties prevent a clear aerosol type separation.

Further studies on the aerosol classification were done by *Burton et al.* [2012] based on measurements of the NASA Langley Airborne HSRL. The authors used four aerosol intensive parameters in the aerosol classification that do not depend on the aerosol amount: the lidar ratio at 532 nm; the backscatter-related color ratio, which they define as the ratio of the backscattering coefficient at 532 and 1064 nm (what is different from the definition used for CALIOP; cf. next chapter); the particle linear depolarization at 532 nm (“actually the natural logarithm of this quantity, since it is more normally distributed” [*Burton et al.*, 2012]); and the spectral depolarization ratio, which is the ratio of the particle linear depolarization measured at two wavelengths (532 and 1064 nm).

Aerosol classification from depolarization information at two wavelengths was also applied by *Sugimoto and Lee* [2006], *Groß et al.* [2011b], and *Kanitz et al.* [2014b]. Even depolarization measurements at three wavelengths were used by *Ansmann et al.* [2014] and *Müller et al.* [2014].

For the aerosol classification *Burton et al.* [2012] defined seven aerosol types: pure dust, dusty mix, marine, polluted marine, urban, smoke, and fresh smoke with the following specifications. The aerosol types dust and dusty mix were said to consist of non-spherical particles and primarily distinguished from other types by their particle linear depolarization ratio, which is an indicator of non-sphericity. For the identification of pure dust values of 30%–35% [e.g., *Shimizu et al.*, 2004; *Freudenthaler et al.*, 2009] were defined. Dust from other sources (such as wind-blown road dust) is likewise assumed to be a mixture. Therefore, *Burton et al.* [2012] introduced the dusty-mix type containing dust mixed with pollution aerosol, but also cases of dust mixed with marine aerosol. The dusty-mix type is characterized by an intermediate amount of particle linear depolarization between about 10% and 30%. Maritime aerosol causes low particle linear depolarization values, indicating spherical particles, and a small backscatter-related color ratio, indicating relatively large particles. Optical properties of polluted marine aerosol are intermediate between marine air and urban pollution. *Burton et al.* [2012] distinguished urban and smoke aerosols from other types by their high lidar ratios (43–87 sr), low particle linear depolarization, and large backscatter-related color ratio, indicating small, spherical, absorbing particles. In addition, the authors tried to distinguish urban and smoke aerosol from each other by the spectral depolarization ratio, but admitted that these two aerosol types are, nevertheless, difficult to separate.

Müller et al. [2007a] already showed that for the separation of pollution from smoke the wavelength dependency of the lidar ratio (355–532 nm) could be useful. The authors presented for smoke higher lidar ratios (70–80 sr) at 532 nm compared to urban aerosols (50–70 sr) what is consistent with previous Raman lidar measurements of smoke [*Wandinger et al.*, 2002].

Furthermore, *Burton et al.* [2012] observed slightly higher smoke particle linear depolarization at 532 nm (8%–10%) in lofted and advected smoke layers that had traveled over several days to the measurement site. These findings are consistent with other lidar measurements of long-range smoke transport [*Fiebig et al.*, 2002; *Murayama et al.*, 2004]. In contrast, their observations of fresh smoke in the boundary layer close to the source showed that it is comprised of small spherical particles as indicated by the depolarization and backscatter-related color ratio and lower lidar ratios (24–52 sr) than usually observed in the pollution or smoke categories. These findings agree with results from *Amiridis et al.* [2009] and *Alados-Arboledas et al.* [2011] who presented that the lidar ratio can be affected by the age of smoke. *Burton et al.* [2012] also observed new formation of particles having optical properties close to those of fresh smoke, but without being connected to a fresh smoke plume, obviously. The authors found out that the formation of new particles is associated with sulfate or organics, but does not rule out pollution-related aerosol. *Burton et al.* [2012] pointed out that there is no equivalent type in the CALIOP aerosol classification scheme that includes only a single biomass-burning type. A summary of the literature values of aerosol-type-dependent optical parameters for major aerosol types, especially findings from EARLINET studies as well as from *Burton et al.* [2012, 2013], *Groß et al.* [2013, 2015], and references therein, can be found in Tables 2.2–2.6.

In a further study *Burton et al.* [2014] investigated aerosol mixtures in measurements from an airborne HSRL. The authors inferred mixing ratios and extinction mixing ratios (extinction partitions) for various cases of external mixing by using expanded mixing equations of *Léon et al.* [2003]. *Burton et al.* [2014] emphasized that the mixing equations (the equations for each observable) can be written in the form of a linear combination of pure types. Instead of eight aerosol types described by multi-normal distributions, a continuum of multi-normal distributions sample the range of possible extinction mixing ratios from 0% to 100%. *Russell et al.* [2014] also applied multivariate normal distributions to provide a more complete picture of aerosol properties. With this technique it is possible to precisely describe mixing rules not only for single measurements, but also for measurement distributions. *Burton et al.* [2014] provided the relationships between the mixing coefficients for different intensive quantities at different wavelengths.

For the data evaluation performed within this thesis the intention was not to separate identified mixtures. Only the presence of an aerosol mixture was taken into account for the determination of aerosol optical properties. In case an aerosol mixture was identified to be present within an observed aerosol layer, the mixture was described by applying a combination of the defined pure types used in the CALIPSO classification scheme.

Table 2.2: Summary of the key findings of optical properties (lidar ratios S_λ , Ångström exponents \hat{a}_λ , particle linear depolarization ratio $\delta_{par,532}$) found for **marine aerosol**; indices indicate the wavelength in nm and the related scattering coefficient. Planetary boundary layer (PBL) indicates local and regional aerosol, free troposphere (FT) indicates aged particles after long-range transport.

| Source region Measurement site (campaign) | Layer | S_{355} , sr | S_{532} , sr | $\hat{a}_{\alpha,355-532}$ | $\hat{a}_{\beta,532-1064}$ | $\delta_{par,532}$, % | Reference |
|---|-------|----------------|----------------|----------------------------|----------------------------|------------------------|--|
| North Atlantic | | | | | | | |
| Thessaloniki, Greece | FT | 28±10 | | | | | <i>Amiridis et al.</i> [2005] |
| Cape Verde Islands (SAMUM-2a) | | 18±4 | 18±5 18±2 | | 0.71±0.10 | 3±1 1-3 | <i>Groß et al.</i> [2013] <i>Groß et al.</i> [2011b,a] |
| Portugal (ACE-2) ¹ | PBL | | 23±3 | 0.3±0.1 | | | <i>Müller et al.</i> [2007a] |
| North America | | | 15-25 17-27 | | | <10 4-9 | <i>Burton et al.</i> [2012] <i>Burton et al.</i> [2013] |
| Mediterranean | | | | | | | |
| Lecce, Italy | PBL | 10-20 | | | | | <i>De Tomasi et al.</i> [2006] |
| Southern Italy | | 20-25 | | | | | <i>De Tomasi et al.</i> [2003] |
| Greece | | 28±11 | | | | | <i>Amiridis et al.</i> [2005] |

¹ ACE-2 – Aerosol Characterization Experiment 2, over the sub-tropical North-East Atlantic (Canary Islands and Portugal), 16 June to 24 July 1997

Table 2.3: Summary of the key findings of optical properties (lidar ratios S_λ , Ångström exponents \hat{a}_λ , particle linear depolarization ratio $\delta_{par,532}$) found for **desert dust**; indices indicate the wavelength in nm and the related scattering coefficient. Planetary boundary layer (PBL) indicates local and regional aerosol, free troposphere (FT) indicates aged particles after long-range transport.

| Source region Measurement site (campaign/comment) | Layer | S_{355} , sr | S_{532} , sr | $\hat{a}_{\alpha,355-532}$ | $\hat{a}_{\beta,532-1064}$ | $\delta_{par,532}$, % | Reference |
|---|-------|----------------|----------------|----------------------------|----------------------------|------------------------|---------------------------------------|
| Sahara | | | | | | | |
| Europe (EARLINET) | FT | | 59±11 | 0.5±0.5 | 0.5±0.5 | 10–25 | <i>Müller et al.</i> [2007a] |
| Munich, Germany | | 59±4 | 59±10 | | | 30–35 | <i>Wiegner et al.</i> [2011] |
| Granada, Spain | | | 50–65 | | | | <i>Guerrero-Rascado et al.</i> [2009] |
| Lecce, Italy | FT | 40–50 | | | | | <i>De Tomasi et al.</i> [2006] |
| Thessaloniki, Greece | FT | 57±29 | | | | | <i>Amiridis et al.</i> [2005] |
| Morocco (SAMUM–1) | PBL | 55±6 | 55±5 | 0.2±0.2 | 0.2±0.2 | 30–35 | <i>Müller et al.</i> [2007a] |
| | | | 48±5 | | 0.38±0.15 | 32±2 | <i>Groß et al.</i> [2013] |
| | | 55±5 | 56±5 | ~0 | 0.2–0.3 | | <i>Tesche et al.</i> [2009b] |
| | | | | | | 31±3 | <i>Freudenthaler et al.</i> [2009] |
| Cape Verde Islands (SAMUM–2a) | | 58±7 | 62±5 | | | 31±1 | <i>Groß et al.</i> [2011b] |
| Cape Verde Islands (SAMUM–2b) | | 53±10 | 54±10 | 0.22±0.27 | 0.45±0.16 | 31±1 | <i>Tesche et al.</i> [2011a] |
| Arabia | | | | | | | |
| Limassol, Greece | | | 34–39 | | | 28–35 | <i>Mamouri et al.</i> [2013] |

Table 2.4: Summary of the key findings of optical properties (lidar ratios S_λ , Ångström exponents \hat{a}_λ , particle linear depolarization ratio $\delta_{par,532}$) found for **polluted continental aerosol and arctic haze**; indices indicate the wavelength in nm and the related scattering coefficient. Planetary boundary layer (PBL) indicates local and regional aerosol, free troposphere (FT) indicates aged particles after long-range transport.

| Source region Measurement site (campaign/comment) | Layer | S_{355} , sr | S_{532} , sr | $\hat{a}_{\alpha,355-532}$ | $\hat{a}_{\beta,532-1064}$ | $\delta_{par,532}$, % | Reference |
|---|-------|----------------|----------------------|----------------------------|----------------------------|------------------------|---|
| Europe | | | | | | | |
| Central Europe (LACE 98) ² (EARLINET) | PBL | 58±12 | 56±6 53±11 | 1.4±0.5 | 1.28±0.27 1.3±0.5 | 6±1 <5 | <i>Groß et al.</i> [2013] <i>Müller et al.</i> [2007a] <i>Wandinger et al.</i> [2002] |
| Southwestern Europe (ACE-2) | FT | 60–65 | ~50 45±9 30–65 | 1.4±0.2 | 1.4±0.3 | <5 | <i>Müller et al.</i> [2007a] <i>Ansmann et al.</i> [2001] |
| Western Europe | | | | | | | |
| Lecce, Italy | FT | 40–60 | | | | | <i>De Tomasi et al.</i> [2006] |
| Western and Central Europe | | | | | | | |
| Portugal | | | 48±9 | 1.29±0.13 | | | <i>Ansmann et al.</i> [2002] |
| Central Europe | | | | | | | |
| Thessaloniki, Greece | FT | 32±13 | | | | | <i>Amiridis et al.</i> [2005] |
| Leipzig, Germany | FT | 64±19 | 59±13 | 1.6±0.9 | | | <i>Mattis</i> [2003] |
| Southeastern Europe | | | | | | | |
| Lecce, Italy | FT | 40–50 | | | | | <i>De Tomasi et al.</i> [2006] |
| Eastern Europe | | | | | | | |
| Leipzig, Germany | FT | 68±13 | 54±11 | 1.9±0.7 | | | <i>Mattis</i> [2003] |

Table 2.4 Continued: Summary of the key findings of optical properties (lidar ratios S_λ , Ångström exponents \hat{a}_λ , particle linear depolarization ratio $\delta_{par,532}$) found for **polluted continental aerosol and arctic haze**; indices indicate the wavelength in nm and the related scattering coefficient. Planetary boundary layer (PBL) indicates local and regional aerosol, free troposphere (FT) indicates aged particles after long-range transport.

| Source region Measurement site (campaign/comment) | Layer | S_{355} , sr | S_{532} , sr | $\hat{a}_{\alpha,355-532}$ | $\hat{a}_{\beta,532-1064}$ | $\delta_{par,532}$, % | Reference |
|---|-------|----------------|----------------|----------------------------|----------------------------|------------------------|-------------------------------|
| The Balkans | | | | | | | |
| Thessaloniki, Greece (fast transport) | FT | 38±19 | | | | | <i>Amiridis et al.</i> [2005] |
| (smooth transport) | FT | 44±25 | | | | | <i>Amiridis et al.</i> [2005] |
| North America | | | | | | | |
| Europe (EARLINET) | FT | 53±10 | 39±10 | 1.7±0.5 | 1.0±0.5 | <5 | <i>Müller et al.</i> [2007a] |
| Leipzig, Germany | | | | 1.8–2.1 | 1.8–2.1 | | <i>Müller et al.</i> [2005] |
| North America | | | 50–70 | | | <10 | <i>Burton et al.</i> [2012] |
| | | | 53–70 | | 0.77–1.07 | 3–7 | <i>Burton et al.</i> [2013] |
| Arctic haze | | | | | | | |
| North polar region and Northern Europe | | | | | | | |
| Europe (EARLINET) | FT | 60±12 | 60±12 | 1.9±0.3 | 1.2±0.3 | <5 | <i>Müller et al.</i> [2007a] |
| | FT | ~92 | ~81 | 1.1±0.9 | | | <i>Mattis</i> [2003] |

² LACE 98 – Lindenberg Aerosol Characterization Experiment, Germany, 1998

Table 2.5: Summary of the key findings of optical properties (lidar ratios S_λ , Ångström exponents \dot{a}_λ , particle linear depolarization ratio $\delta_{par,532}$) found for **biomass-burning aerosol**; indices indicate the wavelength in nm and the related scattering coefficient. Free troposphere (FT) indicates aged particles after long-range transport.

| Source region Measurement site (campaign/comment) | Layer | $S_{355, \text{sr}}$ | $S_{532, \text{sr}}$ | $\dot{a}_{\alpha, 355-532}$ | $\dot{a}_{\beta, 532-1064}$ | $\delta_{par, 532}, \%$ | Reference |
|---|-------|----------------------|----------------------|-----------------------------|-----------------------------|-------------------------|---------------------------------------|
| Southeastern Europe | | | | | | | |
| Thessaloniki, Greece | | 40–100 | | | | | <i>Amiridis et al.</i> [2009] |
| | | ~60 | ~50 | | | | <i>Balis et al.</i> [2003] |
| Bucharest, Romania | | | | | | | |
| (fresh) | | 73±12 | 46±6 | 1.9±0.4 | | | <i>Nicolae et al.</i> [2013] |
| (aged) | | 39±7 | 54±7 | ~0.97 | | | <i>Nicolae et al.</i> [2013] |
| Granada, Spain | | 60–65 | 60–65 | 1–1.5 | 1–1.5 | | <i>Alados-Arboledas et al.</i> [2011] |
| Canada | | | | | | | |
| Central Europe | | | 69±17 | | 2.23±1.30 | 7±2 | <i>Groß et al.</i> [2013] |
| (LACE 98) | | | 40–80 | | | | <i>Wandinger et al.</i> [2002] |
| Canada and Siberia | | | | | | | |
| Europe (EARLINET) | FT | 46±13 | 53±11 | 1.0±0.5 | 1.0±0.4 | <5 | <i>Müller et al.</i> [2007a] |
| North America | | | | | | | |
| North America | | | 55–73 | | 0.93–1.32 | 4–9 | <i>Burton et al.</i> [2013] |
| (fresh) | | | 33–46 | | 1.07–1.32 | 3–6 | <i>Burton et al.</i> [2013] |
| Africa | | | | | | | |
| Manaus, Brazil (aged) | | 40–50 | 60–70 | ~0 | 0.8–1 | | <i>Ansmann et al.</i> [2009] |
| Cape Verde Islands | | 87±17 | 79±17 | 1.15±0.28 | 1.06±0.65 | 5±2 | <i>Tesche et al.</i> [2011b] |
| (SAMUM-2a) | | 76±12 | 69±8 | | | 16±1 | <i>Groß et al.</i> [2011b, 2013] |

Table 2.6: Summary of the key findings of optical properties (lidar ratios S_λ , Ångström exponents \hat{a}_λ , particle linear depolarization ratio $\delta_{par,532}$) found for **mixtures containing desert dust and other aerosols**; indices indicate the wavelength in nm and the related scattering coefficient. Planetary boundary layer (PBL) indicates local and regional aerosol, free troposphere (FT) indicates aged particles after long-range transport.

| Source region Measurement site (campaign/comment) | Layer | $S_{355, \text{sr}}$ | $S_{532, \text{sr}}$ | $\hat{a}_{\alpha, 355-532}$ | $\hat{a}_{\beta, 532-1064}$ | $\delta_{par, 532}, \%$ | Reference |
|--|-------|----------------------|----------------------|-----------------------------|-----------------------------|-------------------------|---------------------------------|
| Sahara | | | | | | | |
| Europe | | | 40–80 | –0.5–0.5 | –0.5–0.5 | 15–25 | <i>Ansmann et al.</i> [2003] |
| Leipzig, Germany (dust and pollution aerosol) | FT | 63±11 | 50±19 | 1.6±0.5 | | | <i>Mattis</i> [2003] |
| Athens, Greece | | 75–100 | 45–75 | ~1.1 | | | <i>Papayannis et al.</i> [2012] |
| Thessaloniki, Greece (dust and marine aerosol) | FT | 40±16 | | | | | <i>Amiridis et al.</i> [2005] |
| Portugal | | 45±8 | 53±7 | 0.0±0.2 | ~0.4 | 28±4 | <i>Preißler et al.</i> [2011] |
| Africa | | | | | | | |
| Cape Verde Islands (SAMUM–2a) (dust, biomass-burning and marine aerosols) | | 54±3 | | | | 19–28 | <i>Groß et al.</i> [2011b] |
| (biomass burning and dust) | | | 50±4 | | 0.57±0.09 | 27±2 | <i>Groß et al.</i> [2013] |
| | | | 63±7 | | 0.71±0.13 | 14±2 | <i>Groß et al.</i> [2013] |
| | | | 69±8 | | | 16±1 | <i>Groß et al.</i> [2011b] |
| | | 67±14 | 67±12 | 0.67±0.38 | 0.67±0.27 | 16±3 | <i>Tesche et al.</i> [2011a] |

2.4 Verification of CALIPSO observations

The CALIPSO mission with its high resolution in time and in horizontal and vertical dimensions provides the first opportunity to investigate global four-dimensional aerosol fields in detail. Numerous studies were performed to evaluate the representativeness of CALIPSO observations as well as CALIPSO products in detail. In the following, most important findings, especially important for the present study, are summarized.

2.4.1 Representativeness of CALIPSO measurements

It is highly questionable how well CALIPSO measurements represent the atmospheric conditions of a surrounding area over a longer time, because CALIPSO provides only one day/night-time observation at fixed local time for a specific target location and has a long revisiting time of 16 days as well as a small footprint on the ground of about 70 m in diameter [*Hunt et al.*, 2009]. Data of CALIOP observations have been validated with ground-based [e.g., *Pappalardo et al.*, 2010; *Wandinger et al.*, 2011] and airborne [*Burton et al.*, 2013] lidar measurements in order to learn about spatial and temporal representativeness of polar-orbiting satellite measurements also in terms of revisit time. For instance, *Wandinger et al.* [2011] investigated the representativeness of CALIOP measurements within the framework of the ESA–CALIPSO (EARLINET’s Spaceborne-related Activity during the CALIPSO mission) project. The correlation analysis was performed in dependence on the spatial (both horizontal and vertical) and temporal distance of the satellite cross-section observation from a single ground-based measurement. The spatial variability was investigated within 100 km horizontal distance. The horizontal variability on larger scales was studied within 500 km to investigate the variability on different horizontal scales, from regional to continental. For the correlative study *Wandinger et al.* [2011] investigated geometrical (i.e., the difference of aerosol layer base and top heights) and optical properties in detail with specific focus on backscatter-coefficient profiles, because this parameter is the primary CALIPSO product, it is available from all EARLINET stations, and it can be determined with high temporal and spatial resolution. In general, the CALIPSO Version 3 Lidar profiles with 5-km horizontal resolution (cf. Section 3.2.3) are very noisy and, therefore, the realization of the representativeness study was very difficult. Nevertheless, one of the core results is that the correlation coefficient decreases with distance and, in particular, a sharp decrease in the correlation coefficient is found at 300 km horizontal distance. Observations are not correlated for temporal distances larger than 60 minutes.

Similar constraints were found during validation and exploitation of the spaceborne information gathered during the 10 days of LITE measurements. Those first com-

parisons of spaceborne and ground-based measurements showed that aerosols cannot be considered to be homogeneous for distances greater than 50–100 km, or a time difference of more than 2 hours [Anderson *et al.*, 2003].

2.4.2 Validation of CALIPSO aerosol products

Validation of CALIPSO data products was performed by using spaceborne observations from other sensors [Kacenelenbogen *et al.*, 2011; Kittaka *et al.*, 2011; Kim *et al.*, 2013; Ma *et al.*, 2013], airborne measurements of HSRL during CALIPSO underflights [Rogers *et al.*, 2011; Ottaviani *et al.*, 2012; Burton *et al.*, 2013; Rogers *et al.*, 2014], and ground-based data of, e.g., AERONET Sun photometer [Mielonen *et al.*, 2009; Kacenelenbogen *et al.*, 2011; Schuster *et al.*, 2012; Lopes *et al.*, 2013; Omar *et al.*, 2013] as well as lidar [Mamouri *et al.*, 2009; Mona *et al.*, 2009; Pappalardo *et al.*, 2010; Wandinger *et al.*, 2010; Tesche *et al.*, 2013; Kanitz *et al.*, 2014a; Grigas *et al.*, 2015]. Since the lidar onboard CALIPSO is an elastic-backscatter lidar an aerosol classification scheme was developed for the data processing [Omar *et al.*, 2009]. A goal of this thesis was not only the classification of aerosol types observable over Europe by means of their optical properties based on multiwavelength EARLINET measurements, but also the verification of the CALIPSO aerosol classification scheme.

2.4.2.1 Validation of the CALIPSO vertical feature mask and the aerosol typing scheme

Mielonen *et al.* [2009] used AERONET Sun photometer data to provide an evaluation of the aerosol typing with the CALIOP Version 2.01 data. The authors used AERONET measurements of single-scattering albedo and Ångström exponent and derived five aerosol types. Daily mean aerosol types were determined and compared to the most common aerosol types from CALIOP. Mielonen *et al.* [2009] found out that CALIOP can identify coarse absorbing aerosols better than fine-mode-dominated aerosols. Agreement was found in 70% of the cases with best agreement for the dust type (91%), moderate agreement for the polluted dust type (53%), and poorer agreement for fine-mode aerosols like biomass burning (37%) and polluted together with clean continental aerosol (22%).

In studies of Mamouri *et al.* [2009], Pappalardo *et al.* [2010], and Grigas *et al.* [2015] the CALIOP classification results were compared with their own results of specifically classified aerosol types in air masses they investigated by using EARLINET lidar data. Mostly, the authors found good agreement apart from observations in the PBL where large differences occur, indicating how rapidly air masses can change.

Oo and Holz [2011] stated that the criteria in the CALIOP lidar-ratio selection al-

gorithm have too little relation to properties that are directly linked to lidar ratio such as aerosol particle size. Instead, the criteria must rely on loading-dependent lidar measurements and information that is only indirectly related to aerosol type, rather than on aerosol intensive properties. The authors emphasized that the only intensive, i.e., loading-independent, aerosol property that is used in the CALIOP aerosol type selection is an approximate particle depolarization ratio. Even this estimate is affected by attenuation that depends on the aerosol loading, since the aerosol type selection algorithm occurs before the extinction retrieval [*Oo and Holz*, 2011].

Burton et al. [2013] presented an aerosol classification from airborne HSRL measurements. Results were compared to results of the CALIPSO vertical feature mask (cf. Section 3.2.2). The authors pointed out that the multi-resolution layer detection algorithm of CALIOP is well designed for spaceborne observations having a lower signal-to-noise ratio. In addition, *Burton et al.* [2013] mentioned that the identification of internal boundaries between different neighboring aerosol types frequently do not reflect the actual transitions between the aerosol types accurately. Concerning the performed aerosol typing within the CALIOP retrieval the authors arrived at the conclusion that the CALIOP polluted dust type is overused due to an attenuation-related depolarization bias and that it frequently includes mixtures of dust and marine aerosol, although it should not account for that mixture. *Burton et al.* [2013] summarized that the aerosol classification from their HSRL measurements are more accurate based on the available increased information content, in the form of aerosol intensive parameters that give direct insight into aerosol type.

The limitations of the aerosol typing especially in coastal regions was pointed out by, e.g., *Ford and Heald* [2012]. The authors assessed from model simulations that the location and layer elevation criteria in the CALIOP selection algorithm may be too limiting. Particularly, since smoke can only be identified in elevated layers and that elevated layers over the ocean cannot be classified as polluted continental aerosol. In addition, *Schuster et al.* [2012], *Omar et al.* [2013], and *Bridhikitti* [2013] reported on findings that showed that outflows of polluted continental aerosol were not considered and, hence, lead to a defective classification of aerosol layers along coastlines belonging to the clean marine aerosol type. *Oo and Holz* [2011] and *Schuster et al.* [2012] demonstrated that this fact leads to underestimations of the aerosol optical depth in coastal regions.

Another criticism is the differentiation of aerosol type dependent on the underlying surface (observation over land or ocean). Discontinuities in the aerosol typing at coastal regions caused by the fact that certain aerosol types are limited to either land or ocean, especially clean marine aerosol is only permitted over water surfaces, were found by *Campbell et al.* [2013] and *Kanitz et al.* [2014a]. *Kanitz et al.* [2014a] reported on the fact that the lidar ratio immediately changes due to a change in the underlying

surface. They showed a case study where the lidar ratio for example changes drastically from 20 sr for marine to 70 sr for smoke or polluted continental aerosol when CALIPSO crosses a coastal line (from sea to land), what correspondingly can lead to abrupt changes in the particle extinction coefficients by a factor of up to 3.5 and, thus, to an overestimation of the particle extinction coefficients over land. *Kanitz et al.* [2014a] also stated that this could as a consequence explain the positive bias between CALIPSO Lidar Level 3³ aerosol optical depth data and Sun-photometer-derived aerosol optical depth at coastal sites, which was shown in *Winker et al.* [2013]. In addition, *Rogers et al.* [2014] reported that the errors in the CALIOP Aerosol Layer extinction product can largely be attributed to either mistyping of aerosol layers or errors in the modeled lidar ratios for particular types.

2.4.2.2 Optimization of the CALIPSO algorithms

Efforts have been made for providing more accurate aerosol extinction profiles from CALIPSO data. A technique to avoid the need to infer a lidar ratio was applied by, e.g., *Burton et al.* [2010] and *Josset et al.* [2010]. They used column aerosol optical depth as a constraint, but this still requires the assumption of a uniform aerosol mixture throughout the column. *Oo and Holz* [2011] presented how the CALIOP aerosol optical depth could be improved by using combined MODIS-CALIOP observations and CALIOP integrated attenuated total color ratio.

Further attempts were made by, e.g., *Giannakaki et al.* [2011] and *Amiridis et al.* [2013]. *Giannakaki et al.* [2011] showed how the particle linear depolarization ratio can be a key parameter for separating aerosol mixtures, if the particle linear depolarization ratio for pure aerosol types is assumed. *Amiridis et al.* [2013] presented how the CALIPSO Saharan dust retrievals could be optimized, when corrections are applied regarding the Saharan dust lidar ratio assumption, the separation of the dust portion in detected dust mixtures, and the averaging scheme introduced in the CALIPSO Lidar Level 3 product.

³ CALIPSO Lidar Level 3 climatological products are monthly means. [*Winker et al.*, 2013]

2.5 Approaches of the aerosol typing and verification of the CALIPSO classification scheme presented in this thesis

Outputs of the CALIPSO aerosol classification scheme for CALIOP Version 3.01 data (cf. Section 3.2.2) – the latest version of the data available for the investigated period at the time of writing – are compared to results of multiwavelength ground-based measurements of selected EARLINET stations. Therefore, EARLINET measurements were searched for aerosol layers, which were then classified analog the introduced pure aerosol types as well as mixtures of the pure types. The aerosol typing presented here is based on an individual case-by-case study. For each measurement all available lidar parameters were used and the determination of the aerosol source was done carefully by using a set of various information including model simulation, prediction of aerosol load, satellite as well as meteorological data. In Chapter 5 case studies are presented for impressive measurements of pure aerosol types and for often observed aerosol mixtures. Statistical results of the aerosol typing, i.e., optical properties for pure aerosol types and most frequently observed aerosol mixtures over Europe, are summarized in the first part of Chapter 6. In the second part of this chapter results of the verification of the CALIPSO typing scheme are illustrated.

Chapter 3

EARLINET and CALIPSO

In Chapter 2 approaches for aerosol typing and the different types of aerosols that can be observed over Europe were introduced. In this chapter, the techniques applied for the aerosol typing and the theoretical background are presented. Section 3.1 starts with an overview of the ground-based European Aerosol Research Lidar Network. More than 20 stations have been operated in this network since the year 2000. Most of the EARLINET stations perform correlative observations during overpasses of the CALIPSO satellite, since the successful launch in 2006. An overview of CALIPSO with its backscatter lidar CALIOP is given in Section 3.2. Measurement techniques and important optical parameters are introduced. Furthermore, it is illustrated how measurements of long-term experienced EARLINET stations offer perfect opportunities for aerosol typing and how they can be used for the validation and harmonization of spaceborne lidar observations.

3.1 EARLINET – European Aerosol Research Lidar Network

3.1.1 Setup of the network

EARLINET is a continental-scale lidar network with a quality-assurance program for instruments and algorithms [Bösenberg *et al.*, 2001; Böckmann *et al.*, 2004; Matthias *et al.*, 2004; Pappalardo *et al.*, 2004b, 2014]. Figure 3.1 shows the geographical distribution of the 27 currently active EARLINET stations. The setup of the network allows for frequent aerosol profiling in key areas of anthropogenic pollution, in marine and desert dust environments as well as in regions of biomass-burning events. EARLINET stations provide regular observations three times per week. In addition, measurements are carried out for special events like Saharan dust outbreaks, volcanic eruptions, or

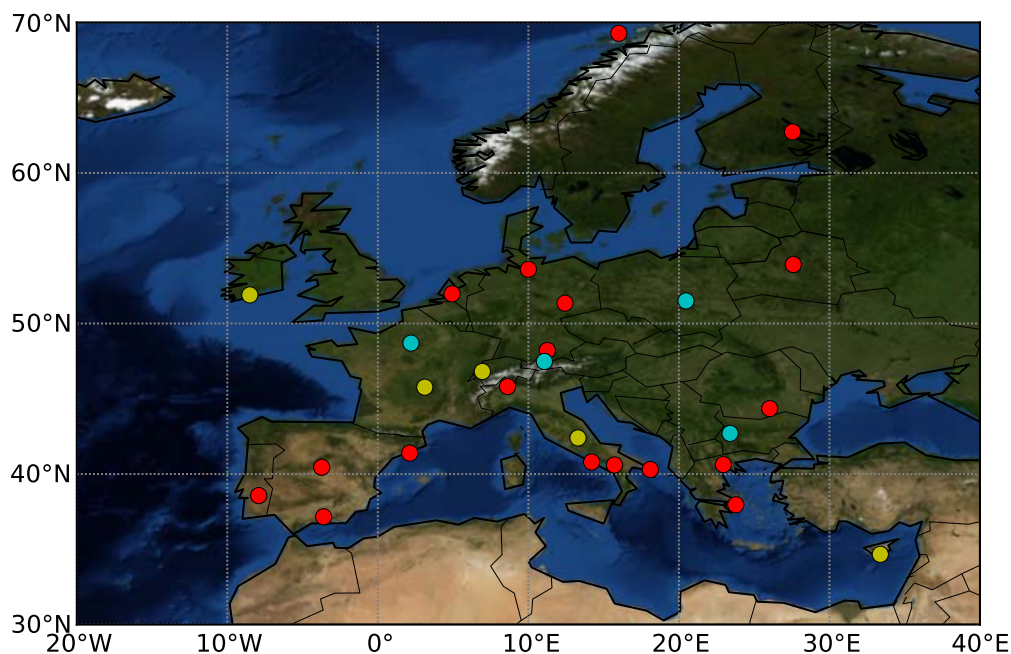


Figure 3.1: Geographical distribution of the 27 currently active EARLINET stations. Red dots indicate multiwavelength Raman lidar stations (EARLINET core stations). Yellow dots correspond to stations with at least one Raman channel. Blue dots denote lidars with only elastic-backscatter channels. Adapted from *Pappalardo et al.* [2014].

forest fires. Long-term measurements have been performed at multiple wavelengths (ultraviolet – UV, visible – VIS, infrared – IR). Based on these measurements aerosol-type-dependent optical parameters can be derived as it is explained below.

3.1.2 Measurement principle and available products

In general, a lidar consists of a transmitter and a receiver unit. The core of the transmitter unit is a pulsed laser. A laser pulse is sent into the atmosphere. On its way the emitted laser light is scattered and partly absorbed by molecules (mol) such as nitrogen and oxygen, but also by present solid or liquid constituents in the air such as aerosol particles, cloud droplets, ice crystals and precipitating hydrometeors, which are all summarized as particles (par). Part of the light is scattered back under 180° and collected and analyzed by the lidar receiver. The sum of the absorption and

scattering is called extinction and, hence, this term describes the attenuation of the emitted signal during its way through the atmosphere. The extinction coefficient at the wavelength λ_0 and the range R can be expressed as:

$$\alpha(\lambda_0, R) = \alpha^{\text{mol}}(\lambda_0, R) + \alpha^{\text{par}}(\lambda_0, R). \quad (3.1)$$

The amount of light that is scattered at 180° is described by the backscatter coefficient, which is also subdivided for molecules and particles:

$$\beta(\lambda_0, R) = \beta^{\text{mol}}(\lambda_0, R) + \beta^{\text{par}}(\lambda_0, R). \quad (3.2)$$

Particle extinction and backscatter coefficients, α^{par} and β^{par} , are extensive aerosol parameters, i.e., they depend on the absolute concentration of aerosol particles in the atmosphere and are not necessarily characteristic values for certain aerosol types.

The detection of the lidar signal is realized in the receiver unit, which is composed of a telescope mirror of the area A_T , an optical detection unit and a data acquisition system. The range-resolved received power, i.e., the detected lidar signal $P(\lambda_0, R)$, depends on the scattering and absorption processes explained above, but is also dependent on other parameters that are summarized in the lidar equation:

$$P(\lambda_0, R) = \frac{P_0(\lambda_0)\tau_p c A_T \mu(\lambda_0)}{2} \frac{O(\lambda_0, R)}{R^2} \beta(\lambda_0, R) \exp \left[-2 \int_0^R \alpha(\lambda_0, \epsilon) d\epsilon \right]. \quad (3.3)$$

The first term denotes the range-independent variables with the emitted laser power $P_0(\lambda_0)$ of a laser pulse at an emitted wavelength λ_0 that is backscattered within a range cell centered at the range R . The range cell is given by $\frac{\tau_p c}{2}$ with the laser pulse length τ_p and the speed of light c . A_T is the already mentioned area of the receiver telescope. $\mu(\lambda_0)$ is the wavelength-dependent transmission of the receiver optics, also called system efficiency. The second term includes correction factors like the geometric form factor $O(\lambda_0, R)$, which characterizes the overlap between the laser beam and the receiver field of view (RFOV) [Wandinger and Ansmann, 2002], and the inverse square distance R^{-2} . This term is followed by the backscatter coefficient $\beta(\lambda_0, R)$ and the transmission term expressed by an exponential function including the extinction coefficient $\alpha(\lambda_0, R)$.

In Bucholtz [1995] it is shown that molecular extinction and backscatter coefficients ($\alpha^{\text{mol}}, \beta^{\text{mol}}$) can be calculated for given profiles of temperature and pressure. In contrast, particle extinction and backscatter coefficients ($\alpha^{\text{par}}, \beta^{\text{par}}$) can be derived by two different approaches, which are used depending on the applied lidar technique. Mostly a photon is scattered from an atom or molecule so that the energy (wavelength and frequency) of the photon is conserved. That process is called elastic or Rayleigh scattering. In contrast, there are processes of inelastic scattering, which is also called

Raman scattering, at which a photon is scattered by an excitation so that the energy of the scattered photon is different from the energy of the incident photon. If the lidar is equipped with receiver channels for the detection of Raman scattering, the backscattering as well as the extinction can be determined from the elastic-backscatter profile and the respective Raman signal [Ansmann *et al.*, 1990, 1992a; Ansmann and Müller, 2005; Wandinger, 2005]. This approach is called Raman method and is applied whenever possible, because no critical assumptions are necessary. In principle, the low signal-to-noise ratios allow Raman measurements throughout the troposphere only at nighttime. At daytime, measurements in the lower troposphere are possible. The majority of daytime data is evaluated by using elastic-backscatter signals and applying the so-called Klett method [Klett, 1981, 1985; Fernald, 1984; Sasano *et al.*, 1985]. For an elastic-backscatter lidar [Hinkley, 1976; Megie, 1985; Kovalev and Eichinger, 2004; Ansmann and Müller, 2005] the problem arises that only one signal is detected while two unknown quantities (α^{par} , β^{par}) remain in the lidar equation (cf. Equation (3.3)). Since the scattering coefficients cannot be retrieved independently of each other, a ratio of extinction to backscattering, also known as lidar ratio S , is introduced to substitute one of the two unknowns. It is defined as the relation between the extinction coefficient α and the backscatter coefficient β measured at λ_0 for a specific range R . Again, contributions of molecules and particles have to be comprised. The molecular lidar ratio S^{mol} is constant ($\approx \frac{8\pi}{3}\text{sr}$) with height. The particle lidar ratio

$$S^{\text{par}}(\lambda_0, R) = \frac{\alpha^{\text{par}}(\lambda_0, R)}{\beta^{\text{par}}(\lambda_0, R)} \quad (3.4)$$

varies with range R , because it is sensitive to the size, shape, and absorption properties of the scattering particles [e.g., Wiegner *et al.*, 2009; Gasteiger *et al.*, 2011; Schuster *et al.*, 2012]. Especially the absorption properties (i.e., the imaginary part of the refractive index) of the scattering particles strongly influence the lidar ratio. Increasing particle absorption efficiency leads to increasing lidar ratio values. Typically, non-spherical particles have higher lidar ratios than spherical particles of the same size. Similar lidar ratios can be observed for totally different particle types due to the possible compensation of the different effects. For instance, lidar ratios of urban haze (small and highly absorbing) and mineral dust (large, non-spherical, and less absorbing) are similar with values of 50–55 sr [Ackermann, 1998; Müller *et al.*, 2007a; Tesche *et al.*, 2009b]. In general, the lidar ratio of tropospheric aerosols is typically lower for coarse-mode particles (i.e., sea salt, dust) with values of 20–50 sr than for small and/or highly absorbing accumulation-mode particles with values of 50–80 sr at 532 nm [Ackermann, 1998; Catrall *et al.*, 2005; Müller *et al.*, 2007a, and references therein].

For the analysis of signals of an elastic-backscatter lidar a reasonable value of

$S^{\text{par}}(\lambda_0, R)$ needs to be assumed to convert the retrieved backscatter-coefficient profiles into extinction profiles. Achievements and limitations of the Klett method have been discussed in the literature for decades [e.g., Fernald *et al.*, 1972; Klett, 1981; Fernald, 1984; Klett, 1985; Sasano *et al.*, 1985; Bissonnette, 1986; Gonzales, 1988; Ansmann *et al.*, 1992b; Kovalev, 1995; Kunz, 1996; Ackermann, 1998; Kovalev and Eichinger, 2004] and will not be repeated here. Since CALIOP onboard CALIPSO is an elastic-backscatter lidar estimates on the lidar ratio are needed. In the CALIPSO classification scheme aerosol-type- and wavelength-dependent lidar ratios are applied (cf. Section 3.2.3).

A further important quantity for aerosol typing is the depolarization ratio, the ratio of the backscattered radiation that is perpendicular and parallel polarized with respect to the plane of the polarization of the emitted laser pulse. The depolarization ratio can be determined when linearly polarized laser light is transmitted and two receiver channels with linear polarization analyzers oriented parallel and perpendicular to the plane of polarization of the transmitted light are employed. In this case, the volume linear depolarization ratio $\delta(\lambda_0, R)$ is defined as the ratio of the calibrated lidar returns received in these two channels:

$$\delta(\lambda_0, R) = C \frac{P_{\perp}(\lambda_0, R)}{P_{\parallel}(\lambda_0, R)}. \quad (3.5)$$

C is the calibration factor. The depolarization ratio can be determined for the whole scattering volume, but also for particles separately (particle linear depolarization ratio $\delta^{\text{par}}(\lambda_0, R)$). The particle linear depolarization ratio depends on particle size and shape. Backscattering by spheres does not alter the state of polarization of light. That means light is not depolarized and, thus, $\delta^{\text{par}}(\lambda_0, R) \approx 0$ for spherical particles. $\delta^{\text{par}}(\lambda_0, R)$ increases with increasing amount of large, non-spherical scatterers. In general, high-quality (highly accurate) measurements of the particle linear depolarization ratio are rare. Often, the easier to obtain volume depolarization ratio is used, but in most cases only for a qualitative distinction of non-spherical (mainly ice crystals or mineral dust) from spherical particles [Schotland *et al.*, 1971; Sassen, 1991, 2005].

The particle linear depolarization ratio is well accepted as a discriminator of dust [Shimizu *et al.*, 2004; Omar *et al.*, 2009]. In nearly pure dust high values of 30% to 35% depolarization at 532 nm were measured [Sugimoto and Lee, 2006; Liu *et al.*, 2008; Freudenthaler *et al.*, 2009]. Usually, for a mixture of dust with spherical particles smaller values, but larger than about 8%–10%, are observed [Murayama *et al.*, 2003; Sugimoto and Lee, 2006; Tesche *et al.*, 2009a]. High depolarization values can also be an indicator for ice particles, as in cirrus clouds [e.g., Sassen, 1977; Sakai *et al.*, 2003]. Smaller but detectable depolarization values are measured for crystallized sea salt [Murayama *et al.*, 1999; Sakai *et al.*, 2010] and aged biomass-burning and volcanic

aerosols [Sassen, 2008]. The degree of depolarization also varies with relative humidity, since hygroscopic swelling increases the sphericity of particles and decreases their depolarization [Murayama *et al.*, 1996; Sassen, 1999].

Depending on the operated lidar EARLINET stations provide at least one profile of a particle backscatter coefficient — for the sake of simplicity in the following called backscatter profile — but ideally also backscatter profiles for more than one wavelength. In case of a Raman lidar, profiles of the particle extinction coefficient — in the following called extinction profiles — are provided additionally. In general, some stations provide also information about the linear depolarization ratio. For this study only few information on depolarization was available, which then was mostly related to the volume and for the wavelength of $\lambda_0 = 532$ nm. Table 3.1 shows the used optical information from each station. Parameters in parentheses are usually provided by the stations, but were not available for the considered measurement period. The high-performance stations (Athens, Cabauw, Granada, Leipzig, Maisach, Minsk, Potenza, and Thessaloniki) equipped with multiwavelength Raman lidars are highlighted in bold. These stations provided usually extinction and backscatter coefficients at 355 and 532 nm. Most of them also delivered backscatter coefficients at 1064 nm and either the particle or the volume linear depolarization ratio. Raman lidar instruments were operated as well in Barcelona, Hamburg, L’Aquila, and Naples, but not at all wavelengths. At these sites highly reliable extinction and backscatter coefficients were predominantly provided at 355 or 532 nm. The remaining station (Belsk) was equipped with elastic-backscatter channels during the observational period from May 2008 until October 2009.

Extinction and backscatter profiles provided by EARLINET stations were used to determine lidar ratios as well as Ångström exponents and color ratios. The extinction-related Ångström exponent, \mathring{a}_α , at the measurement wavelengths λ_1 and λ_2 is defined by [Ångström, 1964]

$$\frac{\alpha^{\text{par}}(\lambda_1)}{\alpha^{\text{par}}(\lambda_2)} = \left(\frac{\lambda_2}{\lambda_1}\right)^{\mathring{a}_\alpha}. \quad (3.6)$$

Accordingly, the extinction-related, \mathring{a}_α , and backscatter-related, \mathring{a}_β , Ångström exponents are calculated for the indicated wavelengths (at 355 and 532 nm (UV–VIS), 532 and 1064 nm (VIS–IR), as well as 355 and 1064 nm (UV–IR)) as:

$$\mathring{a}_{\alpha,\text{UV-VIS}}(R) = \frac{\ln[\alpha^{\text{par}}(355 \text{ nm}, R)/\alpha^{\text{par}}(532 \text{ nm}, R)]}{\ln(532 \text{ nm}/355 \text{ nm})}, \quad (3.7)$$

$$\mathring{a}_{\beta,\text{UV-VIS}}(R) = \frac{\ln[\beta^{\text{par}}(355 \text{ nm}, R)/\beta^{\text{par}}(532 \text{ nm}, R)]}{\ln(532 \text{ nm}/355 \text{ nm})}, \quad (3.8)$$

$$\mathring{a}_{\beta,\text{VIS-IR}}(R) = \frac{\ln[\beta^{\text{par}}(532 \text{ nm}, R)/\beta^{\text{par}}(1064 \text{ nm}, R)]}{\ln(1064 \text{ nm}/532 \text{ nm})}, \quad (3.9)$$

Table 3.1: List of EARLINET stations whose data were used for this work. Station ID according to EARLINET convention, coordinates, and measured parameters are given (α –extinction coefficient, β –backscatter coefficient, δ –linear depolarization ratio; indices indicate the wavelength; parameters in parentheses were not provided for the considered measurement period). High-performance core stations equipped with multiwavelength Raman lidars are highlighted in bold.

| Station | ID | Coord. | α_{355} | α_{532} | β_{355} | β_{532} | β_{1064} | δ_{532} |
|---------------------|----|------------------|----------------|----------------|---------------|---------------|----------------|----------------|
| Athens | at | 38.0 N 23.8 E | x | x | x | x | x | – |
| Barcelona | ba | 41.4 N 2.1 E | – | x | – | x | x | – |
| Belsk | be | 51.8 N 20.8 E | – | – | x | x | x | – |
| Cabauw | ca | 52.0 N 4.9 E | x | x | x | x | x | (x) |
| Granada | gr | 37.2 N 3.6 W | x | x | x | x | x | (x) |
| Hamburg | hh | 53.6 N 10.0 E | (x) | (x) | x | x | (x) | (x) |
| L’Aquila | la | 42.4 N 13.3 E | x | – | x | – | – | – |
| Leipzig | le | 51.4 N 12.4 E | x | x | x | x | x | x |
| Maisach | ms | 48.2 N 11.2 E | x | x | x | x | x | x |
| Minsk | mi | 53.9 N 27.6 E | x | – | x | x | x | x |
| Naples | na | 40.8 N 14.2 E | (x) | x | (x) | x | – | – |
| Potenza | po | 40.6 N 15.7 E | x | x | x | x | x | (x) |
| Thessaloniki | th | 40.6 N 23.0 E | x | x | x | x | – | – |

$$\mathring{a}_{\beta,UV-IR}(R) = \frac{\ln[\beta^{\text{par}}(355 \text{ nm}, R)/\beta^{\text{par}}(1064 \text{ nm}, R)]}{\ln(1064 \text{ nm}/355 \text{ nm})}. \quad (3.10)$$

Ångström exponents describe the relative spectral relationship of the scattering coefficient. This behavior depends on the size of the scattering particles. Hence, the Ångström exponent contains information about the dominating particle size. Ångström exponents for the short-wavelength range are sensitive to particles of the fine-mode fraction of the size distribution (particle diameters $< 1 \mu\text{m}$), typically for urban pollution aerosols [Müller *et al.*, 2007a]. Scattering by small particles shows a strong wavelength dependence and causes Ångström exponents that are larger than unity [Eck *et al.*, 1999]. On the other hand, values of $\mathring{a} \approx 0$ denote wavelength independence of the investigated quantity, which is due to scattering by coarse-mode particles (with diameters typically $> 1 \mu\text{m}$), e.g., desert dust and marine particles.

The extinction- and backscatter-related color ratio, C , in principle, contains the same information as the Ångström exponent, because it describes also the ratio of two scattering coefficients for different wavelengths. Color ratios typically are inversely related to aerosol particle size [Sasano and Browell, 1989; Sugimoto *et al.*, 2002]. Following the CALIPSO convention [Winker *et al.*, 2009] the value for the longer wavelength is divided by the value for the shorter wavelength. This fact has to be kept in mind when comparing the results with literature data, because the opposite wavelength definition is often used. For the particle extinction coefficients measured at 532 and 355 nm (VIS–UV) the respective color ratio is defined as

$$C_{\alpha,VIS-UV}(R) = \frac{\alpha^{\text{par}}(532 \text{ nm}, R)}{\alpha^{\text{par}}(355 \text{ nm}, R)}. \quad (3.11)$$

The ratio of the particle backscatter coefficients measured at 532 and 355 nm (VIS–UV), 1064 and 532 nm (IR–VIS), as well as 1064 and 355 nm (IR–UV) are determined correspondingly:

$$C_{\beta,VIS-UV}(R) = \frac{\beta^{\text{par}}(532 \text{ nm}, R)}{\beta^{\text{par}}(355 \text{ nm}, R)}, \quad (3.12)$$

$$C_{\beta,IR-VIS}(R) = \frac{\beta^{\text{par}}(1064 \text{ nm}, R)}{\beta^{\text{par}}(532 \text{ nm}, R)}, \quad (3.13)$$

$$C_{\beta,IR-UV}(R) = \frac{\beta^{\text{par}}(1064 \text{ nm}, R)}{\beta^{\text{par}}(355 \text{ nm}, R)}. \quad (3.14)$$

Per definition color ratios are wavelength conversion factors, which are needed to relate results from the different space missions as already introduced in Chapter 1.

If extinction and backscatter coefficients at 355 and 532 nm were available and, hence,

the lidar ratios at both wavelengths could be determined, the ratio of the lidar ratios, the so-called S -ratio, defined as

$$s_{\text{VIS-UV}}(R) = \frac{S^{\text{par}}(532 \text{ nm}, R)}{S^{\text{par}}(355 \text{ nm}, R)} \quad (3.15)$$

was computed. Errors of the above-listed parameters are given in terms of the standard deviation of the layer mean value. Atmospheric variability as well as statistical noise present in the primary extinction and backscatter profiles contribute to this error.

3.1.3 Data set

The geographical distribution of EARLINET stations over Europe enables covering a large variety of different aerosol contents in the free troposphere and the local planetary boundary layer [Matthias *et al.*, 2004; Pappalardo *et al.*, 2004a; Wandinger *et al.*, 2004; Papayannis *et al.*, 2008; Amiridis *et al.*, 2009]. After the successful launch of CALIPSO a special measurement strategy for EARLINET stations was developed, including additional measurements by EARLINET stations during a defined time frame around a satellite overpass to sample enough correlated data for direct comparison of ground-based and spaceborne lidar data.

For this thesis, data from EARLINET stations that provide high-quality data since years were chosen. Especially, observational data between May 2008 and October 2009, a period of increased measurement activity during CALIPSO overpasses performed in the framework of the ESA–CALIPSO project, were evaluated in detail [Wandinger *et al.*, 2011]. This data set of correlative measurements from ground and space provides the opportunity to derive on the one hand typical aerosol optical properties as a function of geographical region and on the other hand to compare the identified aerosol layers with the ones seen by the spaceborne lidar CALIOP, always keeping in mind that it is a comparison between a single ground-based and a single satellite-borne measurement with a non-negligible horizontal distance between the two sampled air volumes and a different integration time.

Figure 3.2 shows the EARLINET stations whose data were used for this work. These stations are located such that European core regions and, hence, source regions of different aerosol types are covered. Observational data were evaluated from Central European stations in Germany (Leipzig, Hamburg, Maisach near Munich) and the Netherlands (Cabauw), as well as from Mediterranean stations from Spain (Granada, Barcelona) representing the Western Mediterranean, Italy (Potenza, Naples) in the Central Mediterranean, to Greece (Athens, Thessaloniki) in the Eastern Mediterranean. Measurements were also investigated from stations in Eastern Europe (Belsk, Minsk). In this way, a broad variety of aerosol types and scenarios could be investigated, which include marine aerosols (Barcelona, Cabauw, Hamburg), rural (Maisach,

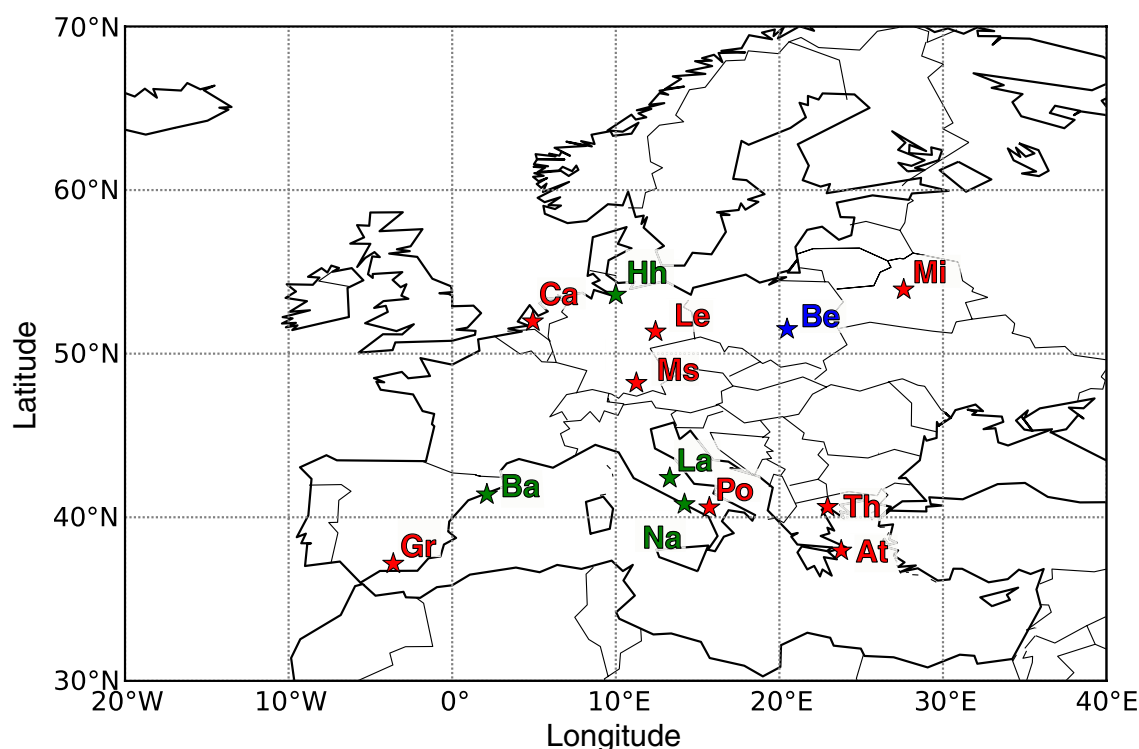


Figure 3.2: Map of EARLINET stations whose data were used for this thesis. The colors of the stars indicate the instrumentation of the stations during the investigated measurement period 2008–2009. Red stars show the high-performance core stations equipped with multiwavelength Raman lidar (At-Athens, Ca-Cabauw, Gr-Granada, Le-Leipzig, Ms-Maisach, Mi-Minsk, Po-Potenza, Th-Thessaloniki). Green stars represent stations with at least one Raman channel (Ba-Barcelona, Hh-Hamburg, La-L’Aquila, Na-Naples). The blue star denotes the lidar with only elastic-backscatter channels (Be-Belsk).

Potenza) and urban aerosols (Athens, Leipzig, Naples) as well as biomass-burning smoke (fresh: Mediterranean stations, aged: Central European stations) and aerosols from intercontinental transports in the free troposphere like Saharan dust (fresh: Mediterranean stations, aged: all stations), volcanic aerosols, and other aerosols from America and Asia (all stations). In addition to the tropospheric aerosol layers even stratospheric aerosols have been observed.

Figure 3.3 illustrates CALIPSO satellite night- and day-time cross sections on 21 August 2008 (dotted lines). The EARLINET stations closest to the satellite cross sections are indicated. As can be seen from Figure 3.3 one CALIPSO overpass is close to more than one EARLINET station which is good for the comparison and validation of the satellite data against ground-based network measurements. To account for the non-negligible horizontal distance between the footprint of CALIOP and the position of the EARLINET station a special measurement strategy took care of the variability and

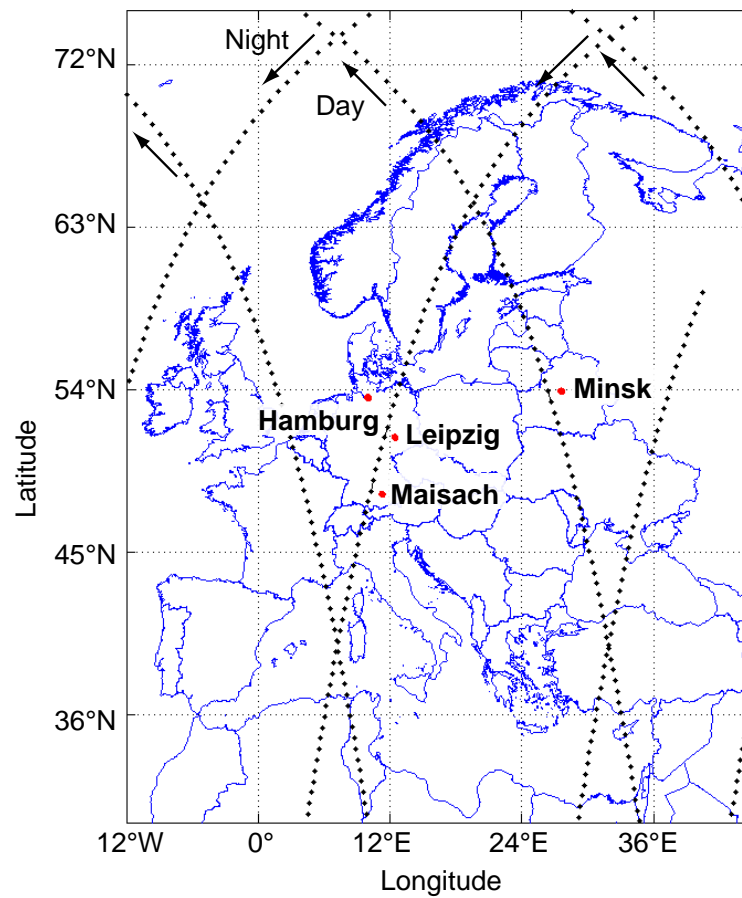


Figure 3.3: CALIPSO satellite night- and day-time cross sections on 21 August 2008 (dotted lines). The EARLINET stations closest to the satellite cross sections are indicated.

the movement of the probed air volume. For the direct comparison of aerosol layers only measurements within 100 km distance are considered. A special measurement time schedule was calculated and distributed to the EARLINET stations based on the 16-day CALIPSO observation cycle and the 1-s resolution of the CALIPSO ground track provided and updated weekly by NASA. For this special measurement strategy the distance between the footprint of CALIOP and the location of the EARLINET station is considered to define the observation time that should be as close in time as possible. Measurements were only performed during good atmospheric conditions (in absence of rain, fog, low clouds) and, if possible, over 150 minutes centered around a CALIPSO overpass. In this way, also the movement of the sensed air volume can be considered in the data evaluation. For each measurement profiles of extinction and backscatter coefficients at different wavelengths and, if possible, linear depolarization ratio at 532 nm were evaluated at each station individually and uploaded to

the EARLINET database [*The EARLINET publishing group 2000-2010*, 2014], where the profiles can be visualized and also downloaded for further investigations. These profiles were used to calculate intensive particle parameters like lidar ratios as well as extinction- and backscatter-related Ångström exponents and color ratios (cf. Section 3.1.2).

So far, EARLINET does not apply automated algorithms for the identification of aerosol or cloud layers. Usually, layer boundaries are determined with the help of derivative methods or wavelet analysis [e.g., *Flamant et al.*, 1997; *Menuet et al.*, 1999; *Brooks*, 2003; *Matthias et al.*, 2004; *Mattis et al.*, 2004; *Baars et al.*, 2008]. For this study, measurements were searched individually for the presence of aerosol layers, which are also called *features* analog to the CALIPSO terminology. The type/origin, age, and state of humidification of each distinct feature in a measurement was investigated in detail by interpreting the ground-based data themselves and with the help of atmospheric state parameters, trajectory and transport models that are introduced in Chapter 4. Aerosol layers have been investigated in detail with respect to layer-mean values of spectral backscatter and extinction coefficients, lidar ratios, depolarization ratio, extinction- and backscatter-related Ångström exponents, and color ratios. Chapter 5 provides a detailed discussion of the data evaluation concept.

3.2 CALIPSO – Cloud–Aerosol Lidar and Infrared Pathfinder Satellite Observations

The CALIPSO satellite was launched on 28 April 2006 to study the impact of clouds and aerosols on the Earth’s radiation budget and climate. It is a joint satellite mission of NASA and CNES, the French government space agency (Centre national d’études spatiales, English: National Centre for Space Studies). CALIPSO flies in formation with five other satellites (e.g., Aqua and CloudSat) in the international “A-Train” constellation for coincident Earth observations. It is a polar-orbiting satellite located at an altitude of about 705 km with a flight velocity of 7 kms^{-1} and a revisiting time of 16 days. The CALIPSO satellite comprises three instruments, the space lidar CALIOP, the Imaging Infrared Radiometer (IIR), and the Wide Field Camera (WFC). For this thesis data from CALIOP were used.

3.2.1 CALIOP instrument

CALIOP is the first satellite lidar optimized for cloud and aerosol observations and, hence, provides the first unique opportunity to study the four-dimensional distribution of aerosols and clouds on a global scale [*Winker et al.*, 2007]. CALIOP is a

two-wavelength, polarization-sensitive lidar providing information on the attenuated backscatter signal at 532 and 1064 nm and depolarization at 532 nm. The lidar is very sensitive with a high horizontal as well as a very high vertical resolution. The laser has a pulse repetition rate of 20.16 Hz and a small footprint on the ground of about 70 m in diameter, which enables the profiling of the atmosphere every 0.05 s or 330 m horizontally. The vertical resolution is 30 m [Hunt *et al.*, 2009]. Thanks to laser purity and small bandwidth the discrimination against noise is said to be excellent. Measurements between clouds and the penetration of optically thin clouds and, therefore, the profiling of the atmosphere underneath are possible. The data processing is realized in an automated way using different algorithms [Winker *et al.*, 2009]. The aerosol-cloud discrimination, aerosol classification and extinction retrieval are described by Liu *et al.* [2009], Omar *et al.* [2009] and Vaughan *et al.* [2009], respectively. A summary of the data evaluation is given in the following.

3.2.2 Data evaluation

Optical data of CALIOP are evaluated starting with the identification of aerosol and cloud layers and the determination of their base and top heights. In the CALIPSO terminology an aerosol or cloud layer is named *feature*. Vaughan *et al.* [2009] specified that features are “composed of a generic substance called particulates and are defined as any extended, vertically contiguous region of enhanced backscatter that rises significantly above the signal magnitude expected from a purely molecular atmosphere”. CALIOP profiles are scanned for features and their boundaries based on a threshold algorithm [Vaughan *et al.*, 2004, 2005, 2009]. This method can only be applied for strong features whereas faint features are identified by using a multi-resolution spatial averaging scheme called SIBYL (Selective Iterated Boundary Location). This averaging of lidar profiles has to be done because automated algorithms especially for spaceborne observations are limited by the low signal-to-noise ratio, which can be improved by averaging lidar signals. For CALIOP data this is done in steps of 5, 20, and 80 km. For the discrimination of the feature boundaries the attenuated scattering ratio is used [Vaughan *et al.*, 2009],

$$R'(r) = \frac{\beta'_{532}(r)}{\beta'_{\text{GMAO}}(r)} = \left[1 + \frac{\beta_{532}^{\text{par}}(r)}{\beta_{532}^{\text{mol}}(r)} \right] [T_{532}^{\text{par}}(r)]^2, \quad (3.16)$$

which is the ratio of the attenuated backscatter and the molecular part gained from the Global Modeling and Assimilation Office (GMAO). For clear air $R'(r) = 1$. For a profile containing a feature $R'(r) > 1$. With SIBYL not only aerosol and cloud features are identified, but also regions with clear air, features in the stratosphere, the surface return as well as subsurface regions, and regions with bad or missing data. Parameters

that are provided by this scheme are feature boundaries, layer-integrated attenuated backscatter, volume depolarization ratio, and the color ratio (1064 nm/532 nm).

In a next step, the scene classification algorithms (SCA) are applied to discriminate clouds from aerosols, the cloud phase (water, randomly-oriented ice, horizontally-oriented ice), and aerosol subtypes. The discrimination of clouds and aerosols is performed based on characteristic optical properties: clouds show a stronger attenuation than aerosols, steeper boundaries (both in the horizontal and vertical direction), a higher signal variation in space and time, and neutral scattering that results in a color ratio of about one due to their large size.

The cloud–aerosol discrimination (CAD) algorithm implemented for CALIOP separates clouds and aerosols based on multi-dimensional probability density functions (PDFs), more precisely histograms of scattering properties (e.g., intensity and spectral dependence) are used as a function of geophysical location [Vaughan *et al.*, 2004, 2005; Liu *et al.*, 2009]. In the current release (Version 3), the CAD algorithm uses five-dimensional (5D) PDFs, rather than the three-dimensional (3D) PDFs used in previous versions. In addition to the parameters used in the earlier 3D version of the algorithm (the layer-integrated attenuated backscatter at 532 nm, the layer-integrated attenuated backscatter-related color ratio (1064 nm/532 nm), and the mid-feature altitude [Liu *et al.*, 2004, 2009]), the 5D PDFs also include feature latitude and the layer-integrated volume depolarization ratio. For the classification of layers by the CALIOP CAD algorithm the CAD score, a numerical confidence level, is indicated, which is reported in the CALIPSO Lidar Level 2 products (1-km and 5-km Layer products, and in Version 3 also for the 5-km Cloud and Aerosol Profile products; cf. Section 3.2.3).

Enhancements made to incorporate the 5D PDFs used in Version 3 release are described in Liu *et al.* [2010]. However, the authors also reported on recognized misclassification that may still occur. For example, when moderately dense dust layers are occasionally transported to high latitudes, where ice clouds can be present even in the low altitudes, they may be misclassified. This is also the case for volcanic aerosol injected into the high altitudes that may have a large cross-polarized backscatter signal and, thus, may be misclassified as cloud.

After feature finding and aerosol-cloud discrimination only “cloud-free” profiles are used for the aerosol typing. The determination of specific aerosol types is done by applying further scene classification algorithms. The CALIPSO aerosol classification scheme [Omar *et al.*, 2009] is shown in Figure 3.4. The scheme categorizes observed layers among the six introduced aerosol types by using a decision tree that takes into account external information on geographical location, surface type, and season and lidar-derived information on the feature height and feature-integrated values of depolarization, attenuated backscattering, and attenuated backscatter-related color ratio.

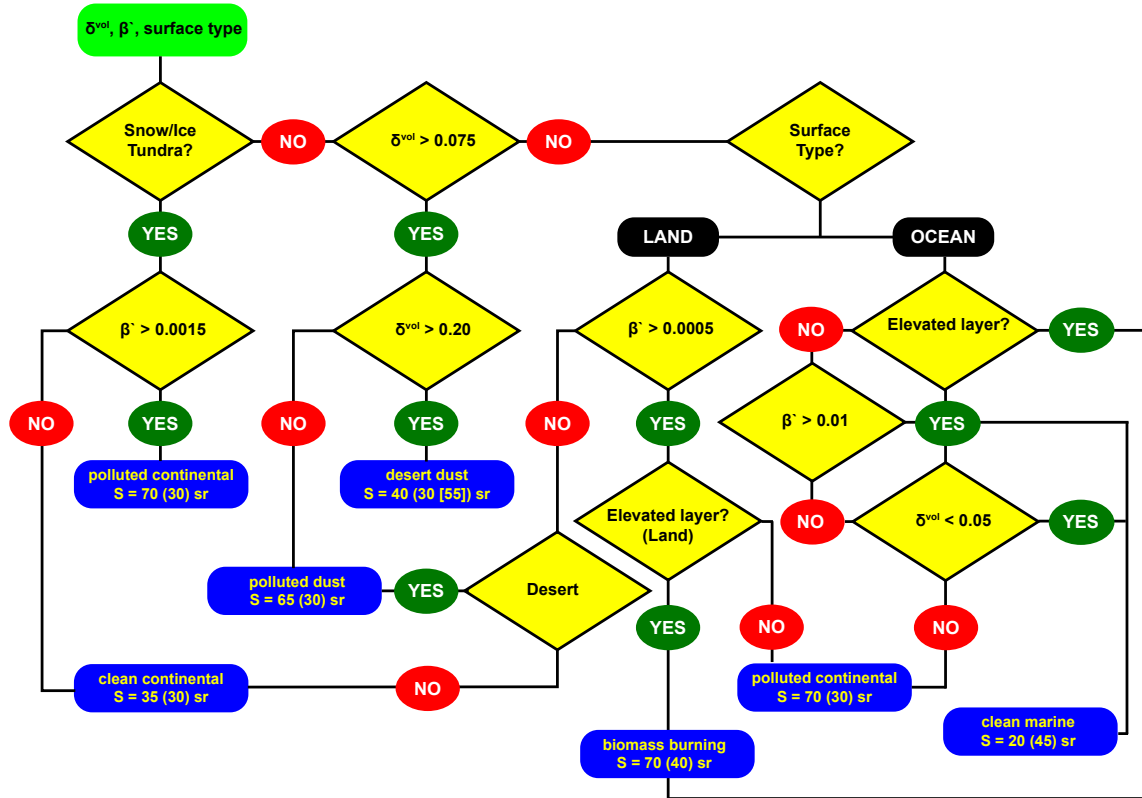


Figure 3.4: Flowchart of the CALIPSO lidar ratio selection scheme for tropospheric aerosols (δ^{vol} –volume linear depolarization ratio, β' –integrated attenuated backscatter, S –initial estimates of the lidar ratio at 532 (1064) nm used for CALIPSO extinction and backscatter retrievals for the selected aerosol subtype), adapted from *Omar et al.* [2009]. The lidar ratio for dust at 1064 nm was changed for the CALIPSO Version 3.01 data release from 30 to 55 sr.

Based on this decision tree aerosol-type-dependent lidar ratios at 532 and 1064 nm are selected that are used in the Hybrid Extinction Retrieval Algorithm (HERA) [Young and Vaughan, 2009].

As explained in Chapter 2 the CALIPSO aerosol typing is based on modeled aerosol properties and on experimental findings. The input parameters mainly rely on AERONET Sun photometer retrievals and the respective studies by *Cattrall et al.* [2005] and *Omar et al.* [2005]. For dust a spheroid particle model is applied to calculate the optical data (lidar ratios), whereas Mie scattering is used for the other types [Omar et al., 2009]. The *a priori* lidar ratio for dust at 1064 nm was updated for Version 3.01 using dust measurements from the NASA African Monsoon Multidisciplinary

Analyses (NAMMA) field campaign and T-Matrix calculations of particle phase functions [Omar *et al.*, 2010]. The feature-integrated depolarization value in this case is an estimate, an intermediate product, which is affected by attenuation. It belongs to CALIPSO Lidar Level 1 products (cf. Section 3.2.3). In contrast, CALIOP's measurement of volume depolarization, which is provided within CALIPSO Lidar Level 2 products, is highly reliable [Liu *et al.*, 2013].

3.2.3 CALIPSO Lidar products

CALIPSO data are accessible via the NASA Langley Research Center Atmospheric Science Data Center (LaRC ASDC) available at https://eosweb.larc.nasa.gov/project/calipso/calipso_table. Information is stored in Hierarchical Data Format (HDF), the standard data format for all NASA Earth Observing System (EOS) data products. The CALIPSO lidar data (also referred to as CALIOP lidar data) are stored for day- and night-time conditions (day and night orbit) and for different levels:

- Level 1B data contain calibrated and geo-located profiles (half orbit, night and day);
- Level 2 data sets provide geophysical products subdivided in aerosol or cloud information reported for layers (Layer data) as well as for profiles (Profile data). They also contain information on the vertical feature mask (aerosol particle properties, cloud type, cloud particle phase) and of polar stratospheric clouds;
- Level 3 data are globally gridded and monthly averaged Aerosol Profile data and ancillary data.

For this work CALIPSO Lidar Level 1 and Level 2 Aerosol Layer and Profile data of Version 3.01, which are provided at the same horizontal resolution of 5 km, were used.

3.2.3.1 CALIPSO Lidar Level 2 Aerosol Layer data

The main products of this kind of files are the optical and geometrical properties of identified aerosol layers. For each observation a Level 2 Aerosol Layer file at 5 km horizontal resolution is produced, but up to 80 km horizontal averaging is used for the layer detection. The layer identification is performed by means of a complex algorithm that is mainly based on a threshold routine with the specification that the threshold is height-dependent. Advanced procedures are used to avoid false alarm due to noise. The layer detection is performed from space down to the Earth's surface. For each layer, the following quantities are reported.

The *integrated attenuated backscatter* at 532 nm and 1064 nm is defined as [Omar *et al.*, 2009]:

$$\beta'_{\text{feature}} = \int_{\text{top}}^{\text{base}} \beta^{\text{par}}(\lambda_0, R) [T^{\text{par}}(\lambda_0, R)]^2 dR, \quad (3.17)$$

where $\beta^{\text{par}}(\lambda_0, R)$ is the particle backscatter coefficient at wavelength λ_0 (532 nm or 1064 nm) at range R . $T^{\text{par}}(\lambda_0, R)$ is the transmission term present in the elastic lidar equation due to the particles contained in the atmospheric feature.

The feature backscatter intensity

$$B'_{\text{feature}} = \frac{\beta'(\lambda_0, R)}{[T^{\text{mol}}(\lambda_0, R)]^2 [T^{\text{O}_3}(\lambda_0, R)]^2} \quad (3.18)$$

is given by the corrected total attenuated backscatter $\beta'(\lambda_0, R)$, which is the calibrated CALIOP range-corrected signal obtained after the subtraction of the background, divided by atmospheric transmission due to molecular scattering T^{mol} and ozone absorption T^{O_3} . $\beta'(\lambda_0, R)$ is reported in Level 1 data [Hostetler *et al.*, 2006] and defined as [Vaughan *et al.*, 2009]:

$$\beta'(\lambda_0, R) = [\beta^{\text{par}}(\lambda_0, R) + \beta^{\text{mol}}(\lambda_0, R)] [T^{\text{par}}(\lambda_0, R)]^2 [T^{\text{mol}}(\lambda_0, R)]^2 [T^{\text{O}_3}(\lambda_0, R)]^2. \quad (3.19)$$

Starting from the feature backscatter intensity, the attenuated total color ratio is calculated as:

$$\chi'(R) = \frac{B'_{1064}(R)}{B'_{532}(R)}. \quad (3.20)$$

It follows that the *integrated attenuated total color ratio* is:

$$\chi'_{\text{feature}} = \frac{\sum_{k=\text{top}}^{\text{base}} B'_{1064}(r_k)}{\sum_{k=\text{top}}^{\text{base}} B'_{532}(r_k)}. \quad (3.21)$$

Furthermore, the volume depolarization ratio is defined as the ratio of attenuated backscatter received in the two channels for the detection of perpendicular and parallel polarized backscatter signals with respect to the plane of polarization of the transmitted laser light [Liu *et al.*, 2013]:

$$\delta^{\text{vol}} = \frac{\beta'_{532,\perp}}{\beta'_{532,\parallel}}. \quad (3.22)$$

The *integrated volume depolarization ratio* is defined as:

$$\delta^{\text{vol}}_{\text{feature}} = \frac{\sum_{k=\text{top}}^{\text{base}} \beta'_{532,\perp}(r_k)}{\sum_{k=\text{top}}^{\text{base}} \beta'_{532,\parallel}(r_k)}. \quad (3.23)$$

For each of these quantities mean, standard deviation, minimum, maximum, centroid, and skewness values are reported. Level 2 Layer data contain also additional information about the nature of identified layers, namely feature classification flags and the CAD score. The feature classification flags provide information about the feature type (e.g., cloud vs. aerosol vs. stratospheric feature), the feature subtype (kind of aerosol), and the amount of horizontal averaging required for layer detection. Moreover, the CAD score provides information on the results obtained for each layer by the CAD algorithm [Liu *et al.*, 2009].

3.2.3.2 CALIPSO Lidar Level 2 Aerosol Profile data

The CALIPSO data processing system generates profile products separated for clouds and aerosols. All features detected in the stratosphere are provided in the Aerosol Profile product. The Aerosol Profile products with a horizontal resolution of 5 km are reported over an altitude range from 30 km to -0.5 km. Due to constraints imposed by CALIPSO's onboard data averaging scheme, the vertical resolution of the Aerosol Profile data varies as a function of altitude. The products in Version 3.01 are reported on a horizontal grid with 5 km grid size; the spatial resolution is 60 m vertically between the surface and 20.2 km and 180 m above that altitude [Powell *et al.*, 2011]. CALIPSO calibrated Level 2 Aerosol Profile data contain vertical profiles of the particle backscatter coefficients (at 532 and 1064 nm), the perpendicular particle backscatter coefficient at 532 nm, the particle linear depolarization ratio at 532 nm, and particle extinction coefficients (at 532 and 1064 nm).

Retrieving optical depth and profiles of extinction and backscatter coefficients from the CALIOP measurements requires an estimate of the lidar ratio. These initial estimates are selected based on the type and subtype of the layer being analyzed and

Table 3.2: Initial estimates of the lidar ratio, S , at 532 and 1064 nm used for extinction and backscatter retrievals of the current CALIPSO data (Version 3) release for defined aerosol subtypes and stratospheric features, after Omar *et al.* [2009].

| Type | Subtype | Initial S_{532} | Initial S_{1064} |
|---------------|-------------------------|-------------------|--------------------|
| aerosol | clean marine | 20 sr | 45 sr |
| aerosol | desert dust | 40 sr | 55 sr |
| aerosol | polluted continental | 70 sr | 30 sr |
| aerosol | clean continental | 35 sr | 30 sr |
| aerosol | polluted dust | 65 sr | 30 sr |
| aerosol | biomass burning (smoke) | 70 sr | 40 sr |
| stratospheric | all | 15 sr | 15 sr |

are mainly derived from AERONET climatological studies and model calculations as already introduced above [Cattrall *et al.*, 2005; Young *et al.*, 2008; Omar *et al.*, 2009]. The values used in the current release are summarized in Table 3.2. The initial lidar ratio is adjusted, if the extinction retrieval leads to a non-physical solution [Young *et al.*, 2008]. However, because of the natural variability of each aerosol species, even for cases for which the aerosol type is correctly identified, the initial lidar ratio represents an imperfect estimate of the effective lidar ratio of any specific aerosol layer. Several quality-control procedures are applied to the CALIOP data and documented in the appendix of Winker *et al.* [2013]. They are used to remove bad or highly uncertain aerosol extinction data. Additional tests are applied to remove several known artifacts. The detailed description of the so-called quality flags including the atmospheric volume description, the CAD score [Liu *et al.*, 2009], the feature classification flags [Omar *et al.*, 2009], and information on the extinction quality check [Young and Vaughan, 2009] can be found in the mentioned data-quality summaries archived at the LaRC ASDC.

3.2.3.3 Errors in CALIPSO Lidar Version 3 data

The Version 3 5-km profiles are known to be very noisy what influences not only the mean profiles. When averaging these profiles only one so-called outlier (one profile that strongly differs from the others without being influenced by specific atmospheric factors) can pretend an optical depth that the algorithm tries to correct for, although it is not there. It has to be kept in mind that once a positive bias is produced at a certain height, the effect builds up toward the ground, because of the integration procedure in the attenuation correction. A further source of error are the lidar-ratio assumptions made in the automated CALIOP algorithm. For instance, when the *a priori* lidar ratio is too small, the signal attenuation is underestimated and not completely corrected for and, thus, the resulting backscatter coefficient is also too small. In addition, the error originating from horizontal inhomogeneities due to large concentration gradients can never be ruled out and is a large source of variability. These errors complicate a comparison of CALIOP data against, e.g., EARLINET data and deviations are expected to show up not only because of the spatial differences between the observation points.

In spite of all new and unique results from CALIPSO different questions arise. How well do the automated algorithms for the data evaluation perform and how reliable are such kind of spaceborne measurements? As already mentioned above, ground-based observations can be used for the validation and direct measurement of, e.g., lidar ratios, to verify the required assumptions. Within this thesis the CALIPSO aerosol subtype was compared to the one derived from correlative EARLINET observations.

Chapter 4

Auxiliary data and tools for stand-alone aerosol typing

For an aerosol-type identification in all conscience a careful analysis of the air-mass transport and of meteorological parameters near the aerosol source regions, along the transport pathways, and during the final observation is required. Therefore, a number of auxiliary data and modeling tools have been used and are briefly explained in this chapter.

4.1 Meteorological parameters

Information about temperature, pressure, and humidity can, e.g., be derived from surface observations or radiosondes. Radiosonde data from national meteorological services in Europe are collected in a radiosonde network, which provides atmospheric state parameters on a fixed spatial and temporal grid (cf. <http://weather.uwyo.edu/upperair/sounding.html>). In addition, so-called “modeled” radiosonde data for specific times and grid points can be used, which are available from the re-analysis of meteorological fields with forecast models. The relative humidity for the determined aerosol layers in the EARLINET profiles was evaluated by using final assimilated data fields including surface observations as well as radiosonde and satellite-based data stored in the global data assimilation system (GDAS) [Kanamitsu, 1989]. These so-called GDAS1 data are available at <ftp://arlftp.arlhq.noaa.gov/pub/archives/gdas1/>. Based on GDAS the National Centers for Environmental Prediction (NCEP) of the U.S. National Weather Service maintain a data archive containing assimilated observational data, which are used to initialize model runs for weather forecasts, e.g., the Global Forecast System (GFS) Model. Outputs of the GFS and GME (Global Model of Germany’s National Meteorologi-

cal Service, the Deutscher Wetterdienst (DWD)) were applied to obtain an overview of meteorological conditions during the measurements. Prevailing circulation pattern and associated airflows serve as a clue for a first estimation of possible aerosol sources.

4.2 Modeling tools for aerosol source identification

4.2.1 FLEXPART

The Lagrangian model FLEXPART [Stohl *et al.*, 1998; Stohl and Thomson, 1999; Stohl *et al.*, 2005], operated by the Norwegian Institute for Air Research, is used to determine the origin, transport, and mixing of the identified aerosol layers. “Lagrangian particle models compute trajectories of a large number of so-called particles (not necessarily representing real particles, but infinitesimally small air parcels) to describe the transport and diffusion of tracers in the atmosphere” [Stohl *et al.*, 2005].

FLEXPART can be used to simulate long-range and mesoscale transport, diffusion, dry and wet deposition, and radioactive decay of tracers released from point, line, area or volume sources. The model parameterizes turbulence in the boundary layer and in the free troposphere by solving Langevin equations [Stohl and Thomson, 1999]. To account for convection, a parameterization scheme is used [Emanuel and Živković-Rothman, 1999], which is based on the buoyancy sorting principle [Stohl and Thomson, 1999; Stohl *et al.*, 2005].

The working group Ground-Based Remote Sensing of the Leibniz Institute for Tropospheric Research (TROPOS) has implemented FLEXPART on an own server what allows extensive model runs. Wind fields from global model-level data are used as input – more precisely the archived NCEP FNL (final analysis) Operational Global Analysis data on a $1^\circ \times 1^\circ$ grid prepared operationally every six hours (00, 06, 12, 18 UTC). “This product is from the GDAS, which continuously collects observational data from the Global Telecommunications System (GTS), and other sources, for many analysis. The FNLs are made with the same model which NCEP uses in the GFS, but the FNLs are prepared about an hour or so after the GFS is initialized. The FNLs are delayed so that more observational data can be used. The GFS is run earlier in support of time critical forecast needs, and uses the FNL from the previous 6 hour cycle as part of its initialization” (cf. <http://dss.ucar.edu/datasets/ds083.2/>).

The FNL data are provided by the CISL (Computational & Information Systems Laboratory) Research Data Archive, which is managed by NCAR’s (National Center for Atmospheric Research) data support section available at <http://rda.ucar.edu/>.

Particles are transported both by the resolved winds and by parameterized sub-grid motions. For the present work 50000 “particles” and a simulation of 10 days backwards in time were used. These values have proven valuable to provide reliable results

for such kind of studies (cf. *Preißler* [2008] for basic experiments concerning variation of number of chosen air parcels and simulation time). As output the residence time of air parcels accumulated over the chosen simulation time period plotted as time series and/or footprints were used (cf. Chapter 5).

4.2.2 HYSPLIT

Backward trajectories calculated with the on- and offline versions of the Hybrid Single-Particle Lagrangian Integrated Trajectory (HYSPLIT) model [*Draxler and Rolph*, 2014; *Stein et al.*, 2015] can also be used to investigate the origin of air masses. For this study, HYSPLIT was mainly applied to calculate trajectories for the identification of corresponding CALIOP profiles for the comparison with ground-based measurements. A discussion of the model is given by *Draxler and Hess* [1997], *Draxler and Hess* [1998], and *Draxler* [2003]. HYSPLIT is a product of the NOAA ARL (National Oceanic and Atmospheric Administration Air Resources Laboratory) and is available at <http://ready.arl.noaa.gov/HYSPLIT.php>. As input meteorological fields of the already introduced archived model assimilation data set GDAS1 were used.

4.3 Aerosol source information

Aerosol source information is needed for the interpretation of the findings from the trajectory and transport modeling in combination with the determined meteorological parameters. Whereas the anthropogenic emissions from industry or traffic remain more or less constant in time and with respect to the source locations, other aerosol sources, especially those of dust and smoke, are highly variable in space and time. For instance, dust uptake is determined by the atmospheric dynamic over the deserts. It can, thus, be modeled and forecast.

4.3.1 NAAPS Global Aerosol Model

The actual aerosol situation over Europe and especially over the identified aerosol source region was evaluated for each analyzed measurement by using aerosol model data provided by the Navy Aerosol Analysis and Prediction System (NAAPS) sourced by the Naval Research Laboratory (NRL)/Monterey. A 120-h forecast on a global scale is provided for tropospheric sulfate, smoke, and dust. Furthermore, NAAPS provides near-real-time access to global aerosol observational products such as satellite images and AERONET data (cf. <http://www.nrlmry.navy.mil/aerosol/>).

4.3.2 DREAM dust forecast

The Dust REgional Atmospheric Model (DREAM) [Nickovic *et al.*, 2001; Pérez *et al.*, 2006a,b; Basart *et al.*, 2012] operated in the Earth Sciences Division of the Barcelona Supercomputing Center-Centro Nacional de Supercomputación (BSC-CNS) delivers operational dust forecasts up to 72 h for North Africa, the Middle East, and Europe. The atmospheric life cycle of the eroded desert dust is predicted. DREAM was developed as a pluggable component of the NCEP/ETA model, the forecast model of the National Centers for Environmental Prediction. The current operational version is the BSC-DREAM8b model. It is available at <http://www.bsc.es/earth-sciences/mineral-dust-forecast-system/bsc-dream8b-forecast/>.

DREAM is used within EARLINET for the coordination of intensive measurement periods during dust outbreaks over Europe. For the aerosol typing done in this thesis images of the horizontal distribution of the dust load and dust concentration profiles available for selected EARLINET stations were used.

4.3.3 AERONET Sun photometer data

Sun photometer measurements provide spectral information on the columnar aerosol optical depth and on scattering-angle-resolved sky radiances. Via an inversion model it is possible to derive microphysical aerosol properties. Europe is covered by a dense network of Cimel Sun photometers of AERONET [Holben *et al.*, 1998]. Measurements of the aerosol optical depth are performed at 340, 380, 440, 500, 675, 870, and 1020 nm. The angular distribution of sky radiances is provided at four wavelengths (440, 675, 870, and 1020 nm). The optical and microphysical data (single-scattering albedo and complex refractive index) from AERONET Sun photometers are retrieved operationally at the AERONET Data Center of the NASA Goddard Space Flight Center (Greenbelt, VA, USA) and are made available every 15 minutes during daytime. The results can be downloaded from the AERONET website (<http://aeronet.gsfc.nasa.gov>). Several of the EARLINET stations are directly equipped with an AERONET Sun photometer. Since Sun photometers only provide column-integrated information, optical properties of boundary-layer particles that originate from local sources and regional aerosol transport cannot be separated from optical properties of lofted, free-tropospheric aerosol layers that predominantly originate from long-range transport on regional to intercontinental scales [Müller *et al.*, 2007a]. In this study, Sun photometer data were used to get information on the present aerosol load in the atmosphere in order to distinguish polluted from clean measurement cases.

4.3.4 MODIS fire maps

Fire counts from the Moderate Resolution Imaging Spectroradiometer (MODIS, cf. <http://modis.gsfc.nasa.gov/> and Giglio *et al.* [2003]) give a hint to areas of high fire activity and, thus, the production of smoke aerosols. MODIS flies onboard NASA's Aqua and Terra satellites and covers most of the globe every day. MODIS fire location data are distributed in a variety of forms (e.g., interactive web mapper, GIS, Google Earth, text files) through the Fire Information for Resource Management System (FIRMS) at the University of Maryland. The official monthly MODIS active fire location text files are distributed by the University of Maryland via the file transfer protocol (FTP) server [fuoco.geog.umd.edu](ftp://fuoco.geog.umd.edu) (login name is fire and password is burnt) in the directory *modis/C5/mcd14ml*. Fire counts are used to create fire maps, which are of major value to characterize smoke source regions. Fire maps are available from NASA's Earth Observing System Data And Information System (EOSDIS) and can be accessed via <https://earthdata.nasa.gov/data/near-real-time-data/firms/active-fire-data>. Each colored dot indicates a location where MODIS detected at least one fire during the compositing period. Color ranges from red where the fire count is low to yellow where the number of fires is large. The compositing periods are referenced by their start and end dates (Julian day). The duration of each compositing period for the fire maps shown in Section 2.2.3 was set to 10 days.

Chapter 5

Vertically resolved aerosol characterization over Europe

In this chapter the data evaluation concept for the aerosol classification based on EARLINET measurements is presented. In Section 5.1 the approach of the discrimination and classification of aerosol layers in EARLINET lidar data and the comparison to CALIPSO data is illustrated using a case study of a night-time overpass near Cabauw on 12–13 May 2008. Further exemplary observations of pure aerosol types and aerosol mixtures are shown in Section 5.2.

5.1 Data evaluation concept

EARLINET stations provide backscatter and most of them also extinction profiles for at least one wavelength, some of the stations additionally provide the depolarization ratio depending on the lidar system (cf. Chapter 3). These profiles were derived from the measured lidar signals by each station individually in case of good measurement conditions for aerosol observations with less clouds and good signal-to-noise ratio. The profiles are stored in the EARLINET database in the Network Common Data Format (NetCDF). Within the framework of this thesis an IDL (short for Interactive Data Language) program was designed for the visualization of EARLINET NetCDF profiles. Profiles being available in the EARLINET database and especially belonging to the considered period of intensive observations between May 2008 and October 2009 with more than 1000 performed measurements were checked for their quality individually. The IDL program has also been used to calculate and visualize optical properties like profiles of the lidar ratios, backscatter- and extinction-related Ångström exponents and color ratios (cf. equations in Chapter 3).

The search for the presence of aerosol layers as well as further investigations were

done manually for those measurements for which sufficient information (backscatter profile for at least two different wavelengths, or backscatter and extinction profiles for the same wavelength) needed for a reliable aerosol typing were available. Hence, not all quality-checked profiles could be used for the aerosol typing. The discrimination of aerosol layers and the identification of respective source regions were done for 240 measurements, 180 of them belong to high-performance stations. 709 individual aerosol layers could be selected. In the following subsections, the steps of the performed data evaluation for the aerosol typing are explained in more detail.

5.1.1 Feature finding

The term feature finding denotes discrimination of aerosol layers in measurement data, in this case EARLINET data. Practically, it was done by searching for coherent structures in time–height plots, so-called quicklooks, which illustrate the temporal evolution of the lidar range-corrected signal at a specific wavelength. In Figure 5.1 (left), a typical lidar measurement is visualized. The 1064-nm range-corrected signal from a measurement performed at Cabauw on 13 May 2008 is shown. Brown and yellow areas symbolize the presence of aerosol or cloud layers with high backscattering, whereas blue regions show low backscattering of, e.g., background or lost signal because of an optically too thick cloud below. The respective profiles of backscatter and extinction coefficients, lidar ratios, and Ångström exponents are presented in Figure 5.1 (right). High aerosol load up to about 3.2 km can be seen for almost the whole time interval of the measurement. Data above are corrupted by noise.

As introduced previously, only measurements with backscatter profiles for at least two different wavelengths, or backscatter and extinction profiles for the same wavelength have been investigated in detail for existing aerosol layers. Therefore, the quicklooks

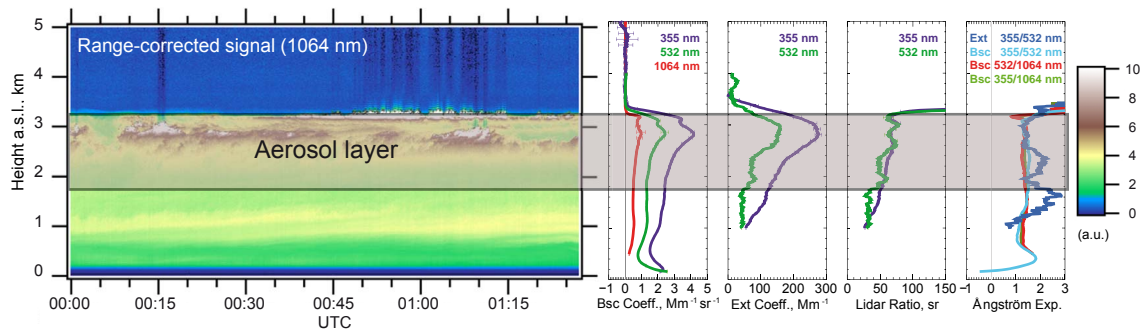


Figure 5.1: Time–height contour plot of the range-corrected signal at 1064 nm (left) and optical data of cloud-screened profiles (right) measured at Cabauw between 00:01 and 01:23 UTC on 13 May 2008. The observed aerosol layer between 1.7 and 3.2 km is marked.

and the single backscatter profiles were investigated for parts of enhanced atmospheric backscattering, which is clearly distinguishable from parts of the molecular return caused by clear air. Layer boundaries are characterized by a more or less rapid change of the backscattered signal with height. These changes result in extrema of the derivative of the backscattered signal, which can also be calculated with the developed IDL program. A clear and obvious maximum of the derivative of the backscatter coefficient marks the bottom height of the identified aerosol layer and a minimum is characteristic for its top height. This procedure for the discrimination of layer boundaries is called gradient or derivative method. However, not only these extrema are crucial, also profiles of further optical parameters show a specific gradient being different from regions of low aerosol. Values of the extinction are enhanced and profiles of the lidar ratio or Ångström exponents show an almost constant behavior over height within a distinct layer of specific type. When the depolarization ratio is provided, changes of this parameter are also used for layer boundary identification.

Afterwards, mean values of all optical parameters were calculated for each identified EARLINET aerosol layer. In case of the Cabauw measurement (Figure 5.1, right) lidar ratios of 64 sr at 355 nm and 59 sr at 532 nm and Ångström exponents of 1.3–1.7 were found in the aerosol layer between 1.7 and 3.2 km height indicating the presence of small particles.

5.1.2 Feature classification

For the classification of aerosols with respect to their source regions, age, and state of humidification auxiliary information like results of model calculations (FLEXPART, HYSPLIT, DREAM) or satellite data (MODIS) are used to obtain knowledge about the origin and movement of air masses, the predicted dust or other aerosol load in the atmosphere, and the presence of fires (cf. Chapter 4). For the measurement performed at Cabauw the result of the FLEXPART transport modeling of 50000 air parcels is illustrated in the left panel of Figure 5.2. This so-called footprint shows the air mass that traveled in heights below 2 km (above ground level) for the last ten days and arrived at Cabauw between 1.7 and 3.2 km at 01:23 UTC on 13 May 2008, in accordance with the defined aerosol layer height. The model output (color code) is given in terms of the decimal logarithm of the integrated residence time in seconds in a grid box. The integration time used here is ten days backward starting from the stop time of the observation. Results of the FLEXPART simulation show that the air mass circled above Northern and Central Europe for a longer time and, thus, could take up pollution over industrialized areas, which was present during this period as can be seen from the NAAPS Total optical depth (at 550 nm) indicating sulfate over wide areas of Central Europe (right panel of Figure 5.2).

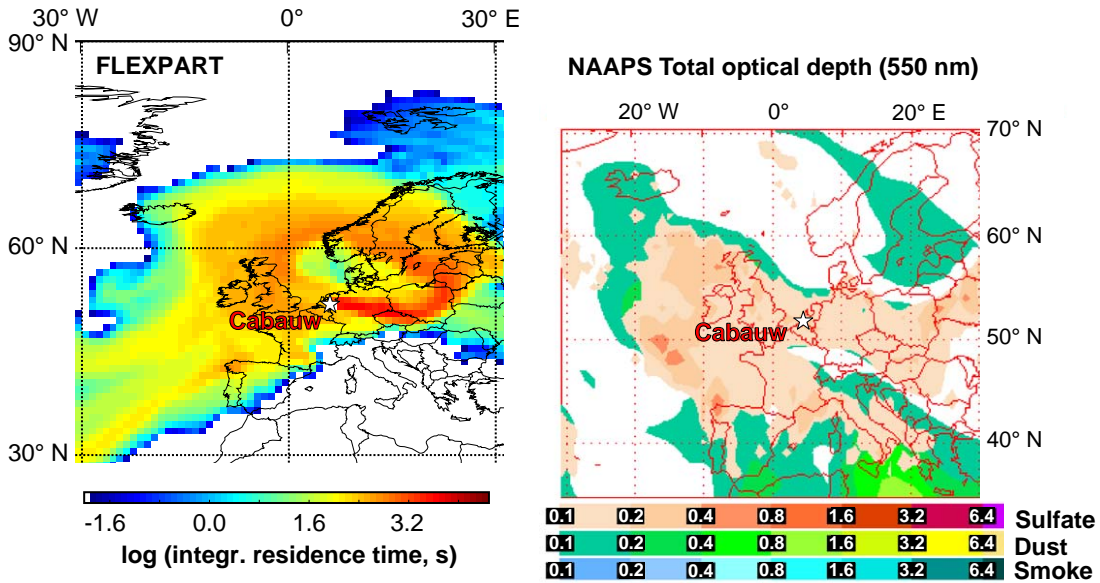


Figure 5.2: Left: FLEXPART footprint for the air mass traveling below 2 km height and arriving at Cabauw between 1.7 and 3.2 km height (above ground level) at 01:23 UTC on 13 May 2008. The colors represent the logarithm of the integrated residence time in a grid box in seconds for 10-day integration time. Right: NAAPS Total optical depth (550 nm) for 00:00 UTC on 13 May 2008 indicating the presence of sulfate (red colors) over Central Europe during the measurement period.

After interpreting the information offered by all different tools, the most probable aerosol source region and the belonging aerosol type was assigned. The decision to classify the aerosol layer containing a pure aerosol type or an aerosol mixture was made as best estimate in all conscience. The defined aerosol layer in the presented observation of Cabauw was classified as pure polluted continental aerosol originating from Central Europe. From the time-series plots of the FLEXPART simulation (shown in Figure 5.3), the age of the aerosol layer was quantified from the intensity of the color code. In this case, the age of the aerosol layer was determined to be two days on average.

Information about the relative humidity within the defined aerosol layer was gained from GDAS1 data (cf. Section 4.1). A mean value of the relative humidity was calculated from values of the relative humidity at base, top, and in the middle of the aerosol layer. In this case, the aerosol layer was rather humid with a layer-mean relative humidity of about 75%.

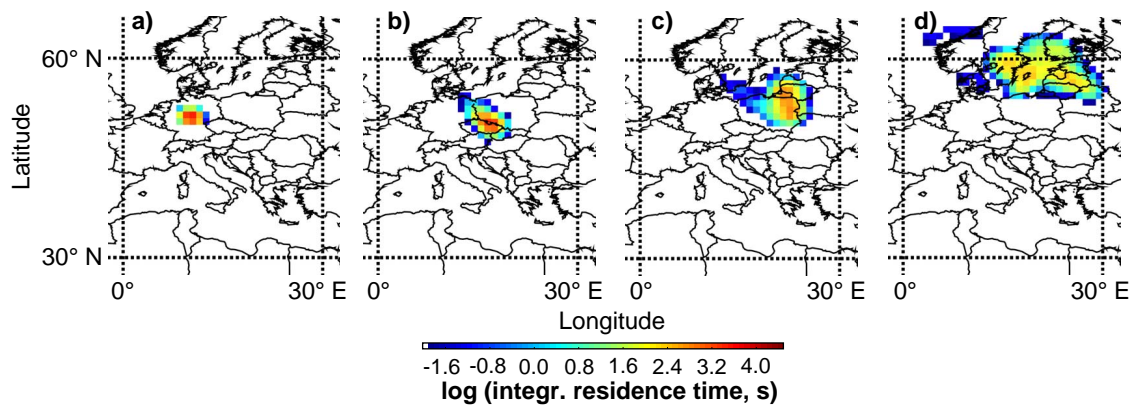


Figure 5.3: FLEXPART footprints as time series for the air mass traveling below 2 km height (above ground level) and arriving at Cabauw between 1.7 and 3.2 km height at 01:23 UTC on 13 May 2008. Shown are the footprints each for 24-h integration time for the last 4 days before observation with the following integration start and stop times: (a) 12 May 2008, 01:23 UTC until 11 May 2008, 01:23 UTC, (b) 11 May 2008, 01:23 UTC until 10 May 2008, 01:23 UTC, (c) 10 May 2008, 01:23 UTC until 9 May 2008, 01:23 UTC, and (d) 9 May 2008, 01:23 UTC until 8 May 2008, 01:23 UTC. The colors represent the logarithm of the integrated residence time in a grid box in seconds for the defined integration time.

5.1.3 Feature comparison

The aerosol layers detected and the aerosol type determined in the EARLINET data were used to validate the aerosol subtype being the output of the automatic CALIPSO classification scheme. The CALIOP data subsets used for the comparison were selected under the assumption of stable atmospheric conditions. Investigations concerning the representativeness of satellite against ground-based observations done in the framework of the ESA–CALIPSO project [Wandinger *et al.*, 2011] result in the following recommendations: boundary-layer aerosol has a very local nature and, hence, comparison between EARLINET and CALIPSO data should only be reported for satellite overpasses within 10 km and 10 minutes to the EARLINET observation. For investigations of free-tropospheric aerosol usually temporal distances within 150 minutes and spatial distances within 100 km between satellite ground track and ground-based lidar observation should be considered. Thus, for the comparison of satellite-borne with ground-based network data so-called EARLINET Case A measurements were evaluated having a satellite footprint at maximum 100 km away from the EARLINET lidar site. From 240 investigated measurements 164 remain for the comparison of aerosol subtype.

During the observation at Cabauw on 13 May 2008 the nearest footprint of the

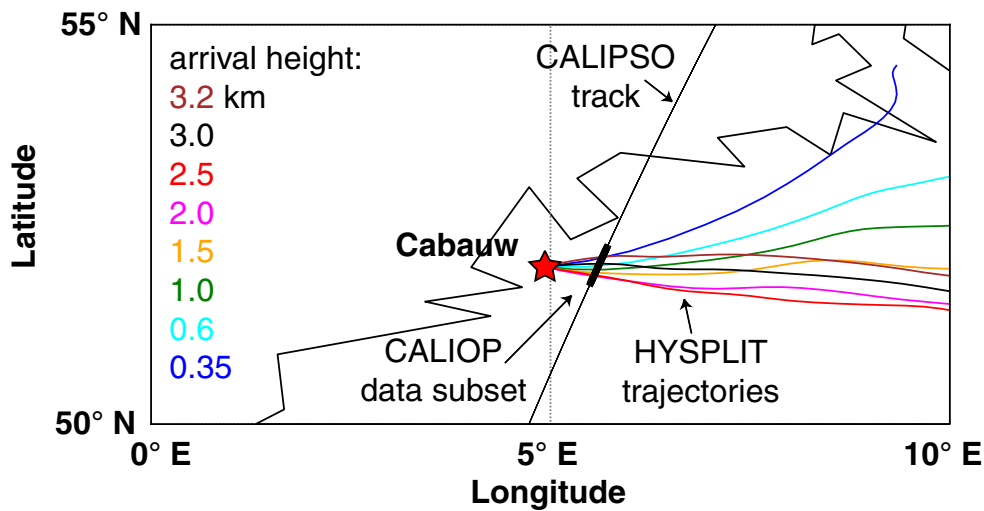


Figure 5.4: Map of CALIPSO overpass (thin black line) with period of CALIOP observation (thick black line) used for comparison, HYSPLIT 24-h backward trajectories (colored lines) starting at Cabauw (red star) at 01:00 UTC on 13 May 2008.

simultaneous CALIPSO overpass was about 44 km away. Figure 5.4 shows the CALIPSO track (black line) for 13 May 2008, 02:02–02:07 UTC. For the identified aerosol layer in the Cabauw measurement (cf. Figure 5.1) and for further heights HYSPLIT backward trajectory ensembles (colored lines in Figure 5.4; respective arrival heights are given on the left) were calculated to determine that part of the CALIOP data containing approximately the same air mass and, therefore, should be used for comparison with ground-based data. The selected CALIOP data subset for this observation is shown by a thick black line in Figure 5.4. CALIOP profiles of this data subset are from 44 to 59 km away from the measurement site at Cabauw.

Figure 5.5 (left) shows the CALIPSO cross section of the total attenuated backscatter measured at 532 nm on 13 May 2008 corresponding to the measurement presented above. The surface is marked by a straight red line. The observed aerosols are indicated by yellow coloring. Results of the applied automatic feature classification and aerosol identification [Omar *et al.*, 2009; Liu *et al.*, 2010] are presented in Figure 5.5 (middle and right). While for the EARLINET measurement polluted continental aerosol was assigned to be present in the determined aerosol layer between 1.7 and 3.2 km, the correlative CALIOP profiles were categorized as smoke (65%) and polluted dust (35%) as indicated by black and brown colors.

In general, identified EARLINET aerosol layers were compared to CALIPSO Level 2 Aerosol Layer products provided at 5-km horizontal resolution (cf. Chapter 3.2.3). The comparison was done with respect to the aerosol subtype determined

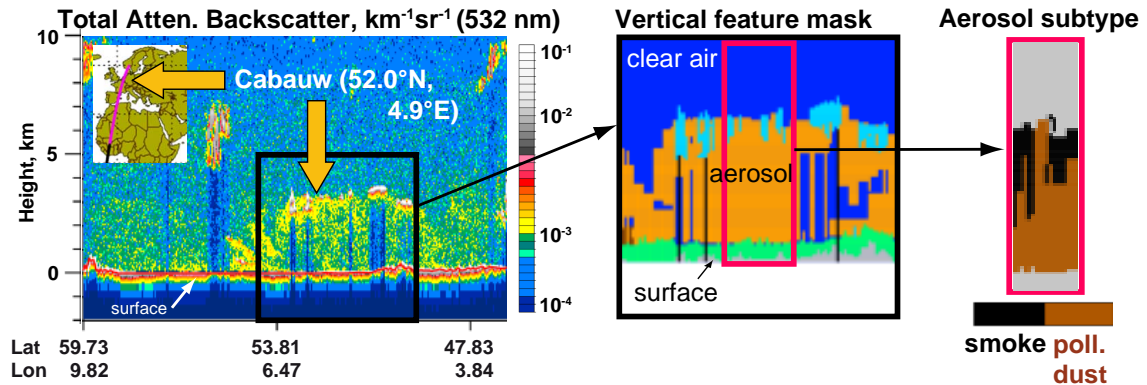


Figure 5.5: Cross sections of the total attenuated backscatter coefficient measured at 532 nm for the CALIPSO overpass at 02:02–02:07 UTC on 13 May 2008 (left) and the results of the classification mask (center: related vertical feature mask, right: respective aerosol subtype) corresponding to the EARLINET observation at Cabauw.

by CALIPSO within the height ranges of previously identified EARLINET aerosol layers. The comparison has to be done with care, especially when neighboring aerosol layers are present. In this context, *Burton et al.* [2013] mentioned that in such case the CALIOP algorithm defines the layer boundaries solely by changes in aerosol backscatter intensity and not changes in aerosol type. The authors also stated that the fact, that certain aerosol types are limited to either land or water surfaces, causes distinct boundaries between aerosol types in the CALIOP aerosol type mask with discontinuities in the lidar ratio and retrieved products.

The data quality assurance of the CALIOP products used within this study is based on feature classification flags and the CAD score, which are provided within the CALIPSO Lidar Level 2 Aerosol Layer data (cf. Section 3.2). These information are produced for each observation at 5 km horizontal resolution. The following conservative thresholds were used analog to *Kanitz et al.* [2014a]. Firstly, a confident aerosol sub-typing is expressed by the feature sub-typing flag = 1. Secondly, a CAD score ≤ -90 indicates that the observed layer likely contains aerosols with very high probability.

For each comparison a set of ten 5-km CALIOP profiles was chosen (thick black line in Figure 5.4) and searched for the presence of aerosols within the height ranges defined from the corresponding EARLINET measurement as shown above (Figure 5.1). Per EARLINET aerosol layer the following occasions are possible: a) Aerosol was also present for the entire layer height in all ten selected CALIOP profiles. b) Aerosol was present within this height range, but not in all ten CALIOP profiles. c) Aerosol was present in all ten CALIOP profiles, but not for the entire height range. d) Aerosol was present only in some of the ten selected CALIOP profiles and not for the entire height

range. e) No aerosol was present in the ten CALIOP profiles within the EARLINET aerosol layer height at all. f) One aerosol subtype was classified within the aerosol layer height. g) More than one aerosol subtype was classified within the aerosol layer height. For the statistical analysis of the comparison results a weighing factor was applied to account for the different occasions. A detailed description and an example is given in Section 6.2.

5.2 Case studies

The following case studies of pure aerosol types and important aerosol mixtures illustrate the dependence of intensive optical properties on the size, shape, and refractive index of the present aerosol, as it was already introduced in Chapter 2. Two case studies on pure aerosol types show the different spectral behavior of Saharan dust and biomass-burning aerosol. The change in optical properties for combinations of different pure aerosol types is illustrated for mixtures of smoke and pollution aerosol as well as dust and marine aerosol.

5.2.1 Saharan dust: Potenza, 16–17 April 2009

The time–height contour plot of the range-corrected signal at 1064 nm (Figure 5.6, left) and the profiles of optical data (Figure 5.6, right) of a measurement taken at Potenza in the night of 16–17 April 2009, between 21:05–01:01 UTC, are shown. During the measurement several aerosol layers were present. The corresponding BSC-DREAM8b

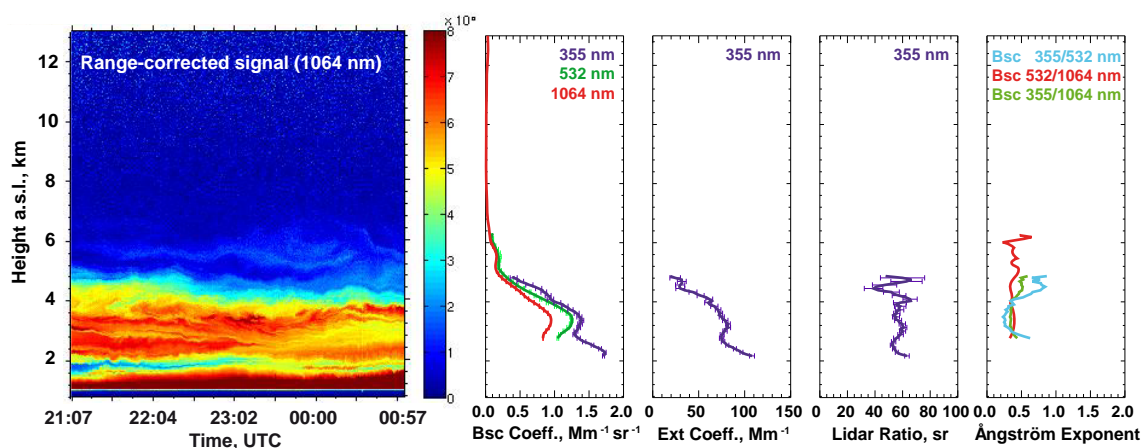


Figure 5.6: Time–height contour plot of the range-corrected 1064-nm signal and profile data from the measurement at Potenza on 16–17 April 2009, 21:05–01:01 UTC.

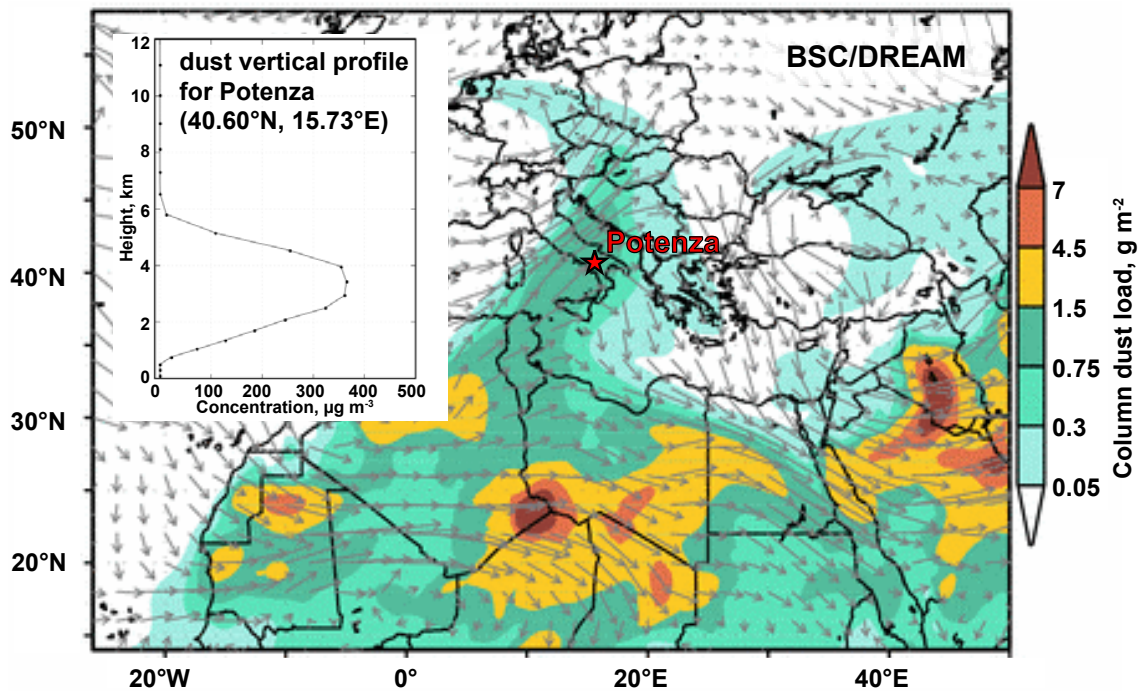


Figure 5.7: Dust concentration profile for Potenza and predicted column dust load as well as 3000 m wind over North Africa, Middle East, and Europe for 17 April 2009, 00:00 UTC, from BSC/DREAM8b v2.0, available at <http://www.bsc.es/earth-sciences/mineral-dust-forecast-system/bsc-dream8b-forecast/north-africa-europe-and-middle-ea-0>.

column dust load and the vertical profile of the dust concentration (cf. Section 4.3.2) are illustrated in Figure 5.7. Elevated dust concentrations are indicated for the northern Sahara and the middle parts of the Mediterranean. For Potenza a column dust load of up to 1.5 g m^{-2} is given. In the range of the observed aerosol layers extending from about 2 to 4 km height a dust concentration of about $375 \mu\text{g m}^{-3}$ is predicted. Results of the FLEXPART transport simulation (not shown) confirm that the respective layers were advected directly from the Western Sahara. Thus, most likely, the determined aerosol layers are dominated by Saharan dust particles.

For the aerosol layer between 3 and 4.1 km a mean lidar ratio at 355 nm of $58 \pm 3 \text{ sr}$ as well as backscatter-related Ångström exponents of the order of 0.31–0.38, which correspond to color ratios of 0.68–0.88, were found. These values are in very good agreement with previous findings for pure Saharan dust (cf. Chapter 2). From the FLEXPART time-series plots (not shown) the age of this aerosol layer was estimated to be three days. The layer-mean relative humidity was determined to about 60%.

5.2.2 Biomass-burning aerosol: Thessaloniki, 14–15 August 2008

Fresh biomass-burning smoke layers were observed at the stations in the Eastern Mediterranean region in the summer season of 2008. Figure 5.8 shows the 10-day MODIS map of active fires for the period of 8–17 August 2008. Several fire sources are visible in the vicinity of the EARLINET stations in Greece, but also in general on the Balkans, north of the Black Sea, and in Southern Italy.

In the following, one event measured at Thessaloniki is presented. The time–height contour plot at 532 nm for a Case A observation in the night of 14–15 August 2008 is shown in Figure 5.9 on the left. The black box indicates the period of 23:58–00:27 UTC for which the profiles of optical data, which are illustrated in Figure 5.9 on the right, were evaluated. Aerosol layers up to about 3.2 km were observed. High lidar ratios of 64–68 sr at both 355 and 532 nm and high extinction- and backscatter-related Ångström exponents of about 1.6, and accordingly color ratios of 0.55, were found. Results of the FLEXPART simulations in Figure 5.10 suggest the advection of air masses from the Black Sea region. The FLEXPART time-series plots (not shown)



Figure 5.8: MODIS map of active fires (red spots) for the period 8–17 August 2008. The EARLINET stations of Athens and Thessaloniki are indicated.

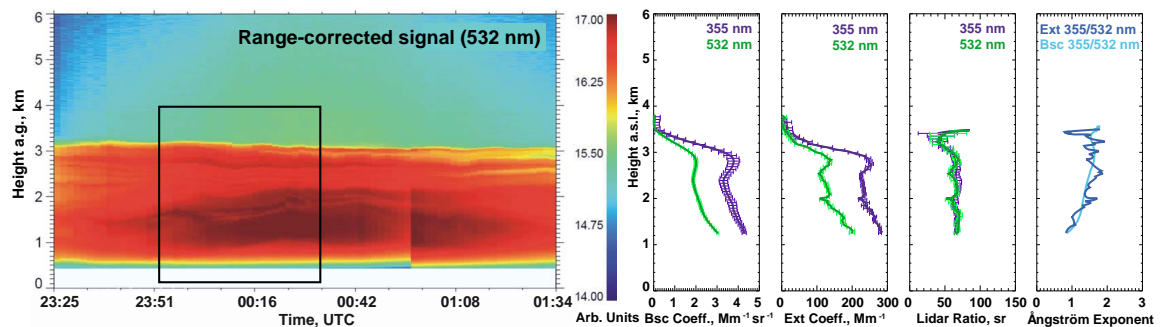


Figure 5.9: Time–height contour plot of the 532-nm range-corrected signal from the measurement taken at Thessaloniki on 14–15 August 2008. The black box highlights the period between 23:58–00:27 UTC for which the profiles of optical data were evaluated.

indicate that this aerosol layer could contain aerosol from two days before observation, but due to the enormous number of fires during this period it cannot be ruled out that also fresh smoke is included. The layer-mean relative humidity was determined to be less than 50%.

The corresponding CALIPSO cross sections of the 532-nm attenuated backscatter coefficient and the results of the classification mask presented in Figure 5.11 show the detection of a large amount of aerosol in the surrounding of Thessaloniki (the location of Thessaloniki is indicated). In coincidence with the overpass at Thessaloniki (approximately 5 km away from the satellite footprint) an aerosol layer reaching up to about 4 km was observed. As can be seen in Figure 5.11 the aerosol was classified as smoke together with polluted dust.

In contrast, FLEXPART simulations clearly show that the influence of dust from desert regions can be ruled out what was investigated also for other measurement cases (not shown) from this period of active fires in July/August 2008. The aerosol subtype polluted dust is selected over non-desert surfaces when the depolarization ratio is between 0.075 and 0.2 (cf. Figure 3.4) what is normally the case when large, non-spherical particles are present. Hence, there must have been large soil and ash particles present in this aerosol layer, which were brought into the atmosphere by the fires causing such high depolarization ratios and the respective classification of the aerosol as polluted dust.

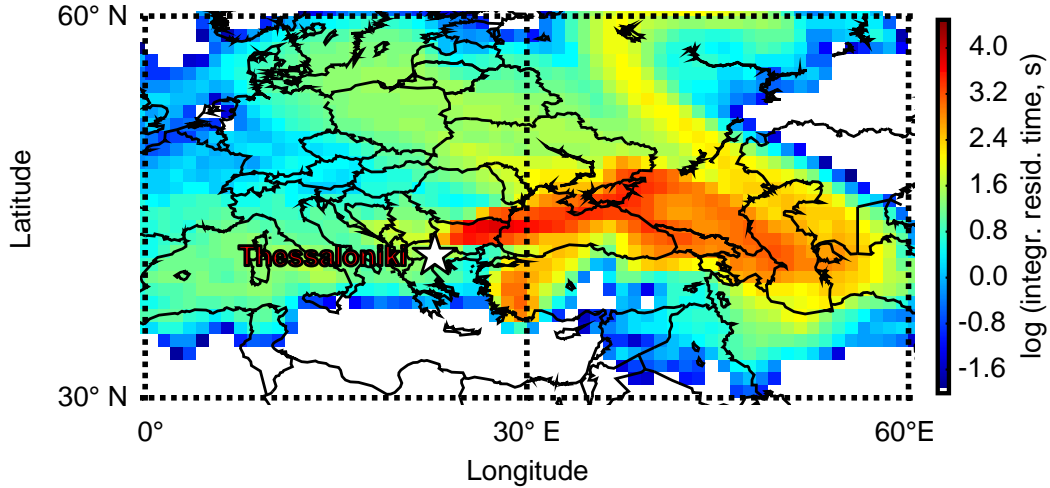


Figure 5.10: FLEXPART footprint for the air mass traveling below 2 km and arriving at Thessaloniki between 2.57 and 3.2 km at 00:27 UTC on 15 August 2008. The colors represent the logarithm of the integrated residence time in a grid box in seconds for 10-day integration time.

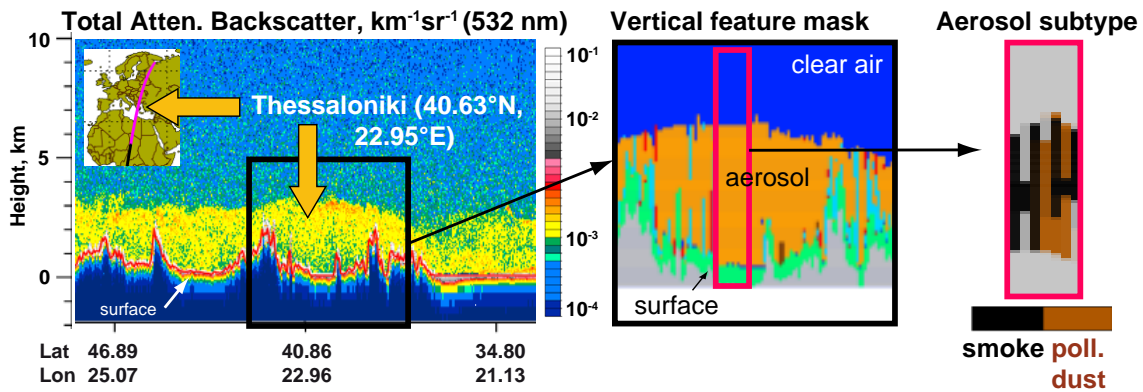


Figure 5.11: Cross sections of the total attenuated backscatter coefficient measured at 532 nm for the CALIPSO overpass at 00:35–00:49 UTC on 15 August 2008 (left) and the results of the classification mask (center: related vertical feature mask, right: respective aerosol subtype) corresponding to the EARLINET observation at Thessaloniki.

5.2.3 Mixture of dust and marine aerosol: Potenza, 8 July 2008

An example for a measurement containing a mixture of dust and marine aerosol is shown in Figure 5.12. The measurement was performed at Potenza on 8 July 2008, 00:19–02:26 UTC. The profiles show two distinct aerosol layers above the PBL (1.75 km.). The first one is centered at 2.35 km, the second extends from 3.2 to 4.6 km. In the lower layer between 2.1 and 2.6 km mean lidar ratios of 43 ± 2 sr and 41 ± 4 sr are found at 355 and 532 nm, respectively. The extinction-related Ångström exponent in the 355–532-nm range is 0.65 ± 0.08 , and the backscatter-related Ångström exponents are 0.51 ± 0.19 , 0.50 ± 0.02 , and 0.51 ± 0.08 in the 355–532-nm, the 532–1064-nm, and the 355–1064-nm range, respectively.

Figure 5.13 shows results of FLEXPART transport simulations for both layers. The layers are traced back to Northwestern Africa. From the time-resolved simulation (not shown), it can be seen that the air mass was above the Western Sahara more than three days before the observation. During the last three days, it traveled along the coastlines of Morocco and Algeria before it crossed the Mediterranean. In addition, a part of the air mass arrived directly from the North Atlantic. Thus, in both layers an influence of marine aerosol is very likely. The optical data support this finding. Lidar ratios are smaller and Ångström exponents are larger than typically measured in pure dust. As mentioned above, such kind of mixing of dust with marine aerosol is often observed over the Mediterranean region. The CALIPSO definition of polluted dust

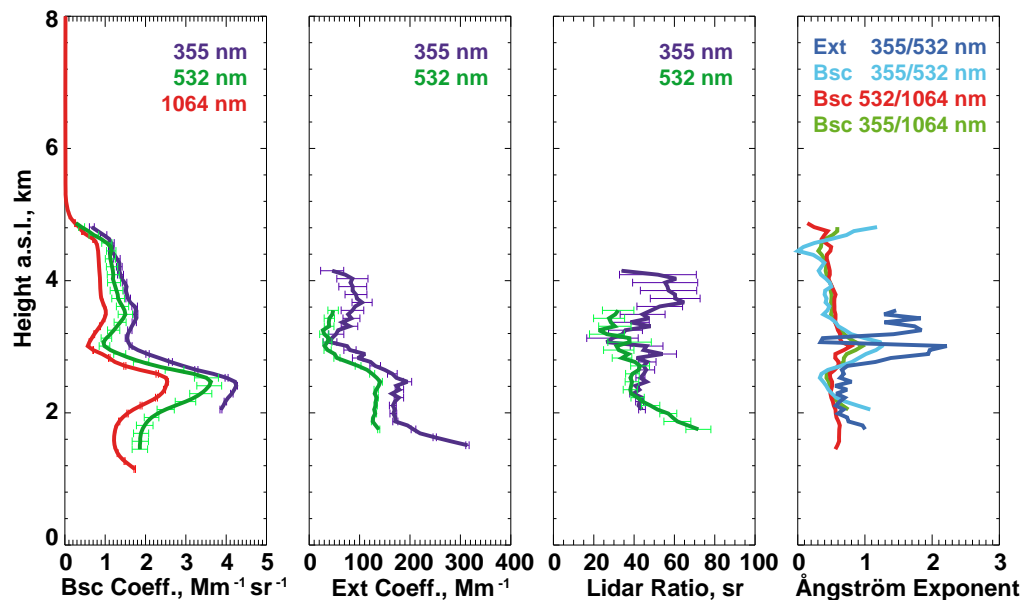


Figure 5.12: Profile data from the measurement taken at Potenza on 8 July 2008, 00:19–02:26 UTC.

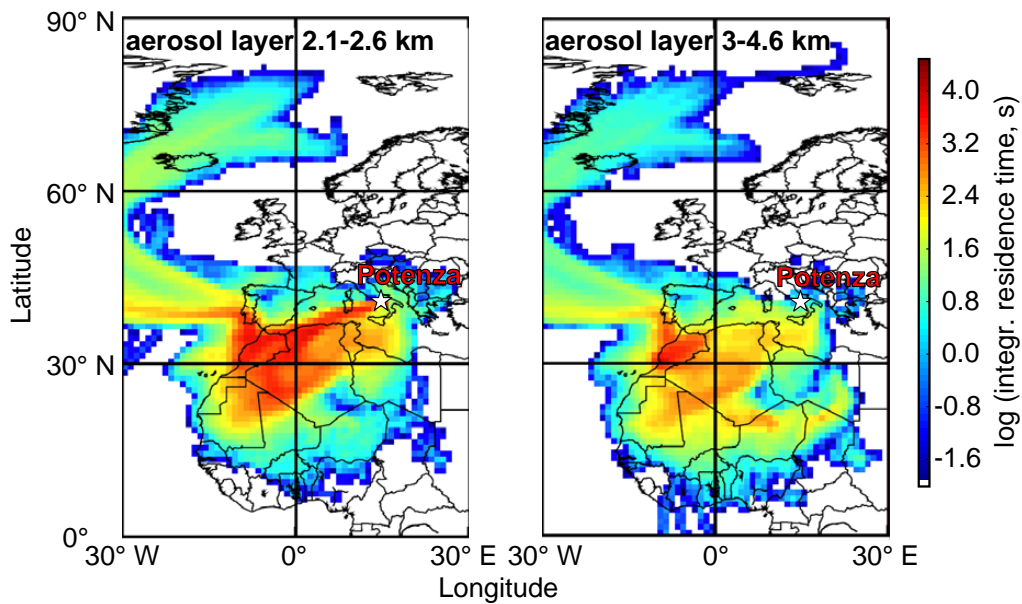


Figure 5.13: FLEXPART footprints for the air mass traveling below 2 km height and arriving at Potenza between 2.1 and 2.6 km height (left panel) and 3.0 and 4.6 km height (right panel) at 02:26 UTC on 8 July 2008. The colors represent the logarithm of the integrated residence time in a grid box in seconds for 10-day integration time.

does not fit to such mixtures, because the marine aerosol has a low lidar ratio of the order of 25 sr and, thus, decreases the lidar ratio of mixed dust compared to the one of pure dust. In contrast, the lidar ratio of polluted dust in the CALIPSO look-up table is 65 sr at 532 nm compared to 40 sr for pure dust.

The age of the aerosol present in both layers is about four days and the layer-mean relative humidity was rather low (34% and 18%). These values of relative humidity are only given for completeness. It should be mentioned that they have to be taken with care, because they may have a large error due to very limited information and assumptions for their calculations.

5.2.4 Mixture of smoke and pollution aerosol: Athens, 29–30 July 2008

Finally, a mixture of pollution and smoke aerosol observed over Athens during the night of 29–30 July 2008 is illustrated. Figure 5.14 contains the corresponding backscatter and extinction profiles as well as profiles of the determined lidar ratios and Ångström exponents. In the aerosol layer up to 2.5 km high lidar ratios around 80 sr and large Ångström exponents up to 1.24 were found indicating that the aerosol layer

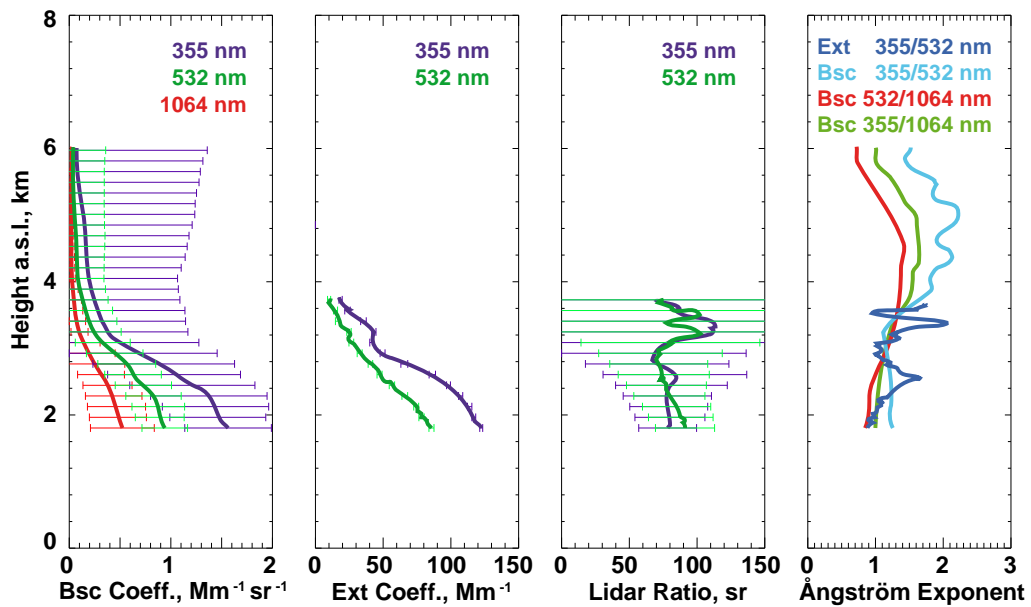


Figure 5.14: Profile data from the measurement taken at Athens on 29–30 July 2008, 22:32–00:29 UTC.

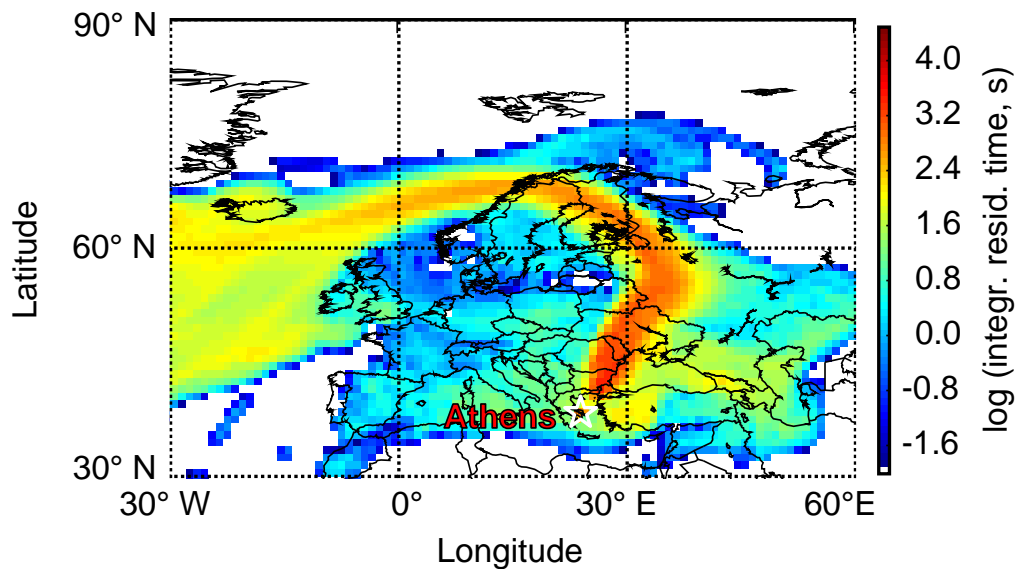


Figure 5.15: FLEXPART footprint for the air mass traveling below 2 km height and arriving at Athens between 2 and 2.5 km height at 00:29 UTC on 30 July 2008. The colors represent the logarithm of the integrated residence time in a grid box in seconds for 10-day integration time.

is supposed to contain small and absorbing particles. The respective FLEXPART simulation in Figure 5.15 represents the typical flow pattern of the air from the north over regions with active fires (cf. Figure 5.8) towards Greece. This measurement shows the typical situation in Greece in the summer season, when smoke from local and regional fires is observed and heavy pollution and photochemical smog are present simultaneously around the metropolitan areas like, e.g., Athens and Thessaloniki. Sometimes, the smoke plumes are well separated as shown in Section 5.2.2, but often the smoke is mixed into the PBL, which typically reaches heights of up to 2–3 km in summer. In such cases, when no isolated aerosol layer was identified, the aerosol was classified as a mixture of smoke and pollution. The FLEXPART time-series plots (not shown) indicate that the aerosol layer took up aerosol about two days before the observation, but it cannot be ruled out that also more recent smoke and pollution aerosol is present as well. The layer-mean relative humidity was about 52%.

Chapter 6

Statistical analysis

In this chapter statistical findings resulting from observations at 16 EARLINET stations (Section 6.1) and from the comparison of the aerosol typing based on EARLINET data against the CALIPSO classification scheme (Section 6.2) are discussed. Most of the underlying EARLINET measurements were performed during an intensive observational period for the ESA–CALIPSO project [*Wandinger et al.*, 2011]. In the project framework a MySQL¹ database manageable via PostgreSQL had been set up to relate the evaluated data from the ground-based and spaceborne observations. The comprehensive PostgreSQL database design and management system pgAdmin III is implemented as graphical user interface to the database. All determined layer-mean feature properties and the conversion factors were stored in this relational database and were statistically evaluated. Within the relational database, any kind of search function can be executed and any pre-defined parameters can be related to each other by SQL statements. The relational database is also accessible with external programs by SQL statements and can, thus, be implemented in automated algorithms. The structure of the database is explained in detail by *Wandinger et al.* [2011]. The statistical results shown in the following are obtained from this relational database.

In Section 6.1 results of the statistical evaluation of EARLINET measurements are summarized. Section 6.1.1 provides an overview on the frequency of occurrence of pure aerosol types and aerosol mixtures as obtained from the analysis of several hundreds aerosol layers from EARLINET data investigated in detail so far. Mean optical properties of pure aerosol types are presented in Section 6.1.2. The findings for mixed aerosols are discussed in Section 6.1.3. In Section 6.1.4 the conversion factors to relate spaceborne lidar observations with different instruments to each other are summarized for pure aerosol types and typical aerosol mixtures. In Section 6.2 findings of the comparison of the aerosol typing based on data of selected EARLINET lidars against

¹ SQL – Structured Query Language

results of the CALIPSO aerosol classification scheme are shown. For this purpose, the data set used for Section 6.1 was screened for EARLINET measurements that were performed in correlation with a CALIPSO overpass. EARLINET aerosol layers from the selected EARLINET measurements were then searched in the respective CALIOP profiles. General results of the investigations are presented in Section 6.2.1, whereas in Section 6.2.2 results of the validation of the CALIPSO aerosol classification scheme are summarized.

6.1 Aerosol optical parameters from EARLINET measurements

The statistical results presented in this section are based on an in-depth investigation of 240 EARLINET measurements provided by 16 EARLINET stations, with focus on the high-performance stations (cf. Section 3.1.3). Each measurement has been inspected regarding quality and the occurrence of distinct aerosol layers. Altogether 709 aerosol layers were defined. For each selected layer, a FLEXPART transport simulation was performed to determine its origin, transport path, and age. The DREAM and NAAPS models together with MODIS fire maps, and other tools (cf. Chapter 4) were used to cross-check the sources and to assign a pure aerosol type or an aerosol mixture to the layers, in the way discussed for several examples in Chapter 5. For 54 aerosol layers no distinct aerosol source and type could be assigned. Statistical considerations presented below were done for the remaining 655 aerosol layers, which could be related to aerosol sources.

The aerosol typing was performed in analogy to the CALIPSO classification scheme. That means, optical properties were determined for clean marine, desert dust, polluted continental, clean continental, biomass-burning (smoke), and polluted dust aerosol. The CALIPSO aerosol type polluted dust is defined as dust mixed with smoke and/or pollution aerosol. For the evaluation of EARLINET data this type was separated into mixtures of either dust with pollution, dust with smoke or dust with smoke and pollution. Statistical results for other observed mixtures are shown additionally, although they are not included in the CALIPSO classification scheme. For instance, mixtures that contain marine aerosol were considered separately and were separated regarding the presence of dust in addition. For aerosol mixtures a combination of the names for pure aerosol types were used. Table 6.1 summarizes the aerosol types used in the following.

Table 6.1: Overview on aerosol types used in this thesis for the statistical evaluation of EARLINET data.

| | Aerosol types | Acronym |
|-------------------------------|-----------------------------------|-----------|
| Pure Types: | | |
| Marine | Marine | (M) |
| Desert dust | Dust | (D) |
| Biomass burning (smoke) | Smoke | (S) |
| Polluted continental | Pollution | (P) |
| Clean continental | Continental | (C) |
| Tropospheric volcanic | Volcanic | (V) |
| Stratospheric | Stratospheric | (Str) |
| Aerosol mixtures: | | |
| Mixtures with dust | Dust + Smoke | (D+S) |
| | Dust + Pollution | (D+P) |
| | Dust + Smoke + Pollution | (D+S+P) |
| | ----- | |
| | Dust + Marine | (D+M) |
| | Dust + Marine + Pollution | (D+M+P) |
| | Dust + Marine + Smoke | (D+M+S) |
| | Dust + Marine + Pollution + Smoke | (D+M+P+S) |
| | Dust + Marine + Continental | (D+M+C) |
| | ----- | |
| Other mixtures | Dust + Continental | (D+C) |
| | ----- | |
| | Marine + Continental | (M+C) |
| | Marine + Continental + Smoke | (M+C+S) |
| | Marine + Pollution | (M+P) |
| | Marine + Pollution + Smoke | (M+P+S) |
| | Marine + Smoke | (M+S) |
| | ----- | |
| Pollution + Smoke | (P+S) | |
| ----- | | |
| Volcanic + Marine | (V+M) | |
| Volcanic + Marine + Pollution | (V+M+P) | |

6.1.1 Occurrence of major aerosol types

In Figure 6.1 the frequency of occurrence of the pure aerosol types and aerosol mixtures for measurements taken between 2008 and 2010 is shown. In 38% of the cases a pure aerosol type was assigned, whereas in 62% a mixing of different aerosol types could not be ruled out.

The majority of the pure aerosol types was classified as polluted (38%) or clean (18%) continental aerosol (cf. Figure 6.1b). 17%, 10%, and 8% of the layers of the pure-type fraction were identified as desert dust, smoke, and volcanic aerosols, respectively. Clean marine conditions were found for 3% (i.e., 1.1% of all layers) only. 6% of the layers were detected in the stratosphere. In addition, all kinds of mixtures of pure tropospheric aerosol types occurred over Europe in the investigated period as the analysis shows (cf. Figure 6.1c). Predominantly, the mixed aerosols contain pollution and/or dust. The mixture of dust, marine, and pollution aerosol is most frequently obtained (28%), followed by the mixtures of marine and pollution (19%) as well as dust and marine aerosols (14%). This can be explained by the large number of measurements contributed by stations in the Mediterranean region.

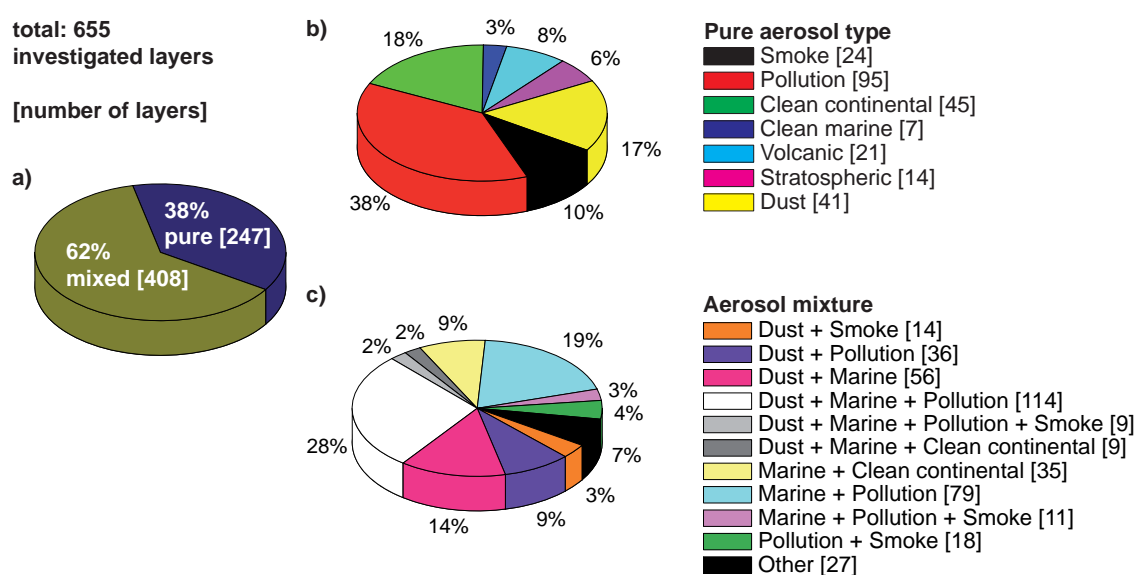


Figure 6.1: Frequency of occurrence of pure and mixed aerosol types as obtained from the aerosol-layer analysis: a) fraction of layers containing either pure or mixed aerosols, b) distribution of smoke, pollution, clean continental, clean marine, volcanic, stratospheric, and dust aerosol within the fraction of pure aerosol types, c) distribution of different mixtures within the fraction of mixed aerosols. The number of defined aerosol layers are added within brackets, respectively.

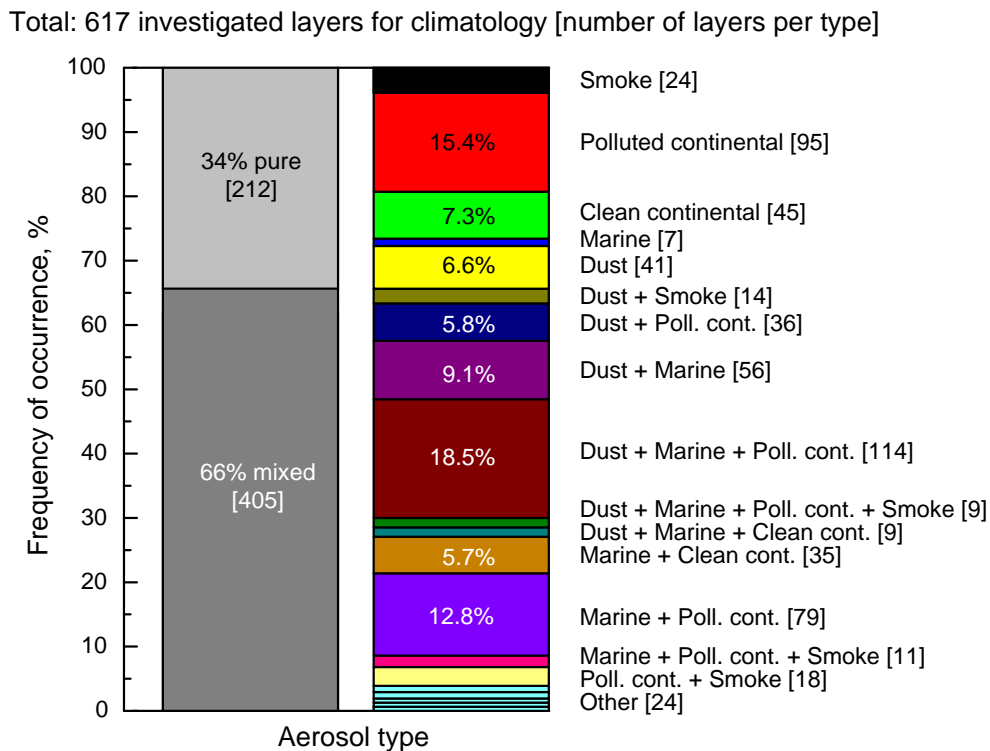


Figure 6.2: Frequency of occurrence of the pure and mixed aerosol types without volcanic events.

As this work is focused on providing a climatology of the vertical distribution of tropospheric aerosols over Europe, aerosol from special events like volcanic eruptions and resulting stratospheric features are not further considered. Thus, the number of aerosol layers that were used for the following investigations reduced from 655 to 617. The frequency of occurrence of the different pure aerosol types and aerosol mixtures cleared from aerosol originating from special events is shown in Figure 6.2. In 34% of the cases a pure aerosol type was assigned, whereas in 66% a mixing of different aerosol types could not be ruled out. In general, results are similar to the values shown before. For the pure aerosol types the majority is defined as polluted (15.4% of all) and clean continental aerosol (7.3% of all), followed by desert dust with 6.6% of all layers, and smoke with 3.9%. Clean marine conditions were found for 1.2% of all aerosol layers only. When a mixture of aerosols cannot be ruled out, it mainly contains pollution and/or dust. The mixture of dust, marine, and pollution aerosol is most frequently obtained (18.5% of all), followed by the mixtures of marine and pollution (12.8% of all) and dust and marine aerosols (9.1%).

In general, clean marine aerosol is found seldom, but a marine influence cannot be ruled out for more than half (54%) of the analyzed aerosol layers (cf. Figure 6.3).

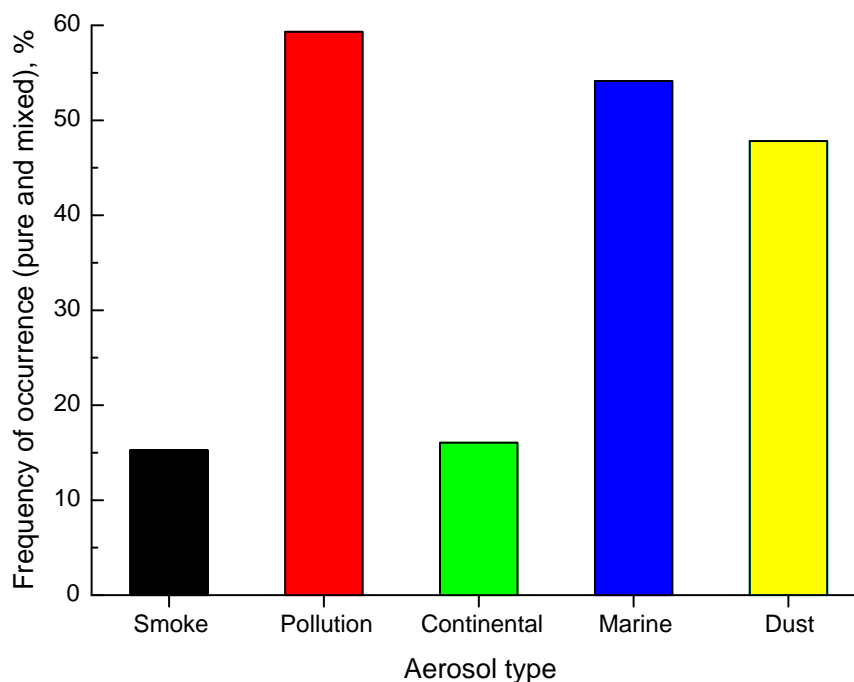


Figure 6.3: Frequency of occurrence of the aerosol types smoke, pollution, continental, marine, and dust in pure and mixed states.

The mixing with marine aerosol is caused by typical transport pattern from the North Atlantic or from the Sahara over the Mediterranean Sea toward Europe. Figure 6.3 also shows that pollution and dust occur in 59% and 48% of the layers, respectively, in either pure or mixed state. It should be noted that, with the tools applied here, it is estimated whether the presence of a certain aerosol type is likely or not. It is not possible to determine the absolute contribution of different aerosol types to a mixture. Results of investigations on the vertical extent of aerosol layers of dust, continental, pollution, and smoke aerosol and frequently observed aerosol mixtures are summarized in Figure 6.4. For each aerosol type mean bottom and top heights were calculated based on the respective bottom and top heights of the identified EARLINET aerosol layers. The black bars in Figure 6.4 indicate the height range where aerosol layers of the respective aerosol type were found. As expected dust layers and mixtures with dust were at about 3 km height and above, whereas pollution and mixtures containing marine and pollution aerosol were found in lower heights.

Finally, findings of a more detailed analysis for selected stations are illustrated in Figure 6.5. Again, the frequency of occurrence of pure and mixed aerosols is shown. The geographical location is nicely represented. For example, the results for Cabauw, The Netherlands on the left show the marine influence that is present for often observed westerly flows. Leipzig and Maisach are examples for Central European stations where

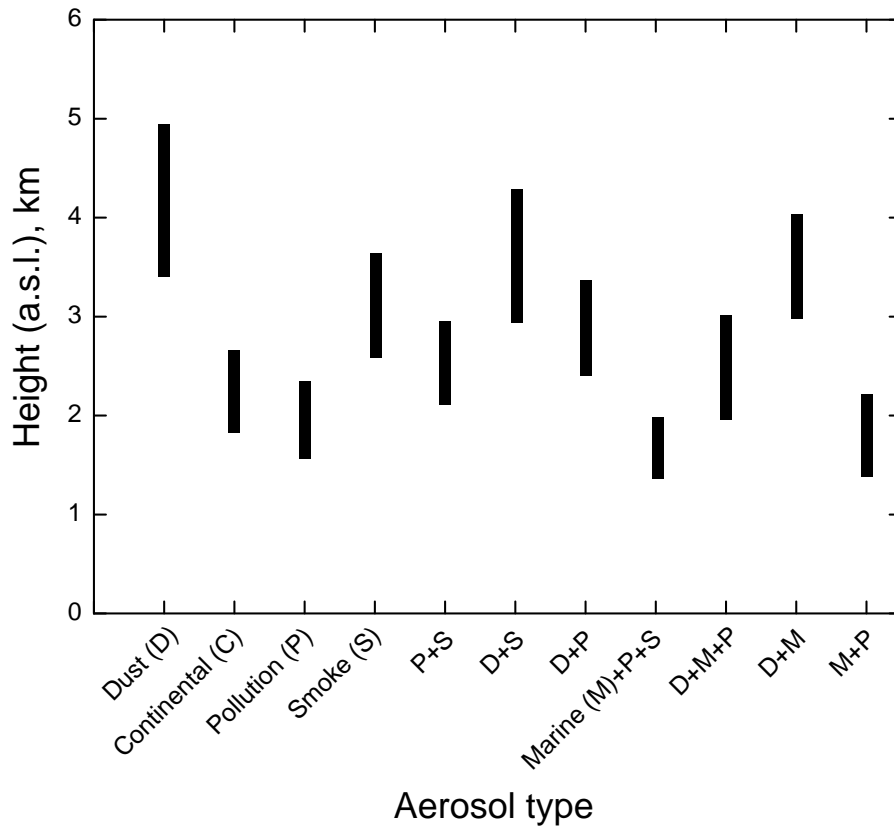


Figure 6.4: Distribution of mean layer base and top heights and the resulting vertical extent (black bars) for aerosol layers containing dust, continental, pollution, and smoke aerosol and frequently observed aerosol mixtures.

mostly pollution can be observed. Observations of the Spanish station Granada support the known influence of desert dust from the Sahara, which is also often mixed with marine aerosol from the Mediterranean before it reaches the station. This is also the case for the Italian stations of L'Aquila and Potenza, but for those stations aerosol mixtures often contain pollution in addition. Athens and Thessaloniki are stations in Greece showing the large influence of smoke aerosol, which can often be observed in the summer months (cf. Chapter 2).

In the following, mean optical properties calculated for the pure aerosol types (Section 6.1.2) and a selection of aerosol mixtures (Section 6.1.3) are presented. For each of the pure types and aerosol mixtures considered in Figure 6.2, there were at least seven and on average 40 individual layers available in the database, which contribute to the statistics. Mixtures with lower frequency of occurrence were sampled in the category “other” in Figure 6.2. The number of individual layers available in the database contributing to the statistical values for each type are given in brackets.

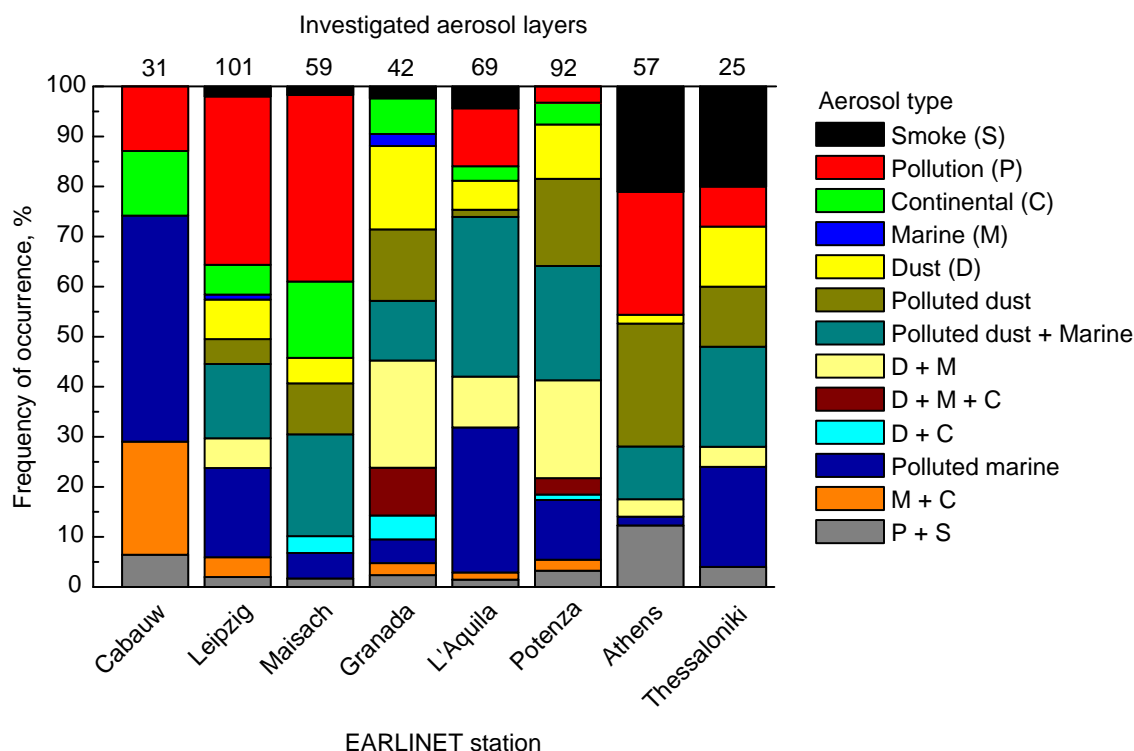


Figure 6.5: Frequency of occurrence of the pure and mixed aerosol types for the EARLINET stations Cabauw, Leipzig, Maisach, Granada, L'Aquila, Potenza, Athens, and Thessaloniki.

6.1.2 Optical properties of pure aerosol types

A list of extensive and intensive optical properties for the pure tropospheric aerosol types marine, dust, pollution, continental, and smoke are summarized in Table 6.2. Mean values and standard deviation are shown. The conversion factors are indicated in bold, i.e., those parameters that are relevant to relate spaceborne observations with different instruments (cf. Chapter 1) to each other. In addition, the absolute number of aerosol layers used for the statistical evaluation is given.

The limited number of observations at fully equipped stations (channels for backscatter and extinction for more than one wavelength) as well as the fact that clean marine conditions are rarely found over Europe explains missing numbers in Table 6.2. The whole set of parameters shown in Table 6.2 and Table 6.3 could not be determined for each classified layer and, thus, the real number of values for the statistical evaluation of each parameter is usually lower than the number of classified aerosol layers. For instance, seven layers could be identified for marine aerosol, but only for two of them Ångström exponents, and respective color ratios, could be calculated. Therefore, results of marine aerosol are not included in the following. Figures 6.6–6.8 illustrate

Table 6.2: Mean values and standard deviation of extensive and intensive optical properties for the pure aerosol types marine, dust, pollution, continental, and smoke. Conversion factors as defined in Chapter 3 are indicated in bold. In addition, the absolute number of classified aerosol layers is given.

| Parameter, unit | Marine | Dust | Pollution | Continental | Smoke |
|--|------------------|------------------|------------------|------------------|------------------|
| Classified layers | 7 | 41 | 95 | 45 | 24 |
| α_{UV} , 10^{-6} m^{-1} | | 68.7±32.7 | 125.2±69.5 | 77.0±55.1 | 116.7±81.0 |
| α_{VIS} , 10^{-6} m^{-1} | | 61.8±33.3 | 72.2±36.3 | 50.8±42.2 | 70.6±38.7 |
| β_{UV} , $10^{-6} \text{ m}^{-1} \text{ sr}^{-1}$ | 0.85±0.80 | 1.61±0.92 | 2.17±1.70 | 1.56±1.20 | 2.37±3.39 |
| β_{VIS} , $10^{-6} \text{ m}^{-1} \text{ sr}^{-1}$ | 1.06±1.33 | 1.42±0.92 | 1.30±1.11 | 0.91±0.71 | 1.33±1.70 |
| β_{IR} , $10^{-6} \text{ m}^{-1} \text{ sr}^{-1}$ | 0.54±0.36 | 0.81±0.55 | 0.50±0.45 | 0.49±0.35 | 0.33±0.20 |
| S_{UV} , sr | | 60.0±11.7 | 67.6±13.5 | 51.5±10.7 | 74.0±15.5 |
| S_{VIS} , sr | | 56.8±8.1 | 63.6±14.1 | 39.4±8.8 | 76.8±13.7 |
| s_{VIS-UV} | | 0.95±0.17 | 0.99±0.26 | 0.80±0.28 | 0.98±0.16 |
| $\hat{a}_{\alpha,UV-VIS}$ | | 0.41±0.48 | 1.58±0.40 | 1.90±0.93 | 1.41±0.31 |
| $\hat{a}_{\beta,UV-VIS}$ | 0.50±0.42 | 0.20±0.47 | 1.52±0.36 | 1.30±0.45 | 1.52±0.32 |
| $\hat{a}_{\beta,VIS-IR}$ | 0.28±0.04 | 0.40±0.38 | 1.28±0.31 | 1.00±0.35 | 1.18±0.20 |
| $\hat{a}_{\beta,UV-IR}$ | | 0.48±0.28 | 1.40±0.28 | 1.14±0.36 | 1.30±0.11 |
| $C_{\alpha,VIS-UV}$ | | 0.87±0.15 | 0.53±0.09 | 0.49±0.18 | 0.57±0.07 |
| $C_{\beta,VIS-UV}$ | 0.80±0.14 | 0.94±0.19 | 0.55±0.07 | 0.60±0.10 | 0.55±0.07 |
| $C_{\beta,IR-VIS}$ | 0.87±0.04 | 0.78±0.18 | 0.42±0.09 | 0.52±0.13 | 0.45±0.06 |
| $C_{\beta,IR-UV}$ | | 0.61±0.16 | 0.23±0.06 | 0.31±0.13 | 0.24±0.03 |

the findings for lidar ratios and Ångström exponents for the pure aerosol types dust, continental, pollution, and smoke. Boxes ranging from the 25% to the 75% percentile as well as the 5%, 50%, and 95% percentiles are shown in addition to mean, minimum, and maximum values. The numbers of identified layers per aerosol type and parameter that contribute to the statistical values are given as well.

In general, the results agree well with findings of other aerosol typing studies as discussed in Chapter 2. Highest lidar ratios and Ångström exponents are obtained for smoke, indicating small and highly absorbing particles, followed by the values for pollution. The dust lidar ratios are 60.0 ± 11.7 and 56.8 ± 8.1 sr at 355 and 532 nm, respectively, and agree very well with the findings of SAMUM-1 in the Saharan dust source region [Tesche *et al.*, 2009b]. Ångström exponents are also in good agreement with findings from other measurements (cf. Section 2.2). For smoke and pollution Ångström exponents of the order of 1.5 at 355 and 532 nm (UV-VIS), around 1.2 at 532 and 1064 nm (VIS-IR), and around 1.35 at 355 and 1064 nm (UV-IR) were found. For dust and marine aerosol values ≤ 0.5 were derived.

The variability of the parameters has both natural and technical reasons. A limited number of observations enhances the influence of single outliers, which may be caused by misclassification or measurement errors. In addition, e.g., *Burton et al.* [2012] clearly showed that there can be a considerable spread in the observations for aerosols that belong to the same type but have been observed in different locations.

6.1.3 Optical properties of aerosol mixtures

For a selection of aerosol mixtures with the highest frequency of occurrence (cf. Figure 6.1c) mean values and standard deviation of extensive and intensive optical properties are given in Table 6.3. Conversion factors are indicated in bold. In addition, the absolute number of aerosol layers used for the statistical evaluation is given. Again, box plots are used to visualize the optical properties. Lidar ratios are presented in Figure 6.9, Ångström exponents are shown in Figure 6.10 and 6.11. The numbers of identified layers per aerosol type and parameter that contribute to the statistical

Table 6.3: Mean values and standard deviation of extensive and intensive optical properties for different mixtures of dust, pollution, smoke, and marine aerosol. Conversion factors as defined in Chapter 3 are indicated in bold. In addition, the absolute number of classified aerosol layers is given.

| Parameter, unit | Dust and Smoke | Dust and Pollution | Dust, Poll. and Marine | Dust and Marine | Pollution and Marine |
|--|------------------|--------------------|------------------------|------------------|----------------------|
| Classified layers | 14 | 36 | 114 | 56 | 79 |
| α_{UV} , 10^{-6} m^{-1} | 39.9±21.2 | 94.2±62.3 | 93.8±74.4 | 101.5±61.3 | 70.4±46.9 |
| α_{VIS} , 10^{-6} m^{-1} | 36.3±4.0 | 78.8±36.6 | 110.2±84.8 | 81.7±50.9 | 51.4±27.9 |
| β_{UV} , $10^{-6} \text{ m}^{-1} \text{ sr}^{-1}$ | 1.38±1.02 | 1.33±0.89 | 2.06±1.67 | 2.07±1.49 | 1.77±1.15 |
| β_{VIS} , $10^{-6} \text{ m}^{-1} \text{ sr}^{-1}$ | 0.74±0.47 | 0.99±0.65 | 1.51±1.70 | 1.63±1.21 | 1.31±1.35 |
| β_{IR} , $10^{-6} \text{ m}^{-1} \text{ sr}^{-1}$ | 0.33±0.20 | 0.52±0.46 | 0.65±0.64 | 0.98±0.71 | 0.67±0.44 |
| S_{UV} , sr | 53.8±13.3 | 61.6±6.8 | 50.1±13.6 | 47.3±8.3 | 44.0±8.9 |
| S_{VIS} , sr | 63.5±11.3 | 70.1±12.6 | 53.2±14.3 | 45.3±7.0 | 41.7±13.3 |
| s_{VIS-UV} | 1.28±0.39 | 1.12±0.17 | 0.93±0.22 | 1.15±0.20 | 0.95±0.20 |
| $\hat{a}_{\alpha,UV-VIS}$ | 0.57±0.21 | 0.94±0.53 | 1.04±0.91 | 0.40±0.30 | 1.19±0.48 |
| $\hat{a}_{\beta,UV-VIS}$ | 1.34±0.66 | 1.02±0.52 | 0.95±0.47 | 0.73±0.34 | 1.27±0.39 |
| $\hat{a}_{\beta,VIS-IR}$ | 1.15±0.38 | 0.98±0.41 | 0.78±0.41 | 0.49±0.32 | 0.94±0.38 |
| $\hat{a}_{\beta,UV-IR}$ | 1.23±0.47 | 0.97±0.38 | 0.91±0.33 | 0.56±0.32 | 1.12±0.28 |
| $C_{\alpha,VIS-UV}$ | 0.80±0.10 | 0.70±0.15 | 0.70±0.25 | 0.87±0.12 | 0.64±0.13 |
| $C_{\beta,VIS-UV}$ | 0.61±0.15 | 0.69±0.15 | 0.68±0.18 | 0.76±0.10 | 0.61±0.10 |
| $C_{\beta,IR-VIS}$ | 0.47±0.11 | 0.53±0.14 | 0.61±0.18 | 0.73±0.15 | 0.54±0.15 |
| $C_{\beta,IR-UV}$ | 0.29±0.14 | 0.37±0.13 | 0.38±0.17 | 0.58±0.21 | 0.31±0.11 |

values are given as well.

Mean and median values for aerosol mixtures clearly show the influence of the different pure aerosol types. Highest lidar ratios and Ångström exponents are normally found for mixtures containing smoke or pollution, indicating small and highly absorbing particles. When marine aerosols contribute to the mixture, the lidar ratios as well as the Ångström exponents are decreased. Smallest values of Ångström exponents are found for the mixture of dust and marine aerosol, where both components contribute with relatively large particles. The fact that the variability of these data is higher than for the pure types is caused by the amount of single components in a mixture, which varies from case to case. In addition, the identification of certain mixtures is rather difficult and misclassification can easily happen.

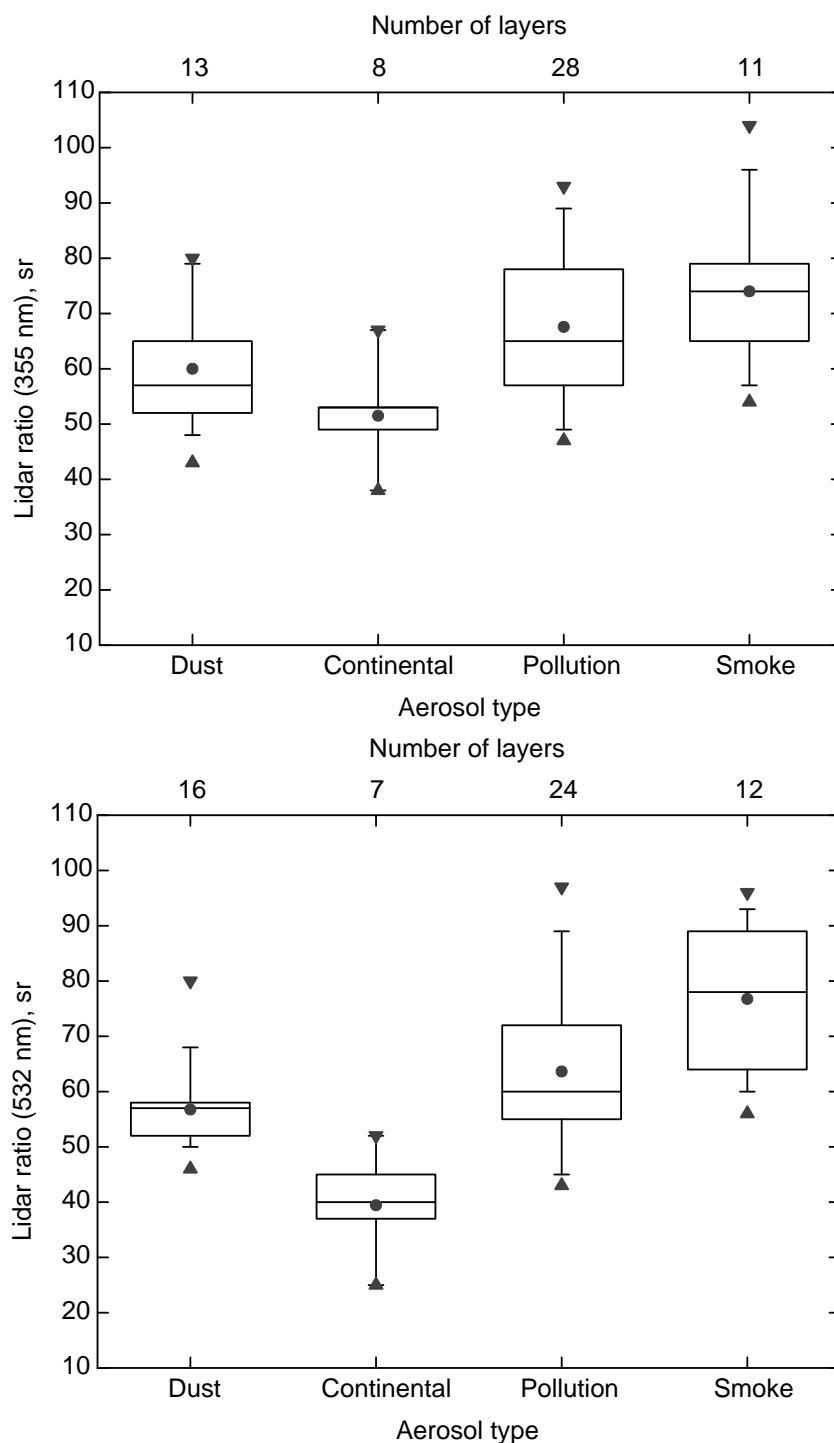


Figure 6.6: Lidar ratio at 355 nm (top) and 532 nm (bottom) for pure aerosol types. Mean, minimum, and maximum values and boxes from the 25% to the 75% percentile are indicated. The 5%, 50%, and 95% percentiles are shown in addition. Numbers of identified layers per aerosol type that contribute to the statistical values are given as well.

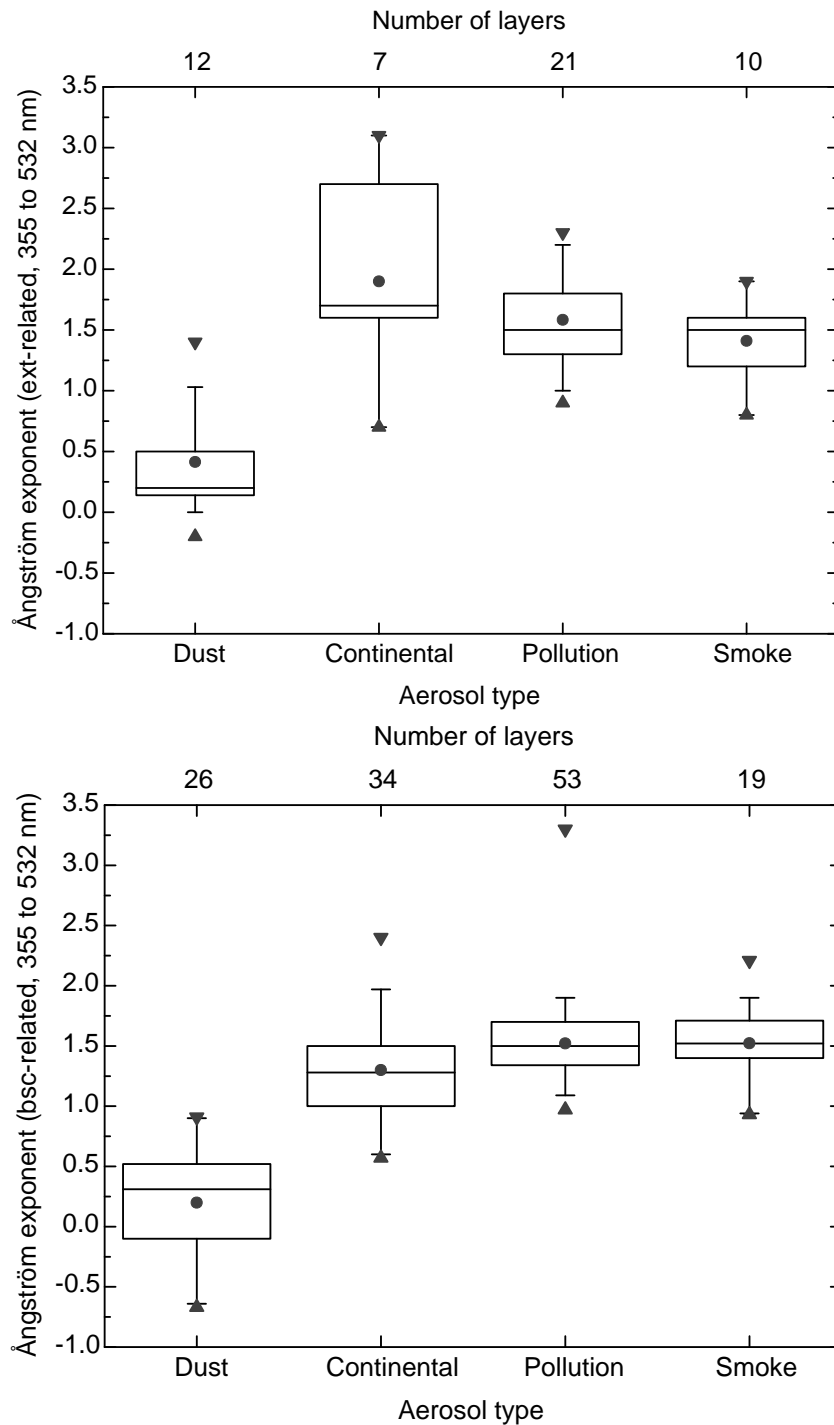


Figure 6.7: Extinction- (top) and backscatter-related (bottom) 355-to-532-nm Ångström exponents for pure aerosol types. Mean, minimum, and maximum values and boxes from the 25% to the 75% percentile are indicated. The 5%, 50%, and 95% percentiles are shown in addition. Numbers of identified layers per aerosol type that contribute to the statistical values are given as well.

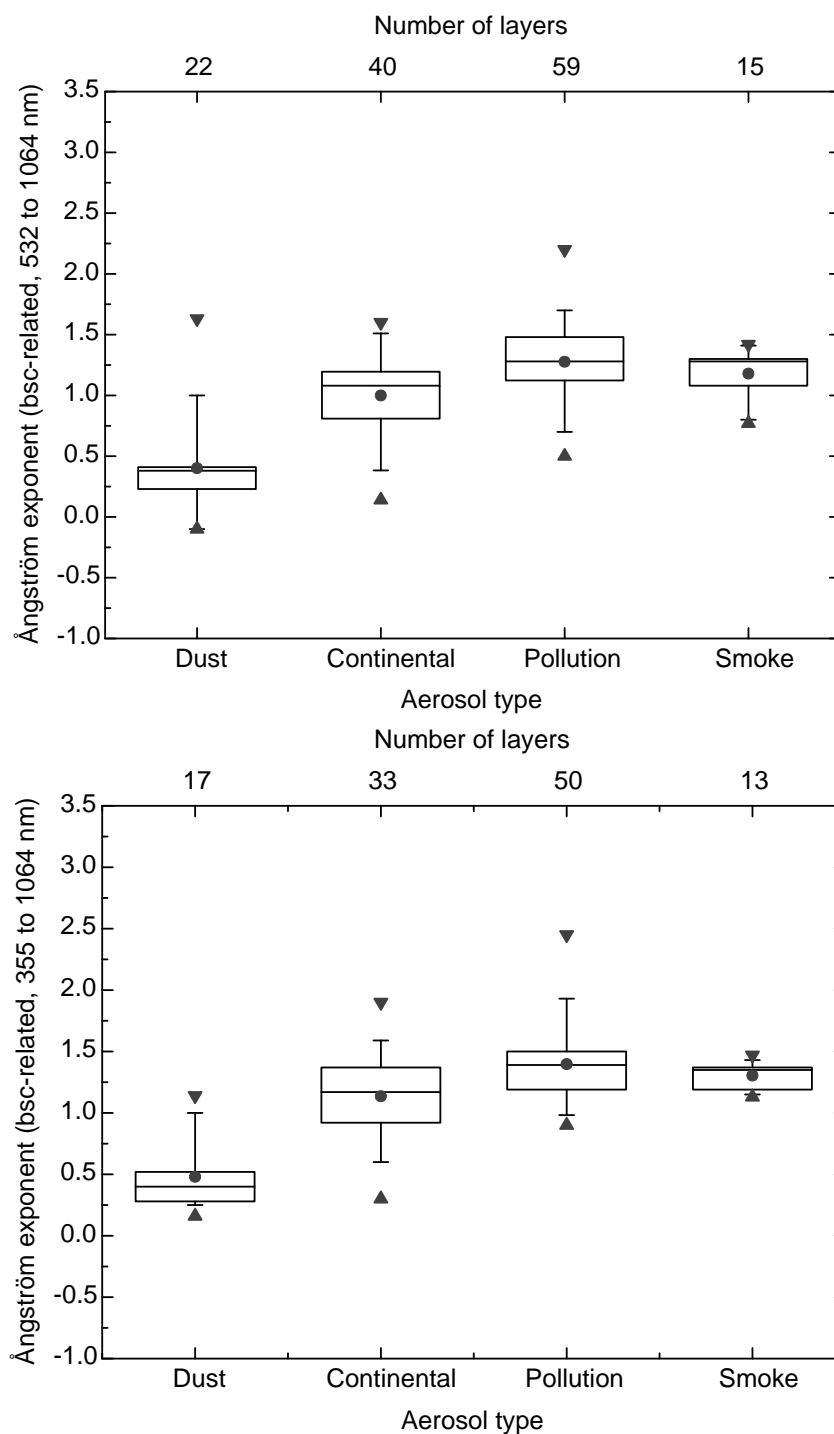


Figure 6.8: 532-to-1064-nm (top) and 355-to-1064-nm (bottom) backscatter-related Ångström exponents for pure aerosol types. Mean, minimum, and maximum values and boxes from the 25% to the 75% percentile are indicated. The 5%, 50%, and 95% percentiles are shown in addition. Numbers of identified layers per aerosol type that contribute to the statistical values are given as well.

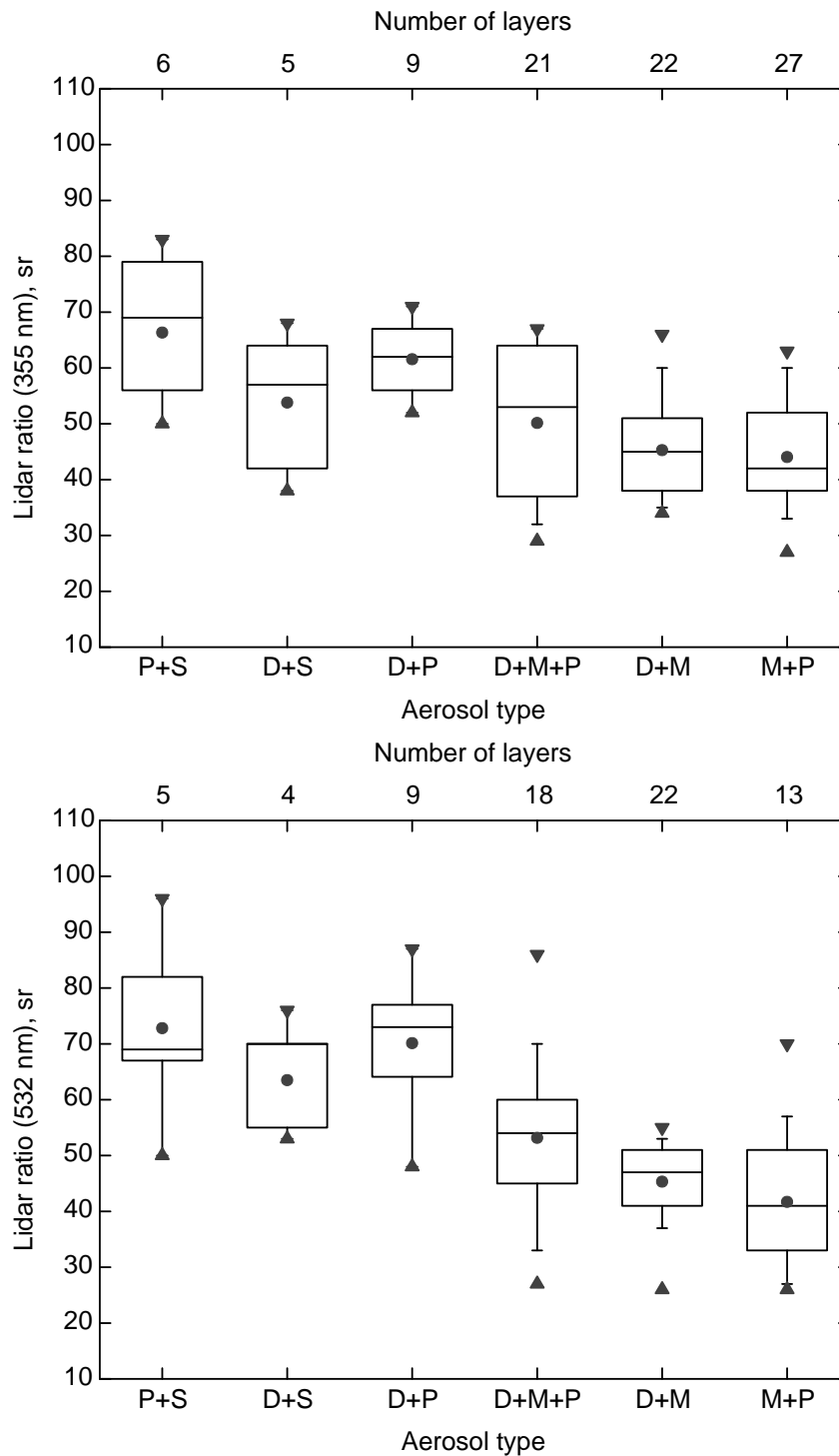


Figure 6.9: Same as Figure 6.6, but for aerosol mixtures (P+S = Pollution and Smoke, D+S = Dust and Smoke, D+P = Dust and Pollution, D+M+P = Dust, Marine and Pollution, D+M = Dust and Marine, M+P = Marine and Pollution).

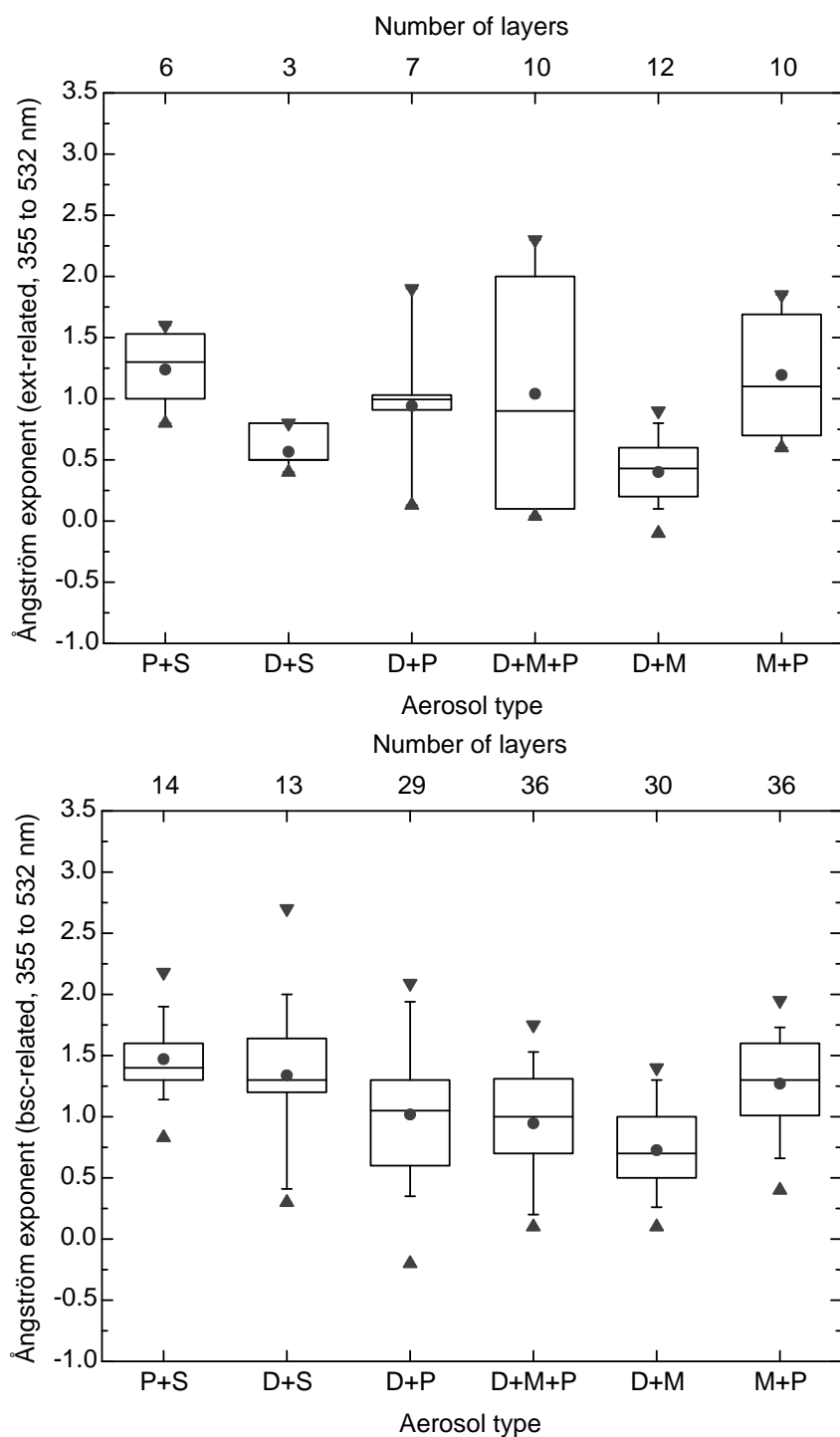


Figure 6.10: Same as Figure 6.7, but for aerosol mixtures (P+S = Pollution and Smoke, D+S = Dust and Smoke, D+P = Dust and Pollution, D+M+P = Dust, Marine and Pollution, D+M = Dust and Marine, M+P = Marine and Pollution).

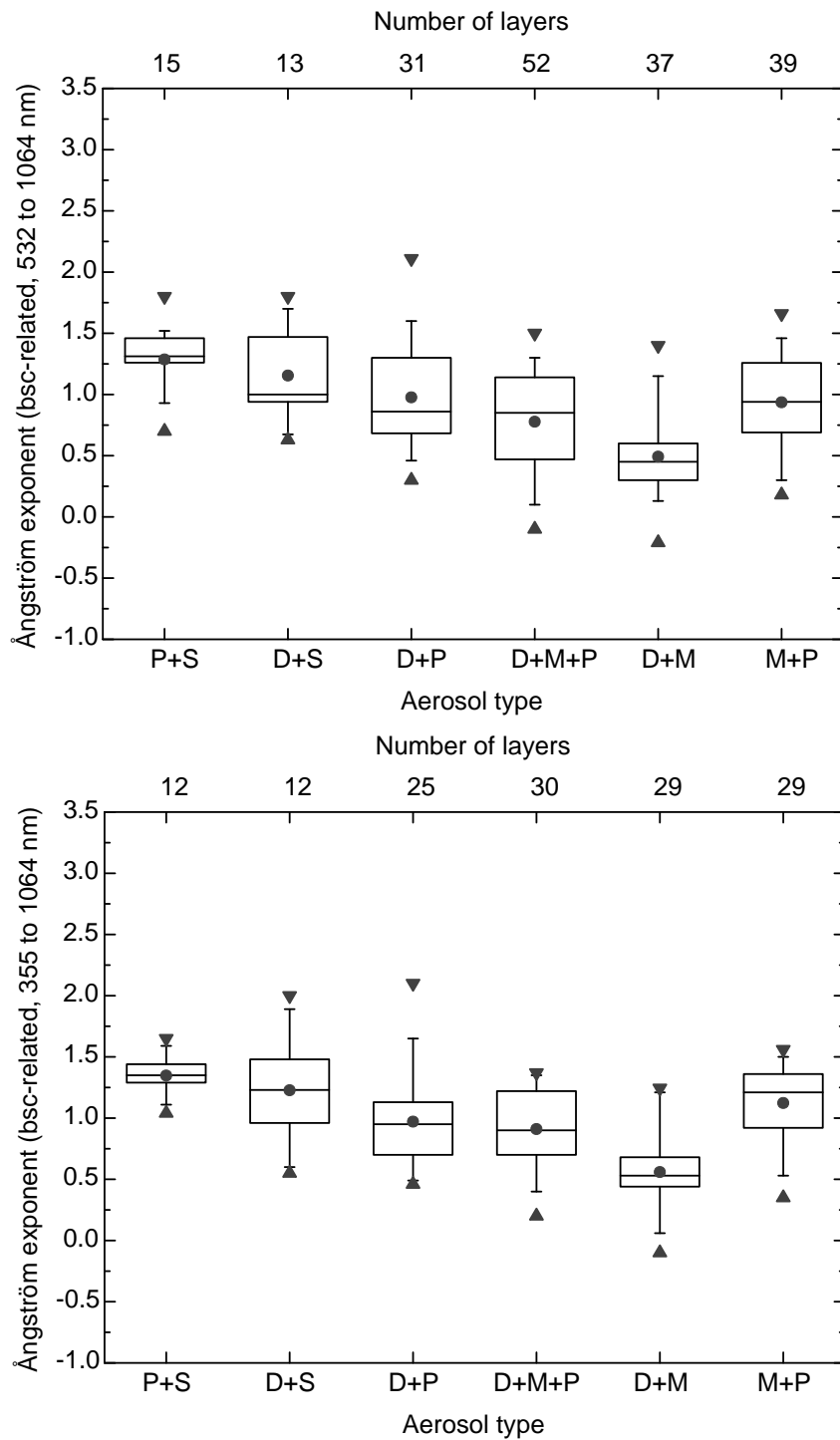


Figure 6.11: Same as Figure 6.8, but for aerosol mixtures (P+S = Pollution and Smoke, D+S = Dust and Smoke, D+P = Dust and Pollution, D+M+P = Dust, Marine and Pollution, D+M = Dust and Marine, M+P = Marine and Pollution).

6.1.4 Conversion factors for the harmonization of space missions

Conversion factors for the harmonization of spaceborne lidar observations with different instruments were calculated based on the statistical evaluation of more than 700 aerosol layers. This data set already provides a valuable insight into the benefits and limits of aerosol typing schemes for spaceborne lidar missions. The following conversion factors are of specific interest to relate ALADIN and AT Lid products to CALIPSO observations (cf. also Chapter 1):

- 532-to-355-nm extinction(-related color) ratio ($C_{\alpha, \text{VIS-UV}}$),
- 532-to-355-nm backscatter(-related color) ratio ($C_{\beta, \text{VIS-UV}}$),
- 1064-to-355-nm backscatter(-related color) ratio ($C_{\beta, \text{IR-UV}}$),
- ratio of the 532-nm lidar ratio to the 355-nm lidar ratio ($s_{\text{VIS-UV}}$).

Aerosol-type-dependent values for these wavelength conversion factors were already given in Table 6.2 and 6.3. At this point, further exploitations with special view on the spaceborne lidar products are made.

Figure 6.12 shows a two-dimensional distribution of the pure aerosol types in terms of the backscatter-related 1064-to-532-nm color ratio as measured with CALIOP versus the 355-nm lidar ratio as it will be measured with AT Lid. Figure 6.13 includes also different mixtures of aerosol types. Big color dots stand for the pure aerosol types, whereas smaller dots represent the mixtures discussed in the previous section. The same relation is shown in Figure 6.14, but this time mean values are used and colored lines were added indicating which pure types contribute to the mixtures. The fixed lidar ratio of 25 sr for marine aerosol is taken from the literature (from SAMUM-2 and ACE-2), because of the lack of data for this aerosol type from the investigations presented above. In Figure 6.14 it can be seen that the pure types of smoke, dust, pollution, and marine aerosol define the corner points of this two-dimensional distribution and that most of the mixtures lie on nearly straight connection lines between their constituents. This finding may hint to a dominance of external mixing, for which individual properties of the constituents are preserved, when air masses cross different source regions. In the case of internal mixtures, the individual properties of the constituents are usually not conserved and optical parameters may completely change. For instance, when discussing the aging (and, thus, mixing) of dust during transport, it is often assumed that soluble substances (e.g., sea salt or organic matter) condense on the dust particles and produce a coating. In such a case the particles would grow, change their absorption properties, and probably lose their non-spherical shape, so that it is not very likely that the optical parameters of the mixture remain

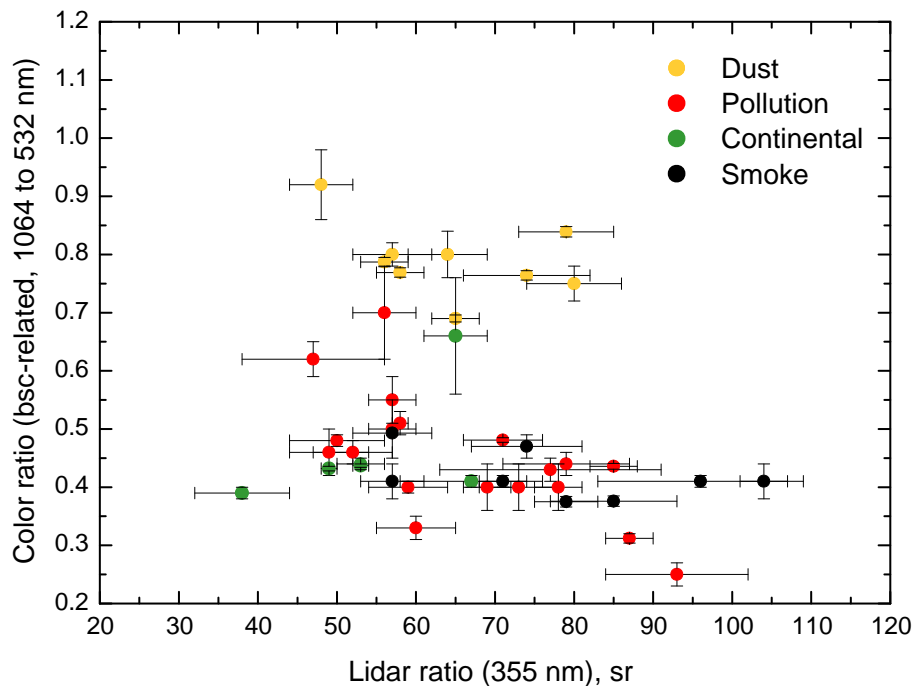


Figure 6.12: Relation between backscatter-related 1064-to-532-nm color ratio as measured with CALIOP and lidar ratio at 355 nm as it will be measured with ATLID for all investigated EARLINET aerosol layers separated for pure aerosol types. The standard deviation is indicated.

on a straight line in between those of the constituents. An example that coating could have taken place is the mixture of dust and smoke, which is not on a straight line between dust and smoke, but shows lidar ratios smaller than expected from external mixing processes. Further reasons for this result could be errors in the aerosol typing or bad underlying data. Except from the result for the mixture of dust and smoke these observations show that properties of pure types are conserved and mixed only. If the internal mixing can be neglected, probability density functions can be used to describe the state of mixing of the aerosol, i.e., “trajectories” between pure aerosol types can be defined in a multi-dimensional parameter space on which the mixtures occur.

Groß et al. [2013] reported on similar findings. The authors showed additionally that the values for the African biomass-burning-mixture cluster are clearly located within the mixing lines of Saharan dust and (Canadian) biomass-burning aerosols, which is in agreement with findings of the SAMUM-2 campaign, where *Lieke et al.* [2011] and *Weinzierl et al.* [2011] found a contribution of different amounts of Saharan dust within these aerosol layers. *Groß et al.* [2013] mentioned that besides the African

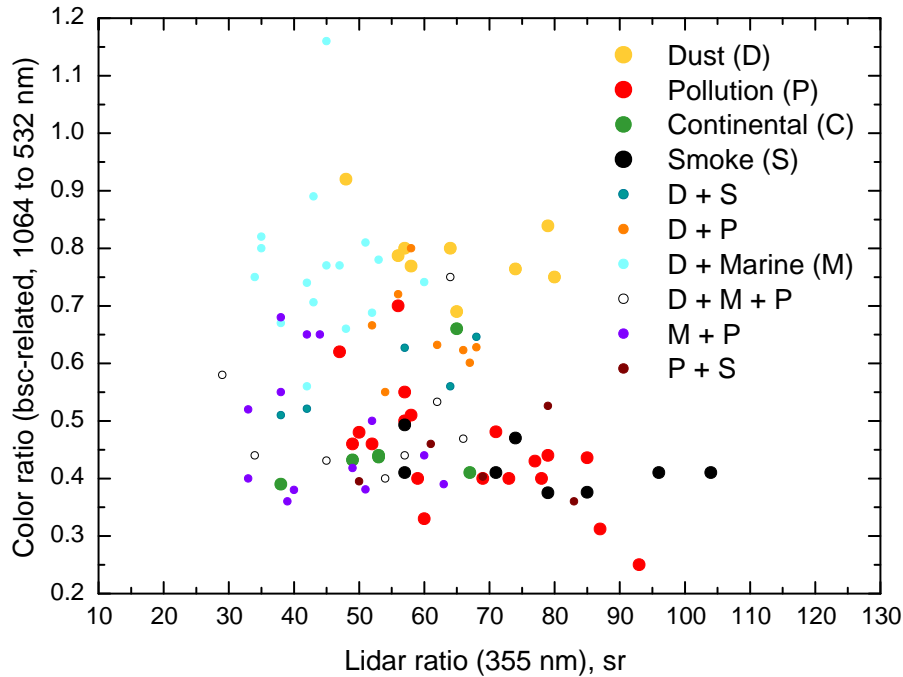


Figure 6.13: Relation between backscatter-related 1064-to-532-nm color ratio as measured with CALIOP and lidar ratio at 355 nm as it will be measured with ATLID for all investigated EARLINET aerosol layers separated for pure and mixed aerosol types (D+S = Dust and Smoke, D+P = Dust and Pollution, D+M = Dust and Marine, D+M+P = Dust, Marine and Pollution, M+P = Marine and Pollution, P+S = Pollution and Smoke).

biomass-burning-mixture cluster, also the mixed Saharan-dust cluster is within the mixing lines. They also found that the observed pattern of aerosol optical properties derived from lidar measurements can be linked empirically to their intensive micro-physical and optical properties, especially in summary.

Table 6.4 summarizes findings of the lidar ratio at 532 nm and the backscatter-related 1064-to-532-nm color ratio presented by *Burton et al.* [2013] and *Groß et al.* [2013, 2015] compared to results found within this study. In general, values derived within this study are in very good agreement with former findings. Only a slightly higher color ratio was observed for marine aerosol.

If only one of the two intensive optical parameters shown in Figure 6.14 is available, a clear aerosol typing is not possible. The color ratio (i.e., CALIOP-like instruments) is helpful to distinguish aerosols with a strong coarse particle mode (dust and marine aerosol) from aerosols with a dominating fine particle mode (smoke and pollution). The lidar ratios (i.e., ATLID-like instruments) of different aerosol types were spread a

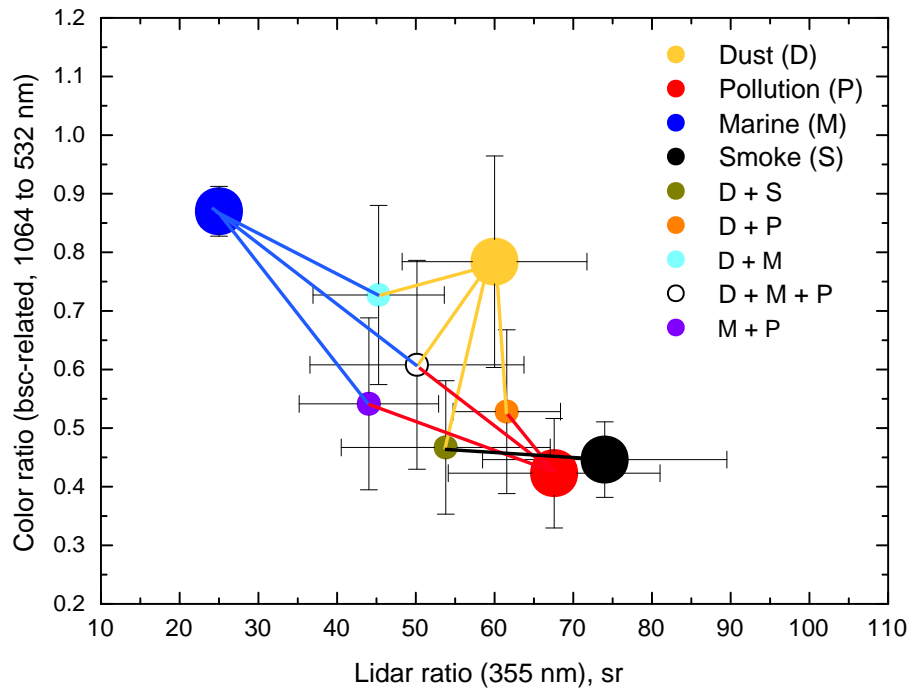


Figure 6.14: Relation between backscatter-related 1064-to-532-nm color ratio as measured with CALIOP and lidar ratio at 355 nm as it will be measured with ATLID for derived mean values for pure and mixed aerosol types (D+S = Dust and Smoke, D+P = Dust and Pollution, D+M = Dust and Marine, D+M+P = Dust, Marine and Pollution, M+P = Marine and Pollution). The lidar ratio of marine aerosol is set to the literature value of 25 sr because of the lack of data from the investigations presented above.

bit more, but were not clearly separated from each other except the value for marine aerosol. Thus, it is very important to consider the particle depolarization ratio as an additional intensive parameter to achieve better results of the aerosol classification. Measurements of the particle depolarization ratio are not trivial and require a careful instrument characterization and a specific calibration [Freudenthaler *et al.*, 2009]. The particle depolarization ratio is not an EARLINET standard product yet and during the intensive measurement period only a few stations performed quality-assured depolarization measurements with well-calibrated systems. In the present study, data of the depolarization ratio were made available only for a few measurements. In addition, mostly the volume linear depolarization ratio (cf. Equation (3.5)) was provided. However, it is a rather qualitative measure and not suitable for a distinct aerosol typing, because it describes the depolarizing properties of the scattering volume containing both air and particles. For aerosols it is better to use the particle depolarization ratio, i.e., the depolarization ratio corrected for molecular scattering. Due to the lack in the

Table 6.4: Summary of findings of the lidar ratio S_{532} and color ratio $C_{\beta,1064-532}$ found for the listed aerosol types; indices indicate the wavelength in nm and the related scattering coefficient.

| Aerosol type | S_{532} , sr | $C_{\beta,1064-532}$ | Reference |
|-----------------------|-------------------------|----------------------|---------------------------------|
| Marine | 17–27 | 0.63–0.77 | <i>Burton et al.</i> [2013] |
| | 18 ± 5 | 0.61 ± 0.10 | <i>Groß et al.</i> [2013] |
| | – | 0.87 ± 0.04 | this study |
| Dust | 45–51 | 0.63–0.71 | <i>Burton et al.</i> [2013] |
| | 48 ± 5 , 56 ± 5 | 0.77 ± 0.15 | <i>Groß et al.</i> [2013, 2015] |
| | 57 ± 8 | 0.78 ± 0.18 | this study |
| Pollution | 53–70 | 0.48–0.59 | <i>Burton et al.</i> [2013] |
| | 56 ± 6 | 0.41 ± 0.27 | <i>Groß et al.</i> [2013] |
| | 64 ± 14 | 0.42 ± 0.09 | this study |
| Smoke | 55–73 | 0.4–0.53 | <i>Burton et al.</i> [2013] |
| | 69 ± 17 | 0.21 ± 1.3 | <i>Groß et al.</i> [2013] |
| | 77 ± 14 | 0.45 ± 0.06 | this study |
| Dust + Smoke | 63 ± 7 | 0.61 ± 0.13 | <i>Groß et al.</i> [2013] |
| | 64 ± 11 | 0.47 ± 0.11 | this study |
| Dust + Smoke + Marine | 29–49 | 0.56–0.77 | <i>Burton et al.</i> [2013] |
| | 50 ± 4 | 0.68 ± 0.09 | <i>Groß et al.</i> [2013] |
| | 46 ± 20 | 0.44 ± 0.10 | this study |
| Marine + Pollution | 36–45 | 0.59–0.67 | <i>Burton et al.</i> [2013] |
| | 42 ± 13 | 0.54 ± 0.15 | this study |

used data set a brief discussion shall be given on values from the literature in order to complete the discussion on aerosol typing.

Large efforts to measure the particle linear depolarization ratio have been made during the SAMUM campaigns [*Freudenthaler et al.*, 2009; *Groß et al.*, 2011b, 2013; *Tesche*, 2011]. For pure mineral dust, values of $31 \pm 3\%$ and $26 \pm 6\%$ at 532 and 355 nm, respectively, were found in the Saharan source region during SAMUM–1 [*Freudenthaler et al.*, 2009]. Higher values of $36 \pm 2\%$ at 532 nm [*Ansmann et al.*, 2010] and $35 \pm 2\%$ at 355 nm [*Groß et al.*, 2012] were observed in the fresh ash plume of Eyjafjallajökull. For marine aerosol and smoke obtained at Cape Verde during SAMUM–2 the typical values were 3% and 5%, respectively [*Groß et al.*, 2011b]. Especially for the purpose

of aerosol typing, *Sakai et al.* [2010] measured linear depolarization ratios of mineral, sea-salt, and ammonium-sulfate particles in the laboratory. The authors found values of $39\pm 4\%$ for large and $17\pm 3\%$ to $14\pm 3\%$ for small Asian and Saharan dust particles. Dry sea salt, which occurs at relative humidity below 45% only, showed values of $8\pm 1\%$. In the liquid state, the number dropped to $1.0\pm 0.1\%$. The same value was found for liquid ammonium-sulfate particles. It can be seen that only large mineral particles as contained in desert or soil dust and ash generate a considerable light depolarization, which can be used to distinguish this kind of material from other aerosols. By knowing the depolarization properties of these particles, it is even possible to quantify their contribution to a two-component mixture, as it has been demonstrated for mixtures of dust and smoke [*Tesche et al.*, 2009a] and volcanic ash and sulfate [*Ansmann et al.*, 2011b].

By assuming typical particle linear depolarization values of 30%, 5%, 3%, and 1% for dust, smoke, marine, and pollution aerosol, respectively, it is possible to illustrate the location of these four aerosol types in the three-dimensional space of the intensive particle properties backscatter-related color ratio (1064/532 nm), lidar ratio (at 355 nm), and particle linear depolarization ratio (at 532 nm) like it was done in Figure 6.15. A wavelength dependence of the depolarization ratio is not considered (although a small wavelength dependence has been found for dust, cf. above). The projections into the x-z and y-z planes show the two-dimensional parameter spaces of ATLID and CALIOP, respectively. It can be seen that with both lidar types primarily three groups of aerosols can be clearly discriminated: dust (and ash, not shown), marine aerosol, and pollution/smoke. A clear discrimination of pollution and smoke is difficult. Here, it is noteworthy that smoke and pollution properties are quite variable and that only mean values for Europe are shown. The properties of smoke change in dependence of the fire type (smoldering or flaming) and of the transport time (cf. also Section 2.2). The properties of anthropogenic pollution are obviously different in highly industrialized regions of Europe and North America with their strong environmental regulations and in Southeast Asia [*Franke et al.*, 2003; *Catrrall et al.*, 2005]. Nevertheless, threshold values to distinguish small and highly absorbing particles (higher lidar ratio, smaller color ratio) from coarser and less-absorbing particles (smaller lidar ratio, higher color ratio) can be introduced. Hence, Figure 6.15 leads to the major conclusion that it is possible to apply a common aerosol typing scheme to CALIOP and ATLID data and, thus, to harmonize the long-term observations with both instruments by applying respective conversion factors, as derived in this study.

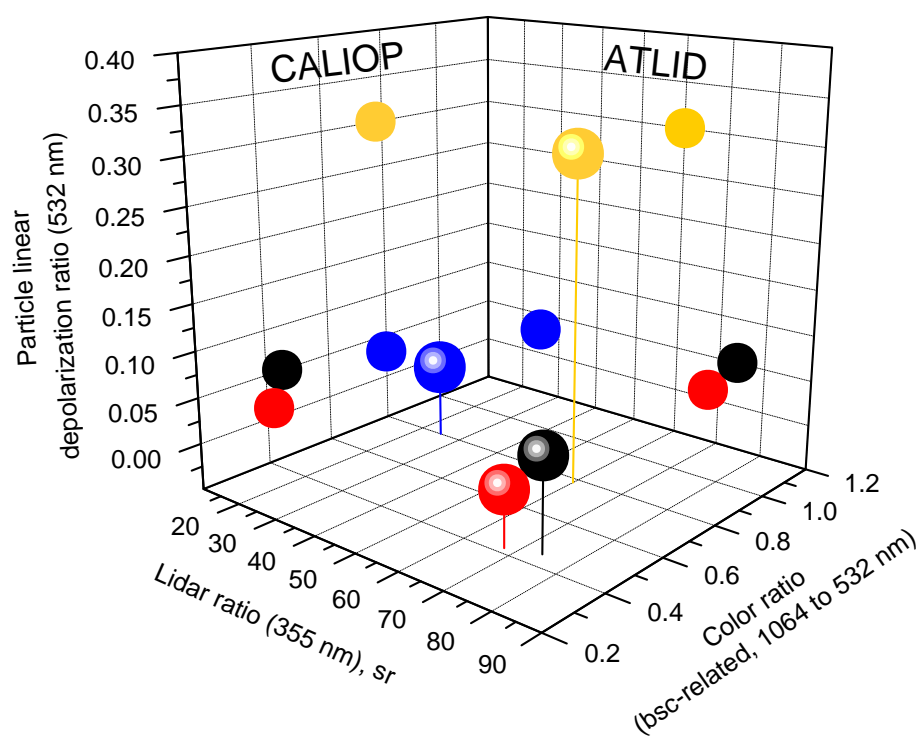


Figure 6.15: Three-dimensional relation between backscatter-related 1064-to-532-nm color ratio, lidar ratio at 355 nm, and particle linear depolarization ratio at 532 nm for the pure aerosol types (marine – blue, dust – yellow, pollution – red, smoke – black). The two-dimensional projections into the x - z and y - z planes show the separation of aerosol types as seen by ATLID and CALIOP, respectively. Because of the lack of data from the present study, the lidar ratio of marine aerosol and particle linear depolarization ratios are taken from the literature.

6.2 Aerosol layers in correlative EARLINET and CALIOP data – A comparison study

This section shows (statistical) results of the comparison of aerosol layers derived from data of selected ground-based EARLINET lidars against CALIOP data sampled from space. The aerosol typing based on EARLINET data was performed by using the aerosol types that are applied in the CALIPSO classification scheme (clean marine, desert dust, polluted continental, clean continental, biomass burning (smoke), and polluted dust). Aerosol mixtures that were used separately in Section 6.1 are now summarized as shown in Table 6.5 in order to simplify the comparison of correlative observations of EARLINET and CALIPSO.

In fact, the term polluted dust is defined in the CALIPSO terminology as a mixture of dust with smoke and/or pollution aerosol. However, each profile that shows a considerable depolarization ($7.5\% < \delta < 20\%$), which is, however, lower than the depolarization for pure dust, is categorized by CALIPSO as polluted dust. Since

Table 6.5: Aerosol types used for the validation of the CALIPSO typing scheme.

| Aerosol type | CALIPSO convention | Used in this thesis |
|--------------------------|--|--|
| Pure Types: | | |
| Marine | Clean marine | Marine |
| Desert dust | (Desert) Dust | Dust |
| Biomass burning (smoke) | Smoke | Smoke |
| Polluted continental | Polluted continental | Pollution |
| Clean continental | Clean continental | Continental |
| Tropospheric volcanic | Other | Volcanic |
| Stratospheric | Stratospheric | Stratospheric |
| Aerosol mixtures: | | |
| Mixtures with dust | Polluted dust (Dust and Smoke and/or Polluted continental) | Dusty mix (Dust and Smoke and/or Pollution and/or Marine and/or Continental) |
| Other mixtures | No equivalent types | Marine mix (Marine and Smoke and/or Pollution and/or Continental) Pollution + Smoke |

Table 6.6: Selection of EARLINET data for the validation of the automatic CALIPSO classification scheme (BL aerosol – boundary-layer aerosol).

| | Measurements | Aerosol layers |
|--|--------------|----------------|
| Case A observation | 164 | |
| CALIOP data not available | 9 | |
| CALIOP profiles free of aerosol | 9 | |
| Failure in quality-assurance criteria | 5 | |
| | 141 | 411 |
| Aerosol type undetermined | | 33 |
| Too far away for BL aerosol comparison | | 36 |
| Comparison based on | | 342 |

there is no other mixture included in the CALIPSO classification scheme, also dust mixed with marine aerosol is classified as polluted dust. For this study, mixtures in EARLINET data that contain dust and other aerosol are called dusty mix. Two additional mixtures are separated although there is no equivalent aerosol subtype within the CALIPSO classification scheme: marine mix and the mixture of pollution and smoke (cf. Table 6.5).

Table 6.6 summarizes the data set on which this comparison study is based. As already introduced in Chapter 5, so-called EARLINET Case A measurements were chosen, for which the CALIPSO overpass is at maximum 100 km away from the EARLINET lidar site. That requirement reduces the number of measurements from the data set investigated above from 240 to 164 measurements. Within that reduced data set, CALIOP data were not available to nine measurements, in nine other cases the CALIOP profiles were free of aerosol, and for further five measurements the data quality-assurance criteria (cf. Section 5.1.3) were not fulfilled. Thus, 141 EARLINET measurements with 411 aerosol layers remain. Unfortunately, for 33 of these aerosol layers no distinct aerosol type could be assigned and so they are excluded from the comparison. From the remaining 378 aerosol layers, 36 aerosol layers, which contain boundary-layer aerosol but correspond to a satellite overpass of more than 10 km away from the EARLINET observation, have to be excluded (cf. Section 5.1.3). Hence, the validation of CALIPSO's automatic feature classification and aerosol typing scheme is based on 342 classified EARLINET aerosol layers.

6.2.1 EARLINET aerosol layers detected by CALIPSO

In Section 5.1.3 the performance of the comparison of the classified aerosol subtypes was briefly introduced. For each comparison a set of ten along-track individual CALIOP profiles averaged horizontally over 5 km was chosen and within each set, aerosol features were searched. The heights of the EARLINET aerosol layers served as lower and upper limits of each layer.

Each correlative CALIOP data subset, for which aerosol subtypes were compared to results of the EARLINET data, was checked to get a feeling for the data quality and errors that occur during the comparison. Possible aerosol distributions, which were observed within the CALIOP profiles for the height ranges of interest, were already presented (cf. Section 5.1.3 occasions (a)–(g)). Investigations showed that mostly about two third of the height ranges of the CALIOP profiles were classified to contain aerosol or about six of ten profiles show the presence of aerosol for the entire height range. A weighing factor was determined by counting the frequency of occurrence of each aerosol type within the ten CALIOP profiles related only to those height bins of all profiles of this CALIOP scene that were typed as illustrated in Table 6.7 for one specific CALIOP example. This example illustrates the following results for the comparison. Firstly, the EARLINET aerosol layer was also detected by CALIPSO. Secondly, within this aerosol layer the types polluted continental (CALIPSO aerosol type number 3) and smoke (CALIPSO aerosol type number 6), but also some parts of clear air (CALIPSO “aerosol” type number 0) were classified by CALIPSO.

Table 6.7: CALIOP profiles of a cross section used for the comparison to the correlative EARLINET measurement. Per bin and profile the occurrence of each CALIPSO aerosol type is shown, on the right side (Counts per type), the frequency of occurrence is shown (1–clean marine, 2–dust, 3–polluted continental, 4–clean continental, 5–polluted dust, 6–smoke, 7–other). Clear air is indicated by 0.

| Height | Profile number | | | | | | | | | | Counts per type | | | | | | | |
|---|----------------|---|---|---|---|---|---|---|---|-------------|-----------------|---|---|----|---|---|---|---|
| | 1 | 2 | 3 | 4 | 5 | 6 | 7 | 8 | 9 | 10 | 0 | 1 | 2 | 3 | 4 | 5 | 6 | 7 |
| Bin 1 | 6 | 6 | 6 | 0 | 0 | 0 | 0 | 0 | 0 | 0 | 7 | 0 | 0 | 0 | 0 | 0 | 3 | 0 |
| Bin 2 | 6 | 6 | 6 | 0 | 0 | 3 | 3 | 3 | 3 | 0 | 3 | 0 | 0 | 4 | 0 | 0 | 3 | 0 |
| Bin 3 | 3 | 3 | 3 | 3 | 3 | 3 | 3 | 3 | 3 | 0 | 1 | 0 | 0 | 9 | 0 | 0 | 0 | 0 |
| Bin 4 | 3 | 3 | 3 | 3 | 3 | 3 | 3 | 3 | 3 | 0 | 1 | 0 | 0 | 9 | 0 | 0 | 0 | 0 |
| Bin 5 | 3 | 3 | 3 | 3 | 3 | 3 | 3 | 3 | 3 | 0 | 1 | 0 | 0 | 9 | 0 | 0 | 0 | 0 |
| All height bins with aerosol: 37 | | | | | | | | | | Sum: | 13 | 0 | 0 | 31 | 0 | 0 | 6 | 0 |

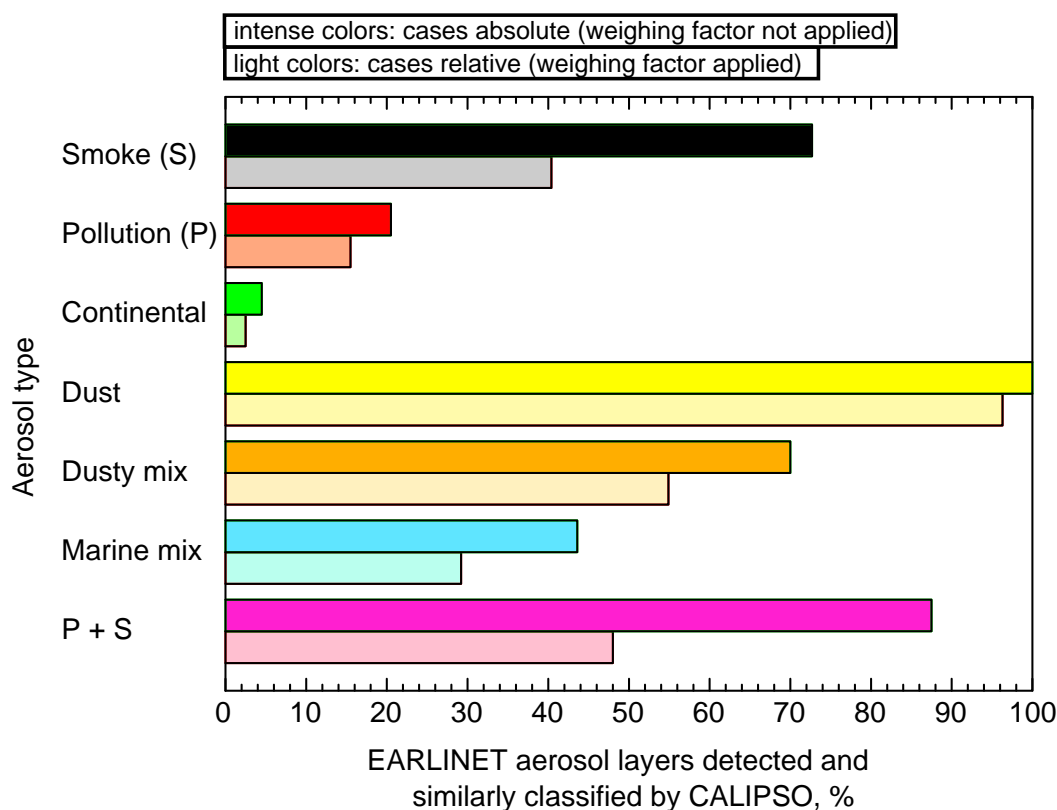


Figure 6.16: Histogram of EARLINET aerosol layers that were detected and similarly classified by CALIPSO separated for investigated aerosol types with and without applied weighing factor.

The weighing factor describes the relation of the counts per aerosol type to the sum of all height bins within the respective CALIOP scene that were classified as aerosol but not as clear air. The example presented in Table 6.7 shows in sum 31 counts for all height bins and all profiles for the aerosol type polluted continental. This number was divided by the sum of all height bins that were typed as aerosol (in this case 37). Hence, the weighing factor for polluted continental aerosol for this example is 0.84. Based on this calculation the weighing factor for smoke for this example is 0.16. The effect of the weighing factor on results of the aerosol type comparison is presented in the following.

Figure 6.16 illustrates the results of the CALIPSO classification scheme for EARLINET aerosol layer heights within the correlative CALIPSO profiles separated for the applied aerosol types. Intensively colored bars represent the cases for which the same aerosol type was simultaneously classified by the CALIPSO typing scheme somewhere in the aerosol layer, without taking into account other aerosol types

Table 6.8: All EARLINET aerosol layers (EAL) separated for specific aerosol types (AT). In addition, the corresponding results of the CALIPSO feature classification and aerosol typing are given.

| Aerosol type (AT) | EARLINET aerosol layers (EAL) cases | CALIPSO | | | |
|----------------------|--|-----------------------------|--|---------------------|---|
| | | detected EAL cases, % | detected EAL of same/similar typing cases, % | weight. cases, % | most frequ. classified AT instead |
| Smoke (S) | 18 | 61.1 | 72.7 | 40.4 | Poll. dust |
| Pollution (P) | 65 | 67.7 | 20.5 | 15.5 | Smoke |
| Continental | 27 | 81.5 | 4.5 | 2.5 | Poll. dust |
| Marine | 3 | – | – | – | – |
| Dust | 8 | 75.0 | 100 | 96.3 | Poll. dust |
| Dusty mix | 111 | 72.1 | 70.0 | 54.9 | Dust |
| Marine mix | 65 | 60.0 | 43.6 | 29.2 | Poll. dust |
| P + S | 10 | 80.0 | 87.5 | 48.0 | Poll. dust |
| Volcanic | 20 | 35.0 | – | – | Poll. dust |
| Stratospheric | 15 | 46.7 | 100 | 100 | – |
| All types | 342 | 65.5 | 49.6 | 37.4 | |

that were classified additionally within the same layer. Light colored bars illustrate the results when the above introduced weighing factor was applied for each case individually. Figure 6.16 clearly shows that the number of aerosol layers that were classified similarly by EARLINET and CALIPSO is on average reduced by about 66% per aerosol type, if the classification of other aerosol types within the considered aerosol layer is taken into account. The light colored bars represent the effective results, which are used for further investigations.

Table 6.8 shows how often CALIPSO detected aerosol within the EARLINET aerosol layer height range. Numbers are given separately for specific aerosol types. In addition, it is presented how often the same aerosol subtype, or in case of an aerosol mixture at least one of the pure aerosol types within the mixture, was classified by CALIPSO. For example, if a mixture of polluted dust with marine aerosol was found in the EARLINET data, results of CALIOP were counted as same aerosol type, if either the polluted dust or the clean marine aerosol type was classified. Furthermore, the aerosol type, which was most frequently classified instead, is given.

In general, aerosol was found by CALIPSO within the EARLINET aerosol layer height range for 224 cases (i.e., 65.5% of all 342 layers). Within these cases, aerosol was classified for the entire height range in 157 cases. For 67 cases aerosol was found

Table 6.9: EARLINET aerosol layers (EAL) classified in data of **Potenza** separated for specific aerosol types (AT). In addition, the corresponding results of the CALIPSO feature classification and aerosol typing are given.

| Aerosol type (AT) | EARLINET aerosol layers (EAL) cases | CALIPSO | | | |
|----------------------|--|-----------------------------|--|---------------------|---|
| | | detected EAL cases, % | detected same/similar typing cases, % | weight. cases, % | most frequ. classified AT instead |
| Smoke (S) | – | – | – | – | – |
| Pollution (P) | 2 | 50 | – | – | P. dust, S |
| Continental | 3 | 100 | – | – | Poll. dust |
| Marine | – | – | – | – | – |
| Dust | 1 | 100 | 100 | 100 | – |
| Dusty mix | 18 | 100 | 55.6 | 50.2 | Dust |
| Marine mix | 11 | 81.8 | 33.3 | 15.6 | Poll. dust |
| P + S | 3 | 100 | 66.7 | 51.7 | Poll. dust |
| Volcanic | – | – | – | – | – |
| Stratospheric | 5 | 40 | 100 | 100 | – |
| All types | 43 | 86.1 | 48.7 | 40.5 | |

at least in some parts of this height range. The following results were found for the different aerosol types. Best agreement regarding the presence of aerosol layers within the same height range, was found for EARLINET aerosol layers that were typed as continental aerosol (22 layers, i.e., 81.5% of all 27 layers). However, the same aerosol type (continental aerosol) was classified by CALIOP only once, whereas most of the other EARLINET continental aerosol layers were classified as polluted dust. A different result was found for pure dust. From the EARLINET measurements eight layers were classified as containing pure dust, and six of them (i.e., 75%) were found in the CALIOP data with nearly always the same classification (96.3%). Only small parts of those aerosol layers were typed by CALIPSO as polluted dust.

The same overview, but for comparison results for Potenza only, is shown in Table 6.9. For Potenza 86.1% of the EARLINET aerosol layers were also detected in the corresponding CALIOP profiles, but only for about 40% of these layers the same aerosol type was classified. It is noteworthy that mostly polluted dust was assigned instead.

A different result is found for Leipzig (cf. Table 6.10). Here only half of the defined aerosol layers were also detected in the corresponding CALIOP profiles, but for 69% of these layers the same aerosol type was classified. Over Leipzig five stratospheric

Table 6.10: EARLINET aerosol layers (EAL) classified in data of **Leipzig** separated for specific aerosol types (AT). In addition, the corresponding results of the CALIPSO feature classification and aerosol typing are given.

| Aerosol type (AT) | EARLINET aerosol layers (EAL) cases | CALIPSO | | | |
|----------------------|--|-----------------------------|---|--|---|
| | | detected EAL cases, % | detected same/similar typing cases, % | detected EAL of weight. cases, % | most frequ. classified AT instead |
| Smoke (S) | 1 | – | – | – | – |
| Pollution (P) | 18 | 72.2 | 61.5 | 48.2 | Smoke |
| Continental | 5 | 40 | 50 | 28.0 | Poll. dust |
| Marine | – | – | – | – | – |
| Dust | 1 | 100 | 100 | 100 | – |
| Dusty mix | 6 | 33.3 | 100 | 71.0 | – |
| Marine mix | 12 | 41.7 | 80 | 54.0 | Pollution |
| P + S | 2 | 50 | 100 | 10 | Poll. dust |
| Volcanic | 8 | 25 | – | – | Smoke |
| Stratospheric | 5 | 60 | 100 | 100 | – |
| All types | 58 | 50 | 69 | 51.9 | |

layers were observed during the investigated measurement period. CALIPSO detected and identified three of those five stratospheric features, the other two stratospheric layers were too thin for detection by CALIPSO.

Figure 6.17 shows the results for matches of aerosol layers and aerosol types separately for the EARLINET stations Cabauw, Maisach, Granada, L’Aquila, Athens, and Thessaloniki. Results of Potenza and Leipzig, already discussed above, are also included in this overview. Figure 6.17 illustrates the results presented in Table 6.8. On average, for about two third of the cases, aerosol layers were identified in both data sets. Comparison results of the classified aerosol subtypes within the corresponding aerosol layers differ for the selected EARLINET stations. For most stations, about 30%–40% of the aerosol layers are classified similarly however, for some stations (e.g., Maisach, Thessaloniki), there is less agreement, while for others (e.g., Leipzig, Granada), there is better agreement.

A detailed analysis for Maisach reveals that pollution was classified for 16 of the 18 EARLINET aerosol layers (i.e., 89%). In the correlative CALIOP profiles the aerosol layers were mainly classified as smoke with some sections of pollution and dust. For these selected EARLINET aerosol layers the presence of dust and smoke was not considered, because the source analysis and the cross check of other available

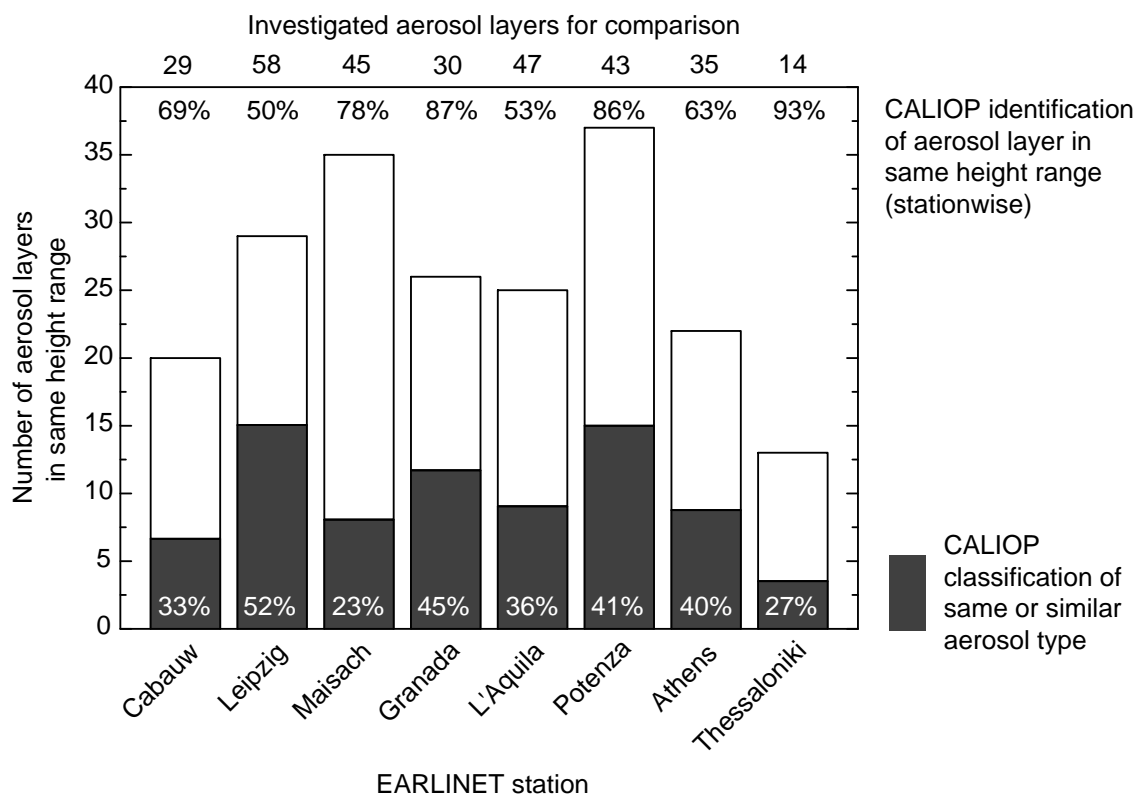


Figure 6.17: Histogram of aerosol layers identified in data of the given EARLINET stations and searched for in corresponding CALIPSO overpass profiles. In addition, it is indicated how often the same or similar aerosol type was classified by the CALIPSO aerosol typing scheme. The number of investigated aerosol layers is given for each station.

data (cf. Chapter 4) did not give any hint for the presence of dust and smoke. The classification for the EARLINET aerosol layers of Maisach was done without information about the depolarization, since it was not available in the EARLINET database. However, within the CALIPSO classification scheme just the depolarization information itself leads to the selection of dust for some parts of the data subsets used for the comparison with the Maisach data.

Table 6.11 shows again how often CALIPSO detected aerosol within the EARLINET aerosol layer height range, but now statistics are separated for different distances from the cross section of the satellite overpass. In addition, it is presented how often the same aerosol subtype, or in case of an aerosol mixture at least one of the pure aerosol types within the mixture, was classified by CALIPSO. Obviously, the comparison results do not significantly differ for cases when the corresponding observations of the EARLINET station and CALIPSO were performed for satellite overpasses of distances

Table 6.11: EARLINET aerosol layers (EAL) found in correlative CALIPSO overpass profiles and results of the CALIPSO aerosol typing scheme separated with respect to the distance between the EARLINET station and the cross section of CALIPSO.

| Distance from satellite overpass | EARLINET aerosol layers (EAL) cases | CALIPSO | | |
|---|--|-----------------------------|--|-------------------|
| | | detected EAL cases, % | detected EAL of same/similar typing cases, % | weighted cases, % |
| 0–50 km | 157 | 65.6 | 54.4 | 40.8 |
| 50–100 km | 185 | 65.4 | 45.5 | 34.5 |

less (65.6%) or more than 50 km (65.4%). Slightly different results were found for the classified aerosol types. For 40.8% of all cases the same or similar aerosol type was classified for observations at maximum 50 km away from the satellite overpass, whereas for observations with a distance of more than 50 km only 34.5% were typed similarly. This minor difference might be due to aerosol layer inhomogeneities above the continent, or limited classification options within the CALIPSO typing scheme, which will be discussed later on.

6.2.2 Validation of the CALIPSO aerosol typing scheme

For each EARLINET aerosol layer the correlative CALIPSO profiles were checked for the presence of aerosols. In Figure 6.18 the frequency of occurrence of aerosol types for EARLINET aerosol layers in the EARLINET data selected for the comparison and in the correlative CALIPSO profiles are illustrated. For the EARLINET profiles the majority of the aerosol layers was classified as dusty mix (33.9%), while only 2.4% of all comparison layers contained pure dust. Marine mix and pollution aerosol were both found in 19.9% of all cases. 8.3% of the layers were identified as continental and 6.1% of the layers from the investigated period contained volcanic aerosol. Smoke was classified for 5.5%, and a mixture of pollution and smoke for 3.1% of all cases. Clean marine conditions were found for 0.9% of all EARLINET aerosol layers only.

A somewhat different occurrence statistics is shown for the subset of EARLINET aerosol layers searched for within the correlative CALIPSO profiles. The mixture of polluted dust is most frequently classified (37.0%), followed by smoke (25.4%) and pure dust (20.8%). 9.0% and 4.9% of the cases were grouped into the categories pollution and continental aerosol, respectively. Again, only few aerosol layers (2.9%) were classified as clean marine.

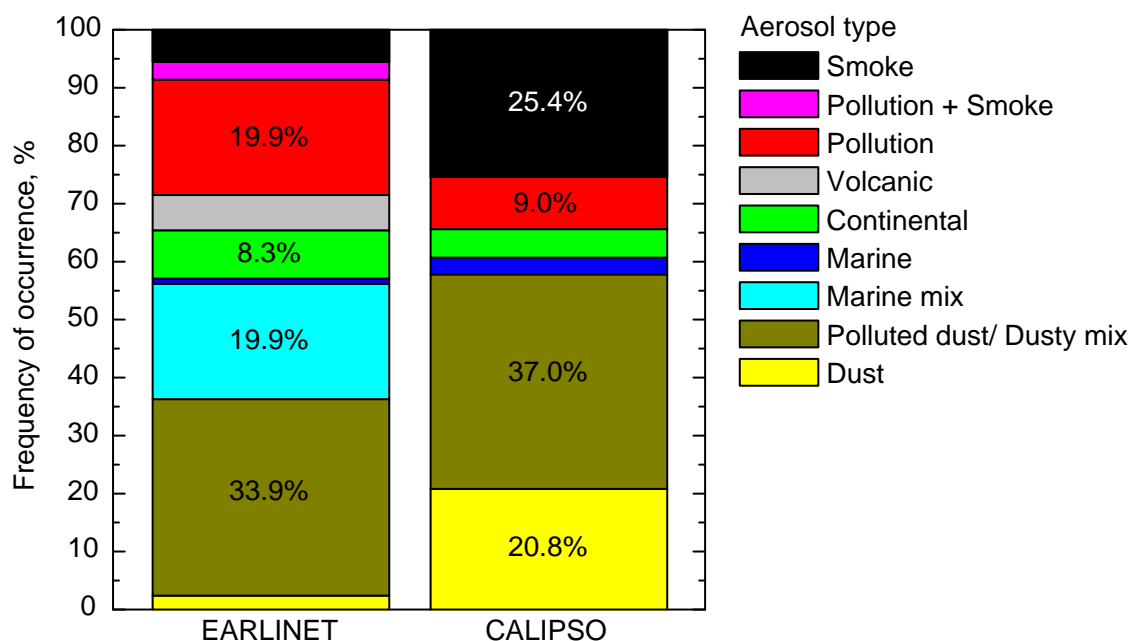


Figure 6.18: Frequency of occurrence of aerosol types in correlative EARLINET and CALIPSO data used for the comparison.

Several points are noteworthy here. Firstly, it should be kept in mind that the CALIPSO classification scheme was designed to select the clean marine type only above water surfaces. Since EARLINET is a continental-scale lidar network, only in coastal regions, where some profiles of the used CALIOP scene were sampled over water surfaces, this aerosol subtype was classified. The few observations of clean marine aerosol and the large number of marine-mix aerosol layers in the EARLINET data is caused by several EARLINET stations located in coastal regions at which mostly a mixture of marine and other aerosol types is present. Secondly, the large number of measurements contributed by stations in the Mediterranean region explains that in both data sets dusty mix or polluted dust is the most frequent aerosol type. A further noteworthy result is that totally about 35% of the aerosol layers were classified in both data sets as containing smoke and pollution and in case of EARLINET also containing volcanic aerosol and a mixture of pollution and smoke aerosol.

A detailed investigation of each EARLINET aerosol layer within the correlative CALIPSO profiles is presented in the following. In case aerosol was simultaneously found in the EARLINET and CALIPSO profiles for the EARLINET aerosol layer height, the aerosol type that was classified from the EARLINET data was used to validate the aerosol subtype that was selected by the automatic CALIPSO classification scheme. Comparison results for EARLINET aerosol layers, except for

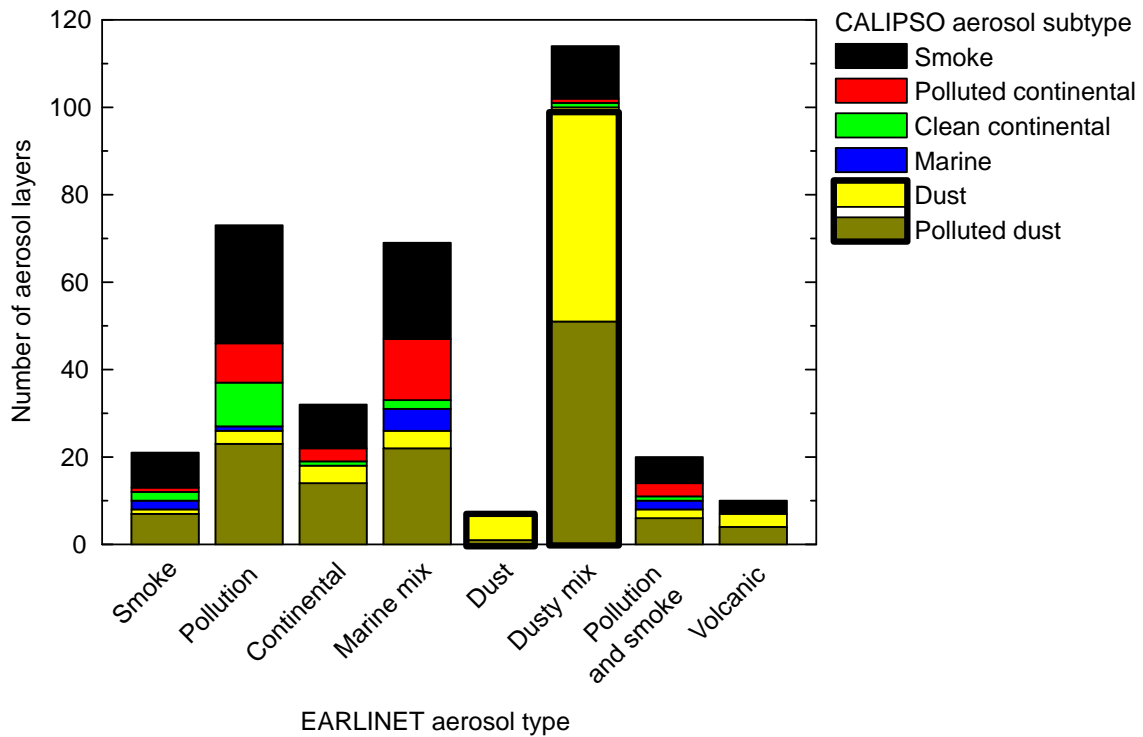


Figure 6.19: Results of the CALIPSO aerosol typing scheme for EARLINET aerosol layers versus classified EARLINET aerosol types. The EARLINET aerosol types are shown on the x-axis whereas the colors represent the six CALIPSO aerosol subtypes. The black boxes indicate the presence of dust in either pure or mixed state.

the stratospheric layers, are shown in Figure 6.19. 38.1% of the EARLINET aerosol layers that were classified as smoke or for which smoke was part of the mixture were also typed as smoke aerosol by CALIPSO. For about one third (33.3%) of those measurements the mixture polluted dust was selected. For the remaining cases clean marine or clean continental aerosol was classified for 9.5% and dust or polluted continental aerosol for 4.8% of the EARLINET smoke layers.

When pollution was classified in the EARLINET aerosol layer the same aerosol type was classified by the CALIPSO algorithm for only 12.3%, whereas most of these EARLINET pollution aerosol layers were typed by CALIPSO as smoke (37.0%) and 31.5% as polluted dust. Relatively poor agreement (3.1%) was found for continental aerosol classification. Almost 44% of the EARLINET aerosol layers that consist of continental aerosol were simultaneously classified by CALIPSO as polluted dust and 31.3% were wrongly classified as smoke.

For the few case A measurements with pure marine aerosol no correlative aerosol layers were found within the CALIOP profiles. As shown by the fourth bar in

Figure 6.19, 69 EARLINET aerosol layers were classified as a mixture of marine and other aerosols. 31.9% of these EARLINET aerosol layers were classified by CALIPSO as smoke or polluted dust, 20.3% and 7.2% as polluted continental and clean marine, respectively.

Best agreement was found for dust. 85.7% of all EARLINET dust layers were classified by CALIPSO as pure dust and 14.3% as polluted dust. Similar results were found for the EARLINET type dusty mix. 44.7% of the EARLINET aerosol layers that were labeled as mixtures of dust with further constituents were classified by CALIPSO as polluted dust. 43.0% were typed as pure dust. There is no corresponding aerosol subtype for the EARLINET mixture of pollution and smoke aerosol. However, CALIPSO selected the pure types smoke for 30.0% and pollution for 15.0% of these aerosol layers. 30.0% were classified as polluted dust. 40.0% of all EARLINET volcanic aerosol layers were classified by CALIPSO as polluted dust and 30.0% as dust or smoke.

Summarizing, it was shown that the CALIPSO typing performed well for EARLINET aerosol layers classified as smoke, dust, and dusty mix. Depolarization measurements are sensitive to non-spherical dust particles. Hence, for these cases the depolarization measurements of CALIOP are a big advantage. In the CALIOP data aerosol layers are classified as pure dust, if the particle depolarization was above a threshold of 20%. For depolarization values of $7.5\% < \delta < 20\%$ the mixture polluted dust was selected. This threshold-based selection of the aerosol subtype can lead to the following misclassification in the CALIPSO data. If an aerosol mixture was present, but the depolarization within the EARLINET aerosol layer height range was high enough (larger than 20%), pure dust was classified by CALIPSO. Polluted dust was selected by CALIPSO only for depolarization values lower than 20%. For the EARLINET aerosol layers the dusty mix type was classified, if investigations of the aerosol source region hint to the presence of other aerosol components apart from dust. The category polluted dust within the CALIPSO typing scheme was designed for mixtures of dust with smoke and/or pollution. In addition, since the marine component reduces the depolarization value, mixtures of dust and marine aerosol are classified by CALIPSO as polluted dust. This misuse of the CALIPSO category polluted dust implies a further error in the aerosol subtyping.

As previously mentioned, the aerosol type clean marine is selected within the CALIPSO aerosol typing scheme only for aerosol layers over the ocean (cf. Figure 3.4). Therefore, this aerosol type can only be classified similarly in both data sets when some parts of the ten 5-km profiles of CALIOP used for the comparison were over water surfaces, e.g., in coastal regions. Within the range of the EARLINET aerosol layers of the marine type used for the validation, no aerosol layer was found in the correlative CALIOP profiles. Instead, the comparison could be performed for

aerosol layers that were classified as marine mix due to the influence of local pollution in the coastal areas of the corresponding EARLINET stations. Since this mixture does not exist in the CALIPSO typing scheme, most of these aerosol layers were classified by CALIPSO as pollution.

Pollution and smoke aerosol show similar optical properties and, hence, a differentiation is difficult. Within the CALIPSO typing scheme the distinction of these two aerosol types is based on the height of the aerosol layer. Pollution aerosol is classified by CALIPSO only for aerosol layers that are close to the surface, whereas elevated aerosol layers are typed as smoke. In this study, most EARLINET aerosol layers that were classified as pollution were typed by CALIPSO as smoke, because the aerosol layer was elevated. The determination of the aerosol source region and investigation of other observational data, e.g., MODIS fire maps did not show the presence of fires for the EARLINET pollution aerosol layers. Consequently, the aerosol type smoke is clearly overrepresented and simultaneously pollution is underrepresented by CALIPSO. This statement is emphasized by the fact that this study is based on EARLINET measurements showing the aerosol distribution over Europe, which is dominated by pollution aerosol.

Results of the comparison of aerosol types classified in EARLINET aerosol layers with selected aerosol subtypes in the CALIPSO classification scheme can be summarized as follows. For EARLINET aerosol layers often a mixture was classified. There are no equivalent types in the CALIOP aerosol classification scheme besides polluted dust. Therefore, the aerosol subtype classified by CALIPSO was not only counted as a match, if it was the same type but also, if at least one aerosol type of the classified mixture was selected by CALIPSO. This procedure revealed that for almost 40% of all cases the same aerosol type was classified by the CALIPSO typing scheme.

In general, the findings of this study agree well with the results of the systematic comparison of the CALIPSO aerosol classification scheme presented by *Burton et al.* [2013], although the identification of aerosol layer heights was done in a different way. The authors used aerosol layers classified by CALIOP and investigated their HSRL data from satellite validation under-flights for the presence of these aerosol layers and compared the classified aerosol subtypes. *Burton et al.* [2013] found a misuse of the CALIPSO category polluted dust in cases of mixtures with marine aerosol, like it was shown within this thesis.

The comparison between aerosol layers found in EARLINET data and searched for in corresponding CALIOP data also shows that the aerosol layer definition in the CALIPSO data is independent of the classified aerosol type. Sometimes the classification of aerosol subtypes looks “a bit wild”, especially when different aerosol types were defined within one aerosol layer. This finding was also reported by *Burton et al.* [2013], who, in addition, said that the detection algorithm of CALIOP was not

designed to separate aerosol by type and could fail to identify different aerosol types within a column.

Within the literature only few systematic studies of the aerosol subtyping by CALIPSO are available [e.g., *Schuster et al.*, 2012; *Burton et al.*, 2013]. They show similar results and suggest that the CALIOP scheme is successful for about 70% of the cases. Best agreement was found for dust. Difficulties were found for aerosol layers dominated by the fine mode [*Mielonen et al.*, 2009].

As it could be demonstrated within this study, the classification of smoke and pollution aerosol is critical, since the only differentiating factor for these two aerosol types within the CALIPSO classification scheme is the height of the observed aerosol layer. In case the aerosol layer is elevated, it is classified by CALIPSO as smoke, otherwise it is typed as pollution aerosol. It was shown that a multitude of elevated aerosol layers that contained pollution were wrongly classified as containing smoke. Consequently, that leads to an overestimation of smoke and underestimation of pollution aerosol by CALIOP. Another implication of this misclassification is that the respective lidar ratio that is selected for the data retrieval is higher for smoke than for pollution. Accordingly, the retrieved extinction coefficient might be too large and the single-scattering albedo selected for radiative-transfer calculations too small, which leads to an overestimation of the warming effect of the respective aerosol layer. The same effect is caused by the classification of mixtures of dust and marine aerosol as polluted dust. The classification is based on the lower depolarization compared to aerosol layers of pure dust. The respective lidar ratio for polluted dust is reasonable for mixtures of dust with pollution or smoke, but too high for mixtures of dust and marine aerosol resulting in an overestimation of the warming effect of the respective aerosol layers. This overestimation of the warming effect has to be kept in mind for simulations of the global aerosol radiative effect based on CALIPSO data, which were presented by, e.g., *Oikawa et al.* [2013] and *Winker et al.* [2015]. The authors showed that the aerosol direct radiative effect is less negative when the distribution of aerosols above clouds provided by vertically resolved CALIPSO measurements are considered in radiative-transfer simulations.

Chapter 7

Summary and Outlook

Aerosols show type-specific characteristics, which depend on intensive aerosol optical and microphysical properties that influence the radiation processes in the atmosphere in various ways. The classification of aerosols and the characterization of the vertical aerosol distribution is needed in radiative-transfer simulations. Especially, the classification regarding absorbing aerosols and the distinction of coarse- and fine-mode particles is required for the optimization of calculations of the Earth's radiation budget. Climate-relevant optical properties that are needed in such models are aerosol optical depth and aerosol extinction coefficient. Both can be derived from multiwavelength aerosol lidar measurements without further assumptions of aerosol type. Subsequent analyses of the origin of the observed aerosol layers enable the relation of measured optical parameters to the respective aerosol type. Measured aerosol type-specific properties are summarized in aerosol classification models to account for type-dependent scattering and absorption characteristics of different aerosol species. Those aerosol classification models are used in radiative-transfer simulations, in processing schemes of passive measurements and, e.g., in retrievals of spaceborne lidars, but also for the development of algorithms that allow the determination of different aerosol types on-line or at least in near-real time.

The present work provides an overview of different possibilities for an aerosol classification and aerosol types that can be observed over Europe. Former aerosol classification studies were summarized. Representative values for aerosol-type-dependent parameters were verified based on multiwavelength lidar measurements from ground-based EARLINET stations. For this thesis 240 measurements of selected EARLINET stations performed in the years 2008 to 2010 were searched for the presence of aerosol layers. More than 700 aerosol layers were found by applying the derivative method as explained in Section 5.1.1.

For each aerosol layer mean optical properties of, e.g., the lidar ratio and Ångström exponents were calculated. The respective aerosol source region and, hence, the aerosol

type was determined by an in-depth investigation of the source region and transport pattern of each individual aerosol layer. For that purpose, a set of different auxiliary data and tools (transport and trajectory models, and other observational data), especially the transport model FLEXPART [Stohl *et al.*, 1998; Stohl and Thomson, 1999; Stohl *et al.*, 2005], were used to locate possible aerosol source regions.

The aerosol classification was carried out for marine, dust, pollution, continental, and biomass-burning (smoke) aerosol. These aerosol types are similar to those of the CALIPSO aerosol classification scheme in order to allow validation studies. In addition, not only polluted dust, which is the only mixture contained in the CALIPSO typing scheme, but also other mixtures of the pure aerosol types were considered.

The statistical evaluation of EARLINET measurements was performed for the pure aerosol types and frequently observed aerosol mixtures. In 38% of the cases a pure aerosol type was assigned, whereas in 62% a mixing of different aerosol types could not be ruled out. The majority of the pure aerosol types was classified as polluted continental aerosol (38%). 18%, 17%, 10%, and 8% of the layers of the pure-type fraction were identified as clean continental aerosol, desert dust, smoke, and volcanic aerosols, respectively. Clean marine conditions were found for 3% (i.e., 1.1% of all layers) only. 6% of the layers of the pure-type fraction were detected in the stratosphere. In addition, all kinds of mixtures of pure tropospheric aerosol types occurred over Europe throughout the investigated period. Predominantly, mixed aerosol layers contained pollution and/or dust. The mixture of dust, marine, and pollution aerosol was most frequently obtained (28%), followed by the mixtures of marine and pollution (19%) as well as dust and marine aerosols (14%), which can be explained with the large number of measurements contributed by stations in the Mediterranean region. The frequency of occurrence of aerosol types for observations cleared from aerosol originating from volcanic events showed similar results. It is noteworthy that generally clean marine aerosol was seldomly identified, but a marine influence could not be ruled out for more than half (54%) of the analyzed aerosol layers.

Investigations of the vertical extent of aerosol layers of dust, continental, pollution, and smoke aerosol and frequently observed aerosol mixtures confirmed expected results. Dust layers and mixtures with dust were situated at about 3 km height and above, whereas pollution and mixtures containing marine and pollution aerosol were found in lower heights. The frequency of occurrence of aerosol types for selected EARLINET stations represented the geographical distribution of the considered stations. Observations of stations near coastlines were influenced by marine aerosol. Mainly the Southern European stations showed the influence of desert dust. At continental sites predominantly pollution and especially at Southeastern European stations also smoke was observed.

Mean optical properties of pure aerosol types derived within this study showed highest

lidar ratios and Ångström exponents for smoke, indicating small and highly absorbing particles, followed by the values for pollution. Lidar ratios for smoke were 74 ± 16 sr and 77 ± 14 sr and for pollution 68 ± 14 sr and 64 ± 14 sr at 355 and 532 nm, respectively. For smoke and pollution backscatter-related Ångström exponents of the order of 1.5 for 355–532 nm, around 1.2 for 532–1064 nm, and around 1.35 for 355–1064 nm were found, respectively. The dust lidar ratios were 60 ± 12 sr and 57 ± 8 sr at 355 and 532 nm, respectively. Ångström exponents for dust and marine aerosol were ≤ 0.5 . Mean and median values for aerosol mixtures clearly showed the influence of the different pure aerosol types. Highest lidar ratios and Ångström exponents were normally found for mixtures containing smoke or pollution, indicating small and highly absorbing particles. When marine aerosols contributed to the mixture, the lidar ratios as well as the Ångström exponents were decreased. Smallest values of the extinction-related Ångström exponent of 0.4 and of the backscatter-related Ångström exponent of 0.73 for 355–532 nm were found for the mixture of dust and marine aerosol, where both components contributed with relatively large particles.

This study shows that there were mainly mixtures of aerosol and not only pure types present in the atmosphere over the European continent. It was illustrated that these aerosol mixtures can be regarded as external mixtures, for which individual properties of the constituents are preserved, when air masses cross different source regions. Obviously, other mechanisms that affect aerosol intensive parameters like humidification of aerosol, aging and deposition during transport, and internal mixing are of minor importance. This information is of value for model simulations of the aerosol radiative forcing and for the development of algorithms for satellite data retrievals. If the internal mixing can be neglected, probability density functions can be used to describe the state of mixing of the aerosol, i.e., “trajectories” between pure aerosol types can be defined in a multi-dimensional parameter space on which the mixtures occur. Mixtures of different aerosol types can be simulated by composing modes from the pure aerosol types.

A disadvantage of ground-based measurements is their incapability to deliver information on a global scale, especially over the oceans, whereas satellite measurements supply a global coverage of the Earth. Current lidar measurements from space are provided by CALIOP onboard CALIPSO and further missions are planned. While CALIOP is operating at 532 nm and 1064 nm, future ESA Earth Explorer Missions, namely ADM-Aeolus and EarthCARE, will deliver information at 355 nm with high-spectral-resolution lidars. The harmonization of these global observations from space poses a challenge due to the use of different lidar instrument types, observations at different wavelengths, and different measured parameters. So-called wavelength conversion factors like color ratios are needed.

Nevertheless, threshold values to distinguish small and highly absorbing particles

(higher lidar ratio, smaller color ratio) from coarser and less-absorbing particles (smaller lidar ratio, higher color ratio) were introduced within this thesis. The major conclusion of the presented investigations is that it is possible to apply a common aerosol typing scheme to CALIOP and AT Lidar data and, thus, to harmonize the long-term observations with both instruments by applying respective conversion factors, as derived in this study. It was shown that the color ratio (i.e., CALIOP-like instruments) is helpful to distinguish aerosols with a strong coarse particle mode (dust and marine aerosol) from aerosols with a dominating fine particle mode (smoke and pollution). The extinction-related 532-to-355-nm color ratio was 0.87 ± 0.15 for dust compared to 0.57 ± 0.07 and 0.53 ± 0.09 for smoke and pollution. The backscatter-related 532-to-355-nm color ratio was 0.94 ± 0.19 for dust compared to 0.55 ± 0.07 for both pollution as well as smoke. The backscatter-related 1064-to-355-nm color ratio was 0.61 ± 0.16 for dust compared to 0.24 ± 0.03 and 0.23 ± 0.06 for smoke and pollution aerosol. The lidar ratios (i.e., AT Lidar-like instruments) of different aerosol types were spread a bit more, but were not clearly separated from each other. A lidar ratio of 60.0 ± 11.7 sr was observed for dust, whereas lidar ratios of 67.6 ± 13.5 sr and 74.0 ± 15.5 sr were determined for pollution and smoke at 355 nm, respectively. Thus, it is very important to consider the particle depolarization ratio as an additional intensive parameter to achieve better results of the aerosol classification. Values for the particle linear depolarization ratio used within this thesis were taken from the literature due to the lack of data from the present study. It was illustrated that with both lidar types primarily three groups of aerosols can be clearly discriminated: dust (and ash, not shown), marine aerosol, and pollution/smoke based on the respective intensive particle properties backscatter-related color ratio (1064/532 nm), lidar ratio (at 355 nm), and particle linear depolarization ratio (at 532 nm). A clear discrimination of pollution and smoke is difficult. Here, it is noteworthy that smoke and pollution properties are quite variable and that only mean values for Europe are shown.

Optical properties of pure aerosol types and aerosol mixtures derived within this study agree well with findings of former studies [e.g., Müller *et al.*, 2007a; Burton *et al.*, 2012; Groß *et al.*, 2013, 2015]. The dominance of external mixtures as found in this work was similarly reported by Groß *et al.* [2013]. In addition, Burton *et al.* [2014] presented studies that implied the application of external mixtures.

In a further step, the detected aerosol layers and the determined aerosol type of EARLINET observations were used to validate the feature classification and the aerosol subtype provided by the automatic CALIPSO classification scheme. For this purpose, only those ground-based network measurements of EARLINET were chosen for which the satellite overpass was at maximum 100 km away from the EARLINET lidar site. Consequently, the comparison was performed for 342 aerosol layers, which are called EARLINET aerosol layers. The heights of the EARLINET aerosol layers

served as lower and upper limits of each aerosol layer, which was investigated within the CALIOP data subset. The following critical points have to be considered: the performed aerosol classification has some inherent subjectivity and even selecting the best spatial and temporal matches of satellite and ground-based observation does not provide an unequivocal guarantee that both instruments are measuring the same air mass.

Nevertheless, for almost 50% of all cases the same aerosol type was similarly classified by the CALIPSO typing scheme. Best agreement was found for EARLINET aerosol layers that were labeled as mixtures of dust with further constituents. CALIPSO classified 44.7% of those aerosol layers as polluted dust and 43.0% as pure dust. In general, polluted dust is the aerosol type that was mostly classified by CALIPSO including also aerosol layers that contain marine aerosol. Relatively poor agreement was found for aerosol layers that were labeled as clean continental and pollution. The CALIPSO classification of smoke and pollution aerosol is critical, since the only differentiating factor for these two aerosol types within the CALIPSO classification scheme is the height of the observed aerosol layer. It was shown that a multitude of elevated aerosol layers that contained pollution were wrongly classified by CALIPSO as containing smoke. Consequently, that leads to an overestimation of smoke and an underestimation of pollution aerosol by CALIOP and, furthermore, to an overestimation of the warming effect of the wrongly typed aerosol layer. In addition, the classification of polluted dust for aerosol mixtures that contain also marine aerosol and, thus, the selection of too high lidar ratios for the data retrieval and the underestimation of the single-scattering albedo lead to an overestimation of the warming effect of the respective aerosol layers. This overestimation of the warming effect has to be kept in mind for simulations of the global aerosol radiative effect based on CALIPSO data, which were presented by, e.g., *Oikawa et al.* [2013] and *Winker et al.* [2015]. The authors showed that the aerosol direct radiative effect is less negative when the distribution of aerosols above clouds provided by vertically resolved CALIPSO measurements are considered in radiative-transfer simulations.

In the framework of the ESA–CALIPSO project the results of this work were stored in a long-term aerosol and cloud database, which already served as a valuable tool for a variety of investigations. The database has been used in VRAME (Vertically Resolved Aerosol Model for Europe from a Synergy of EARLINET and AERONET data) to derive characteristic aerosol optical properties for an aerosol model used for atmospheric corrections in ocean-color retrievals [*Wandinger et al.*, 2011]. The database as well as other results from the present study have also been made available for LIVAS (cf. Chapter 1) [*Amiridis et al.*, 2015]. Cases from the ESA–CALIPSO database have been used in addition to other EARLINET data sets to train a neural network for aerosol typing from optical data [*Nicolae et al.*, 2015].

Bibliography

- Ackermann, J. (1998), The Extinction-to-Backscatter Ratio of Tropospheric Aerosol: A Numerical Study, *J. Atmos. Ocean. Tech.*, *15*, 1043–1050, doi:10.1175/1520-0426(1998)015<1043:TETBRO>2.0.CO;2.
- Alados-Arboledas, L., D. Müller, J. L. Guerrero-Rascado, F. Navas-Guzmán, D. Pérez-Ramírez, and F. J. Olmo (2011), Optical and microphysical properties of fresh biomass burning aerosol retrieved by Raman lidar, and star-and sun-photometry, *Geophys. Res. Lett.*, *38*, doi:10.1029/2010GL045999.
- Allen, C. J. T., R. Washington, and S. Engelstaedter (2013), Dust emission and transport mechanisms in the central Sahara: Fennec ground-based observations from Bordj Badji Mokhtar, June 2011, *J. Geophys. Res.-Atmos.*, *118*, 6212–6232, doi:10.1002/jgrd.50534.
- Amiridis, V., D. S. Balis, S. Kazadzis, A. Bais, E. Giannakaki, A. Papayannis, and C. Zerefos (2005), Four-year aerosol observation with a Raman lidar at Thessaloniki, Greece, in the framework of the European Aerosol Research Lidar Network (EARLINET), *J. Geophys. Res.*, *110*, doi:10.1029/2004GL019881.
- Amiridis, V., D. S. Balis, E. Giannakaki, A. Stohl, S. Kazadzis, M. E. Koukouli, and P. Zanis (2009), Optical characteristics of biomass burning aerosols over Southeastern Europe determined from UV-Raman lidar measurements, *Atmos. Chem. Phys.*, *9*, 2431–2440, doi:10.5194/acp-9-2431-2009.
- Amiridis, V., U. Wandinger, E. Marinou, E. Giannakaki, A. Tsekeri, S. Basart, S. Kazadzis, A. Gkikas, M. Taylor, J. M. Baldasano, and A. Ansmann (2013), Optimizing CALIPSO Saharan dust retrievals, *Atmos. Chem. Phys.*, *13*, 12089–12106, doi:10.5194/acp-13-12089-2013.
- Amiridis, V., E. Marinou, A. Tsekeri, U. Wandinger, A. Schwarz, E. Giannakaki, R. Mamouri, P. Kokkalis, I. Biniotoglou, S. Solomos, T. Herekakis, S. Kazadzis, E. Gerasopoulos, E. Proestakis, M. Kottas, D. Balis, A. Papayannis, C. Kontoes,
-

- K. Kourtidis, N. Papagiannopoulos, L. Mona, G. Pappalardo, O. Le Rille, and A. Ansmann (2015), LIVAS: a 3-D multi-wavelength aerosol/cloud database based on CALIPSO and EARLINET, *Atmos. Chem. Phys.*, *15*, 7127–7153, doi:10.5194/acp-15-7127-2015.
- Anderson, T. L., S. J. Masonis, D. S. Covert, N. C. Ahlquist, S. G. Howell, A. D. Clarke, and C. S. McNaughton (2003), Variability of aerosol optical properties derived from in situ aircraft measurements during ACE-Asia, *J. Geophys. Res.*, *108*, doi:10.1029/2002JD003247.
- Ångström, A. (1964), The parameters of atmospheric turbidity, *Tellus*, *16*, 64–75, doi:10.1111/j.2153-3490.1964.tb00144.x.
- Ansmann, A., and D. Müller (2005), Lidar and atmospheric aerosol particles, in *Lidar: Range-Resolved Optical Remote Sensing of the Atmosphere*, edited by C. Weitkamp, pp. 105–141, Springer, New York.
- Ansmann, A., M. Riebesell, and C. Weitkamp (1990), Measurement of atmospheric aerosol extinction profiles with a Raman lidar, *Opt. Lett.*, *15*, 746–748, doi:10.1364/OL.15.000746.
- Ansmann, A., M. Riebesell, U. Wandinger, C. Weitkamp, E. Voss, W. Lahmann, and W. Michaelis (1992a), Combined Raman Elastic–Backscatter LIDAR for Vertical Profiling of Moisture, Aerosol Extinction, Backscatter, and LIDAR Ratio, *Appl. Phys. B*, *55*, 18–28, doi:10.1007/BF00348608.
- Ansmann, A., U. Wandinger, M. Riebesell, C. Weitkamp, and W. Michaelis (1992b), Independent measurement of extinction and backscatter profiles in cirrus clouds by using a combined Raman elastic-backscatter lidar, *Appl. Opt.*, *31*, 7113–7131, doi:10.1364/AO.31.007113.
- Ansmann, A., I. Mattis, U. Wandinger, F. Wagner, J. Reichardt, and T. Deshler (1997), Evolution of the Pinatubo aerosol: Raman lidar observations of particle optical depth, effective radius, mass, and surface area over central Europe at 53.4° N, *J. Atmos. Sciences*, *54*, 2630–2641, doi:10.1175/1520-0469(1997)054<2630:EOTPAR>2.0.CO;2.
- Ansmann, A., F. Wagner, D. Althausen, D. Müller, A. Herber, and U. Wandinger (2001), European pollution outbreaks during ACE 2: Lofted aerosol plumes observed with Raman lidar at the Portuguese coast, *J. Geophys. Res.*, *106*, 20,725–20,733, doi:10.1029/2000JD000091.
-

- Ansmann, A., F. Wagner, D. Müller, D. Althausen, A. Herber, W. v. Hoyningen-Huene, and U. Wandinger (2002), European pollution outbreaks during ACE 2: Optical particle properties inferred from multiwavelength lidar and star/Sun photometry, *J. Geophys. Res.*, *107*, doi:10.1029/2001JD001109.
- Ansmann, A., J. Bösenberg, A. Chaikovsky, A. Comerón, S. Eckhardt, R. Eixmann, V. Freudenthaler, P. Ginoux, L. Komguem, H. Linné, M. Á. L. Márquez, V. Matthias, I. Mattis, V. Mitev, D. Müller, S. Music, S. Nickovic, J. Pelon, L. Sauvage, P. Sobolewsky, M. K. Srivastava, A. Stohl, O. Torres, G. Vaughan, U. Wandinger, and M. Wiegner (2003), Long-range transport of Saharan dust to northern Europe: The 11–16 October 2001 outbreak observed with EARLINET, *J. Geophys. Res.*, *108*, doi:10.1029/2003JD003757.
- Ansmann, A., R. Engelmann, D. Althausen, U. Wandinger, M. Hu, Y. Zhang, and Q. He (2005), High aerosol load over the Pearl River Delta, China, observed with Raman lidar and Sun photometer, *Geophys. Res. Letts.*, *32*, doi:10.1029/2005GL023094.
- Ansmann, A., U. Wandinger, O. Le Rille, D. Lajas, and A. G. Straume (2006), Particle backscatter and extinction profiling with the spaceborne high-spectral-resolution Doppler lidar ALADIN: methodology and simulations, *Appl. Opt.*, *46*, 6606–6622, doi:10.1364/AO.46.006606.
- Ansmann, A., H. Baars, M. Tesche, D. Müller, D. Althausen, R. Engelmann, T. Pauliquevis, and P. Artaxo (2009), Dust and smoke transport from Africa to South America: Lidar profiling over Cape Verde and the Amazon rainforest, *Geophys. Res. Lett.*, *36*, doi:10.1029/2009GL037923.
- Ansmann, A., M. Tesche, S. Groß, V. Freudenthaler, P. Seifert, A. Hiebsch, J. Schmidt, U. Wandinger, I. Mattis, D. Müller, and M. Wiegner (2010), The 16 April 2010 major volcanic ash plume over central Europe: EARLINET lidar and AERONET photometer observations at Leipzig and Munich, Germany, *Geophys. Res. Letts.*, *37*, doi:10.1029/2010GL043809.
- Ansmann, A., A. Petzold, K. Kandler, I. Tegen, M. Wendisch, D. Müller, B. Weinzierl, T. Müller, and J. Heintzenberg (2011a), Saharan Mineral Dust Experiments SAMUM-1 and SAMUM-2: what have we learned?, *Tellus B*, *63*, 403–429, doi:10.1111/j.1600-0889.2011.00555.x.
- Ansmann, A., M. Tesche, P. Seifert, S. Groß, V. Freudenthaler, A. Apituley, K. M. Wilson, I. Serikov, H. Linné, B. Heinold, A. Hiebsch, F. Schnell, J. Schmidt, I. Mat-
-

- tis, U. Wandinger, and M. Wiegner (2011b), Ash and fine-mode particle mass profiles from EARLINET-AERONET observations over central Europe after the eruptions of the Eyjafjallajökull volcano in 2010, *J. Geophys. Res.-Atmos.*, *116*, doi:10.1029/2010JD015567.
- Ansmann, A., P. Seifert, M. Tesche, and U. Wandinger (2012), Profiling of fine and coarse particle mass: case studies of Saharan dust and Eyjafjallajökull/Grimsvötn volcanic plumes, *Atmos. Chem. Phys.*, *12*, 9399–9415, doi:10.5194/acp-12-9399-2012.
- Ansmann, A., D. Althausen, T. Kanitz, R. Engelmann, A. Skupin, H. Baars, A. Klepel, M. Haarig, B. Heinold, I. Tegen, C. Toledano, D. Prescod, and D. Farrell (2014), Saharan dust longrange transport: SALTRACE lidar observations at Barbados and aboard RV Meteor (Guadeloupe to Cape Verde) versus dust transport modelling, Proceedings, DUST 2014 - International Conference on Atmospheric Dust, Castelana Marina, Italy, 1-6 June 2014.
- Baars, H., A. Ansmann, R. Engelmann, and D. Althausen (2008), Continuous monitoring of the boundary-layer top with lidar, *Atmos. Chem. Phys.*, *8*, 7281–7296, doi:10.5194/acp-8-7281-2008.
- Baars, H., A. Ansmann, D. Althausen, R. Engelmann, P. Artaxo, T. Pauliquevis, and R. Souza (2011), Further evidence for significant smoke transport from Africa to Amazonia, *Geophys. Res. Lett.*, *38*, doi:10.1029/2011GL049200.
- Baars, H., A. Ansmann, D. Althausen, R. Engelmann, B. Heese, D. Müller, P. Artaxo, M. Paixao, T. Pauliquevis, and R. Souza (2012), Aerosol profiling with lidar in the Amazon Basin during the wet and dry season, *J. Geophys. Res.-Atmos.*, *117*, doi:10.1029/2012JD018338.
- Baars, H., P. Seifert, and U. Wandinger (2015), Aerosol and cloud typing with an automated 24/7 aerosol lidar, in *European Geosciences Union (EGU) General Assembly 2015 Vienna (Austria), 12–17 April, Session: AS3.17/GI2.2 Lidar and Applications*, vol. 17, EGU2015-9081.
- Balis, D. S., V. Amiridis, C. Zerefos, E. Gerasopoulos, M. Andreae, P. Zanis, A. Kazantzidis, S. Kazadzis, and A. Papayannis (2003), Raman lidar and sunphotometric measurements of aerosol optical properties over Thessaloniki, Greece, during a biomass burning episode, *Atmos. Env.*, *37*, 4529–4538, doi:10.1016/S1352-2310(03)00581-8.
-

- Barrie, L. A., and R. M. Hoff (1985), Five years of air chemistry observations in the Canadian Arctic, *Atmos. Env.*, *19*, 1995–2010, doi:10.1016/0004-6981(85)90108-8.
- Basart, S., C. Pérez, S. Nickovic, E. Cuevas, and J. M. Baldasano (2012), Development and evaluation of the BSC-DREAM8b dust regional model over Northern Africa, the Mediterranean and the Middle East, *Tellus B*, *64*, 1-23, doi:10.3402/tellusb.v64i0.18539.
- Biniotoglou, I., S. Basart, L. Alados-Arboledas, V. Amiridis, A. Argyrouli, H. Baars, J. M. Baldasano, D. Balis, L. Belegante, J. A. Bravo-Aranda, P. Burlizzi, V. Carrasco, A. Chaikovsky, A. Comerón, G. D’Amico, M. Filioglou, M. J. Granados-Muñoz, J. L. Guerrero-Rascado, L. Ilic, P. Kokkalis, A. Maurizi, L. Mona, F. Monti, C. Muñoz-Porcar, D. Nicolae, A. Papayannis, G. Pappalardo, G. Pejanovic, S. N. Pereira, M. R. Perrone, A. Pietruczuk, M. Posyniak, F. Rocadenbosch, A. Rodríguez-Gómez, M. Sicard, N. Siomos, A. Szkop, E. Terradellas, A. Tsekeri, A. Vukovic, U. Wandinger, and J. Wagner (2015), A methodology for investigating dust model performance using synergistic EARLINET/AERONET dust concentration retrievals, *Atmos. Meas. Tech. Discuss.*, *8*, 3605–3666, doi:10.5194/amtd-8-3605-2015.
- Bissonnette, L. R. (1986), Sensitivity analysis of lidar inversion algorithm, *Appl. Opt.*, *25*, 2112–2125, doi:10.1364/AO.25.002122.
- Böckmann, C. (2001), Hybrid regularization method for the ill-posed inversion of multiwavelength lidar data in the retrieval of aerosol size distributions, *Appl. Opt.*, *40*, 1329–1342, doi:10.1364/AO.40.001329.
- Böckmann, C., U. Wandinger, A. Ansmann, J. Bösenberg, V. Amiridis, A. Boselli, A. Delaval, F. De Tomasi, M. Frioud, I. V. Grigorov, A. Hågård, M. Horvat, M. Iarlori, L. Komguem, S. Kreipl, G. Larchevêque, V. Matthias, A. Papayannis, G. Pappalardo, F. Rocadenbosch, J. A. Rodriguez, J. Schneider, V. Shcherbakov, and M. Wiegner (2004), Aerosol lidar intercomparison in the framework of the EARLINET project. 2. Aerosol backscatter algorithms, *Appl. Opt.*, *43*, 977–989, doi:10.1364/AO.43.000977.
- Bösenberg, J., A. Ansmann, J. M. Baldasano, D. Balis, C. Böckmann, B. Calpini, A. Chaikovsky, P. Flamant, A. Hågård, V. Mitev, A. Papayannis, J. Pelon, D. Resendes, J. Schneider, N. Spinelli, T. Trickl, G. Vaughan, G. Visconti, and M. Wiegner (2001), EARLINET: A European Aerosol Research Lidar Network, in *Laser remote sensing of the atmosphere, Selected papers of the 20th International Laser Radar Conference, Vichy, France*, edited by A. Dabas, C. Loth, and J. Pelon, pp. 155–158, École Polytechnique, Paris, France.
-

- Bösenberg, J., V. Matthias, A. Amodeo, V. Amoiridi, A. Ansmann, J. M. Baldasano, I. Balin, D. Balis, C. Böckmann, A. Boselli, G. Carlson, A. Chaikovsky, G. Chourdakis, A. Comerón, F. De Tomasi, R. Eixmann, V. Freudenthaler, H. Giehl, I. Grigorov, A. Hågård, M. Iarlori, A. Kirsche, G. Kolarov, L. Komguem, S. Kreipl, W. Kumpf, G. Larchevêque, H. Linné, R. Matthey, I. Mattis, L. Mona, D. Müller, S. Music, S. Nickovic, M. Pandolfi, A. Papayannis, G. Pappalardo, J. Pelon, C. Pérez, R. M. Perrone, R. Persson, D. P. Resendes, V. Rizi, R. Roca-denbosch, J. A. Rodriguez, L. Sauvage, L. Schneidenbach, R. Schumacher, V. Shcherbakov, V. Simeonov, P. Sobolewsky, N. Spinelli, I. Stachlewska, D. Stoyanov, T. Trickl, G. Tsaknakis, G. Vaughan, U. Wandinger, X. Wang, M. Wiegner, M. Zavrtnik, and C. Zerefos (2003), EARLINET: A European Aerosol Research Lidar Network to Establish an Aerosol Climatology, Report No. 348, *Tech. rep.*, Max Planck Institute for Meteorology, Hamburg, Germany, Url: http://www.mpimet.mpg.de/fileadmin/publikationen/Reports/max_scirep_348.pdf.
- Bridhikitti, A. (2013), Atmospheric aerosol layers over Bangkok Metropolitan Region from CALIPSO observations, *Atmos. Res.*, *127*, 1–7, doi:10.1016/j.atmosres.2013.02.008.
- Brooks, I. M. (2003), Finding Boundary Layer Top: Application of a Wavelet Covariance Transform to Lidar Backscatter Profiles, *J. Atmos. Ocean. Tech.*, *20*, 1092–1105, doi:10.1175/1520-0426(2003)020<1092:FBLTAO>2.0.CO;2.
- Bucholtz, A. (1995), Rayleigh–scattering calculations for the terrestrial atmosphere, *Appl. Opt.*, *34*, 2765–2773, doi:10.1364/AO.34.002765.
- Burton, S. P., R. A. Ferrare, C. A. Hostetler, J. W. Hair, C. Kittaka, M. A. Vaughan, M. D. Obland, R. R. Rogers, A. L. Cook, D. B. Harper, and L. A. Remer (2010), Using airborne high spectral resolution lidar data to evaluate combined active plus passive retrievals of aerosol extinction profiles, *J. Geophys. Res.-Atmos.*, *115*, doi:10.1029/2009JD012130.
- Burton, S. P., R. A. Ferrare, C. A. Hostetler, J. W. Hair, R. R. Rogers, M. D. Obland, C. F. Butler, A. L. Cook, D. B. Harper, and K. D. Froyd (2012), Aerosol classification using airborne High Spectral Resolution Lidar measurements – methodology and examples, *Atmos. Meas. Tech.*, *5*, 73–98, doi:10.5194/amt-5-73-2012.
- Burton, S. P., R. A. Ferrare, M. A. Vaughan, A. H. Omar, R. R. Rogers, C. A. Hostetler, and J. W. Hair (2013), Aerosol classification from airborne HSRL and comparisons with the CALIPSO vertical feature mask, *Atmos. Meas. Tech.*, *6*, 1397–1412, doi:10.5194/amt-6-1397-2013.
-

- Burton, S. P., M. A. Vaughan, R. A. Ferrare, and C. A. Hostetler (2014), Separating mixtures of aerosol types in airborne High Spectral Resolution Lidar data, *Atmos. Meas. Tech.*, *7*, 419–436, doi:10.5194/amt-7-419-2014.
- Campbell, J. R., J. S. Reid, D. L. Westphal, J. Zhang, J. L. Tackett, B. N. Chew, E. J. Welton, A. Shimizu, N. Sugimoto, K. Aoki, and D. M. Winker (2013), Characterizing the vertical profile of aerosol particle extinction and linear depolarization over Southeast Asia and the Maritime Continent: The 2007–2009 view from CALIOP, *Atmos. Res.*, *122*, 520–543, doi:10.1016/j.atmosres.2012.05.007.
- Catrrall, C., J. Reagan, K. Thome, and O. Dubovik (2005), Variability of aerosol and spectral lidar and backscatter and extinction ratios of key aerosol types derived from selected Aerosol Robotic Network locations, *J. Geophys. Res.*, *110*, doi:10.1029/2004JD005124.
- Chaikovsky, A., O. Dubovik, P. Goloub, N. Balashevich, A. Lopatsin, Y. Karol, S. Denisov, and T. Lapyonok (2008), Software package for the retrieval of aerosol microphysical properties in the vertical column using combined lidar/photometer data (test version), *Tech. rep.*, Institute of Physics, National Academy of Sciences of Belarus, Minsk, Belarus.
- Chaikovsky, A., O. Dubovik, P. Goloub, D. Tanré, G. Pappalardo, U. Wandinger, L. Chaikovskaya, S. Denisov, Y. Grudo, A. Lopatsin, Y. Karol, T. Lapyonok, M. Korol, F. Osipenko, D. Savitski, A. Slesar, A. Apituley, L. A. Arboledas, I. Biniotoglou, P. Kokkalis, M. J. Granados-Muñoz, A. Papayannis, M. R. Perrone, A. Pietruczuk, G. Pisani, F. Rocadenbosch, M. Sicard, F. De Tomasi, J. Wagner, and X. Wang (2012), Algorithm and software for the retrieval of vertical aerosol properties using combined lidar/ radiometer data: Dissemination in EARLINET, pp. 399–402, Proceedings of the 26th International Laser and Radar Conference, vol. 1, Porto Heli, Greece, 25–29 June 2012.
- Dahlkötter, F., M. Gysel, D. Sauer, A. Minikin, R. Baumann, P. Seifert, A. Ansmann, M. Fromm, C. Voigt, and B. Weinzierl (2014), The Pagami Creek smoke plume after long-range transport to the upper troposphere over Europe - aerosol properties and black carbon mixing state, *Atmos. Chem. Phys.*, *14*, 6111–6137, doi:10.5194/acp-14-6111-2014.
- David, G., B. Thomas, T. Nousiainen, A. Miffré, and P. Rairoux (2013), Retrieving simulated volcanic, desert dust and sea-salt particle properties from two/three-component particle mixtures using UV-VIS polarization lidar and T matrix, *Atmos. Chem. Phys.*, *13*, 6757–6776, doi:10.5194/acp-13-6757-2013.
-

- Dawson, K. W., N. Meskhidze, D. Josset, and S. Gassó (2015), Spaceborne observations of the lidar ratio of marine aerosols, *Atmos. Chem. Phys.*, *15*, 3241–3255, doi:10.5194/acp-15-3241-2015.
- De Tomasi, F., A. Blanco, and M. R. Perrone (2003), Raman lidar monitoring of extinction and backscattering of African dust layers and dust characterization, *Appl. Opt.*, *42*, 1699–1709, doi:10.1364/AO.42.001699.
- De Tomasi, F., A. M. Tafuro, and M. R. Perrone (2006), Height and seasonal dependence of aerosol optical properties over southeast Italy, *J. Geophys. Res.*, *111*, doi:10.1029/2005JD006779.
- Deepak, A., and H. E. Gerber (1983), Report of the experts meeting on aerosols and their climatic effects, *Tech. Rep. WCP-55*, 107 pp., World Meteorological Organization.
- Diner, D. J., R. T. Menzies, R. A. Kahn, T. L. Anderson, J. Bösenberg, R. J. Charlson, B. N. Holben, C. A. Hostetler, M. A. Miller, J. A. Ogren, G. L. Stephens, O. Torres, B. A. Wielicki, P. J. Rasch, L. D. Travis, and W. D. Collins (2004), Using the PARAGON Framework to Establish an Accurate, Consistent, and Cohesive Long-Term Aerosol Record, *Bull. American Meteorol. Soc.*, *85*, 1535–1548, doi:10.1175/BAMS-85-10-1535.
- Draxler, R. R. (2003), Evaluation of an Ensemble Dispersion Calculation, *J. Appl. Meteor.*, *42*, 308–317, doi:10.1175/1520-0450(2003)042<0308:EOAEDC>2.0.CO;2.
- Draxler, R. R., and G. D. Hess (1997), Description of the HYSPLIT_4 modeling system, *Tech. rep.*, <http://www.arl.noaa.gov/ready/hysplit4.html>.
- Draxler, R. R., and G. D. Hess (1998), An overview of the HYSPLIT_4 modelling system for trajectories, dispersion and deposition, *Aust. Meteor. Mag.*, *47*, 295–308.
- Draxler, R. R., and G. D. Rolph (2014), HYSPLIT (HYbrid Single-Particle Lagrangian Integrated Trajectory). Model access via NOAA ARL READY website (<http://ready.arl.noaa.gov/HYSPLIT.php>) (last access: 9 July 2015), *NOAA Air Resources Laboratory, Silver Spring, MD*.
- Dubovik, O., B. N. Holben, T. F. Eck, A. Smirnov, Y. J. Kaufman, M. D. King, D. Tanré, and I. Slutsker (2002), Variability of Absorption and Optical Properties of Key Aerosol Types Observed in Worldwide Locations, *J. Atmos. Sciences*, *59*, 590–608, doi:10.1175/1520-0469(2002)059<0590:VOAAOP>2.0.CO;2.
-

- Dubovik, O., A. Sinyuk, T. Lapyonok, B. N. Holben, M. Mishchenko, P. Yang, T. F. Eck, H. Volten, O. Muñoz, B. Veihelmann, W. J. van der Zande, J.-F. Leon, M. Sorokin, and I. Slutsker (2006), Application of spheroid models to account for aerosol particle nonsphericity in remote sensing of desert dust, *J. Geophys. Res.-Atmos.*, *111*, doi:10.1029/2005JD006619.
- Dubovik, O., T. Lapyonok, Y. J. Kaufman, M. Chin, P. Ginoux, R. A. Kahn, and A. Sinyuk (2008), Retrieving global aerosol sources from satellites using inverse modeling, *Atmos. Chem. Phys.*, *8*, 209–250, doi:10.5194/acp-8-209-2008.
- Eck, T. F., B. N. Holben, J. S. Reid, O. Dubovik, A. Smirnov, N. T. O’Neill, I. Slutsker, and S. Kinne (1999), Wavelength dependence of the optical depth of biomass burning, urban, and desert dust aerosols, *J. Geophys. Res.*, *104*, 31,333–31,349, doi:10.1029/1999JD900923.
- Eloranta, E. W. (2005), High Spectral Resolution Lidar, in *Lidar: Range-Resolved Optical Remote Sensing of the Atmosphere*, edited by C. Weitkamp, pp. 143–163, Springer, New York, doi:10.1007/0-387-25101-4_5.
- Emanuel, K. A., and M. Živković-Rothman (1999), Development and Evaluation of a Convection Scheme for Use in Climate Models, *J. Atmos. Sciences*, *56*, 1766–1782, doi:10.1175/1520-0469(1999)056<1766:DAEOAC>2.0.CO;2.
- Esselborn, M., M. Wirth, A. Fix, M. Tesche, and G. Ehret (2008), Airborne high spectral resolution lidar for measuring aerosol extinction and backscatter coefficients, *Appl. Opt.*, *47*, 346–358, doi:10.1364/AO.47.000346.
- Esselborn, M., M. Wirth, A. Fix, B. Weinzierl, K. Rasp, M. Tesche, and A. Petzold (2009), Spatial distribution and optical properties of Saharan dust observed by airborne high spectral resolution lidar during SAMUM 2006, *Tellus B*, *61*, 131–143, doi:10.1111/j.1600-0889.2008.00394.x.
- Fernald, F. G. (1984), Analysis of atmospheric lidar observations: some comments, *Appl. Opt.*, *23*, 652–653, doi:10.1364/AO.23.000652.
- Fernald, F. G., B. M. Herman, and J. A. Reagan (1972), Determination of Aerosol Height Distributions by Lidar, *J. Appl. Meteor.*, *11*, 482–489, doi:10.1175/1520-0450(1972)011<0482:DOAHDB>2.0.CO;2.
- Fiebig, M., A. Petzold, U. Wandinger, M. Wendisch, C. Kiemle, A. Stifter, M. Ebert, T. Rother, and U. Leiterer (2002), Optical closure for an aerosol column: Method, accuracy, and inferable properties, applied to a biomass-burning aerosol and its radiative forcing, *J. Geophys. Res.*, *107*, doi:10.1026/2000JD000192.
-

- Fitzgerald, J. W. (1991), Marine aerosols: A review, *Atmos. Env.*, *25*, 533–545, doi:10.1016/0960-1686(91)90050-H.
- Flamant, C., J. Pelon, P. H. Flamant, and P. Durand (1997), Lidar Determination Of The Entrainment Zone Thickness At The Top Of The Unstable Marine Atmospheric Boundary Layer, *Boundary-Layer Meteorol.*, *83*, 247–284, doi:10.1023/A:1000258318944.
- Ford, B., and C. L. Heald (2012), An A-train and model perspective on the vertical distribution of aerosols and CO in the Northern Hemisphere, *J. Geophys. Res.-Atmos.*, *117*, doi:10.1029/2011JD016977.
- Forster, P., V. Ramaswamy, P. Artaxo, T. Berntsen, R. Betts, D. W. Fahey, J. Haywood, J. Lean, D. C. Lowe, G. Myhre, J. Nganga, R. Prinn, G. Raga, M. Schulz, and R. Van Dorland (2007), Changes in Atmospheric Constituents and in Radiative Forcing, in *Climate Change 2007: The Physical Science Basis, Contribution of Working Group I to the Fourth Assessment Report of the Intergovernmental Panel on Climate Change*, edited by S. Solomon, D. Qin, M. Manning, Z. Chen, M. Marquis, K. B. Averyt, M. Tignor, and H. L. Miller, Cambridge Univ. Press (<http://www.ipcc.ch>), Cambridge, UK and New York, NY, USA.
- Franke, K., A. Ansmann, D. Müller, D. Althausen, F. Wagner, and R. Scheele (2001), One-year observations of particle lidar ratio over the tropical Indian Ocean with Raman lidar, *Geophys. Res. Letts.*, *28*, 4559–4562, doi:10.1029/2001GL013671.
- Franke, K., A. Ansmann, D. Müller, D. Althausen, C. Venkataraman, M. S. Reddy, F. Wagner, and R. Scheele (2003), Optical properties of the Indo-Asian haze layer over the tropical Indian Ocean, *J. Geophys. Res.*, *108*, doi:10.1029/2002JD002473.
- Freudenthaler, V., M. Esselborn, M. Wiegner, B. Heese, M. Tesche, A. Ansmann, D. Müller, D. Althausen, M. Wirth, A. Fix, G. Ehret, P. Knippertz, C. Toledano, J. Gasteiger, M. Garhammer, and M. Seefeldner (2009), Depolarization ratio profiling at several wavelengths in pure Saharan dust during SAMUM 2006, *Tellus B*, *61*, 165–179, doi:10.1111/j.1600-0889.2008.00396.x.
- Gasteiger, J., M. Wiegner, S. Groß, V. Freudenthaler, C. Toledano, M. Tesche, and K. Kandler (2011), Modelling lidar-relevant optical properties of complex mineral dust aerosols, *Tellus B*, *63*, 725–741, doi:10.1111/j.1600-0889.2011.00559.x.
- Giannakaki, E., D. Balis, V. Amiridis, and C. Zerefos (2010), Optical properties of different aerosol types: seven years of combined Raman-elastic backscatter lidar
-

- measurements in Thessaloniki, Greece, *Atmos. Meas. Tech.*, *3*, 569–578, doi:10.5194/amt-3-569-2010.
- Giannakaki, E., E. Vraimaki, and D. Balis (2011), Validation of CALIPSO level-2 products using a ground based lidar in Thessaloniki, Greece, in *SPIE Remote Sensing*, pp. 818,215–818,215, International Society for Optics and Photonics.
- Giglio, L., J. Descloitres, C. O. Justice, and Y. J. Kaufman (2003), An Enhanced Contextual Fire Detection Algorithm for MODIS, *Remote Sens. Environ.*, *87*, 273–282, doi:10.1016/S0034-4257(03)00184-6.
- Gonzales, R. (1988), Recursive technique for inverting the lidar equation, *Appl. Opt.*, *27*, 2741–2745, doi:10.1364/AO.27.002741.
- Granados-Muñoz, M. J., R. F. Navas-Guzmán, J. A. Bravo-Aranda, J. L. Guerrero-Rascado, H. Lyamani, A. Valenzuela, G. Titos, J. Fernández-Gálvez, and L. Alados-Arboledas (2015), Hygroscopic growth of atmospheric aerosol particles based on active remote sensing and radiosounding measurements: selected cases in southeastern Spain, *Atmos. Meas. Tech.*, *8*, 705–718, doi:10.5194/amt-8-705-2015.
- Grigas, T., M. Hervo, G. Gimmetstad, H. Forrister, P. Schneider, J. Preißler, L. Tarra-son, and C. O’Dowd (2015), CALIOP near-real-time backscatter products compared to EARLINET data, *Atmos. Chem. Phys. Discuss.*, *15*, 6041–6075, doi:10.5194/acpd-15-6041-2015.
- Groß, S., J. Gasteiger, V. Freudenthaler, M. Wiegner, A. Geiß, A. Schladitz, C. Toledano, K. Kandler, M. Tesche, A. Ansmann, and A. Wiedensohler (2011a), Characterization of the planetary boundary layer during SAMUM-2 by means of lidar measurements, *Tellus B*, *63*, 695–705, doi:10.1111/j.1600-0889.2011.00557.x.
- Groß, S., M. Tesche, V. Freudenthaler, C. Toledano, M. Wiegner, A. Ansmann, D. Althausen, and M. Seefeldner (2011b), Characterization of Saharan dust, marine aerosols and mixtures of biomass-burning aerosols and dust by means of multi-wavelength depolarization and Raman lidar measurements during SAMUM 2, *Tellus B*, *63*, doi:10.1111/j.1600-0889.2011.00556.x.
- Groß, S., V. Freudenthaler, M. Wiegner, J. Gasteiger, A. Geiß, and F. Schnell (2012), Dual-wavelength linear depolarization ratio of volcanic aerosols: Lidar measurements of the Eyjafjallajökull plume over Maisach, Germany, *Atmos. Env.*, *48*, 85–96, doi:10.1016/j.atmosenv.2011.06.017.
-

- Groß, S., M. Esselborn, B. Weinzierl, M. Wirth, A. Fix, and A. Petzold (2013), Aerosol classification by airborne high spectral resolution lidar observations, *Atmos. Chem. Phys.*, *13*, 2487–2505, doi:10.5194/acp-13-2487-2013.
- Groß, S., V. Freudenthaler, M. Wirth, and B. Weinzierl (2015), Towards an aerosol classification scheme for future EarthCARE lidar observations and implications for research needs, *Atmos. Sci. Lett.*, *16*, 77–82, doi:10.1002/asl2.524.
- Grund, C. J., and E. W. Eloranta (1991), University of Wisconsin High Spectral Resolution Lidar, *Opt. Eng.*, *30*, 6–12, doi:10.1117/12.55766.
- Guerrero-Rascado, J. L., F. J. Olmo, I. Avilés-Rodríguez, F. Navas-Guzmán, D. Pérez-Ramírez, H. Lyamani, and L. Alados-Arboledas (2009), Extreme Saharan dust event over the southern Iberian Peninsula in september 2007: active and passive remote sensing from surface and satellite, *Atmos. Chem. Phys.*, *9*, 8453–8469, doi:10.5194/acp-9-8453-2009.
- Hair, J. W., C. A. Hostetler, A. L. Cook, D. B. Harper, R. A. Ferrare, T. L. Mack, W. Welch, L. R. Izquierdo, and F. E. Hovis (2008), Airborne High Spectral Resolution Lidar for profiling aerosol optical properties, *Appl. Opt.*, *47*, 6734–6752, doi:10.1364/AO.47.006734.
- Hamburger, T., G. McMeeking, A. Minikin, A. Petzold, H. Coe, and R. Krejci (2012), Airborne observations of aerosol microphysical properties and particle ageing processes in the troposphere above Europe, *Atmos. Chem. Phys.*, *12*, 11533–11554, doi:10.5194/acp-12-11533-2012.
- Hamonou, E., P. Chazette, D. Balis, F. Dulac, X. Schneider, E. Galani, G. Ancellet, and A. Papayannis (1999), Characterization of the vertical structure of Saharan dust export to the Mediterranean basin, *J. Geophys. Res.-Atmos.*, *104*, 22257–22270, doi:10.1029/1999JD900257.
- Hansen, J., M. Sato, and R. Ruedy (1997), Radiative forcing and climate response, *J. Geophys. Res.-Atmos.*, *102*, 6831–6864.
- Hasekamp, O. P., P. Litvinov, and A. Butz (2011), Aerosol properties over the ocean from PARASOL multiangle photopolarimetric measurements, *J. Geophys. Res.-Atmos.*, *116*, doi:10.1029/2010JD015469.
- Heald, C. L., D. A. Ridley, J. H. Kroll, S. R. H. Barrett, K. E. Cady-Pereira, M. J. Alvarado, and C. D. Holmes (2014), Contrasting the direct radiative effect and direct radiative forcing of aerosols, *Atmos. Chem. Phys.*, *14*, 5513–5527, doi:10.5194/acp-14-5513-2014.
-

- Heese, B., and M. Wiegner (2008), Vertical aerosol profiles from Raman polarization lidar observations during the dry season AMMA field campaign, *J. Geophys. Res.-Atmos.*, *113*, doi:10.1029/2007JD009487.
- Heintzenberg, J. (2009), The SAMUM-1 experiment over Southern Morocco: overview and introduction, *Tellus B*, *61*, 2–11, doi:10.1111/j.1600-0889.2008.00403.x.
- Heintzenberg, J., D. C. Covert, and R. van Dingenen (2000), Size distribution and chemical composition of marine aerosols: a compilation and review, *Tellus B*, *52*, 1104–1122, doi:10.1034/j.1600-0889.2000.00136.x.
- Heintzenberg, J., T. Tuch, B. Wehner, A. Wiedensohler, H. Wex, A. Ansmann, I. Mattis, D. Müller, M. Wendisch, S. Eckhardt, and A. Stohl (2003), Arctic haze over Central Europe, *Tellus, Ser. B*, *55*, 796–807, doi:10.1034/j.1600-0889.2003.00057.x.
- Hess, M., P. Koepke, and I. Schult (1998), Optical properties of Aerosols and Clouds: The Software Package OPAC, *Bull. Amer. Meteorol. Soc.*, *79*, 831–844, doi:10.1175/1520-0477(1998)079<0831:OPOAAC>2.0.CO;2.
- Hinkley, E. D. (1976), *Laser Monitoring of the Atmosphere*, vol. 14, 396 pp., Springer.
- Holben, B. N., T. F. Eck, I. Slutsker, D. Tanré, J. P. Buis, A. Setzer, E. Vermote, J. A. Reagan, Y. J. Kaufman, T. Nakajima, F. Lavenu, I. Jankowiak, and A. Smirnov (1998), AERONET — A Federated Instrument Network and Data Archive for Aerosol Characterization, *Remote Sens. Environ.*, *66*, 1–16, doi:10.1016/S0034-4257(98)00031-5.
- Holzer-Popp, T., G. de Leeuw, J. Griesfeller, D. Martynenko, L. Klüser, S. Bevan, W. Davies, F. Ducos, J. L. Deuzé, R. G. Grainger, A. Heckel, W. von Hoyningen-Huene, P. Kolmonen, P. Litvinov, P. North, C. A. Poulsen, D. Ramon, R. Siddans, L. Sogacheva, D. Tanré, G. E. Thomas, M. Vountas, J. Descloitres, J. Griesfeller, S. Kinne, M. Schulz, and S. Pinnock (2013), Aerosol retrieval experiments in the ESA Aerosol_cci project, *Atmos. Meas. Tech.*, *6*, 1919–1957, doi:10.5194/amt-6-1919-2013.
- Hoppel, W. A., J. W. Fitzgerald, G. M. Frick, R. E. Larson, and E. J. Mack (1990), Aerosol size distributions and optical properties found in the marine boundary layer over the Atlantic Ocean, *J. Geophys. Res.-Atmos.*, *95*, 3659–3686, doi:10.1029/JD095iD04p03659.
- Hostetler, C. A., Z. Liu, J. Reagan, M. Vaughan, D. Winker, M. Osborne, W. H. Hunt, K. A. Powell, and C. Trepte (2006), CALIOP Algorithm Theoretical Basis Document, Calibration and Level 1 Data Products, *Tech. rep.*
-

- Houghton, J. T., Y. Ding, D. J. Griggs, M. Noguer, P. J. van der Linden, X. Dai, K. Maskell, and C. A. Johnson (Eds.) (2001), *Climate Change 2001: The Scientific Basis. Contribution of Working Group I to the Third Assessment Report of the Intergovernmental Panel on Climate Change*, 892 pp., Cambridge University Press (<http://www.ipcc.ch>), New York.
- Huang, J., J. Guo, F. Wang, Z. Liu, M.-J. Jeong, H. Yu, and Z. Zhang (2015), CALIPSO Inferred Most Probable Heights of Global Dust and Smoke Layers, *J. Geophys. Res.-Atmos.*, *120*, 5085–5100, doi:10.1002/2014JD022898.
- Hunt, W. H., D. M. Winker, M. A. Vaughan, K. A. Powell, P. L. Lucker, and C. Weimer (2009), CALIPSO Lidar Description and Performance Assessment, *J. Atmos. Ocean. Tech.*, *26*, 1214–1228, doi:10.1175/2009JTECHA1223.1.
- Illingworth, A. J., R. J. Hogan, E. J. O’Connor, D. Bouniol, M. E. Brooks, J. Delanoë, D. P. Donovan, J. D. Eastment, N. Gaussiat, J. W. F. Goddard, M. Haeffelin, H. Klein Baltink, O. A. Krasnov, J. Pelon, J.-M. Piriou, A. Protat, H. W. J. Russchenberg, A. Seifert, A. M. Tompkins, G.-J. van Zadelhoff, F. Vinit, U. Willén, D. R. Wilson, and C. L. Wrench (2007), Cloudnet — Continuous Evaluation of Cloud Profiles in Seven Operational Models Using Ground-Based Observations, *Bull. Amer. Meteorol. Soc.*, *88*, 883–898, doi:10.1175/BAMS-88-6-883.
- Illingworth, A. J., H. W. Barker, A. Beljaars, M. Ceccaldi, H. Chepfer, J. Cole, J. Delanoë, C. Domenech, D. P. Donovan, S. Fukuda, M. Hidakata, R. J. Hogan, A. Hünerbein, P. Kollias, T. Kubota, T. Nakajima, T. Y. Nakajima, T. Nishizawa, Y. Ohno, H. Okamoto, R. Oki, K. Sato, M. Satoh, M. Shephard, U. Wandinger, T. Wehr, and G.-J. van Zadelhoff (2014), THE EARTHCARE SATELLITE: The next step forward in global measurements of clouds, aerosols, precipitation and radiation., *Bull. Amer. Meteorol. Soc.*, doi:10.1175/BAMS-D-12-00227.1.
- Jäger, H., and T. Deshler (2002), Lidar backscatter to extinction, mass and area conversions for stratospheric aerosols based on midlatitude balloonborne size distribution measurements, *Geophys. Res. Letts.*, *29*, doi:10.1029/2002GL015609.
- Josset, D., J. Pelon, and Y. Hu (2010), Multi-Instrument Calibration Method Based on a Multiwavelength Ocean Surface Model, *Geoscience and Remote Sensing Letters, IEEE*, *7*, 195–199, doi:10.1109/LGRS.2009.2030906.
- Kacenenbogen, M., M. A. Vaughan, J. Redemann, R. M. Hoff, R. R. Rogers, R. A. Ferrare, P. B. Russell, C. A. Hostetler, J. W. Hair, and B. N. Holben (2011), An accuracy assessment of the CALIOP/CALIPSO version 2/version 3 daytime aerosol
-

- extinction product based on a detailed multi-sensor, multi-platform case study, *Atmos. Chem. Phys.*, *11*, 3981–4000, doi:10.5194/acp-11-3981-2011.
- Kanamitsu, M. (1989), Description of the NMC Global Data Assimilation and Forecast System, *Weather and Forecasting*, *4*, 335–342, doi:10.1175/1520-0434(1989)004<0335:DOTNGD>2.0.CO;2.
- Kanitz, T., A. Ansmann, R. Engelmann, and D. Althausen (2013), North-south cross sections of the vertical aerosol distribution over the Atlantic Ocean from multiwavelength Raman/polarization lidar during Polarstern cruises, *J. Geophys. Res.-Atmos.*, *118*, 2643–2655, doi:10.1002/jgrd.50273.
- Kanitz, T., A. Ansmann, A. Foth, P. Seifert, U. Wandinger, R. Engelmann, H. Baars, D. Althausen, C. Casaccia, and F. Zamorano (2014a), Surface matters: limitations of CALIPSO V3 aerosol typing in coastal regions, *Atmos. Meas. Tech.*, *7*, 2061–2072, doi:10.5194/amt-7-2061-2014.
- Kanitz, T., R. Engelmann, B. Heinold, H. Baars, A. Skupin, and A. Ansmann (2014b), Tracking the Saharan Air Layer with shipborne lidar across the tropical Atlantic, *Geophys. Res. Lett.*, *41*, 1044–1050, doi:10.1002/2013GL058780.
- Kaufman, Y. J., D. Tanré, H. R. Gordon, T. Nakajima, J. Lenoble, R. Frouin, H. Grassl, B. M. Herman, M. D. King, and P. M. Teillet (1997), Passive remote sensing of tropospheric aerosol and atmospheric correction for the aerosol effect, *J. Geophys. Res.-Atmos.*, *102*, 16815–16830, doi:10.1029/97JD01496.
- Kent, G. S., C. R. Trepte, K. M. Skeens, and D. M. Winker (1998), LITE and SAGE II measurements of aerosols in the southern hemisphere upper troposphere, *J. Geophys. Res.*, *103*, 19,111–19,127, doi:10.1029/98JD00364.
- Kim, M.-H., S.-W. Kim, S.-C. Yoon, and A. H. Omar (2013), Comparison of aerosol optical depth between CALIOP and MODIS-Aqua for CALIOP aerosol subtypes over the ocean, *J. Geophys. Res.-Atmos.*, *118*, 13,241–13,252, doi:10.1002/2013JD019527.
- Kittaka, C., D. M. Winker, M. A. Vaughan, A. Omar, and L. A. Remer (2011), Intercomparison of column aerosol optical depths from CALIPSO and MODIS-Aqua, *Atmos. Meas. Tech.*, *4*, 131–141, doi:10.5194/amt-4-131-2011.
- Klett, J. D. (1981), Stable analytical solution for processing lidar returns, *Appl. Opt.*, *20*, 211–220, doi:10.1364/AO.20.000211.
- Klett, J. D. (1985), Lidar inversion with variable backscatter/extinction ratios, *Appl. Opt.*, *24*, 1638–1643, doi:10.1364/AO.24.001638.
-

- Knippertz, P., A. Ansmann, D. Althausen, D. Müller, M. Tesche, E. Bierwirth, T. Dinter, T. Müller, W. von Hoyningen-Huene, K. Schepanski, M. Wendisch, B. Heinold, K. Kandler, A. Petzold, L. Schütz, and I. Tegen (2009), Dust mobilization and transport in the northern Sahara during SAMUM 2006 – a meteorological overview, *Tellus B*, *61*, 12–31, doi:10.1111/j.1600-0889.2008.00380.x.
- Koepke, P., J. Gasteiger, and M. Hess (2015), Technical Note: Optical properties of desert aerosol with non-spherical mineral particles: data incorporated to OPAC, *Atmos. Chem. Phys.*, *15*, 5947–5956, doi:10.5194/acp-15-5947-2015.
- Kolgotin, A., and D. Müller (2008), Theory of inversion with two-dimensional regularization: profiles of microphysical particle properties derived from multiwavelength lidar measurements, *Appl. Opt.*, *47*, 4472–4490, doi:10.1364/AO.47.004472.
- Koren, I., Y. J. Kaufman, R. Washington, M. C. Todd, Y. Rudich, J. V. Martins, and D. Rosenfeld (2006), The Bodélé depression: a single spot in the Sahara that provides most of the mineral dust to the Amazon forest, *Env. Res. Lett.*, *1*, doi:10.1088/1748-9326/1/1/014005.
- Kovalev, V. A. (1995), Sensitivity of the lidar solution to errors of the aerosol backscatter-to-extinction ratio: Influence of a monotonic change in the aerosol extinction coefficient, *Appl. Opt.*, *34*, 3457–3462, doi:10.1364/AO.34.003457.
- Kovalev, V. A., and W. E. Eichinger (2004), *Elastic Lidar. Theory, Practice, and Analysis Methods*, 615 pp., John Wiley & Sons, Weinheim, Germany.
- Kunz, G. J. (1996), Transmission as an input boundary value for an analytical solution of a single-scatter lidar equation, *Appl. Opt.*, *35*, 3255–3260, doi:10.1364/AO.35.003255.
- Léon, J.-F., D. Tanré, J. Pelon, Y. J. Kaufman, J. M. Haywood, and B. Chatenet (2003), Profiling of a Saharan dust outbreak based on a synergy between active and passive remote sensing, *J. Geophys. Res.-Atmos.*, *108*, doi:10.1029/2002JD002774.
- Lesins, G., P. Chylek, and U. Lohmann (2002), A study of internal and external mixing scenarios and its effect on aerosol optical properties and direct radiative forcing, *J. Geophys. Res.-Atmos.*, *107*, doi:10.1029/2001JD000973.
- Lieke, K., K. Kandler, D. Scheuven, C. Emmel, C. von Glahn, A. Petzold, B. Weinzierl, A. Veira, M. Ebert, S. Weinbruch, and L. Schütz (2011), Particle chemical properties in the vertical column based on aircraft observations in the vicinity of Cape Verde Islands, *Tellus B*, *63*, doi:10.1111/j.1600-0889.2011.00553.x.
-

- Liu, Z., I. Matsui, and N. Sugimoto (1999), High-spectral-resolution lidar using an iodine absorption filter for atmospheric measurements, *Opt. Eng.*, *38*, 1661–1670, doi:10.1117/1.602218.
- Liu, Z., M. A. Vaughan, D. M. Winker, C. Hostetler, L. R. Poole, D. Hlavka, W. Hart, and M. McGill (2004), Use of probability distribution functions for discriminating between cloud and aerosol in lidar backscatter data, *J. Geophys. Res.*, *109*, doi:10.1029/2004JD004732.
- Liu, Z., A. Omar, M. Vaughan, J. Hair, C. Kittaka, Y. Hu, K. Powell, C. Trepte, D. Winker, C. Hostetler, R. Ferrare, and R. Pierce (2008), CALIPSO lidar observations of the optical properties of Saharan dust: A case study of long-range transport, *J. Geophys. Res.*, *113*, doi:10.1029/2007JD008878.
- Liu, Z., M. Vaughan, D. Winker, C. Kittaka, B. Getzewich, R. Kuehn, A. Omar, K. Powell, C. Trepte, and C. Hostetler (2009), The CALIPSO Lidar Cloud and Aerosol Discrimination: Version 2 Algorithm and Initial Assessment of Performance, *J. Atmos. Ocean. Tech.*, *26*, 1198–1213, doi:10.1175/2009JTECHA1229.1.
- Liu, Z., R. Kuehn, M. Vaughan, D. Winker, A. Omar, K. Powell, C. Trepte, Y. Hu, and C. Hostetler (2010), The CALIPSO cloud and aerosol discrimination: version 3 algorithm and test results, in *Proceedings of the 25th International Laser Radar Conference*, pp. 1245–1248, St. Petersburg, Russia, 5–9 July 2010.
- Liu, Z., T. D. Fairlie, I. Uno, J. Huang, D. Wu, A. Omar, J. Kar, M. Vaughan, R. Rogers, D. Winker, C. Trepte, Y. Hu, W. Sun, B. Lin, and A. Cheng (2013), Transpacific transport and evolution of the optical properties of Asian dust, *J. Quant. Spectrosc. Radiat. Transfer*, *116*, 24–33, doi:10.1016/j.jqsrt.2012.11.011.
- Lopatin, A., O. Dubovik, A. Chaikovsky, P. Goloub, T. Lapyonok, D. Tanré, and P. Litvinov (2013), Enhancement of aerosol characterization using synergy of lidar and sun-photometer coincident observations: the GARRLiC algorithm, *Atmos. Meas. Tech.*, *6*, 2065–2088, doi:10.5194/amt-6-2065-2013.
- Lopes, F. J. S., E. Landulfo, and M. A. Vaughan (2013), Evaluating CALIPSO’s 532 nm lidar ratio selection algorithm using AERONET sun photometers in Brazil, *Atmos. Meas. Tech.*, *6*, 3281–3299, doi:10.5194/amt-6-3281-2013.
- Ma, X., K. Bartlett, K. Harmon, and F. Yu (2013), Comparison of AOD between CALIPSO and MODIS: significant differences over major dust and biomass burning regions, *Atmos. Meas. Tech.*, *6*, 2391–2401, doi:10.5194/amt-6-2391-2013.
-

- Mahalanobis, P. C. (1936), On the generalized distance in statistics, *Proceedings of the National Institute of Sciences India (Calcutta)*, *2*, 49–55.
- Mahowald, N., S. Albani, J. F. Kok, S. Engelstaeder, R. Scanza, D. S. Ward, and M. G. Flanner (2014), The size distribution of desert dust aerosols and its impact on the Earth system, *Aeolian Research*, *15*, 53–71, doi:10.1016/j.aeolia.2013.09.002.
- Mamouri, R. E., and A. Ansmann (2014), Fine and coarse dust separation with polarization lidar, *Atmos. Meas. Tech.*, *7*, 3717–3735, doi:10.5194/amt-7-3717-2014.
- Mamouri, R. E., V. Amiridis, A. Papayannis, E. Giannakaki, G. Tsaknakis, and D. S. Balis (2009), Validation of CALIPSO space-borne-derived attenuated backscatter coefficient profiles using a ground-based lidar in Athens, Greece, *Atmos. Meas. Tech.*, *2*, 513–522, doi:10.5194/amt-2-513-2009.
- Mamouri, R. E., A. Ansmann, A. Nisantzi, P. Kokkalis, A. Schwarz, and D. Hadjimitsis (2013), Low Arabian dust extinction-to-backscatter ratio, *Geophys. Res. Lett.*, *40*, 4762–4766, doi:10.1002/grl.50898.
- Marelle, L., J.-C. Raut, J. L. Thomas, K. S. Law, B. Quennehen, G. Ancellet, J. Pelon, A. Schwarzenboeck, and J. D. Fast (2015), Transport of anthropogenic and biomass burning aerosols from Europe to the Arctic during spring 2008, *Atmos. Chem. Phys.*, *15*, 3831–3850, doi:10.5194/acp-15-3831-2015.
- Matthias, V., D. Balis, J. Bösenberg, R. Eixmann, M. Iarlori, L. Komguem, I. Mattis, A. Papayannis, G. Pappalardo, M. Perrone, and X. Wang (2004), Vertical aerosol distribution over Europe: Statistical analysis of Raman lidar data from 10 European Aerosol Research Lidar Network (EARLINET) stations, *J. Geophys. Res.*, *109*, doi:10.1029/2004JD004638.
- Mattis, I. (2003), Compilation of trajectory data. EARLINET: A European Aerosol Research Lidar Network to Establish an Aerosol Climatology, Report No. 348, Max Planck Institute for Meteorology, Hamburg, Germany, Url: http://www.mpimet.mpg.de/fileadmin/publikationen/Reports/max_scirep_348.pdf.
- Mattis, I., A. Ansmann, D. Müller, U. Wandinger, and D. Althausen (2002), Dual-wavelength Raman lidar observations of the extinction-to-backscatter ratio of Saharan dust, *Geophys. Res. Letts.*, *29*, doi:10.1029/2002GL014721.
- Mattis, I., A. Ansmann, U. Wandinger, and D. Müller (2003), Unexpectedly high aerosol load in the free troposphere over central Europe in spring/summer 2003, *Geophys. Res. Letts.*, *30*, doi:10.1029/2003GL018442.
-

- Mattis, I., A. Ansmann, D. Müller, U. Wandinger, and D. Althausen (2004), Multiyear aerosol observations with dual-wavelength Raman lidar in the framework of EARLINET, *J. Geophys. Res.*, *109*, doi:10.1029/2004JD004600.
- Mattis, I., P. Seifert, D. Müller, M. Tesche, A. Hiebsch, T. Kanitz, J. Schmidt, F. Finger, U. Wandinger, and A. Ansmann (2010), Volcanic aerosol layers observed with multiwavelength Raman lidar over central Europe in 2008–2009, *J. Geophys. Res.*, *115*, doi:10.1029/2009JD013472.
- McCormick, M. P., D. M. Winker, E. V. Browell, J. A. Coakley, C. S. Gardner, R. M. Hoff, G. S. Kent, S. H. Melfi, R. T. Menzies, C. M. R. Platt, D. A. Randall, and J. A. Reagan (1993), Scientific investigations planned for the Lidar In-space Technology Experiment (LITE), *Bull. Amer. Meteorol. Soc.*, *74*, 205–214, doi:10.1175/1520-0477(1993)074<0205:SIPFTL>2.0.CO;2.
- Megie, G. (1985), Laser remote sensing: Fundamentals and applications, *Eos, T. Am. Geophys. Union*, *66*, 686–686, doi:10.1029/EO066i040p00686-05.
- Menut, L., C. Flamant, J. Pelon, and P. H. Flamant (1999), Urban boundary-layer height determination from lidar measurements over the Paris area, *Appl. Opt.*, *38*, 945–954, doi:10.1364/AO.38.000945.
- Mielonen, T., A. Arola, M. Komppula, J. Kukkonen, J. Koskinen, G. de Leeuw, and K. E. J. Lehtinen (2009), Comparison of CALIOP level 2 aerosol subtypes to aerosol types derived from AERONET inversion data, *Geophys. Res. Lett.*, *36*, doi:10.1029/2009GL039609.
- Mishchenko, M. I., L. D. Travis, R. A. Kahn, and R. A. West (1997), Modeling phase functions for dustlike tropospheric aerosols using a shape mixture of randomly oriented polydisperse spheroids, *J. Geophys. Res.*, *102*, 16,831–16,847, doi:10.1029/96JD02110.
- Mishchenko, M. I., G. Videen, V. A. Babenko, N. G. Khlebtsov, and T. Wriedt (2004), T-matrix theory of electromagnetic scattering by particles and its applications: A comprehensive reference database, *J. Quant. Spectrosc. Radiat. Transfer*, *88*, 357–406, doi:10.1016/j.jqsrt.2004.05.002.
- Mona, L., A. Amodeo, M. Pandolfi, and G. Pappalardo (2006), Saharan dust intrusions in the Mediterranean area: Three years of Raman lidar measurements, *J. Geophys. Res.*, *111*, doi:10.1029/2005JD006569.
-

- Mona, L., G. Pappalardo, A. Amodeo, G. D'Amico, F. Madonna, A. Boselli, A. Giunta, F. Russo, and V. Cuomo (2009), One year of CNR–IMAA multi-wavelength Raman lidar measurements in coincidence with CALIPSO overpasses: Level 1 products comparison, *Atmos. Chem. Phys.*, *9*, 7213–7228, doi:10.5194/acp-9-7213-2009.
- Müller, D., U. Wandinger, and A. Ansmann (1999), Microphysical particle parameters from extinction and backscatter lidar data by inversion with regularization: Theory, *Appl. Opt.*, *38*, 2346–2357, doi:10.1364/AO.38.002346.
- Müller, D., A. Ansmann, F. Wagner, K. Franke, and D. Althausen (2002), European pollution outbreaks during ACE 2: Microphysical particle properties and single-scattering albedo inferred from multiwavelength lidar observations, *J. Geophys. Res.*, *107*, doi:10.1029/2001JD001110.
- Müller, D., K. Franke, A. Ansmann, D. Althausen, and F. Wagner (2003a), Indo-Asian pollution during INDOEX: Microphysical particle properties and single-scattering albedo inferred from multiwavelength lidar observations, *J. Geophys. Res.*, *108*, doi:10.1029/2003JD003538.
- Müller, D., I. Mattis, U. Wandinger, A. Ansmann, D. Althausen, O. Dubovik, S. Eckhardt, and A. Stohl (2003b), Saharan dust over a central European EARLINET–AERONET site: Combined observations with Raman lidar and Sun photometer, *J. Geophys. Res.*, *108*, doi:10.1029/2002JD002918.
- Müller, D., I. Mattis, B. Wehner, D. Althausen, U. Wandinger, A. Ansmann, and O. Dubovik (2004), Comprehensive characterization of Arctic haze from combined observations with Raman lidar and Sun photometer, *J. Geophys. Res.*, *109*, doi:10.1029/2003JD004200.
- Müller, D., I. Mattis, U. Wandinger, A. Ansmann, D. Althausen, and A. Stohl (2005), Raman lidar observations of aged Siberian and Canadian forest fire smoke in the free troposphere over Germany in 2003: Microphysical particle characterization, *J. Geophys. Res.*, *110*, doi:10.1029/2004JD005756.
- Müller, D., M. Tesche, H. Eichler, R. Engelmann, D. Althausen, A. Ansmann, Y. F. Cheng, Y. H. Zhang, and M. Hu (2006), Strong particle light-absorption over the Pearl River Delta (south China) and Beijing (north China) determined from combined Raman lidar and Sun photometer observations, *Geophys. Res. Letts.*, *33*, doi:10.1029/2006GL027196.
- Müller, D., A. Ansmann, I. Mattis, M. Tesche, U. Wandinger, D. Althausen, and G. Pisani (2007a), Aerosol–type–dependent lidar ratios observed with Raman lidar, *J. Geophys. Res.*, *112*, doi:10.1029/2006jd008292.
-

- Müller, D., I. Mattis, A. Ansmann, U. Wandinger, C. Ritter, and D. Kaiser (2007b), Multiwavelength Raman lidar observations of particle growth during long-range transport of forest-fire smoke in the free troposphere, *Geophys. Res. Letts.*, *34*, doi:10.1029/2006GL027936.
- Müller, D., A. Kolgotin, I. Mattis, A. Petzold, and A. Stohl (2011), Vertical profiles of microphysical particle properties derived from inversion with two-dimensional regularization of multiwavelength Raman lidar data: experiment, *Appl. Opt.*, *50*, 2069–2079, doi:10.1364/AO.50.002069.
- Müller, D., C. A. Hostetler, R. A. Ferrare, S. P. Burton, E. Chemyakin, A. Kolgotin, J. W. Hair, A. L. Cook, D. B. Harper, R. R. Rogers, R. W. Hare, C. S. Cleckner, M. D. Obland, J. Tomlinson, L. K. Berg, and B. Schmid (2014), Airborne Multiwavelength High Spectral Resolution Lidar (HSRL-2) observations during TCAP 2012: vertical profiles of optical and microphysical properties of a smoke/urban haze plume over the northeastern coast of the US, *Atmos. Meas. Tech.*, *7*, 3487–3496, doi:10.5194/amt-7-3487-2014.
- Murayama, T., M. Furushima, A. Oda, N. Iwasaka, and K. Kai (1996), Depolarization Ratio Measurements in the Atmospheric Boundary Layer by Lidar in Tokyo, *J. Meteorol. Soc. Jpn.*, *74*.
- Murayama, T., H. Okamoto, N. Kaneyasu, H. Kamataki, and K. Miura (1999), Application of lidar depolarization measurement in the atmospheric boundary layer: Effects of dust and sea-salt particles, *J. Geophys. Res.-Atmos.*, *104*, 31781–31792, doi:10.1029/1999JD900503.
- Murayama, T., S. J. Masonis, J. Redemann, T. L. Anderson, B. Schmid, J. M. Livingston, P. B. Russell, B. Huebert, S. G. Howell, C. S. McNaughton, A. Clarke, M. Abo, A. Shimizu, N. Sugimoto, M. Yabuki, H. Kuze, S. Fukagawa, K. Maxwell-Meier, R. J. Weber, D. A. Orsini, B. Blomquist, A. Bandy, and D. Thornton (2003), An intercomparison of lidar-derived aerosol optical properties with airborne measurements near Tokyo during ACE-Asia, *J. Geophys. Res.*, *108*, doi:10.1029/2002JD003259.
- Murayama, T., D. Müller, K. Wada, A. Shimizu, M. Sekigushi, and T. Tsukamoto (2004), Characterization of Asian dust and Siberian smoke with multi-wavelength Raman lidar over Tokyo, Japan in spring 2003, *Geophys. Res. Letts.*, *31*, doi:10.1029/2004GL021105.
-

- Nickovic, S., G. Kallos, A. Papadopoulos, and O. Kakaliagou (2001), A model for prediction of desert dust cycle in the atmosphere, *J. Geophys. Res.*, *106*, 18113–18130, doi:10.1029/2000JD900794.
- Nicolae, D., A. Nemuc, D. Müller, C. Talianu, J. Vasilescu, L. Belegante, and A. Kolgotin (2013), Characterization of fresh and aged biomass burning events using multiwavelength Raman lidar and mass spectrometry, *J. Geophys. Res.-Atmos.*, *118*, 2956–2965, doi:10.1002/jgrd.50324.
- Nicolae, D., L. Belegante, C. Talianu, and J. Vasilescu (2015), Using artificial neural networks to retrieve the aerosol type from multi-spectral lidar data, in *European Geosciences Union (EGU) General Assembly 2015 Vienna (Austria), 12–17 April, Session: AS3.17/GI2.2 Lidar and Applications*, vol. 17, EGU2015-9793.
- Nishizawa, T., H. Okamoto, N. Sugimoto, I. Matsui, A. Shimizu, and K. Aoki (2007), An algorithm that retrieves aerosol properties from dual-wavelength polarized lidar measurements, *J. Geophys. Res.-Atmos.*, *112*, doi:10.1029/2006JD007435.
- Nishizawa, T., H. Okamoto, T. Takemura, N. Sugimoto, I. Matsui, and A. Shimizu (2008a), Aerosol retrieval from two-wavelength backscatter and one-wavelength polarization lidar measurement taken during the MR01K02 cruise of the R/V Mirai and evaluation of a global aerosol transport model, *J. Geophys. Res.-Atmos.*, *113*, doi:10.1029/2007JD009640.
- Nishizawa, T., N. Sugimoto, I. Matsui, A. Shimizu, B. Tatarov, and H. Okamoto (2008b), Algorithm to Retrieve Aerosol Optical Properties From High-Spectral-Resolution Lidar and Polarization Mie-Scattering Lidar Measurements, *Geoscience and Remote Sensing, IEEE Transactions on*, *46*, 4094–4103, doi:10.1109/TGRS.2008.2000797.
- Nishizawa, T., N. Sugimoto, I. Matsui, A. Shimizu, X. Liu, Y. Zhang, R. Li, and J. Liu (2010), Vertical distribution of water-soluble, sea salt, and dust aerosols in the planetary boundary layer estimated from two-wavelength backscatter and one-wavelength polarization lidar measurements in Guangzhou and Beijing, China, *Atmos. Res.*, *96*, 602–611, doi:10.1016/j.atmosres.2010.02.002.
- Nishizawa, T., N. Sugimoto, I. Matsui, A. Shimizu, and H. Okamoto (2011), Algorithms to retrieve optical properties of three component aerosols from two-wavelength backscatter and one-wavelength polarization lidar measurements considering nonsphericity of dust, *J. Quant. Spectrosc. Radiat. Transfer*, *112*, 254–267, doi:10.1016/j.jqsrt.2010.06.002.
-

- Noh, Y. M. (2014), Single-scattering albedo profiling of mixed Asian dust plumes with multiwavelength Raman lidar, *Atmos. Env.*, *95*, 305–317, doi:10.1016/j.atmosenv.2014.06.028.
- Noh, Y. M., D. Müller, D. H. Shin, H. Lee, J. S. Jung, K. H. Lee, M. Cribb, Z. Li, and Y. J. Kim (2009), Optical and microphysical properties of severe haze and smoke aerosol measured by integrated remote sensing techniques in Gwangju, Korea, *Atmos. Env.*, *43*, 879–888, doi:10.1016/j.atmosenv.2008.10.058.
- Oikawa, E., T. Nakajima, T. Inoue, and D. Winker (2013), A study of the shortwave direct aerosol forcing using ESSP/CALIPSO observation and GCM simulation, *J. Geophys. Res.-Atmos.*, *118*, 3687–3708, doi:10.1002/jgrd.50227.
- Omar, A., Z. Liu, M. Vaughan, K. Thornhill, C. Kittaka, S. Ismail, Y. Hu, G. Chen, K. Powell, D. Winker, C. Trepte, E. Winstead, and B. Anderson (2010), Extinction-to-backscatter ratios of Saharan dust layers derived from in situ measurements and CALIPSO overflights during NAMMA, *J. Geophys. Res.-Atmos.*, *115*, doi:10.1029/2010JD014223.
- Omar, A. H., J.-G. Won, D. M. Winker, S.-C. Yoon, O. Dubovik, and M. P. McCormick (2005), Development of global aerosol models using cluster analysis of Aerosol Robotic Network (AERONET) measurements, *J. Geophys. Res.*, *110*, doi:10.1029/2004JD004874.
- Omar, A. H., D. M. Winker, C. Kittaka, M. A. Vaughan, Z. Liu, Y. Hu, C. R. Trepte, R. R. Rogers, R. A. Ferrare, K.-P. Lee, R. E. Kuehn, and C. A. Hostetler (2009), The CALIPSO Automated Aerosol Classification and Lidar Ratio Selection Algorithm, *J. Atmos. Ocean. Tech.*, *26*, 1994–2014, doi:10.1175/2009JTECHA1231.1.
- Omar, A. H., D. M. Winker, J. L. Tackett, D. M. Giles, J. Kar, Z. Liu, M. A. Vaughan, K. A. Powell, and C. R. Trepte (2013), CALIOP and AERONET aerosol optical depth comparisons: One size fits none, *J. Geophys. Res.-Atmos.*, *118*, 4748–4766, doi:10.1002/jgrd.50330.
- Oo, M., and R. Holz (2011), Improving the CALIOP aerosol optical depth using combined MODIS-CALIOP observations and CALIOP integrated attenuated total color ratio, *J. Geophys. Res.-Atmos.*, *116*, doi:10.1029/2010JD014894.
- Ottaviani, M., B. Cairns, J. Chowdhary, B. V. Diedenhoven, K. Knobelspiesse, C. Hostetler, R. Ferrare, S. Burton, J. Hair, M. D. Obland, and R. Rogers (2012), Polarimetric retrievals of surface and cirrus clouds properties in the region affected
-

- by the Deepwater Horizon oil spill, *Remote Sens. Environ.*, *121*, 389–403, doi:10.1016/j.rse.2012.02.016.
- Papayannis, A., V. Amiridis, L. Mona, G. Tsaknakis, D. Balis, J. Bösenberg, A. Chaikovski, F. De Tomasi, I. Grigorov, I. Mattis, V. Mitev, D. Müller, S. Nickovic, C. Pérez, A. Pietruczuk, G. Pisani, F. Ravetta, V. Rizi, M. Sicard, T. Trickl, M. Wiegner, M. Gerding, R. E. Mamouri, G. D’Amico, and G. Pappalardo (2008), Systematic lidar observations of Saharan dust over Europe in the frame of EARLINET (2000-2002), *J. Geophys. Res.*, *113*, doi:10.1029/2007JD9028.
- Papayannis, A., R. E. Mamouri, V. Amiridis, E. Remoundaki, G. Tsaknakis, P. Kokkalis, I. Veselovskii, A. Kolgotin, A. Nenes, and C. Fountoukis (2012), Optical-microphysical properties of Saharan dust aerosols and composition relationship using a multi-wavelength Raman lidar, in situ sensors and modelling: a case study analysis, *Atmos. Chem. Phys.*, *12*, 4011–4032, doi:10.5194/acp-12-4011-2012.
- Pappalardo, G., A. Amodeo, L. Mona, M. Pandolfi, N. Pergola, and V. Cuomo (2004a), Raman lidar observations of aerosol emitted during the 2002 Etna eruption, *Geophys. Res. Letts.*, *31*, doi:10.1029/2003GL019073.
- Pappalardo, G., A. Amodeo, M. Pandolfi, U. Wandinger, A. Ansmann, J. Bösenberg, V. Matthias, V. Amiridis, F. De Tomasi, M. Frioud, M. Iarlori, L. Komguem, A. Papayannis, F. Rocadenbosch, and X. Wang (2004b), Aerosol lidar intercomparison in the framework of the EARLINET project. 3. Raman lidar algorithm for aerosol extinction, backscatter and lidar ratio, *Appl. Opt.*, *43*, 5370–5385, doi:10.1364/AO.43.005370.
- Pappalardo, G., U. Wandinger, L. Mona, A. Hiebsch, I. Mattis, A. Amodeo, A. Ansmann, P. Seifert, H. Linné, A. Apituley, L. Alados-Arboledas, D. Balis, A. Chaikovsky, G. D’Amico, F. De Tomasi, V. Freudenthaler, E. Giannakaki, A. Giunta, I. Grigorov, M. Iarlori, F. Madonna, R. E. Mamouri, L. Nasti, A. Papayannis, A. Pietruczuk, M. Pujadas, V. Rizi, F. Rocadenbosch, F. Russo, F. Schnell, N. Spinelli, X. Wang, and M. Wiegner (2010), EARLINET correlative measurements for CALIPSO: First intercomparison results, *J. Geophys. Res.*, *115*, doi:10.1029/2009JD012147.
- Pappalardo, G., A. Amodeo, A. Apituley, A. Comeron, V. Freudenthaler, H. Linné, A. Ansmann, J. Bösenberg, G. D’Amico, I. Mattis, L. Mona, U. Wandinger, V. Amiridis, L. Alados-Arboledas, D. Nicolae, and M. Wiegner (2014), EARLINET: towards an advanced sustainable European aerosol lidar network, *Atmos. Meas. Tech.*, *7*, 2389–2409, doi:10.5194/amt-7-2389-2014.
-

- Pérez, C., S. Nickovic, J. M. Baldasano, M. Sicard, F. Rocadenbosch, and V. E. Cachorro (2006a), A long Saharan dust event over the western Mediterranean: Lidar, Sun photometer observations, and regional dust modeling, *J. Geophys. Res.*, *111*, doi:10.1029/2005JD006579.
- Pérez, C., S. Nickovic, G. Pejanovic, J. M. Baldasano, and E. Özsoy (2006b), Interactive dust-radiation modeling: A step to improve weather forecasts, *J. Geophys. Res.*, *111*, doi:10.1029/2005JD006717.
- Petzold, A., M. Fiebig, H. Flentje, A. Keil, U. Leiterer, F. Schröder, A. Stifter, M. Wendisch, and P. Wendling (2002), Vertical variability of aerosol properties observed at a continental site during the Lindenberg Aerosol Characterization Experiment (LACE 98), *J. Geophys. Res.-Atmos.*, *107*, doi:10.1029/2001JD001043.
- Petzold, A., A. Veira, S. Mund, M. Esselborn, C. Kiemle, B. Weinzierl, T. Hamburger, G. Ehret, K. Lieke, and K. Kandler (2011), Mixing of mineral dust with urban pollution aerosol over Dakar (Senegal): impact on dust physico-chemical and radiative properties, *Tellus B*, *63*, 619–634, doi:10.1111/j.1600-0889.2011.00547.x.
- Piironen, P., and E. W. Eloranta (1994), Demonstration of a high-spectral-resolution lidar based on an iodine absorption filter, *Opt. Lett.*, *19*, 234–236, doi:10.1364/OL.19.000234.
- Pitari, G., G. Di Genova, E. Coppari, N. De Luca, P. Di Carlo, M. Iarlori, and V. Rizi (2015), Desert dust transported over Europe: Lidar observations and model evaluation of the radiative impact, *J. Geophys. Res.-Atmos.*, *120*, 2881–2898, doi:10.1002/2014JD022875.
- Powell, K. A., M. Vaughan, D. Winker, K.-P. Lee, M. Pitts, C. Trepte, P. Detweiler, W. Hunt, J. Lambeth, P. Lucker, T. Murray, O. Hagolle, A. Lifermann, M. Faivre, A. Garnier, and J. Pelon (2011), *Cloud-aerosol LIDAR Infrared Pathfinder Satellite Observations Data Management System Data Products Catalog*, NASA Langley Research Center Document No: PC-SCI-503, NASA Langley Research Center, Hampton Virginia.
- Preißler, J. (2008), Geometrische und optische Eigenschaften von Aerosolschichten aus verschiedenen Quellregionen Europas (Geometrical and optical properties of aerosol layers from several European source regions), Diploma Thesis, University of Leipzig, Faculty of Physics and Earth Sciences, Leipzig, Germany.
- Preißler, J., F. Wagner, S. N. Pereira, and J. L. Guerrero-Rascado (2011), Multi-instrumental observation of an exceptionally strong Saharan dust outbreak over Portugal, *J. Geophys. Res.-Atmos.*, *116*, doi:10.1029/2011JD016527.
-

- Prospero, J. M., P. Ginoux, O. Torres, S. E. Nicholson, and T. E. Gill (2002), Environmental characterization of global sources of atmospheric soil dust identified with Nimbus 7 Total Ozone Mapping Spectrometer (TOMS) absorbing aerosol product, *Rev. Geophys.*, *40*, doi:10.1029/2000RG000095.
- Rahn, K. A., and N. Z. Heidam (1981), Progress in arctic air chemistry, 1977-1980: A comparison of the first and second symposia, *Atmos. Env.*, *15*, 1345–1348, doi:10.1016/0004-6981(81)90339-5.
- Reitebuch, O., C. Lemmerz, E. Nagel, U. Paffrath, Y. Durand, M. Endemann, F. Fabre, and M. Chaloupy (2009), The Airborne Demonstrator for the Direct-Detection Doppler Wind Lidar ALADIN on ADM-Aeolus. Part I: Instrument Design and Comparison to Satellite Instrument, *J. Atmos. Ocean. Tech.*, *26*, 2501–2515, doi:10.1175/2009JTECHA1309.1.
- Rogers, R. R., C. A. Hostetler, J. W. Hair, R. A. Ferrare, Z. Liu, M. D. Obland, D. B. Harper, A. L. Cook, K. A. Powell, M. A. Vaughan, and D. M. Winker (2011), Assessment of the CALIPSO Lidar 532 nm attenuated backscatter calibration using the NASA LaRC airborne High Spectral Resolution Lidar, *Atmos. Chem. Phys.*, *11*, 1295–1311, doi:10.5194/acp-11-1295-2011.
- Rogers, R. R., M. A. Vaughan, C. A. Hostetler, S. P. Burton, R. A. Ferrare, S. A. Young, J. W. Hair, M. D. Obland, D. B. Harper, A. L. Cook, and D. M. Winker (2014), Looking through the haze: evaluating the CALIPSO level 2 aerosol optical depth using airborne high spectral resolution lidar data, *Atmos. Meas. Tech.*, *7*, 4317–4340, doi:10.5194/amt-7-4317-2014.
- Russell, P. B., M. Kacenelenbogen, J. M. Livingston, O. P. Hasekamp, S. P. Burton, G. L. Schuster, M. S. Johnson, K. D. Knobelspiesse, J. Redemann, S. Ramachandran, and B. Holben (2014), A multiparameter aerosol classification method and its application to retrievals from spaceborne polarimetry, *J. Geophys. Res.-Atmos.*, *119*, 9838–9863, doi:10.1002/2013JD021411.
- Sakai, T., T. Nagai, M. Nakazato, Y. Mano, and T. Matsumura (2003), Ice clouds and Asian dust studied with lidar measurements of particle extinction-to-backscatter ratio, particle depolarization, and water-vapor mixing ratio over Tsukuba, *Appl. Opt.*, *42*, 7103–7116, doi:10.1364/AO.42.007103.
- Sakai, T., T. Nagai, Y. Zaizen, and Y. Mano (2010), Backscattering linear depolarization ratio measurements of mineral, sea-salt, and ammonium sulfate particles simulated in a laboratory chamber, *Appl. Opt.*, *49*, 4441–4449, doi:10.1364/AO.49.004441.
-

- Sasano, Y., and E. V. Browell (1989), Light scattering characteristics of various aerosol types derived from multiple wavelength lidar observations, *Appl. Opt.*, *28*, 1670–1679, doi:10.1364/AO.28.001670.
- Sasano, Y., E. V. Browell, and S. Ismail (1985), Error caused by using a constant extinction/backscatter ratio in the lidar solution, *Appl. Opt.*, *24*, 3929–3932, doi:10.1364/AO.24.003929.
- Sassen, K. (1977), Ice Crystal Habit Discrimination with the Optical Backscatter Depolarization Technique, *J. Appl. Meteorol.*, *16*, 425–431, doi:10.1175/1520-0450(1977)016<0425:ICHDT>2.0.CO;2.
- Sassen, K. (1991), The Polarization Lidar Technique for Cloud Research: A Review and Current Assessment, *Bull. Amer. Meteorol. Soc.*, *72*, 1848–1866, doi:10.1175/1520-0477(1991)072<1848:TPLTFC>2.0.CO;2.
- Sassen, K. (1999), Lidar Backscatter Depolarization Technique for Cloud and Aerosol Research, in *Light scattering by nonspherical particles: theory, measurements, and applications*, edited by M. I. Mishchenko, J. W. Hovenier, and L. D. Travis, Academic press.
- Sassen, K. (2005), Polarization in lidar, in *Lidar: Range-Resolved Optical Remote Sensing of the Atmosphere*, edited by C. Weitkamp, pp. 19–42, Springer.
- Sassen, K. (2008), Identifying Atmospheric Aerosols with Polarization Lidar, in *Advanced Environmental Monitoring*, edited by Y. Kim and U. Platt, pp. 136–142, Springer Netherlands, doi:10.1007/978-1-4020-6364-0_10.
- Schepanski, K., I. Tegen, B. Laurent, B. Heinold, and A. Macke (2007), A new Saharan dust source activation frequency map derived from MSG-SEVIRI IR-channels, *Geophys. Res. Letts.*, *34*, doi:10.1029/2007GL030168.
- Schotland, R. M., K. Sassen, and R. Stone (1971), Observations by Lidar of Linear Depolarization Ratios for Hydrometeors, *J. Appl. Meteorol.*, *10*, 1011–1017, doi:10.1175/1520-0450(1971)010<1011:OBLOLD>2.0.CO;2.
- Schuster, G. L., M. Vaughan, D. MacDonnell, W. Su, D. Winker, O. Dubovik, T. Lapyonok, and C. Trepte (2012), Comparison of CALIPSO aerosol optical depth retrievals to AERONET measurements, and a climatology for the lidar ratio of dust, *Atmos. Chem. Phys.*, *12*, 7431–7452, doi:10.5194/acp-12-7431-2012.
- Shaw, G. E. (1984), Microphysical size spectrum of Arctic haze, *Geophys. Res. Letts.*, *11*, 409–412.
-

-
- Shaw, G. E. (1995), The Arctic Haze Phenomenon, *Bull. American Meteorol. Soc.*, *76*, 2403–2413, doi:10.1175/1520-0477(1995)076<2403:TAHP>2.0.CO;2.
- She, C. Y., R. J. Alvarez, L. M. Caldwell, and D. A. Krueger (1992), High-spectral-resolution Rayleigh-Mie lidar measurement of aerosol and atmospheric profiles, *Opt. Lett.*, *17*, 541–543, doi:10.1364/OL.17.000541.
- Shimizu, A., N. Sugimoto, I. Matsui, K. Arao, I. Uno, T. Murayama, N. Kagawa, K. Aoki, A. Uchiyama, and A. Yamazaki (2004), Continuous observations of Asian dust and other aerosols by polarization lidars in China and Japan during ACE-Asia, *J. Geophys. Res.-Atmos.*, *109*, doi:10.1029/2002JD003253.
- Shimizu, H., S. A. Lee, and C. Y. She (1983), High spectral resolution lidar system with atomic blocking filters for measuring atmospheric parameters, *Appl. Opt.*, *22*, 1373–1381, doi:10.1364/AO.22.001373.
- Shin, S., Y. M. Noh, K. Lee, H. Lee, D. Müller, Y. J. Kim, K. Kim, and D. Shin (2014), Retrieval of the Single Scattering Albedo of Asian Dust Mixed with Pollutants Using Lidar Observations, *Adv. Atmos. Sci.*, *31*, 1417–1426, doi:10.1007/s00376-014-3244-y.
- Shiple, S. T., D. H. Tracy, E. W. Eloranta, J. T. Trauger, J. T. Sroga, F. L. Roesler, and J. A. Weinman (1983), High spectral resolution lidar to measure optical scattering properties of atmospheric aerosols, 1. Theory and instrumentation, *Appl. Opt.*, *22*, 3717–3724, doi:10.1364/AO.22.003716.
- Smirnov, A., B. N. Holben, Y. J. Kaufman, O. Dubovik, T. F. Eck, I. Slutsker, C. Pietras, and R. N. Halthore (2002), Optical Properties of Atmospheric Aerosol in Maritime Environments, *J. Atmos. Sci.*, *59*, 501–523, doi:10.1175/1520-0469(2002)059<0501:OPOAAI>2.0.CO;2.
- Stein, A., R. Draxler, G. Rolph, B. Stunder, M. Cohen, and F. Ngan (2015), NOAA’s HYSPLIT atmospheric transport and dispersion modeling system, *Bull. Amer. Meteorol. Soc.*, doi:10.1175/BAMS-D-14-00110.1, in press.
- Stocker, T. F., D. Qin, G.-K. Plattner, M. Tignor, S. K. Allen, J. Boschung, A. Nauels, Y. Xia, V. Bex, and P. M. Midgley (Eds.) (2014), *Climate Change 2013: The Physical Science Basis. Working Group I Contribution to the Fifth Assessment Report of the Intergovernmental Panel on Climate Change*, Cambridge University Press, Cambridge, United Kingdom and New York, NY, USA (<http://www.ipcc.ch>).
-

- Stoffelen, A., J. Pailleux, E. Källén, J. M. Vaughan, L. Isaksen, P. Flamant, W. Wergen, E. Andersson, H. Schyberg, A. Culoma, R. Meynart, M. Endemann, and P. Ingmann (2005), The Atmospheric Dynamics Mission for global wind field measurement, *Bull. American Meteorol. Soc.*, *86*, 73–87, doi:10.1175/BAMS-86-1-73.
- Stohl, A., and D. J. Thomson (1999), A Density Correction for Lagrangian Particle Dispersion Models, *Boundary-Layer Meteorol.*, *90*, 155–167, doi:10.1023/A:10017411110696.
- Stohl, A., M. Hittenberger, and G. Wotawa (1998), Validation of the lagrangian particle dispersion model FLEXPART against large scale tracer experiment data, *Atmos. Env.*, *32*, 4245–4264, doi:10.1016/S1352-2310(98)00184-8.
- Stohl, A., C. Forster, A. Frank, P. Seibert, and G. Wotawa (2005), Technical note: The Lagrangian particle dispersion model FLEXPART version 6.2, *Atmos. Chem. Phys.*, *5*, 2461–2474, doi:10.5194/acp-5-2461-2005.
- Sugimoto, N., and C. H. Lee (2006), Characteristics of dust aerosols inferred from lidar depolarization measurements at two wavelengths, *Appl. Opt.*, *45*, 7468–7474, doi:10.1364/AO.45.007468.
- Sugimoto, N., I. Matsui, A. Shimizu, I. Uno, K. Asai, T. Endoh, and T. Nakajima (2002), Observation of dust and anthropogenic aerosol plumes in the Northwest Pacific with a two-wavelength polarization lidar on board the research vessel Mirai, *Geophys. Res. Lett.*, *29*, doi:10.1029/2002GL015112.
- Sugimoto, N., I. Uno, M. Nishikawa, A. Shimizu, I. Matsui, X. Dong, Y. Chen, and H. Quan (2003), Record heavy Asian dust in Beijing in 2002: Observations and model analysis of recent events, *Geophys. Res. Lett.*, *30*, doi:10.1029/2002GL016349.
- Tanré, D., Y. J. Kaufman, M. Herman, and S. Mattoo (1997), Remote sensing of aerosol properties over oceans using the MODIS/EOS spectral radiances, *J. Geophys. Res.-Atmos.*, *102*, 16971–16988, doi:10.1029/96JD03437.
- Tanré, D., F. M. Bréon, J. L. Deuzé, O. Dubovik, F. Ducos, P. François, P. Goloub, M. Herman, A. Lifermann, and F. Waquet (2011), Remote sensing of aerosols by using polarized, directional and spectral measurements within the A-Train: the PARASOL mission, *Atmos. Meas. Tech.*, *4*, 1383–1395, doi:10.5194/amt-4-1383-2011.
- Tesche, M. (2011), Vertical profiling of aerosol optical properties with multiwavelength aerosol lidar during the Saharan Mineral Dust Experiments. PhD Dissertation, University of Leipzig, 163 pp.
-

- Tesche, M., A. Ansmann, D. Müller, D. Althausen, R. Engelmann, M. Hu, and Y. Zhang (2007), Particle backscatter, extinction, and lidar ratio profiling with Raman lidar in south and north China, *Appl. Opt.*, *46*, 6302–6308, doi:10.1364/AO.46.006302.
- Tesche, M., A. Ansmann, D. Müller, D. Althausen, R. Engelmann, V. Freudenthaler, and S. Groß (2009a), Vertically resolved separation of dust and smoke over Cape Verde using multiwavelength Raman and polarization lidars during Saharan Mineral Dust Experiment 2008, *J. Geophys. Res.*, *114*, doi:10.1029/2009JD011862.
- Tesche, M., A. Ansmann, D. Müller, D. Althausen, I. Mattis, B. Heese, V. Freudenthaler, M. Wiegner, M. Esselborn, G. Pisani, and P. Knippertz (2009b), Vertical profiling of Saharan dust with Raman lidars and airborne HSRL in southern Morocco during SAMUM, *Tellus B*, *61*, 144–164, doi:10.1111/j.1600-0889.2008.00390.x.
- Tesche, M., S. Groß, A. Ansmann, D. Müller, D. Althausen, V. Freudenthaler, and M. Esselborn (2011a), Profiling of Saharan dust and biomass-burning smoke with multiwavelength polarization Raman lidar at Cape Verde, *Tellus B*, *63*, 649–676, doi:10.1111/j.1600-0889.2011.00548.x.
- Tesche, M., D. Müller, S. Groß, A. Ansmann, D. Althausen, V. Freudenthaler, B. Weinzierl, A. Veira, and A. Petzold (2011b), Optical and microphysical properties of smoke over Cape Verde inferred from multiwavelength lidar measurements, *Tellus B*, *63*, 677–694, doi:10.1111/j.1600-0889.2011.00549.x.
- Tesche, M., U. Wandinger, A. Ansmann, D. Althausen, D. Müller, and A. H. Omar (2013), Ground-based validation of CALIPSO observations of dust and smoke in the Cape Verde region, *J. Geophys. Res.-Atmos.*, *118*, 2889–2902, doi:10.1002/jgrd.50248.
- The EARLINET publishing group 2000-2010 (2014), Earlinet all observations (2000-2010), doi:10.1594/WDCC/EN\$_{all}\$\$_{measurements}\$\$_{2000-2010}.
- Vakkari, V., V.-M. Kerminen, J. P. Beukes, P. Tiitta, P. G. van Zyl, M. Josipovic, A. D. Venter, K. Jaars, D. R. Worsnop, M. Kulmala, and L. Laakso (2014), Rapid changes in biomass burning aerosols by atmospheric oxidation, *Geophys. Res. Lett.*, *41*, 2644–2651, doi:10.1002/2014GL059396.
- Vaughan, M., S. Young, D. Winker, K. Powell, A. Omar, Z. Liu, Y. Hu, and C. Hostetler (2004), Fully automated analysis of space-based lidar data: an overview of the CALIPSO retrieval algorithms and data products, in *Laser Radar Techniques*
-

- for *Atmospheric Sensing, Proc. of SPIE, Vol. 5575*, edited by U. N. Singh, pp. 16–30, SPIE, Bellingham, Wa., doi:10.1117/12.572024.
- Vaughan, M. A., D. M. Winker, and K. A. Powell (2005), CALIOP Algorithm Theoretical Basis Document, Part 2: Feature Detection and Layer Properties Algorithms, *Tech. rep.*
- Vaughan, M. A., K. A. Powell, R. E. Kuehn, S. A. Young, D. M. Winker, C. A. Hostetler, W. H. Hunt, Z. Liu, M. J. McGill, and B. J. Getzewich (2009), Fully Automated Detection of Cloud and Aerosol Layers in the CALIPSO Lidar Measurements, *J. Atmos. Ocean. Tech.*, *26*, 2034–2050, doi:10.1175/2009JTECHA1228.1.
- Veselovskii, I., A. Kolgotin, V. Griaznov, D. Müller, U. Wandinger, and D. N. Whiteman (2002), Inversion with regularization for the retrieval of tropospheric aerosol parameters from multiwavelength lidar sounding, *Appl. Opt.*, *41*, 3685–3699, doi:10.1364/AO.41.003685.
- Veselovskii, I., D. N. Whiteman, M. Korenskiy, A. Kolgotin, O. Dubovik, D. Perez-Ramirez, and A. Suvorina (2013), Retrieval of spatio-temporal distributions of particle parameters from multiwavelength lidar measurements using the linear estimation technique and comparison with AERONET, *Atmos. Meas. Tech.*, *6*, 2671–2682, doi:10.5194/amt-6-2671-2013.
- Villani, M. G., L. Mona, A. Maurizi, G. Pappalardo, A. Tiesi, M. Pandolfi, M. D’Isidoro, V. Cuomo, and F. Tampieri (2006), Transport of volcanic aerosol in the troposphere: The case study of the 2002 Etna plume, *J. Geophys. Res.*, *111*, doi:10.1029/2006JD007126.
- Vuolo, M. R., M. Schulz, Y. Balkanski, and T. Takemura (2014), A new method for evaluating the impact of vertical distribution on aerosol radiative forcing in general circulation models, *Atmos. Chem. Phys.*, *14*, 877–897, doi:10.5194/acp-14-877-2014.
- Wagner, J., A. Ansmann, U. Wandinger, P. Seifert, A. Schwarz, M. Tesche, A. Chaikovsky, and O. Dubovik (2013), Evaluation of the Lidar/Radiometer Inversion Code (LIRIC) to determine microphysical properties of volcanic and desert dust, *Atmos. Meas. Tech.*, *6*, 1707–1724, doi:10.5194/amt-6-1707-2013.
- Wandinger, U. (2005), Raman lidar, in *Lidar. Range-resolved optical remote sensing of the atmosphere*, edited by C. Weitkamp, pp. 241–271, Springer.
- Wandinger, U., and A. Ansmann (2002), Experimental determination of the lidar overlap profile with Raman lidar, *Appl. Opt.*, *41*, 511–514, doi:10.1364/AO.41.000511.
-

- Wandinger, U., A. Ansmann, J. Reichardt, and T. Deshler (1995), Determination of stratospheric aerosol microphysical properties from independent extinction and backscattering measurements with a Raman lidar, *Appl. Opt.*, *34*, 8315–8329, doi:10.1364/AO.34.008315.
- Wandinger, U., D. Müller, C. Böckmann, D. Althausen, V. Matthias, J. Bösenberg, V. Weiß, M. Fiebig, M. Wendisch, A. Stohl, and A. Ansmann (2002), Optical and microphysical characterization of biomass-burning and industrial-pollution aerosols from multiwavelength lidar and aircraft measurements, *J. Geophys. Res.*, *107*, doi:10.1029/2000JD000202.
- Wandinger, U., I. Mattis, M. Tesche, A. Ansmann, J. Bösenberg, A. Chaikovski, V. Freudenthaler, L. Komguem, H. Linné, V. Matthias, J. Pelon, L. Sauvage, P. Sobolewski, G. Vaughan, and M. Wiegner (2004), Air mass modification over Europe: EARLINET aerosol observations from Wales to Belarus, *J. Geophys. Res.*, *109*, doi:10.1029/2004JD005142.
- Wandinger, U., M. Tesche, P. Seifert, A. Ansmann, D. Müller, and D. Althausen (2010), Size matters: Influence of multiple scattering on CALIPSO light-extinction profiling in desert dust, *Geophys. Res. Letts.*, *37*, doi:10.1029/2010GL042815.
- Wandinger, U., A. Hiebsch, I. Mattis, G. Pappalardo, L. Mona, and F. Madonna (2011), Aerosols and Clouds: Long-term Database from Spaceborne Lidar Measurements, *Tech. rep.*, Leipzig, Germany and Potenza, Italy, ESTEC Contract 21487/08/NL/HE, Final Report.
- Wang, X., A. Boselli, L. D’Avino, G. Pisani, N. Spinelli, A. Amodeo, A. Chaikovsky, M. Wiegner, S. Nickovic, A. Papayannis, M. R. Perrone, V. Rizi, L. Sauvage, and A. Stohl (2008), Volcanic dust characterization by EARLINET during Etna’s eruptions in 2001–2002, *Atmos. Env.*, *42*, 893–905, doi:10.1016/j.atmosenv.2007.10.020.
- Weinzierl, B., A. Petzold, M. Esselborn, M. Wirth, K. Rasp, K. Kandler, L. Schütz, P. Koepke, and M. Fiebig (2009), Airborne measurements of dust layer properties, particle size distribution and mixing state of Saharan dust during SAMUM 2006, *Tellus, Ser. B*, *61*, 96–117, doi:10.1111/j.1600-0889.2008.00392.x.
- Weinzierl, B., D. Sauer, M. Esselborn, A. Petzold, A. Veira, M. Rose, S. Mund, M. Wirth, A. Ansmann, M. Tesche, S. Groß, and V. Freudenthaler (2011), Microphysical and optical properties of dust and tropical biomass burning aerosol layers in the Cape Verde region – an overview of the airborne in situ and lidar measurements during SAMUM-2, *Tellus B*, *63*, doi:10.1111/j.1600-0889.2011.00566.x.
-

- Weinzierl, B., A. Ansmann, O. Reitebuch, V. Freudenthaler, T. Müller, K. Kandler, S. Groß, D. Sauer, D. Althausen, and C. Toledano (2014), Modification of Saharan Mineral Dust during Transport across the Atlantic Ocean – Overview and Results from the SALTRACE Field Experiment, in *EGU General Assembly Conference Abstracts*, vol. 16, p. 16876.
- Wiegner, M., J. Gasteiger, K. Kandler, B. Weinzierl, K. Rasp, M. Esselborn, V. Freudenthaler, B. Heese, C. Toledano, M. Tesche, and D. Althausen (2009), Numerical simulations of optical properties of Saharan dust aerosols with emphasis on lidar applications, *Tellus B*, *61*, 180–194, doi:10.1111/j.1600-0889.2008.00381.x.
- Wiegner, M., S. Groß, V. Freudenthaler, F. Schnell, and J. Gasteiger (2011), The May/June 2008 Saharan dust event over Munich: Intensive aerosol parameters from lidar measurements, *J. Geophys. Res.-Atmos.*, *116*, doi:10.1029/2011JD016619.
- Winker, D., S. Kato, and J. Tackett (2015), Global aerosol direct radiative effect from CALIOP and C3M, in *Proceedings of the 27th International Laser Radar Conference, New York City, NY, USA, 6–11 July 2015*.
- Winker, D. M., R. H. Couch, and M. P. McCormick (1996), An overview of LITE: NASA’s lidar in-space technology experiment, *Proceedings of the IEEE*, *84*, 164–180, doi:10.1109/5.482227.
- Winker, D. M., W. H. Hunt, and M. J. McGill (2007), Initial performance assessment of CALIOP, *Geophys. Res. Letts.*, *34*, doi:10.1029/2007GL030135.
- Winker, D. M., M. A. Vaughan, A. Omar, Y. Hu, K. A. Powell, Z. Liu, W. H. Hunt, and S. A. Young (2009), Overview of the CALIPSO mission and CALIOP data processing algorithms, *J. Atmos. Ocean. Tech.*, *26*, 2310–2323, doi:10.1175/2009JTECHA1281.1.
- Winker, D. M., J. L. Tackett, B. J. Getzewich, Z. Liu, M. A. Vaughan, and R. R. Rogers (2013), The global 3-D distribution of tropospheric aerosols as characterized by CALIOP, *Atmos. Chem. Phys.*, *13*, 3345–3361, doi:10.5194/acp-13-3345-2013.
- Young, S. A., and M. A. Vaughan (2009), The Retrieval of Profiles of Particulate Extinction from Cloud–Aerosol Lidar Infrared Pathfinder Satellite Observations (CALIPSO) Data: Algorithm Description, *J. Atmos. Ocean. Tech.*, *26*, 1105–1119, doi:10.1175/2008JTECHA1221.1.
- Young, S. A., D. M. Winker, M. A. Vaughan, Y. Hu, and R. E. Kuehn (2008), CALIOP Algorithm Theoretical Basis Document, Part 4: Extinction Retrieval Algorithms, *Tech. rep.*
-

- Young, S. A., M. A. Vaughan, R. E. Kuehn, and D. M. Winker (2013), The Retrieval of Profiles of Particulate Extinction from Cloud–Aerosol Lidar and Infrared Pathfinder Satellite Observations (CALIPSO) Data: Uncertainty and Error Sensitivity Analyses, *J. Atmos. Ocean. Tech.*, *30*, 395–428, doi:10.1175/JTECH-D-12-00046.1.
- Yu, H., M. Chin, T. Yuan, H. Bian, L. A. Remer, J. M. Prospero, A. Omar, D. Winker, Y. Yang, Y. Zhang, Z. Zhang, and C. Zhao (2015), The fertilizing role of African dust in the Amazon rainforest: A first multiyear assessment based on data from Cloud-Aerosol Lidar and Infrared Pathfinder Satellite Observations, *Geophys. Res. Lett.*, *42*, 1984–1991, doi:10.1002/2015GL063040.
- Zerefos, C., P. Nastos, D. Balis, A. Papayannis, A. Kelepertsis, E. Kannelopoulou, D. Nikolakis, C. Eleftheratos, W. Thomas, and C. Varotsos (2006), A complex study of Etna’s volcanic plume from ground-based, in situ and space-borne observations, *Int. J. Remote Sens.*, *27*, 1855–1864, doi:10.1080/01431160500462154.
-

List of Figures

| | | |
|-----|--|----|
| 2.1 | Color ratio (backscatter-related at 1064 and 532 nm) versus lidar ratio at 355 nm for different aerosol types observed with multiwavelength Raman lidars. Data are derived from Tab. 1 of <i>Müller et al.</i> [2007a]. | 9 |
| 2.2 | Generalized overview of characteristic aerosol types observable over the northern hemisphere. | 13 |
| 2.3 | Selection of 10-day MODIS maps of active fires for the northern hemisphere in the period July 2008 to June 2009. | 17 |
| 2.4 | Definition of European source regions for polluted continental aerosol. | 19 |
| 2.5 | Aerosol classification from measurements of lidar ratio and particle linear depolarization ratio at 355 nm [<i>Illingworth et al.</i> , 2014]. | 26 |
| 3.1 | Geographical distribution of the 27 currently active EARLINET stations, adapted from <i>Pappalardo et al.</i> [2014]. | 42 |
| 3.2 | Map of EARLINET stations whose data were used for this thesis. | 50 |
| 3.3 | CALIPSO satellite cross sections on 21 August 2008. | 51 |
| 3.4 | Flowchart of the CALIPSO lidar ratio selection scheme for tropospheric aerosols, adapted from <i>Omar et al.</i> [2009]. | 55 |
| 5.1 | Time–height contour plot of the range-corrected signal at 1064 nm and optical data of cloud-screened profiles measured at Cabauw between 00:01 and 01:23 UTC on 13 May 2008. | 68 |
| 5.2 | Left: FLEXPART footprint for the air mass traveling below 2 km height and arriving at Cabauw between 1.7 and 3.2 km height at 01:23 UTC on 13 May 2008. Right: NAAPS Total optical depth (550 nm) for 00:00 UTC on 13 May 2008 indicating the presence of sulfate over Central Europe during the measurement period. | 70 |
| 5.3 | FLEXPART footprints as time series for the air mass traveling below 2 km height and arriving at Cabauw between 1.7 and 3.2 km height at 01:23 UTC on 13 May 2008. Shown are the footprints each for 24-h integration time for the last 4 days before observation. | 71 |

| | | |
|------|--|----|
| 5.4 | Map of CALIPSO overpass with period of CALIOP observation used for comparison, HYSPLIT 24-h backward trajectories starting at Cabauw at 01:00 UTC on 13 May 2008 | 72 |
| 5.5 | Cross section of the total attenuated backscatter coefficient measured at 532 nm for the CALIPSO overpass at 02:02–02:07 UTC on 13 May 2008 and the results of the classification mask (related vertical feature mask and respective aerosol subtype) corresponding to the EARLINET observation at Cabauw. | 73 |
| 5.6 | Time–height contour plot of the range-corrected 1064-nm signal and profile data from the measurement at Potenza on 16–17 April 2009, 21:05–01:01 UTC. | 74 |
| 5.7 | Dust concentration profile for Potenza and predicted column dust load as well as 3000 m wind over North Africa, Middle East, and Europe for 17 April 2009, 00:00 UTC, from BSC/DREAM8b v2.0. | 75 |
| 5.8 | MODIS map of active fires (red spots) for the period 8–17 August 2008. The EARLINET stations of Athens and Thessaloniki are indicated. . . | 76 |
| 5.9 | Time–height contour plot of the 532-nm range-corrected signal from the measurement taken at Thessaloniki on 14–15 August 2008. | 77 |
| 5.10 | FLEXPART footprint for the air mass traveling below 2 km and arriving at Thessaloniki between 2.57 and 3.2 km at 00:27 UTC on 15 August 2008. | 78 |
| 5.11 | Cross sections of the total attenuated backscatter coefficient measured at 532 nm for the CALIPSO overpass at 00:35–00:49 UTC on 15 August 2008 and the results of the classification mask (related vertical feature mask and respective aerosol subtype) corresponding to the EARLINET observation at Thessaloniki. | 78 |
| 5.12 | Profile data from the measurement taken at Potenza on 8 July 2008, 00:19–02:26 UTC. | 79 |
| 5.13 | FLEXPART footprints for the air mass traveling below 2 km height and arriving at Potenza between 2.1 and 2.6 km height (left panel) and 3.0 and 4.6 km height (right panel) at 02:26 UTC on 8 July 2008. | 80 |
| 5.14 | Profile data from the measurement taken at Athens on 29–30 July 2008, 22:32–00:29 UTC. | 81 |
| 5.15 | FLEXPART footprint for the air mass traveling below 2 km height and arriving at Athens between 2 and 2.5 km height at 00:29 UTC on 30 July 2008. | 81 |
| 6.1 | Frequency of occurrence of pure and mixed aerosol types as obtained from the aerosol-layer analysis. | 86 |

| | | |
|------|--|-----|
| 6.2 | Frequency of occurrence of the pure and mixed aerosol types without volcanic events. | 87 |
| 6.3 | Frequency of occurrence of the aerosol types smoke, pollution, continental, marine, and dust in pure and mixed states. | 88 |
| 6.4 | Distribution of mean layer base and top heights and the resulting vertical extent for aerosol layers containing dust, continental, pollution, and smoke aerosol and frequently observed aerosol mixtures. | 89 |
| 6.5 | Frequency of occurrence of the pure and mixed aerosol types for the EARLINET stations Cabauw, Leipzig, Maisach, Granada, L'Aquila, Potenza, Athens, and Thessaloniki. | 90 |
| 6.6 | Lidar ratio at 355 and 532 nm for pure aerosol types. | 94 |
| 6.7 | Extinction- and backscatter-related 355-to-532-nm Ångström exponents for pure aerosol types. | 95 |
| 6.8 | 532-to-1064-nm and 355-to-1064-nm backscatter-related Ångström exponents for pure aerosol types. | 96 |
| 6.9 | Lidar ratio at 355 and 532 nm for aerosol mixtures. | 97 |
| 6.10 | Extinction- and backscatter-related 355-to-532-nm Ångström exponents for aerosol mixtures. | 98 |
| 6.11 | 532-to-1064-nm and 355-to-1064-nm backscatter-related Ångström exponents for aerosol mixtures. | 99 |
| 6.12 | Relation between backscatter-related 1064-to-532-nm color ratio as measured with CALIOP and lidar ratio at 355 nm as it will be measured with ATLID for all investigated EARLINET aerosol layers separated for pure aerosol types. | 101 |
| 6.13 | Relation between backscatter-related 1064-to-532-nm color ratio as measured with CALIOP and lidar ratio at 355 nm as it will be measured with ATLID for all investigated EARLINET aerosol layers separated for pure and mixed aerosol types. | 102 |
| 6.14 | Relation between backscatter-related 1064-to-532-nm color ratio as measured with CALIOP and lidar ratio at 355 nm as it will be measured with ATLID for derived mean values for pure and mixed aerosol types. | 103 |
| 6.15 | Three-dimensional relation between backscatter-related 1064-to-532-nm color ratio, lidar ratio at 355 nm, and particle linear depolarization ratio at 532 nm for the pure aerosol types. | 106 |
| 6.16 | Histogram of EARLINET aerosol layers that were detected and similarly classified by CALIPSO separated for investigated aerosol types with and without applied weighing factor. | 110 |
| 6.17 | Histogram of aerosol layers identified in data of the given EARLINET stations and searched for in corresponding CALIPSO overpass profiles. | 114 |

| | | |
|------|--|-----|
| 6.18 | Frequency of occurrence of aerosol types in correlative EARLINET and CALIPSO data used for the comparison. | 116 |
| 6.19 | Results of the CALIPSO aerosol typing scheme for EARLINET aerosol layers versus classified EARLINET aerosol types. | 117 |

List of Tables

| | | |
|-----|--|----|
| 1.1 | Active and planned long-term spaceborne lidar observations. | 3 |
| 2.1 | Lidar parameters retrieved from selected AERONET sites, after <i>Cattrall et al.</i> [2005]. | 25 |
| 2.2 | Summary of the key findings of optical properties (lidar ratios, Ångström exponents, particle linear depolarization ratio) found for marine aerosol. | 30 |
| 2.3 | Summary of the key findings of optical properties (lidar ratios, Ångström exponents, particle linear depolarization ratio) found for desert dust. | 31 |
| 2.4 | Summary of the key findings of optical properties (lidar ratios, Ångström exponents, particle linear depolarization ratio) found for polluted continental aerosol and arctic haze. | 32 |
| 2.5 | Summary of the key findings of optical properties (lidar ratios, Ångström exponents, particle linear depolarization ratio) found for biomass-burning aerosol. | 34 |
| 2.6 | Summary of the key findings of optical properties (lidar ratios, Ångström exponents, particle linear depolarization ratio) found for mixtures containing desert dust and other aerosols. | 35 |
| 3.1 | List of EARLINET stations and respective data used for this work. . . | 47 |
| 3.2 | Initial estimates of the lidar ratio at 532 and 1064 nm used for extinction and backscatter retrievals of the current CALIPSO data (Version 3) release for defined aerosol subtypes and stratospheric features, after <i>Omar et al.</i> [2009]. | 58 |
| 6.1 | Overview on aerosol types used in this thesis for the statistical evaluation of EARLINET data. | 85 |
| 6.2 | Mean values and standard deviation of extensive and intensive optical properties for pure aerosol types. | 91 |

| | | |
|------|--|-----|
| 6.3 | Mean values and standard deviation of extensive and intensive optical properties for different aerosol mixtures. | 92 |
| 6.4 | Summary of findings of the lidar ratio S_{532} and color ratio $C_{\beta,1064-532}$ found for the listed aerosol types; indices indicate the wavelength in nm and the related scattering coefficient. | 104 |
| 6.5 | Aerosol types used for the validation of the CALIPSO typing scheme. . | 107 |
| 6.6 | Selection of EARLINET data for the validation of the automatic CALIPSO classification scheme. | 108 |
| 6.7 | CALIOP profiles of a cross section used for the comparison to the correlative EARLINET measurement. Per bin and profile the occurrence of each CALIPSO aerosol type is shown, on the right side, the frequency of occurrence is shown. | 109 |
| 6.8 | All EARLINET aerosol layers separated for specific aerosol types and corresponding results of the CALIPSO feature classification and aerosol typing. | 111 |
| 6.9 | EARLINET aerosol layers classified in data of Potenza separated for specific aerosol types. In addition, the corresponding results of the CALIPSO feature classification and aerosol typing are given. | 112 |
| 6.10 | EARLINET aerosol layers classified in data of Leipzig separated for specific aerosol types. In addition, the corresponding results of the CALIPSO feature classification and aerosol typing are given. | 113 |
| 6.11 | EARLINET aerosol layers found in correlative CALIPSO overpass profiles and results of the CALIPSO aerosol typing scheme separated with respect to the distance between the EARLINET station and the cross section of CALIPSO. | 115 |

List of Abbreviations

| | |
|-------------|---|
| ACE-2 | Aerosol Characterization Experiment 2, over the sub-tropical North-East Atlantic (Canary Islands and Portugal), 16 June to 24 July 1997 |
| ADM-Aeolus | Atmospheric Dynamics Mission-Aeolus |
| AeroCom | Aerosol Comparisons between Observations and Models |
| AERONET | Aerosol Robotic Network |
| AERO-SAT | International Satellite Aerosol Science Network |
| a.g. | above ground |
| ALADIN | Atmospheric Laser Doppler Lidar Instrument |
| AOD | Aerosol optical depth |
| a.s.l. | above sea level |
| AT | Aerosol type |
| ATLID | Atmospheric Lidar |
| Bsc | Backscatter coefficient |
| BSC-CNS | Barcelona Supercomputing Center-Centro Nacional de Supercomputación |
| BSC-DREAM8b | Current online version of DREAM |
| BeNeLux | Belgium Netherlands Luxembourg |
| CAD | Cloud-Aerosol Discrimination |
| CALIOP | Cloud-Aerosol Lidar with Orthogonal Polarization |
| CALIPSO | Cloud-Aerosol Lidar and Infrared Pathfinder Satellite Observations |
| cf. | <i>confer</i> (latin for 'compare') |
| CISL | Computational & Information Systems Laboratory |
| CNES | Centre national d'études spatiales (English: National Centre for Space Studies) |
| DMS | Dimethyl sulfide |
| DREAM | Dust Regional Atmospheric Model |
| DWD | <i>Deutscher Wetterdienst</i> (German for 'German Meteorological Service') |

| | |
|-------------|---|
| EAL | EARLINET aerosol layer |
| EARLINET | European Aerosol Research Lidar Network |
| EarthCARE | Earth Clouds, Aerosols and Radiation Explorer |
| e.g. | <i>exempli gratia</i> (latin for ‘for example’) |
| EMEP | European Monitoring and Evaluation Programme |
| EOS | Earth Observing System |
| EOSDIS | Earth Observing System Data And Information System |
| ESA | European Space Agency |
| ESA–CALIPSO | EARLINET’s Spaceborne-related Activity during the CALIPSO mission |
| Ext | Extinction coefficient |
| FIRMS | Fire Information for Resource Management System |
| FLEXPART | FLEXible PARTicle dispersion model |
| FNL | Final Analysis |
| FT | Free troposphere |
| FTP | File transfer protocol |
| GARRLiC | Generalized Aerosol Retrieval from Radiometer and Lidar Combined data |
| GDAS | Global Data Assimilation System |
| GFS | Global Forecast System |
| GMAO | Global Modeling and Assimilation Office |
| GME | Global Model of Germany’s National Meteorological Service |
| GTS | Global Telecommunications System |
| et al. | <i>et alii</i> (latin for ‘and others’) |
| HDF | Hierarchical Data Format |
| HERA | Hybrid Extinction Retrieval Algorithm |
| HSRL | High Spectral Resolution Lidar |
| HYSPLIT | Hybrid Single–Particle Lagrangian Integrated Trajectory |
| IDL | Interactive Data Language |
| i.e. | <i>id est</i> (latin for ‘that is’) |
| IIR | Imaging Infrared Radiometer |
| IPCC | International Panel on Climate Change |
| IR | Infrared |
| LACE 98 | Lindenberg Aerosol Characterization Experiment, Germany, 1998 |
| LaRC ASDC | Langley Research Center Atmospheric Science Data Center |
| Laser | Light amplification by stimulated emission of radiation |
| Lidar | Light detection and ranging |

| | |
|----------------------|---|
| LIRIC | Lidar/Radiometer Inversion Code |
| LITE | Lidar In-space Technology Experiment |
| LIVAS | Lidar Climatology of Vertical Aerosol Structure for Space-Based Lidar Simulation Studies |
| MODIS | Moderate Resolution Imaging Spectroradiometer |
| NAAPS | Navy Aerosol Analysis and Prediction System |
| NAMMA | NASA African Monsoon Multidisciplinary Analyses |
| NASA | National Aeronautics and Space Administration |
| NCAR | National Center for Atmospheric Research |
| NCEP | National Center for Environmental Prediction |
| NetCDF | Network Common Data Format |
| NOAA ARL | National Oceanic and Atmospheric Administration Air Resources Laboratory |
| NRL | Naval Research Laboratory |
| OPAC | Optical Properties of Aerosols and Clouds |
| PARASOL | Polarization and Anisotropy of Reflectances for Atmospheric Sciences coupled with Observations from a Lidar |
| PBL | Planetary boundary layer |
| PDF | Probability density function |
| PM | Particle mass |
| PM _{2.5} | Particle mass for particle diameter <2.5 μm |
| PM _{coarse} | Coarse particle mass |
| POLDER 3 | Polarization and Directionality of the Earth's Reflectances 3 |
| POLIPHON | Polarization-lidar photometer networking method |
| POLIS | POrtable LIdar System |
| Polly ^{XT} | Portable aerosol Raman lidar system |
| RFOV | Receiver field of view |
| SALTRACE | Saharan Aerosol Long-range Transport and Aerosol-Cloud-Interaction Experiment |
| SAMUM | Saharan Mineral Dust Experiment |
| SAMUM-1 | Saharan Mineral Dust Experiment, Morocco, 11 May to 10 June 2006 |
| SAMUM-2(a) | Saharan Mineral Dust Experiment, Cape Verde, 15 January to 14 February 2008 |
| SAMUM-2b | Saharan Mineral Dust Experiment, Cape Verde, 24 May to 17 June 2008 |
| SCA | Scene classification algorithms |
| SIBYL | Selective Iterated Boundary Location |
| SQL | Structured Query Language |

| | |
|--------|--|
| TROPOS | Leibniz Institute for Tropospheric Research |
| U.S.A. | United States of America |
| UTC | Universal Time Coordinated |
| UV | Ultraviolet |
| VIS | Visible |
| VRAME | Vertically Resolved Aerosol Model for Europe from a Synergy of EARLINET and AERONET data |
| WFC | Wide Field Camera |

List of Symbols

| Symbol | Description | Unit |
|-----------------------|---|--------------------------------|
| \perp | Cross-polarized component of a quantity | |
| \parallel | Parallel-polarized component of a quantity | |
| Greek Symbol | | |
| α | Extinction coefficient | m^{-1} |
| α^{mol} | Molecular extinction coefficient | m^{-1} |
| α^{par} | Particle extinction coefficient | m^{-1} |
| β | Backscatter coefficient | $\text{m}^{-1} \text{sr}^{-1}$ |
| β' | Attenuated backscatter coefficient | $\text{m}^{-1} \text{sr}^{-1}$ |
| β^{mol} | Molecular backscatter coefficient | $\text{m}^{-1} \text{sr}^{-1}$ |
| β^{par} | Particle backscatter coefficient | $\text{m}^{-1} \text{sr}^{-1}$ |
| δ | Depolarization ratio | |
| δ^{par} | Particle linear depolarization ratio | |
| δ^{vol} | Volume linear depolarization ratio | |
| λ | Wavelength | m |
| λ_0 | Emitted wavelength | m |
| μ | Transmission of receiver optics | |
| π | Constant value | |
| τ_p | Laser pulse length | s |
| χ' | Attenuated total color ratio | |
| Latin Symbol | | |
| A_T | Area of the receiver telescope | m^2 |
| \mathring{a} | Ångström exponent | |
| \mathring{a}_α | Extinction-related Ångström exponent | |
| \mathring{a}_β | Backscatter-related Ångström exponent | |
| B' | Estimated integrated attenuated backscatter | $\text{m}^{-1} \text{sr}^{-1}$ |
| C | Calibration factor | |
| c | Speed of light | ms^{-1} |

| Symbol | Description | Unit |
|------------|---------------------------------|------|
| C_α | Extinction-related color ratio | |
| C_β | Backscatter-related color ratio | |
| g | Asymmetry factor | |
| O | Overlap function | |
| P | Lidar signal/detected energy | W |
| P_0 | Emitted laser energy | W |
| R | Range | m |
| R' | Attenuated scattering ratio | |
| S | Lidar ratio | sr |
| S^{mol} | Molecular lidar ratio | sr |
| S^{par} | Particle lidar ratio | sr |
| s | Ratio of lidar ratios | |
| T | Transmission (Attenuation term) | |
| T^{mol} | Transmission due to molecules | |
| T^{O_3} | Transmission due to Ozone | |
| T^{par} | Transmission due to particles | |
